Doctorate Dissertation
博士論文

Study of the Emission of Gamma-ray Bursts above 10 GeV with the Standard and Newly Recovered Data of the Fermi-LAT
（フェルミガンマ線宇宙望遠鏡の標準データと新たに回復したデータによるガンマ線バーストからの１０ＧｅＶ以上の放射に関する研究）

A Dissertation Submitted for Degree of Doctor of Philosophy
July 2018
平成３０年７月博士 (理学) 申請

Department of Physics, Graduate School of Science,
The University of Tokyo
東京大学大学院理学系研究科物理学専攻

Mitsunari Takahashi
髙橋　光成

Study of the Emission of Gamma-ray Bursts above 10 GeV with the Standard and Newly Recovered Data of the Fermi-LAT

Mitsunari Takahashi

Abstract

Gamma-ray bursts (GRBs) are the most energetic explosions in the Universe. They are cosmologically distant, and each of them releases a huge amount of energy in keV - MeV gamma-rays within a short period. Such "prompt" emission is followed by gradually decaying broadband "afterglow". The GRB emission is radiated by relativistic jets. Their progenitors, engines, mechanisms of jet acceleration and electromagnetic wave radiations are being debated. The afterglow emission is basically well explained by synchrotron radiation from fluid shocked by collisions between the jets and external medium. However, the Energetic Gamma Ray Experiment Telescope detected a 18 GeV photon, and the *Fermi* Large Area Telescope has detected many afterglow photons with energy from tens of GeV up to 95 GeV in these ten years. Such energy is challenging for a popular combination of the fireball jet acceleration and synchrotron radiation from the external shocks and may require another component such as inverse-Compton scattering. Identifying the responsible emission process in this energy range is important for revealing the central engine and energy dissipation process which causes the bursts.

In the energy range above $\sim$ 10 GeV, the sensitivity of the telescope is limited by the signal statistics. I developed novel photon classes of the *Fermi* Large Area Telescope in order to recover untapped events with energy above 20 GeV. Multivariate analysis for rejecting cosmic-ray backgrounds was optimized, and an increase of about 70% in the signal acceptance around the peak energy, $\sim$ 100 GeV, was achieved according to Monte Carlo simulation. In these classes, four candidates of photons correlated to gamma-ray bursts were found. The observed energy of an event correlated to GRB 090926A at $\sim 4.2 \times 10^2$ s after the trigger is 50 GeV. The redshift-corrected energy is 157 GeV. The observed energy of an event correlated to GRB 150902A at $\sim$ 2.1 ks after the trigger is 84 GeV, and the redshift is unknown. Two new events correlate to GRB 160509A at $\sim$ 2.1 ks and at $\sim$ 5.8 ks after the trigger. The observed and redshift-corrected energy is 116 GeV and 252 GeV, respectively, for the first event and 63 GeV and 137 GeV, respectively, for the second event. These events arrived much later than the end of the prompt phase, which is $\sim$ 16 s and $\sim 3.8 \times 10^2$ s after the trigger for GRB 090926A and for GRB 160509A, respectively. Here, the prompt and afterglow mean the periods before and after the time at which 95% of the total fluence has been detected in 10 keV – 1 MeV. Regarding the redshift-corrected energy, the highest energy event ever detected was a 144-GeV event from GRB 080916C in the prompt phase and a 127-GeV event from GRB 130427A in the afterglow phase. The GRB-frame energy of all the three redshift-known events is higher than that of GRB afterglow photons ever detected by any instruments although the background probabilities are not negligible, from 0.02% to 7%. These values exceed the synchrotron energy limit; otherwise, the energy injection to the external shocks might continue much longer than the observed prompt emission.

I also performed likelihood analysis focusing on the afterglows of the two GRBs. Reproducing their temporal and spectral features with synchrotron emission alone requires the loss of the energy of the shocked fluid dominated by radiation and a strong magnetic field. The simplest description for these afterglows is the synchrotron self-Compton emission from the external shocks although potential contributions of prompt components, late-time energy injection and flares cannot be excluded. If this synchrotron self-Compton interpretation is correct, detection of GRBs by Cherenkov Telescope Array in the near future is quite promising. Detailed light curves with little statistical uncertainty will enable us to differentiate effects of the long-term activities of the central engines and the external shock afterglows.

Acknowledgments

I would first like to acknowledge Masahiro Teshima. He invited me to the Institute for Cosmic Ray Research and showed me what experimental scientist is. All this study would not be done, without his great guide and support. David Paneque kindly accepted the fledgling student at the Max-Planck-Institue for Physics and the *Fermi*-LAT collaboration. My activities were fruitful thanks to him. I learned many things from discussion with him. I would like to appreciate that Katsuaki Asano patiently helped me to digest and apply theories of gamma-ray bursts.

I would like to thank Matthew Wood for developing a python module for multivariate analysis, which I heavily used in this study. I took over the development of the Calorimeter-only analysis by Carmelo Sgrò. This study would not have started without his idea and effort. I was supported by Regina Caputo, Francesco Longo, Michele Palatiello, David Green, Luca Baldini, and the members of the *Fermi*-LAT collaboration very much. In this study, I heavily used Jochen Greiner's web page [154] for gathering information of a number of gamma-ray bursts.

I acknowledge all my group colleagues, Masaaki Hayashida, Takanori Yoshikoshi, Koji Noda, Michiko Oishi, Daniel Mazin, Takayuki Saito, Daisuke Nakajima, Yoshitaka Hanabata, Koji Saito, Daniela Hadasch, Tsutomu Nagayoshi, Satoshi Fukami, Yuki Iwamura, Tomohiro Inada, Shunsuke Sakurai, Hayato Kuroda, Taku Kumon, Yukiho Kobayashi, Yoshiki, Otani, Hideyuki Ohoka, Nao Okazaki, Yusuke Inome, Norio Tajima, and Koichi Sekino. Especially, I was always supported by Midori Sugahara. I would also thank all the stuff of the Institute for Cosmic-ray Research.

I was helped by many people when I stayed in the Max-Planck-Institue for Physics. I would like to thank all the members of the experimental astroparticle physics group and the stuff of the institute. Sybille Rodríguez supported my stay kindly. Diana Werner immeasurably helped me to improve English in this thesis.

I acknowledge Hidetoshi Kubo, Tokonatsu Yamamoto, Kazuma Ishio, Shu Masuda, Shimpei Tsujimoto, and all the members of the Cherenkov Telescope Array consortium and the MAGIC collaboration. I would also like to thank friends in Youth Meeting for Astroparticle. I am happy that I

studied in these communities.

I remember my good old days in Ogawa Observatory and Planetarium which led me to astronomy. I thank to Yoshihito Sakai and Masahito Sakai. Lastly, I wish to tell my gratitude to my family. It is difficult to express in words.

Contents

Symbols and abbreviations

Table 1: Symbols used for denoting quantities commonly in the present thesis.

Symbol	Description
A_{eff}	Effective area
α	Power-law index of temporal decaying ($F_\nu \propto t^{-\alpha}\nu^{-\beta}$)
B	Strength of magnetic field
b	Galactic latitude
β	Power-law index of energy spectrum ($F_\nu \propto t^{-\alpha}\nu^{-\beta}$)
c	Light speed
d_L	Luminosity distance
E	(1) Event energy or (2) Isotropic-equivalent-energy of jet
$\mathcal{E}$	Exposure
e	Elementary charge
e	Base of natural logarithm
E_{prompt}	Isotropic-equivalent-energy of prompt emission
ϵ_B	Fraction of magnetic field energy density in shocked fluid
ϵ_e	Fraction of relativistic electron energy density in shocked fluid
$\bar{\epsilon_e}$	$\epsilon_e(p-2)/(p-1)$
F_ν	Specific energy flux
Γ	Lorentz factor of jet or shock front
γ	Lorentz factor of radiating particle
γ_2	Lorentz factor of shocked fluid
$\Gamma_{\gamma(X,O)}$	Power-law index of photon spectrum in γ-ray (X-ray, optical)
h	Planck constant
l	Galactic longitude
L	(1) Luminosity or (2) Sweep-up radius
M	Mass
$\mathrm{M}_\odot$	Mass of the Sun
m_e	Mass of electron
m_p	Mass of proton
N	(1) Number of observable count or (2) integral count flux
n	Number density
n_1	Proton number density in external medium

Table 2: Symbols used for denoting quantities commonly in the present thesis (continued).

Symbol	Description
ν	Frequency
p	Power-law index of particle energy distribution
R	Radius of (1) emission region or (2) shock front
r_0	Classical radius
σ_T	Thomson cross-section
T_0	Trigger time of GRB monitor
T_{05}	Time of 5% of total fluence
T_{75}	Time of 75% of total fluence
T_{90}	90% fluence duration
t	Time
t_{obs}	Time in observer-rest frame
τ	Optical depth
θ	Off-axis angle
ξ	Prompt radiation efficiency: $E_{prompt}/(E_{prompt}+E)$
θ_Z	Zenith angle
ϑ	Angular distance
y	Luminosity ratio of SSC to synchrotron
z	Redshift

Table 3: Abbreviations used in the present thesis.

Abbreviation	Term	*cf.*
ACD	Anti-coincidence Detector	§ 5.2
BAT	Burst Alert Telescope	§ 3.4.2
BATSE	Burst and Transient Source Experiment	§ 3.2.1
BDT	Boosted Decision Tree	§ 5.3.5
CAL	Calorimeter	§ 5.2.2
CalOnly	Calorimeter-only	§ 5.6
CBM	Cuicumburst medium	§ 4.6.1
CGRO	Compton Gamma Ray Observatory	§ 3.2.1
CTA	Cherenkov Telescope Array	§ 3.6.1
EBL	Extragalactic Background Light	§ 3.6.1
EGB	Extragalactic Gamma-ray Background	§ 5.3.5
EGRET	Energetic Gamma Ray Experiment Telescope	§ 3.2.3
FoV	Field of view	§ 3.5.1
GBM	Gamma-ray Burst Monitor	§ 3.4.2
GRB	Gamma-ray Burst	§ 1.1
IACT	Imaging Atmospheric Cherenkov Telescope	§ 3.6.1
IC	Inverse-Compton	§ 2.3.1
IRF	Instrument Response Function	§ 5.7.2
ISM	Interstellar matter	§ 4.6.1
LAT	Large Area Telescope	§ 3.5.1, § 5.1
LLE	LAT Low Energy	§ 3.5.1
MC	Monte Carlo	§ 5.3.5
MET	Mission Elapsed Time	§ 7.3.2
MVA	Multivariate analysis	§ 5.3.5
PSF	Point Spread Function	§ 5.2.1, § 5.4.3
RoI	Region of interest	§ 7.3.1
SED	Spectral Energy Distribution	§ 3.5.2
SSC	Synchrotron Self-Compton	§ 2.3.1
SSD	Silicon Strip Detector	§ 5.2.1
TKR	Tracker	§ 5.2.1
UVOT	UltraViolet and Optical Telescope	§ 3.4.2
VHE	Very high energy	§ 3.6
XRT	X-ray Telescope	§ 3.4.2

Chapter 1

Introduction

In this thesis, I report analyses of the mechanism of radiation with energy above tens of GeV from gamma-ray burst afterglows using data of the *Fermi* Large Area Telescope which I newly recovered. I briefly overview the physics of gamma-ray bursts and observations in high-energy (from $\sim$ 100 MeV to $\sim$ 100 GeV) gamma-ray and write out the structure of this thesis in the following sections.

1.1 Gamma-ray bursts

Gamma-ray bursts (GRBs) are the most energetic explosions in the Universe. They are cosmologically distant, and each of them releases a huge amount of energy in keV - MeV gamma-rays within a short period. Their release energy typically would exceed 10^{50} erg, and the brightest one would exceed 10^{54} erg if the emission was isotropic. The duration time typically ranges from $\sim$ 30 ms to over 1000 s, and the flux of some of GRBs exhibits very fast variabilities with time scales down to $\sim$ 1 ms [1]. Some examples of the GRB light curves are displayed in Fig. 1.1. The spectrum of the prompt emission is described by a smoothly connected broken power-law, which is called the Band function [3]. The peak energy typically locates at $\sim$ 100 keV. The function is expressed as

$$\frac{dN(E)}{dE} = \begin{cases} A(E/100\,\mathrm{keV})^{\alpha} & E < (\alpha-\beta)E_0, \\ A((\alpha-\beta)E_0/100\,\mathrm{keV})^{\alpha-\beta}e^{\beta-\alpha}(E/100\,\mathrm{keV})^{\beta} & E \geq (\alpha-\beta)E_0. \end{cases} \tag{1.1}$$

where $\frac{dN}{dE}dE$ is the photon number in the energy bin with the width dE at the energy E, A is the normalization factor, the photon spectral index is $\alpha \sim -1$ in the low energy side, and $\beta \sim -2$ in the high energy side.

The bursts are followed by gradually decaying broadband emission, which is called the "afterglow" emission. One can find this component in a light curve of, for example, GRB 110731A (Fig. 1.2).

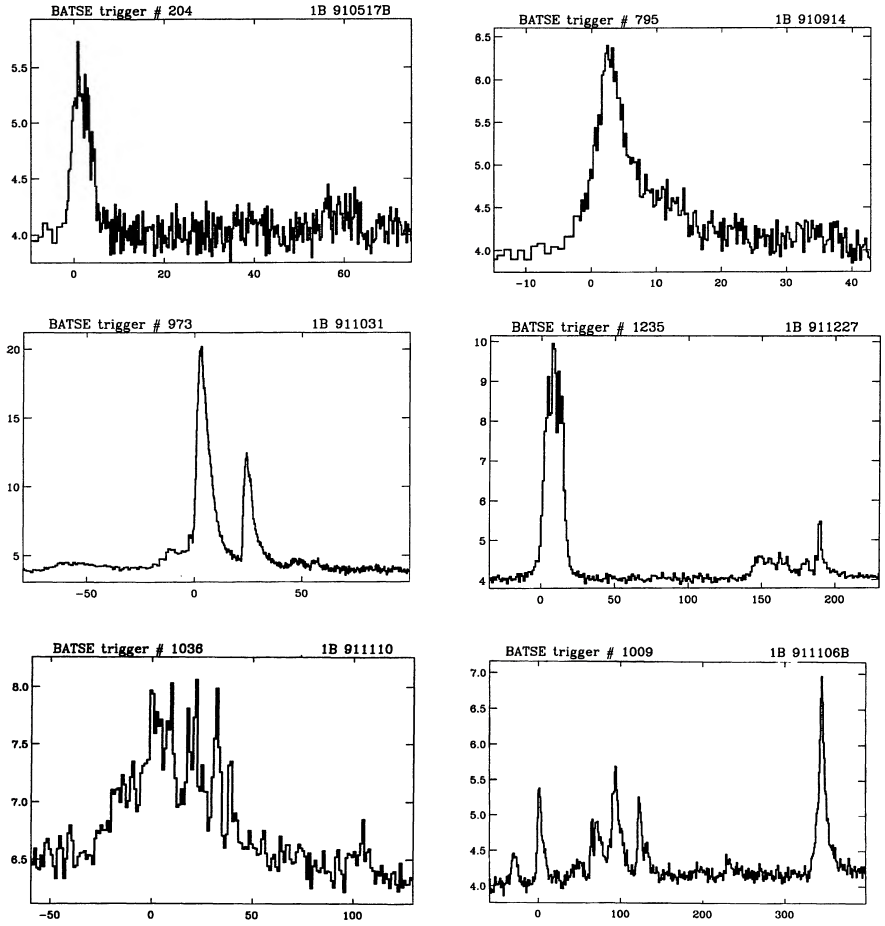

Figure 1.1: Examples of light curves of GRBs detected by the BATSE [2]. A description of the BATSE is in § 3.2.1. The count rates in the unit of $10^3\,\mathrm{counts}\cdot\mathrm{s}^{-1}$ are plotted. The time is in seconds and relative to the trigger time. The energy range is from 50 to 300 keV.

On the other hand, the leading burst component is called the "prompt" emission.

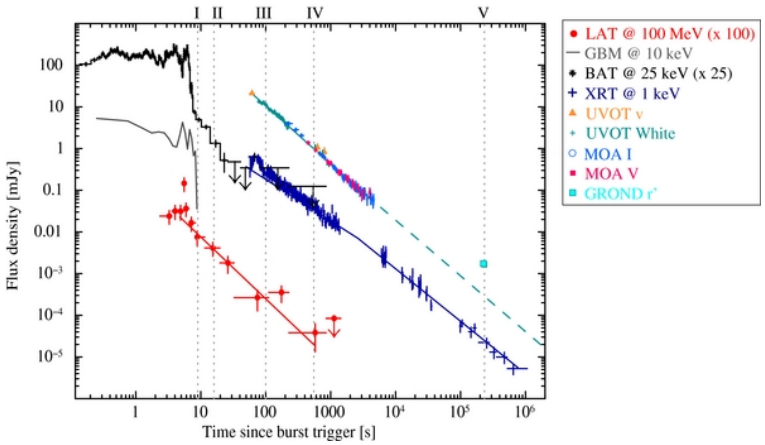

Figure 1.2: Multiwavelength light curves of GRB 110731A [4]. The prompt emission was observed in keV - MeV gamma-ray (GBM and BAT). The afterglow was observed over a broad frequency range, from optical (UVOT, MOA and GROUND), X-ray (XRT) to high-energy gamma-ray (LAT). The power-law index of the LAT light curve is $\alpha_\gamma = 1.55 \pm 0.20$. The XRT light curve follows a broken power law with $\alpha_{X,1} = 1.10 \pm 0.02$, $\alpha_{X,2} = 1.32 \pm 0.03$ and a break at $t_{bk} = 4.6^{+2.6}_{-1.6}$ ks. The UVOT light curve is well fit by a single power law with decay slope $\alpha_O = 1.37 \pm 0.03$.

The GRBs are known to be categorized into two species, "long-GRBs" and "short-GRBs" by their duration time. Observations suggest that the two species have different progenitors. The long-GRBs, or at least some of them are associated to Type Ic supernovae. The short-GRBs are attributed to mergers of neutron star binaries. This hypothesis is supported by a discovery of a short-GRB correlated to the first detection of gravitational waves from a binary neutron star merger. In spite of the difference in their origins, their spectra look similar, and there seems to be common physics.

The total amount of energy of the prompt gamma-rays would range from 10^{49} erg to 10^{55} erg if the emission was isotropic. After discovery of temporal breaks at ~ 1 day after the bursts in the afterglow light curves, such an amount is concluded to be overestimated because the GRB radiation is highly beamed to an opening angle ~ 0.1 radians. Such a break is explained by decay of relativistic beaming of radiations from the jet and side expansion of the jet. Taking the beaming into account, estimates of the released energy during the bursts result in values from 10^{49} erg to 10^{52} erg [5]. The emission from GRBs should be radiated from regions which move toward the observer with relativistic speed. The relativistic effects increase the observable photon energy and shorten the apparent time-scales of the variabilities. If these effects were not considered, a number of high energy photons above MeV would be localized in a small volume, and there would be no chance for them to escape because of pair creation.

Consequently, the relativistically accelerated and collimated jets of GRBs radiate gamma-rays. However, the central engines which drive the relativistic jets and the mechanisms of accelerating the jets have not been elucidated yet. A GRB is triggered by a core collapse of a massive star or merger of a neutron star binary, but its product, which launches the outflows, has not been identified. It may be a black hole or magnetar. A leading model of the jet acceleration is dubbed the fireball model. In this scenario, a huge amount of energy is released in a certain volume. It creates an optically thick region ("fireball"). The fireball adiabatically expands, and particles which are bound by Thompson scattering are accelerated. The termination speed of the jets depends on the amount of the accelerated matter, and the jets are accelerated to a relativistic speed provided the mass of the matter is sufficiently small. However, the radiation is not trapped if the matter is too less, and consequently the Lorentz factor of the jet has a maximum possible value, around 10^3. Another hypothesis is that the jets being dominated by Poynting flux instead of matter. In this case, the jets are launched from black holes through Blandford-Znajek mechanism or from spinning down millisecond magnetars. The jets are accelerated via dissipation of the magnetic field or adiabatic expansion.

On top of that, how the kinetic energy of the jets is converted into the prompt electromagnetic radiation remains open. A popular idea is synchrotron radiation from shocks caused by collisions of shells within the jet (the internal shock model). An alternative solution is radiation of thermal photons up-scattered by hot electrons (the photospheric radiation model). Both of them have difficulties to describe the observed spectra.

Compared with the prompt emission, the afterglow is relatively understood. The mechanism of the afterglows is explained by shocks produced by collisions of the jet and ambient matter. The shocks accelerate electrons and they emit broadband synchrotron radiations. This is called the "external shock" model. The synchrotron spectrum is approximately expressed by a power-law with three breaks. The break frequencies are determined by the characteristics of the jets and shocked fluid. This model was basically successful for explaining the light curves and broadband spectra of the afterglow. However, the energy of several GRB photons appears to be too high for a combination of this model and the fireball jet acceleration, which is canonical. The synchrotron photon energy has a maximum value ~ 50 MeV in the rest frame. Therefore, the photon energy is limited to $\lesssim 50\Gamma$ MeV in the GRB-rest frame where Γ is the jet Lorentz factor and does not typically exceed $\sim 10^3$ under the fireball model. This limit is broken if the photons are radiated by a harder emission mechanism such as inverse-Compton scattering or if the Poynting-flux-dominated jet is accelerated to $\Gamma > 10^3$. In addition to these possibilities, the high energy photons may be radiated by the jet-internal shocks via a non-synchrotron process, not by the external shocks.

From the point of view of the energetics, the energy radiated by the prompt emission and the kinetic energy of the jet are very important. The sum of them indicates the total amount of energy released by the GRB, and it constrains what the central engine is. On the other hand, the ratio of the prompt energy to the sum corresponds to the efficiency of the prompt radiation. It may be a clue of the dissipation mechanism of the jet energy. The prompt gamma-ray energy is measured directly from observations in keV - MeV. The jet energy is indirectly derived from afterglow observations. The flux above the highest spectral break of a broken-power-law spectrum of synchrotron radiation is relatively less dependent on highly uncertain parameters. If an observational band locates in this domain, one can estimate the jet kinetic energy from the observed light curve. Therefore, determining the radiation process dominating the afterglow data in the energy range from 0.1 GeV to > 100 GeV, which is the highest one GRB photons have been detected in, is important.

1.2 High energy gamma-ray observation

Gamma-rays in this energy range are currently observed by the *Fermi* Large Area Telescope (*Fermi*-LAT). The LAT is one of two instruments on board the *Fermi Gamma-ray Space Telescope*. Although the *Fermi*-LAT has detected more than 140 GRBs, a problem is that the sensitivity of the LAT above tens of GeV is limited by the signal statistics. The LAT detects only one or two > 10 GeV photons from one GRB except for few bursts. In order to improve the statistics, I have developed new photon classes which recover a fraction of untapped events, which used to be discarded on the low-level analysis level.

It is however unrealistic to realizing a substantial jump in collection area of a space telescope. A breakthrough in the photon statistics requires observation with ground-based instruments. Detection with state-of-art instruments such as the Cherenkov Telescope Array (CTA), which is under construction, and the High-Altitude Water Cherenkov (HAWC) observatory, which is currently operating, are promising.

1.3 Structure of this thesis

The structure of this thesis is as follows: I review non-thermal emission processes which are relevant to GRB afterglow in chapter 2. I give overviews of observation history and facts in chapter 3, and important theories of GRBs in chapter 4. I use the data of the *Fermi*-LAT intensively in this thesis. I review the details of the instruments and low-level analyses in chapter 5. In chapter 6, I describe the development and performance of the LAT calorimeter-only photon classes. From these classes, I found some candidates of photons originated from GRBs. The energy of the events was higher than tens of GeV. I report the details and the probabilities that they are backgrounds in chapter 7. Next,

I report likelihood analyses for quantifying the spectral and temporal features of two GRB afterglows which were accompanied by the new photon candidates in chapter 8. In chapter 9, I discuss a few topics. The primary topic is whether the results can be interpreted by the synchrotron emission from external shocks, or other components are needed. What impact the results have on the key quantities of the energetics is discussed after that. I also mention the consistency with models of absorption by extragalactic gamma-ray background and prospects of detection by the CTA. Finally the conclusions are given in chapter 10.

Through the present thesis, the units follow the CGS Gaussian system unless otherwise noted. Some plots in this thesis have a label of "Unpublished". This means the plot will be possibly changed when it is published in a journal in the future.

Chapter 2

Non-thermal emission processes

I review some emission mechanisms which are relevant to GRB afterglows. In this chapter, I use the following notations generally: particle energy E, a particle Lorentz factor γ, a particle charge q, particle velocity $\boldsymbol{v}$, time t, the light speed in vacuum c, particle rest mass m, the elementary charge e, and magnetic field $\boldsymbol{B}$.

2.1 Energy radiation of accelerated particles

A particle with non-zero charge q which are being accelerated by some fields emits dipole radiation. The radiation power P, that is the energy loss rate, $-dE/dt$ is derived from Larmor's formula [6, 7].

$$P \equiv -\frac{dE}{dt} = \frac{2|\ddot{\boldsymbol{p}}|^2}{3c^3} = \frac{2q^2|\boldsymbol{a}|^2}{3c^3}, \tag{2.1}$$

where $\boldsymbol{p}$ is the electric dipole moment of the charge and $\boldsymbol{a}$ is the instantaneous acceleration vector. They are connected as $\ddot{\boldsymbol{p}} = q\boldsymbol{a}$. If one measures the acceleration in the laboratory frame, it is resolved into the perpendicular and parallel components with respect to the velocity vector,

$$P = \frac{2q^2\gamma^4}{3c^3}(|a_\perp|^2 + \gamma^2|a_\parallel|^2), \tag{2.2}$$

where γ is the Lorentz factor. If the particle moves on a spiral path in a uniform magnetic field at a constant pitch angle α, $|a_\parallel| = 0$ and $|a_\perp| = qvB\sin\alpha/\gamma m$ because the acceleration vector is always perpendicular to the velocity vector. Then, Eq. 2.2 becomes

$$P = \frac{2}{3}r_0^2 c\left(\frac{v}{c}\right)^2\gamma^2 B^2\sin^2\alpha = 2\sigma_T c\left(\frac{v}{c}\right)^2\gamma^2 U_B\sin^2\alpha, \tag{2.3}$$

where r_0 is the classical radius[i], $\sigma_T = 8\pi r_0^2/3$ is the Thomson cross-section and $U_B = B^2/(8\pi)$ is the energy density of the magnetic field. If the velocity vector of the charged particles is randomized, averaging $\sin^2\alpha$ over an isotropic distribution of the pitch angles α yields

$$P = 2\sigma_T c \left(\frac{v}{c}\right)^2 \gamma^2 U_B \frac{\int_0^\pi \sin^2\alpha \sin\alpha \mathrm{d}\alpha}{\int_0^\pi \sin\alpha \mathrm{d}\alpha} = \frac{4}{3}\sigma_T c \left(\frac{v}{c}\right)^2 \gamma^2 U_B. \tag{2.4}$$

Gyro-radiation The radiation of non-relativistic charged particles deflected by a magnetic field is called the gyro-radiation. Then, $v \ll c$ and

$$P = 2\sigma_T c U_B \left(\frac{v}{c}\right)^2 \sin^2\alpha. \tag{2.5}$$

The radiation is emitted at the non-relativistic gyro-frequency of the particle $\nu_g = qB/(2\pi m)$.

2.2 Synchrotron radiation

The synchrotron radiation is the relativistic limit of the gyro-radiation. The relativistic aberration forces the dipole radiation to concentrate on the direction of motion of the particle. The radiation power P is

$$P = \frac{4}{3}\sigma_T c U_B \gamma^2. \tag{2.6}$$

because $v \approx c$. The characteristic frequency is

$$\nu(\gamma) = \gamma^2 \frac{qB}{2\pi mc}. \tag{2.7}$$

The peak spectral power is given at the characteristic frequency,

$$P_{\nu,max} \approx \frac{P_\nu(\gamma)}{\nu(\gamma)}. \tag{2.8}$$

A remarkable difference from the gyro-radiation is beaming. Because of the relativistic aberration, one of the dipole radiation fields illustrated in Fig. 2.1 (a) is strongly concentrated on the direction of the velocity vector with an opening angle $\sim 1/\gamma$ in Fig. 2.1 (b). This beaming restricts the direction where the electron radiates electromagnetic waves observable for the observer to $1/\gamma$ radians of one orbit of the particle. When the path range is from the point A to B drawn in Fig. 2.1 (c) and the distance between them is L, the difference in arrival time of radiations which emitted at A and at B is

$$\Delta t = \left(\frac{L}{v} + \frac{R-L}{c}\right) - \frac{R}{c} = \frac{L}{v}\left(1 - \frac{v}{c}\right), \tag{2.9}$$

[i] $r_0 = q^2/(mc^2)$ for an electron.

where R is the distance from A to the observer. L/v can be rewritten as

$$\frac{L}{v} = \frac{r_g \theta}{v} = \frac{\gamma mc}{qB}\frac{1}{\gamma} = \frac{1}{\omega_g}, \tag{2.10}$$

where r_g is the radius of the particle orbit, $\theta \sim 1/\gamma$ is the angle between A and B from the guiding center, and $\omega_g = qB/(mc)$ is the non-relativistic angular gyro-frequency. Also $1 - v/c$ is rewritten as

$$1 - \frac{v}{c} = \frac{1 - v^2/c^2}{1 + v/c} \approx \frac{1}{2\gamma^2}. \tag{2.11}$$

Hence,

$$\Delta t \approx \frac{1}{2\gamma^2 \omega_g}, \tag{2.12}$$

and then the typical frequency of the synchrotron emission is

$$\nu \sim \frac{1}{\Delta t} \sim \gamma^2 \nu_g, \tag{2.13}$$

where ν_g is the non-relativistic gyro-frequency.

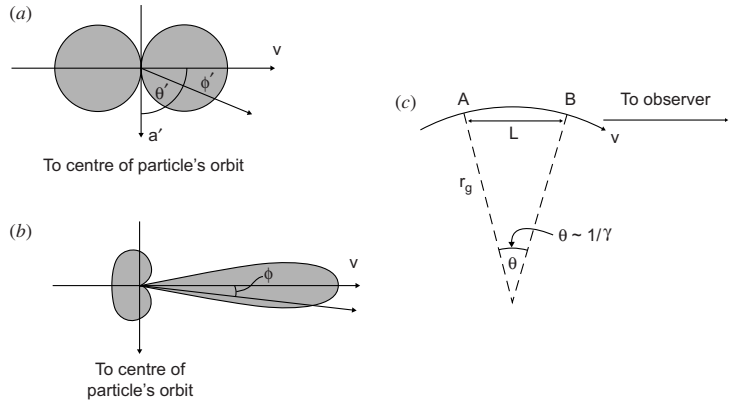

Figure 2.1: Illustrations of the beaming effects of synchrotron radiation [7]. (a) Diagram of dipole radiation of the particle in its instantaneous rest frame. The distance of each point on the circumference from the origin indicates the strength of radiation field. (b) Diagram of the radiation in the laboratory frame. (c) Path of the particle during the time when the beamed radiation is observed.

Detailed calculations elucidate the emissivity of a particle whose angular frequency ω is

$$F_\omega = \frac{\sqrt{3} q^3 B \sin\alpha}{2\pi mc} F(x), \tag{2.14}$$

where $F(x) = x \int_x^\infty K_{5/3}(z) dz$ and $x = 2\omega/(3\gamma^2 \omega_g \sin\alpha)$ [6]. K is the modified Bessel function.

Asymptotically, the dependence of the specific flux at high- and low-frequency limits is

$$F_\nu \propto F(x) \propto \begin{cases} x^{1/2}\mathrm{e}^{-x} & x \gg 1 \\ x^{1/3} & x \ll 1, \end{cases} \tag{2.15}$$

respectively. This function peaks around $\omega = 3\gamma^2\omega_g \sin\alpha/2 = 3qB\gamma^2 \sin\alpha \equiv \omega_{sync}/(2mc)$, which makes x unity. ω_c corresponds to

$$\nu_{sync} = \frac{\omega_{sync}}{2\pi} = \frac{3qB}{4\pi mc}\gamma^2 \sin\alpha. \tag{2.16}$$

This is similar to the typical frequency implied by Eq. 2.13.

2.2.1 A power-law energy distribution of radiating particles

Consider a power-law distribution of relativistic particle energy $dn(\gamma)/d\gamma = \kappa\gamma^{-p}$ hereafter. Using this energy dependence $E = \gamma mc^2$, $\nu = \gamma^2\nu_g$ and $\nu_g = 2\pi qB/(mc)$, the specific flux can be written as

$$F_\nu = \int d\gamma \frac{dn}{d\gamma}\left(-\frac{dE}{dt}\right) \propto \kappa B^{(p+1)/2}\nu^{-(p-1)/2}. \tag{2.17}$$

2.2.2 Characteristic Lorentz factors and frequencies

The energy distribution of particles is modified by effects such as cooling and absorption. Some characteristic Lorentz factors are used for describing the particle energy distribution. They are converted to the counterparts in synchrotron radiation frequency by Eq. 2.16.

Cooling energy The first characteristic Lorentz factor indicates the energy above which the particles are significantly affected by cooling. A particle above the critical Lorentz factor γ_c loses a significant fraction of its energy during a time t. From Eq. 2.6,

$$\frac{mc^2\gamma_c}{t} = \frac{\sigma_T}{6\pi}B^2\gamma_c^2 c, \tag{2.18}$$

and hence the characteristic frequency is

$$\gamma_c = \frac{6\pi mc}{\sigma_T B^2 t}. \tag{2.19}$$

Substituting it to Eq. 2.16, the corresponding synchrotron frequency is

$$\nu_c = \frac{27\pi qmc}{\sigma_T^2 B^3 t^2}. \tag{2.20}$$

Minimum injection energy γ_m is the minimum Lorentz factor of the injected particles. Provided a power-law distribution of the particle energy with a negative index, it is also the peak energies. If cooling does not work effectively, the corresponding synchrotron frequency ν_m is the most typical frequency of the emission of particles with a power-law energy distribution.

Self-absorption energy Synchrotron photons suffer from the inverse process of themselves, the synchrotron self-absorption. It becomes important for particles below the synchrotron self-absorption Lorentz factor γ_a. In the present thesis, I do not consider this effect because it is not relevant to the high energy photon data I use, namely, gamma-ray and X-ray.

2.2.3 Cooling-regimes

A system of radiating particles is classified into fast-cooling regime or slow-cooling regime, depending on whether a majority of particles are affected by radiative cooling.

Fast cooling

Fast cooling means all particles cool down to γ_c roughly faster than the system dynamical time scale. This happens when $\nu_m > \nu_c$. In this case, the spectrum is totally affected by the cooling.

A schematic spectrum of an observed synchrotron radiation in fast cooling regime is displayed in Fig. 2.2 (a). Below the particle distribution peak ν_c, the dependency of $\nu \propto \nu^{1/3}$ is derived from Eq. 2.15. The spectrum above ν_c is given by solving the continuity equation in the energy space.

$$\frac{\partial}{\partial t}\frac{dn}{d\gamma} + \frac{\partial}{\partial \gamma}\left(\dot{\gamma}\frac{dn}{d\gamma}\right) = S(\gamma), \tag{2.21}$$

where $S(\gamma)$ is the injection rate of particles with energy γ. Provided a steady state,

$$\frac{\partial}{\partial \gamma}\left(\dot{\gamma}\frac{dn}{d\gamma}\right) = S(\gamma). \tag{2.22}$$

$\dot{\gamma} \propto \gamma^2$ as shown by Eq. 2.16. For $\nu < \nu_m$, $S(\gamma) = 0$, and then

$$\frac{\partial}{\partial \gamma}\left(\gamma^2\frac{dn}{d\gamma}\right) = 0. \tag{2.23}$$

Consequently, $dn/d\gamma \propto \gamma^{-2}$. Substituting $p = 2$ to Eq. 2.17, we get $F_\nu \propto \nu^{-1/2}$ for $\nu_c < \nu < \nu_m$.

For $\nu > \nu_m > \nu_c$, the equation

$$\frac{\partial}{\partial \gamma}\left(\gamma^2\frac{dn}{d\gamma}\right) = \gamma^{-p} \tag{2.24}$$

results in $dn/d\gamma \propto \gamma^{-p-1}$. It leads to $F_\nu \propto \nu^{-p/2}$. Using the peak flux value $F_{\nu,max}$ for scaling the overall spectrum,

$$F_\nu = \begin{cases} (\nu/\nu_c)^{1/3} F_{\nu,max} & \nu < \nu_c, \\ (\nu/\nu_c)^{-1/2} F_{\nu,max} & \nu_c < \nu < \nu_m, \\ (\nu/\nu_m)^{-p/2} (\nu_m/\nu_c)^{-1/2} F_{\nu,max} & \nu_m < \nu. \end{cases} \tag{2.25}$$

Slow cooling

Slow cooling means the system dynamical time scale is longer than the cooling time scale. The relationship of the characteristic frequencies is $\nu_m < \nu_c$. In this case, the spectrum around the typical synchrotron frequency is not affected by cooling. Then the synchrotron spectral index does not change from $-(p-1)/2$ for $\nu < \nu_m$ (*cf.* Eq. 2.17). Particles above γ_c, however, lose a significant faction of their energy within the dynamical time scale and cool down to γ_c. Above ν_c, thus, it is the same as in fast cooling, $-p/2$. The spectral index below ν_m is also the same as in fast cooling, 1/3.

$$F_\nu = \begin{cases} (\nu/\nu_m)^{1/3} F_{\nu,max} & \nu < \nu_m, \\ (\nu/\nu_m)^{-(p-1)/2} F_{\nu,max} & \nu_m < \nu < \nu_c, \\ (\nu/\nu_c)^{-p/2} (\nu_c/\nu_m)^{-(p-1)/2} F_{\nu,max} & \nu_c < \nu. \end{cases} \tag{2.26}$$

2.2.4 Maximum energy of synchrotron photons

Synchrotron photons have a possible maximum energy determined from the Larmor time, which is the minimum time required for acceleration of a charged particle while crossing a shock front [9]. The Larmor time is

$$t'_L = \gamma \frac{2\pi mc}{qB'}. \tag{2.27}$$

The primes indicate the values in the co-moving frame. If the particle loses a significant fraction of energy during t'_L, it cannot be accelerated to any higher energy. Therefore,

$$P'_{sync} t'_L = \frac{4q^4 B'^2 \gamma^2}{9m^2c^3} t'_L < \frac{4\gamma mc^2}{3}. \tag{2.28}$$

Solving this inequality, we obtain

$$h\nu'_{sync} < \frac{9}{4\pi} mc^2 \frac{\hbar c}{q^2}. \tag{2.29}$$

For electrons, it is $\approx 50\,\mathrm{MeV}$. The limit varies by a factor of a few, depending on the choice of the Larmor time and synchrotron frequency [9]. Some leakage into the higher energy is possible because the synchrotron spectrum has dependence as $F_\nu \propto \nu^{1/2} \mathrm{e}^{-\nu}$ (*cf.* Eq. 2.15). Moreover, it may be violated by a factor of at least a few, if the magnetic field is inhomogeneous [10], although more severe limits have been discussed [11].

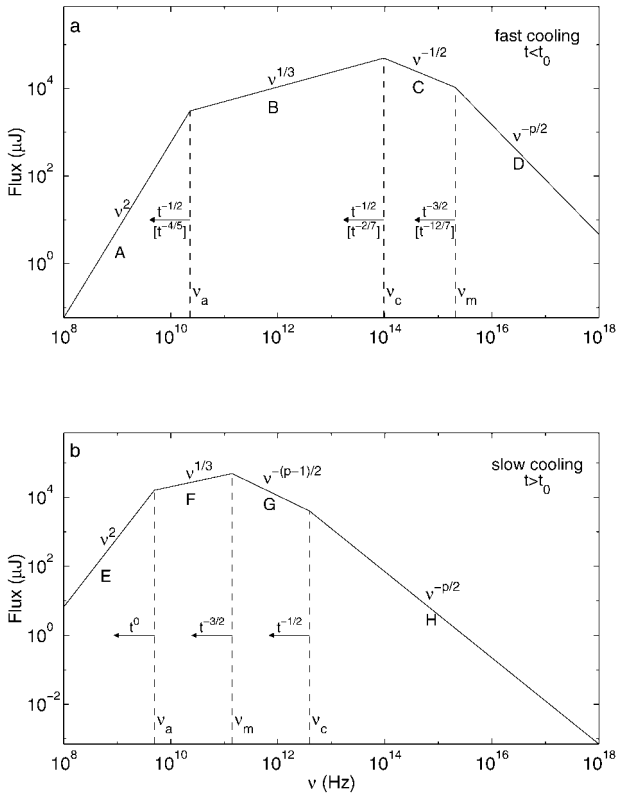

Figure 2.2: Schematic spectra of synchrotron radiation with a power-law electron distribution[8]. (a) Fast cooling. (b) Slow cooling.

2.3 Inverse Compton scattering

2.3.1 Synchrotron self-Compton process

Hereafter I consider electrons as radiating particles. Explaining photons with higher energy than $\sim 50\,\mathrm{MeV}$ needs other emission processes. One candidate is inverse-Compton (IC) scattering. It is a process that a high-energy electron scatters a low-energy photo to high energy. In particlular, if the seed photons are created by a synchrotron process and the electrons of the distribution responsible for the synchrotron radiation themselves upscatter those photons, this process is called synchrotron self-Compton (SSC). The SSC models are simple (with less parameters than other models), but very successful in explaining the two-bump spectrum of BL Lac objects, which are a category of active galactic nuclei [12].

2.3.2 Spectrum

Assume a power-law distribution of particle energy again. The SSC spectrum is analytically and numerically discussed in papers such as [13] and [14]. The SSC component also has three characteristic frequencies $\nu_a^{IC} = 2\gamma_m^2\nu_a$, $\nu_m^{IC} = 2\gamma_m^2\nu_m$, $\nu_c^{IC} = 2\gamma_c^2\nu_c$ and four segments divided by them, as the same as the synchrotron component. The synchrotron and SSC spectrum is displayed in Fig. 2.3. Roughly speaking, the spectral indices of the IC component reproduce those of the synchrotron component. However, the intervals between the characteristic frequencies in logarithmic metric are not proportional to those of the synchrotron component. In addition to the broken power-law components, there is a logarithmic term, which peaks at $\nu = \sqrt{\nu_m^{IC}\nu_c^{IC}}$.

The luminosity ratio between the SSC and synchrotron, which is denoted by y, is written by the energy density of the synchrotron and magnetic field, U_{sync} and U_B, respectively [15, 14].

$$y \equiv \frac{L_{IC}}{L_{sync}} = \frac{U_{sync}}{U_B}. \tag{2.30}$$

because the distribution of scattering electrons is identical. The synchrotron energy density equals the accelerated electron energy multiplied by the fraction that was radiated away, η. The ratio can be rewritten as

$$y = \frac{\eta U_e/(1+y)}{U_B} = \frac{\eta\epsilon_e}{\epsilon_B(1+y)}. \tag{2.31}$$

Solving Eq. 2.31 yields

$$y = \frac{-1+\sqrt{1+4\eta\epsilon_e/\epsilon_B}}{2}. \tag{2.32}$$

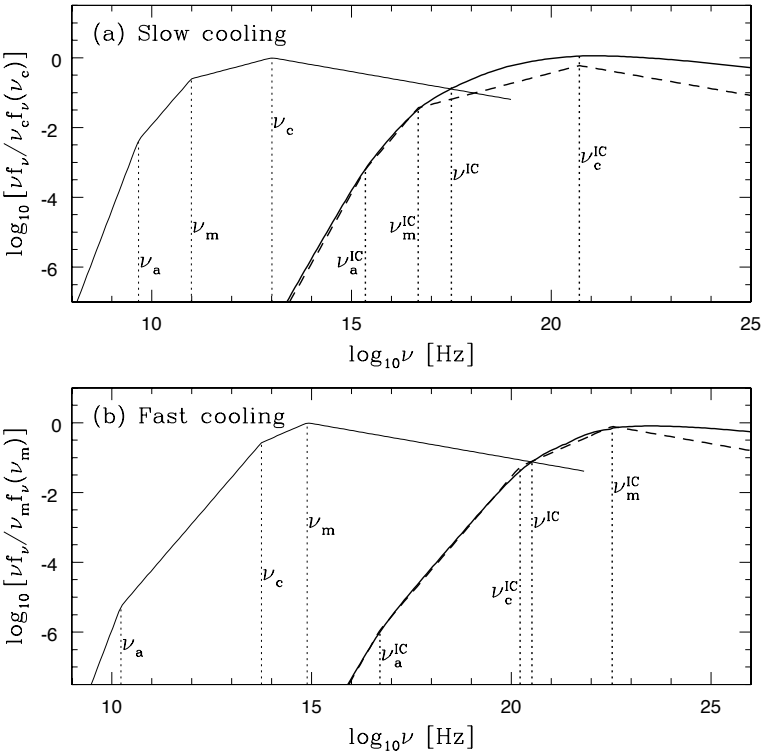

Figure 2.3: Schematic spectra of the synchrotron component (left curve) and SSC component (right curve) with a power-law electron distribution [14]. The curves are calculated for a GRB afterglow model, with the parameters $p = 2.4$, $\epsilon_e = 0.5$, $\epsilon_B = 0.01$, $E = 0.5 \times 10^{52}$, $z = 0.5$, $n_1 = 3$. (a) Spectrum at $t = 12$ days, in the slow cooling regime. (b) Spectrum at $t = 43$ min, in the fast cooling regime. ν^{IC} is the crossing point of the synchrotron and SSC component.

At the two limits, y

$$y \approx \begin{cases} \eta\epsilon_e/\epsilon_B & \eta\epsilon_e/\epsilon_B \ll 1, \\ \sqrt{\eta\epsilon_e/\epsilon_B} & \eta\epsilon_e/\epsilon_B \gg 1. \end{cases} \tag{2.33}$$

The value of the radiated energy fraction is

$$\eta \approx \begin{cases} 1 & \text{Fast cooling}, \\ \int_{\nu_c}^{+\infty} \gamma^{-p+1} d\gamma / \int_{\nu_m}^{+\infty} \gamma^{-p+1} d\gamma = (\gamma_c/\gamma_m)^{-p+2} & \text{Slow cooling}. \end{cases} \tag{2.34}$$

Under a first-order approximation, the flux is expressed by a broken power-law function with the characteristic frequencies and the peak flux $F_{\nu,max}^{IC}$. In the fast-cooling regime, the specific flux is

$$F_\nu^{IC} = \begin{cases} (\nu/\nu_c^{IC})^{1/3} F_{\nu,max}^{IC} & \nu < \nu_c^{IC}, \\ (\nu/\nu_c^{IC})^{-1/2} F_{\nu,max}^{IC} & \nu_c^{IC} < \nu < \nu_m^{IC}, \\ (\nu/\nu_m^{IC})^{-p/2} (\nu_m^{IC}/\nu_c^{IC})^{-1/2} F_{\nu,max}^{IC} & \nu_m^{IC} < \nu. \end{cases} \tag{2.35}$$

In the synchrotron-dominated slow-cooling regime, the specific flux is

$$F_\nu^{IC} = \begin{cases} (\nu/\nu_m^{IC})^{1/3} F_{\nu,max}^{IC} & \nu < \nu_m^{IC}, \\ (\nu/\nu_m^{IC})^{-(p-1)/2} F_{\nu,max}^{IC} & \nu_m^{IC} < \nu < \nu_c^{IC}, \\ (\nu/\nu_c^{IC})^{-p/2} (\nu_c^{IC}/\nu_m^{IC})^{-(p-1)/2} F_{\nu,max}^{IC} & \nu_c^{IC} < \nu. \end{cases} \tag{2.36}$$

2.3.3 Klein-Nishina effect

In Thomson scattering regime, the cross-section is constant for the frequency. It is valid if the photon energy is much lower than the electron rest energy. If the photon energy in the electron rest frame is comparable or larger than $m_e c^2$, we have to use the Klein-Nishina formula instead.

$$\sigma_{KN} = \pi r_0^2 \frac{1}{x} \left[\left(1 - 2\frac{x+1}{x^2} \right) \ln(2x+1) + \frac{1}{2} + \frac{4}{x} - \frac{1}{2(2x+1)^2} \right], \tag{2.37}$$

where $x = h\nu/m_e c^2$ [7]. In the ultra-relativistic limit $\gamma \gg 1$, the cross section decreases roughly $\sigma_T \propto 1/x$.

Chapter 3

Observational history and facts

In this chapter, I overview observational results on GRBs so far.

3.1 Discovery

GRBs were first serendipitously discovered by the *Vela* nuclear test detection satellites, which observe gamma-rays around MeV, and reported in 1973 [16]. The observations were performed by detectors onboard four *Vela* satellite, namely, *Vela* 5A, *Vela* 5B, *Vela* 6A, *Vela* 6B. Each spacecraft had six CsI scintillators, whose volume was $10\,\mathrm{cm}^3$. The gamma-ray detectors of *Vela* 5A/5B and of *Vela* 6A/6B were sensitive for the energy range $0.1 - 1.0$ MeV and $0.3 - 1.5$ MeV, respectively. The four satellites were arranged almost equally spaced in a circular orbit.

The gamma-ray emission lasted for periods from a second to 30 seconds and the light curves exhibited very fast variabilities. Thousands of photons were recorded within one second at the peaks and the instantaneous flux densities exceeded $4 \times 10^{-4}\,\mathrm{erg \cdot cm^{-2} \cdot s^{-1}}$. The source directions were restricted when the difference in the arrival time between multiple satellites of the four ones, although the directions were not determined uniquely. These phenomena were quite puzzling because of no counterparts in other wavebands, the unknown distances and a variation of the temporal profiles. In the 1980s, Galactic neutron stars which, distributed in the Galactic plane, were considered as primary source candidates [17]. In Fig. 3.1, the distribution of the energy fluence is plotted for GRBs detected by the Gamma-ray Burst Monitor (GBM) onboard the *Fermi Space Gamma-ray Observatory* (hereafter *Fermi*), which was launched in 2008 and is operating currently. The GBM is sensitive in 8 keV - 30 MeV.

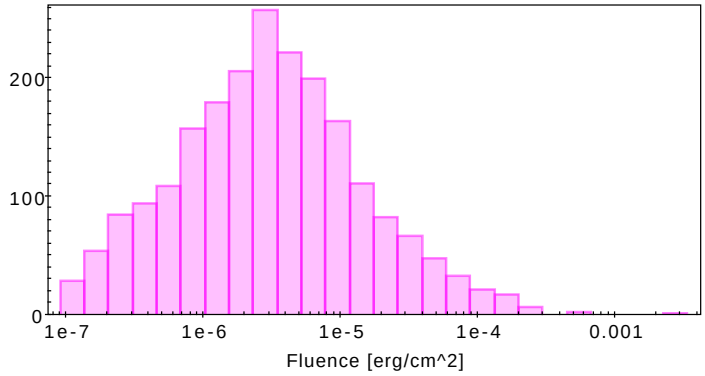

Figure 3.1: Distribution of the energy fluence [erg $\cdot$ cm^{-2}] of the GRB detected by the *Fermi*-GBM. The values are taken from the GBM online catalogue[18, 19, 20].

3.2 Prompt emission

3.2.1 Temporal features

The prompt emission of the long-GRBs exhibits a variety of the durations and light curves. Although it was known from the beginning [16], clarifying the temporal features advanced greatly with the Burst and Transient Source Experiment (BATSE). It was one of four instruments on the *Compton Gamma Ray Observatory* (CGRO), which was launched in 1991 [2] and re-entered the Earth's atmosphere in 2000. The BATSE consisted of eight identical modules at the corners of the *CGRO* spacecraft [21]. Each modules contain two detectors, the large-area detector (LAD) and the spectroscopy detector (SD). The LADs are mainly for detecting GRBs and capturing their time profiles. They covered an energy range from 20 keV to 1.9 MeV. The geometrical area of the NaI scintillator of each LAD was about $2 \times 10^3\,\mathrm{cm}^2$. With the large detecting elements, the BATSE provided a unprecedented sensitivity of GRB observation. The SDs were dedicated to spectral measurement. They had a better energy resolution and covered a broader energy range, compared with the LADs and previous instruments.

The morphologies of the light curves are, for example, categorized like the following list [17].

- Single pulse or spike events
- Smooth, either single or multiple, well-defined peaks
- Distinct, well-separated episodes of emission
- Very erratic, chaotic, and spiky bursts

The light curve examples which were detected by the BATSE are displayed in Fig. 1.1. A few percents of GRBs exhibit very fast variabilities with the time scale of $\lesssim 0.1$ s [17, 22]. Submillisecond structure has been also reported [22].

3.2.2 Long and short gamma-ray bursts

Classifying GRBs by the temporal characteristics, which exhibit a variety, was attempted. The existence of two components in the distribution of the duration time was suggested in [23]. It was established by observations of hundreds of GRBs by the BATSE [24]. For unbiased studies, the T_{90} measure was introduced. It is defined as the time duration which the accumulated flux value increase from 5% to 95% above the background. Thus, T_{90} contains 90% of the GRB flux. The T_{50} measure, which contains 50% of the total flux, is also used. Kouveliotou *et al.* demonstrated the T_{90} distribution has the two log-normal components [23]. These components peak at ~ 0.3 s and ~ 30 s, and they are separated at ~ 2 s. They are called short-GRBs and long-GRBs. The distribution of T_{90} is plotted with the GBM catalogue as Fig. 3.2. The short-GRBs tend to have harder spectra

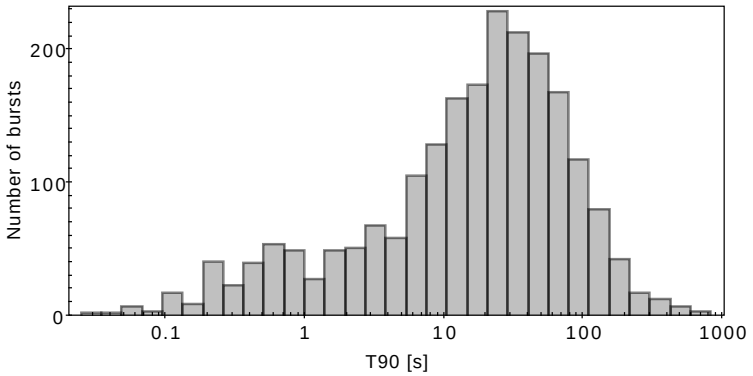

Figure 3.2: Distribution of duration time T_{90} of the GRB detected by the *Fermi*-GBM. The values are taken from the GBM online catalogue [18, 19, 20].

than of the long-GRBs [24]. Although they are considered to have different origins, their spectral shapes are similar, and there appears to be a common physics.

3.2.3 Spectral features

Cline *et al.* [25, 26] found that six and nine GRBs, which were observed in 1971 - 1973 by *IMP-6* and *IMP-7* respectively, had similar spectra. The spectra in ~ 100 keV - 1 MeV were consistent with an exponential function $dN/dE \propto \exp(-E/E_0)$ tangent to a power-law function at the high energy. The exponential cutoff energy and the power-law index distribute around 150 keV and -2.5, respectively. GRB observations with the KONUS instruments onboard *Venera 11* and *Venera 12* [27, 28] were

carried out from 1978 to 1980, and 143 GRBs were detected [29]. Mazets *et al.* [29] derived a conclusion that the GRB spectra in the energy range from 30 keV to 2 MeV were approximated by $dN/dE \propto E^{-1}\exp(-E/E_0)$. Between 1980 and 1983, the Gamma-Ray Spectrometer on the *Solar Maximum Mission Satellite* detected 72 GRBs. The Gamma-Ray Spectrometer covers a higher energy range than the instruments above, namely, 300 keV - 9 MeV. The observed spectra exhibited that GRBs commonly have high-energy emission above $\sim$ 1 MeV [30]. On top of that, other two instruments onboard the *CGRO*, The Imaging Compton Telescope (COMPTEL) and the Energetic Gamma Ray Experiment Telescope (EGRET), which covered 0.8 - 30 MeV and 20 MeV - 30 GeV, respectively found the spectrum of GRB 910513 extended up to $\sim$ 100 MeV [31, 32].

Consequently, spectra of GRB typically are described by $dN/dE \propto E^{\alpha}\exp(-E/E_0)$ flattening out smoothly to $dN/dE \propto E^{\beta}$ where $\beta < \alpha < 0$. Band *et al.* [3] studied time-averaged spectra of GRBs in the BATSE catalogue [2], and found that the spectra are well described by Eq. 1.1, but α, β and E_0 vary depending on each burst. The function is dubbed the Band function. Typically $\alpha \sim -1$ and $\beta \sim -2$. The peak energy of this formula E_{peak} equal $(2+\alpha)E_0$. Here I plot the distributions of α (Fig. 3.3), β (Fig. 3.4), and E_{peak} (Fig. 3.5), with GRBs in the GBM online catalogue [18, 19, 20].

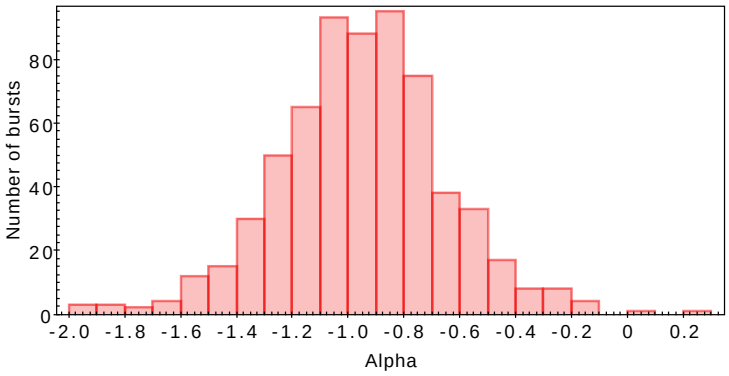

Figure 3.3: Distribution of the Band spectral index below the break energy α of the GBM-GRBs. The samples are from the ones of Fig. 3.6 and restricted to the ones with smaller error of α than 0.1.

3.3 Spatial distribution

The origin of such a spectacular phenomenon, even whether galactic or extragalactic, had been veiled for a long time because of a difficulty of tracing the arrival direction of gamma-rays. In 1978, the space probes *Venera 11* and *Venera 12* were launched toward Venus [27]. Both of them carried the KONUS GRB sensors, and each of them consisted of six NaI(Tl) scintillation detectors whose axes

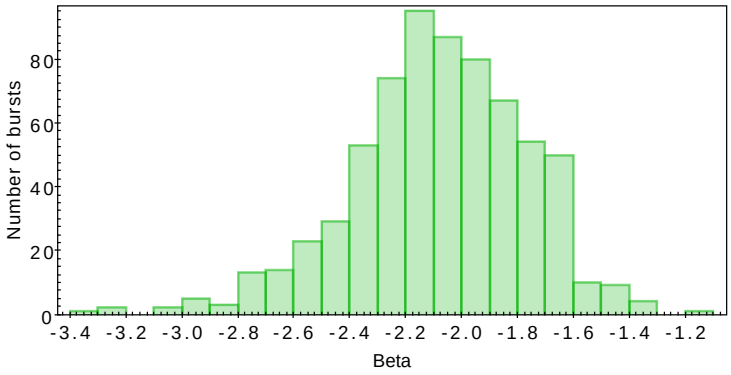

Figure 3.4: Distribution of the Band spectral index above the break energy β of the GBM-GRBs. The samples are from the ones of Fig. 3.6 and restricted to the ones with smaller error of β than 0.2.

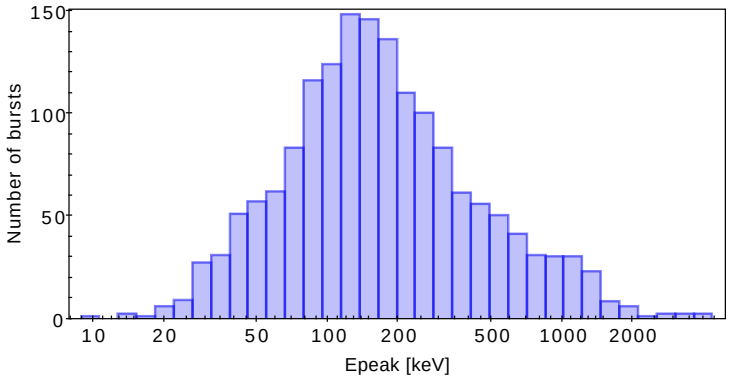

Figure 3.5: Distribution of the Band peak energy E_{peak} of the GBM-GRBs. The samples are from the ones of Fig. 3.6 and restricted to the ones with smaller error of E_{peak} than 50%.

were directed along the Cartesian axes. The KONUS enabled one to restrict the direction of GRBs via two means which were based on the anisotropic response of each detector and the difference in the arrival time of the GRB signals between two spacecrafts. The precision of the localization was typically from one to four degrees [28]. Until the end of the observations, the locations of 58 sources were determined [23]. The obtained sky distribution did not exhibit any sign of anisotropy [23].

About ten years later, the BATSE localized a larger number of GRBs. The distribution of 260 bursts clearly proved the isotropy [2, 33]. The isotropy implied the GRBs were extragalactic phenomena, but it was not decisive. In Fig. 3.6, I plot the sky distribution of 2132 GRBs which were detected by the *Fermi*-GBM [18, 19, 20].

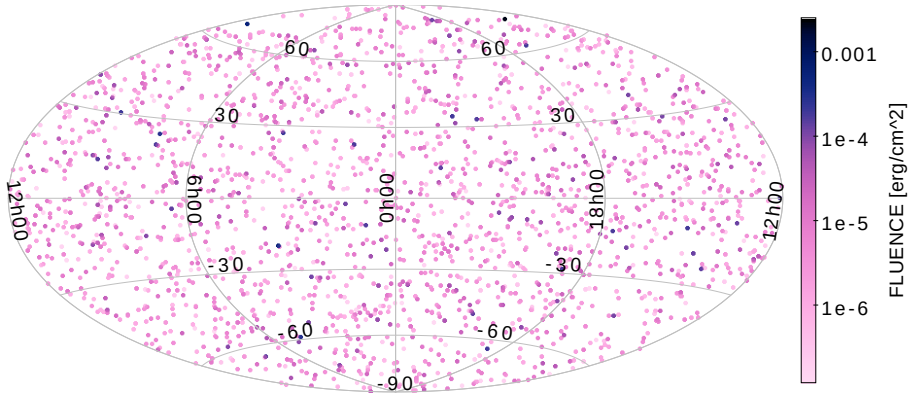

Figure 3.6: All sky plot of 2132 GRBs detected by the *Fermi*-GBM from 14 July 2008 until 2 October 2017, in the Galactic coordinate. The data were obtained from the GBM online catalogue [34, 18, 19, 20]. The marker color indicates the fluence in 10 keV - 1 MeV measured by the GBM in logarithmic scale.

3.4 Afterglow emission

3.4.1 Discovery

A direct evidence for the extragalactic origin was obtained by a discovery done by the *BeppoSAX* satellite, which was operated from 1996 to 2002. It had two X-ray telescopes, the Wide Field Camera and the Narrow Field Instruments. In 1997, the Wide Field Camera detected GRB 970228. The Narrow Field Instruments was immediately pointed at the localized direction and discovered an unknown source [35]. The source was detected also by follow-up optical observations, and a gradually fading source was observed. This was discovery of afterglow. Spectral observations of optical afterglows enable us to find the host galaxies. GRB 970228 was suggested to be associated with a faint galaxy, and then the extragalactic origins of GRBs were established [36].

The afterglows are observed in many wavebands from radio to high-energy gamma ray. Roughly speaking, they typically fade following a power-law function with the index from -1 to -2, for example, Fig. 1.2.

3.4.2 Counterpart objects

Long-GRBs

In the following year, 1998, another important association was reported. The optical afterglow of GRB 980425 was found in a spiral galaxy and the optical spectrum and location indicated a luminous supernova, which was named SN 1998bw [37]. The association of the long-GRB and the Type Ic supernova was suggested, although it was not very clear. In 2003, the *High Energy Transient Explorer II* (*HETE-II*) detected GRB 030329. The spectrum of the optical afterglow in early time consisted of a power-law continuum and emission lines. As these components declined, however, the spectrum exhibited broad peaks characteristic in supernovae [38, 39]. It has been confirmed that at least some of the long-GRBs are associated with core collapse supernovae. It is supported also by the fact that GRBs are typically found in star forming regions of their host galaxies [40]. On the other hand, the central engines which are produced by core-collapsing, providing the energy and causing GRBs have not been elucidated. They may be black holes or magnetars.

Short-GRBs

Because *BeppoSAX* was not able to accurately localize bursts shorter than $\sim$ 1 s and *HETE-II* was not sensitive to hard spectra which short-GRBs tend to have, the information on short-GRB counterparts was unavailable. In 2004, the *Neil Gehrels Swift Observatory* (hereafter *Swift*) was launched. It has three instruments, the Burst Alert Monitor (BAT), the X-ray Telescope (XRT) and the UV/Optical Telescope (UVOT), which cover the 15 - 150 keV, 0.2 - 10 keV energy range, and 170 - 600 nm wavelength band, respectively [41]. The BAT is able to localize a GRB to within a few arcminuites. When the BAT detects a GRB, *Swift* quickly slew to the GRB position and observe the burst with the XRT and the UVOT, which localize the burst by the typical accuracy of five and less than one arcsecond, respectively.

In 2005, the *Swift*-BAT detected a short-GRB 050509B, and the XRT localized the burst to within about nine arcseconds [42]. This was the first discovery of short-GRB afterglows. A luminous, non-star-forming elliptical galaxy was found to be highly likely associated to the GRB. A supernova was not detected. Observations in the following decade led to a conclusion that short-GRBs occur either in early-type and late-type galaxies [43]. In 2013, a short-GRB 130603B was detected, and follow-up observations in optical and near-infrared with the *Hubble Space Telescope* were performed. An image which was captured about nine days after the burst exhibited a significant excess in

near-infrared [44, 45].

Another important discovery was made in 2017 by the *Fermi*-GBM. The GBM monitors all the sky except for the region occulted by the Earth. It localizes the GRB to within about four degrees [46]. The *Fermi*-GBM detected a short-GRB, 170817A just after the first detection of gravitational waves from a binary neutron star inspiral [47, 48]. The detection of the GRB was at 1.7 s after the merger time and their localized sky regions were consistent.

3.4.3 Light curves

The ability of quick slewing of *Swift* revealed new temporal features of the afterglows beyond the simple power-law. The light curves exhibit breaks of power-law decaying and late-time flares with fast variabilities compared with the time scale from the burst. The features of the afterglow light curves are most clearly seen in X-ray. The "canonical" X-ray light curve, which is depicted in Fig. 3.7 is described by a broken power-law with some flares in late time [49]. There are six components but

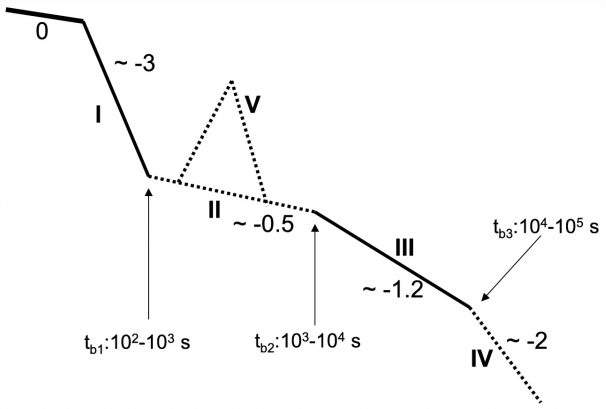

Figure 3.7: Synthetic picture of the canonical X-ray light curve based on the *Swift* XRT observations [49]. The phase 0: the prompt emission. The power-law segments I and Ⅲ are most common, and they are drawn with solid lines. The other three components are seen in some of the GRBs and marked as dashed lines. The details are explained in text.

not all of them are observed in each afterglow.

Phase 0 This phase corresponds to the prompt emission.

Phase I Early steep decay phase with the decay index steeper than -2.

Phase Ⅱ Plateau phase: the decay index is shallow, ~ -0.5. Sometimes it is flatter than this or even slightly increasing.

Phase Ⅲ Normal decay phase: the decay index is typically ~ -1.

Phase IV Late steep decay phase.

Phase V Nearly half of all X-ray afterglows have one or more flares. They exhibit rapid variabilities compared to the time scale they happen.

I refer to three observational samples of the X-ray afterglows as Fig. 3.8, 3.9, and 3.10. In these figures, Phase 0, I, II, III, IV in Fig. 3.8, Phase 0, I, II, III in Fig. 3.9, and Phase III, V in Fig. 3.10 are seen, respectively. The energy spectral indices in X-ray are ~ -1 during Phase II, III and IV. Phase I sometimes has a softer spectrum ~ -1.5 and has a similar index with the other phases in the other cases. The flares V have similar spectra with the phase I [49].

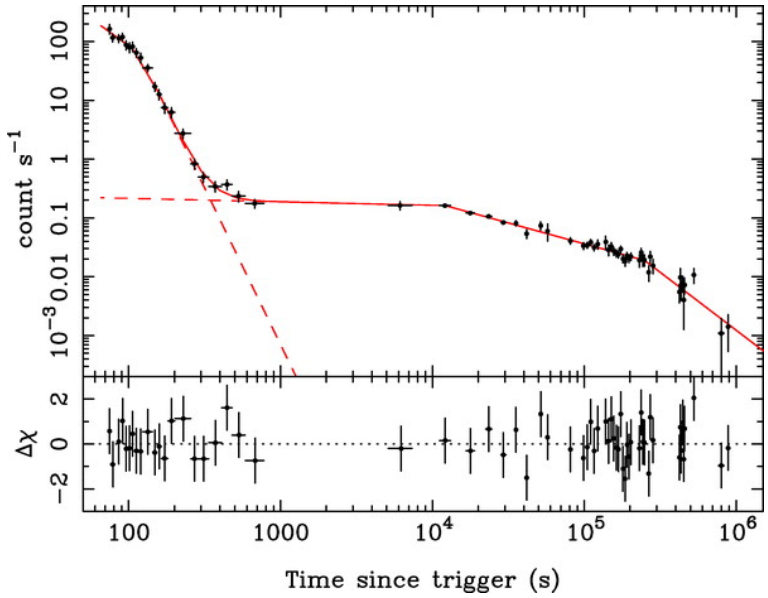

Figure 3.8: Light curve of GRB 050315 which was observed by the *Swift*-XRT in the 0.2 - 5 keV band. These data were corrected for pileup. The plot also shows the best-fitting model comprising a power law with one break and a power law with two breaks, which dominate at early and late times, respectively. The lower panel shows the fitting residuals divided by the errors [50].

3.5 High energy gamma-ray emission

3.5.1 Temporally extended component

The emission of some of GRBs extends to much higher energy, above GeV. The high-energy emission was discovered by the EGRET of the *CGRO* in 1994. The EGRET detected a 18 GeV photon from GRB 940217 at ~ 4.5 ks after the burst [53].

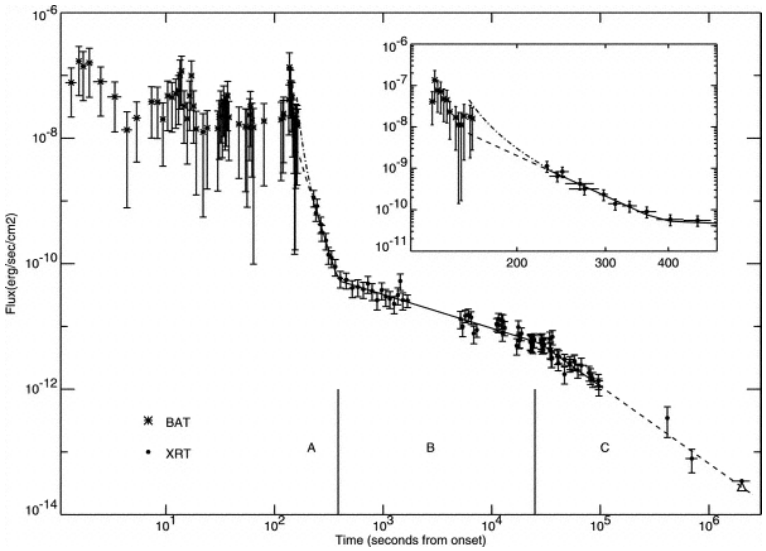

Figure 3.9: Light curve of GRB 050319 which was observed by the *Swift*-XRT and BAT. The XRT covers the 0.2 - 5 keV band. The BAT light curve was extrapolated into the XRT energy band. The solid line represents the best-fit model of a power-law with two breaks, and the dashed line is the extrapolation of this model prior to the first XRT observation. The dot-dashed line represents the extrapolation back to the end of the prompt emission of the best fit, obtained using the double broken power-law model. The inset shows the time interval including the last peak of the GRB and phase A of the afterglow in the main plot [51].

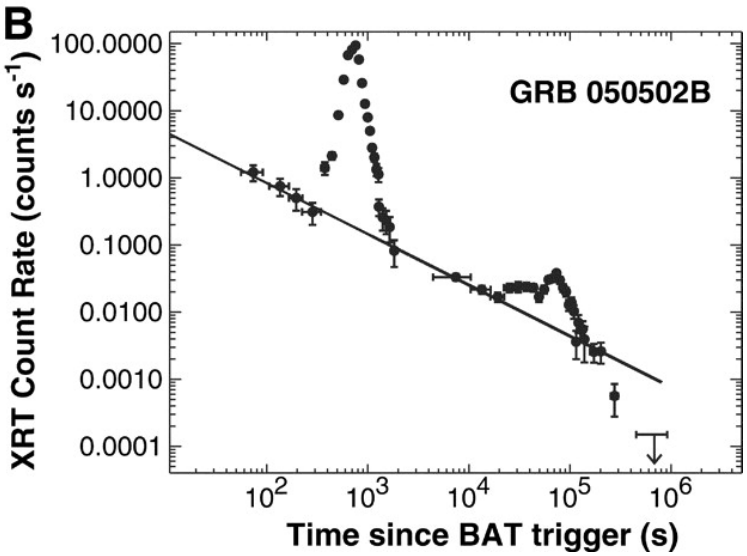

Figure 3.10: Light curve of GRB 050502B which was observed by the *Swift*-XRT. The solid lines represent a power-law fit to the underlying afterglow decays from about 100 s to 10 ks. The bright X-ray flares are superposed on the power-law decay [52].

The *Fermi* satellite has another instrument, the Large Area Telescope (LAT), which covers an energy range from 20 MeV to $>$ 300 GeV. The LAT is promptly pointed at the direction localized by the GBM or another instrument. The LAT is a pair conversion telescope featuring the broad energy coverage, large effective area, and large field of view (FoV). The details are described in § 5. In 2010, a novel event class of the LAT data was introduced [54]. It is called LAT Law Energy (LLE) class. It recovers events between $\sim$ 30 MeV and 100 MeV, and thus it allows to fill the gap between the GBM and LAT bands. The GBM and LAT have detected 2298 [18, 19, 20] and 143 GRBs [55], respectively, until 17 April 2018.

The emission above 100 MeV is described as a delayed, long-lasting component compared with the prompt. The earliest photons with energy above 100 MeV typically arrive a few seconds after the GBM trigger, and the emission in the LAT band lasts for much longer than the duration in the GBM band, gradually decaying by a power-law. A small fraction of the GRBs have been detected in high-energy gamma ray. These bursts are relatively bright in the GBM band as exhibited in Fig. 3.11. Radiations from the bright GRBs are observed for thousands of seconds or longer. The

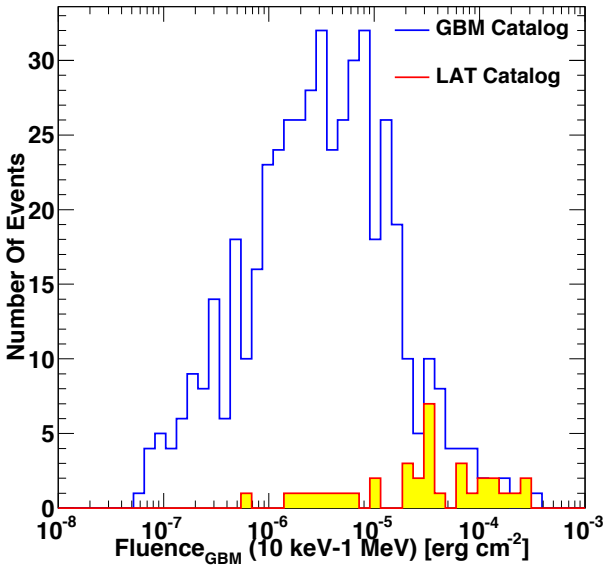

Figure 3.11: Distribution of the energy fluences in the GBM band, namely, 10 keV - 1 MeV for the bursts detected by the LAT compared with the fluences in the same energy band for the entire sample of GRBs [34]. This figure is taken from [56].

prompt and afterglow emission are not separated clearly. In 2013, an extremely bright GRB 130427A was detected [57]. These high-energy features are seen for this GRB. In Fig. 3.12, the bulk of $>$ 100 MeV photons arrived after the peak of the emission in the lower-energy bands. In Fig. 3.13, the

LAT light curves are roughly described by a power-law, and the emission was significantly detected even tens of kiloseconds after the burst. It is natural to consider this component a part of the

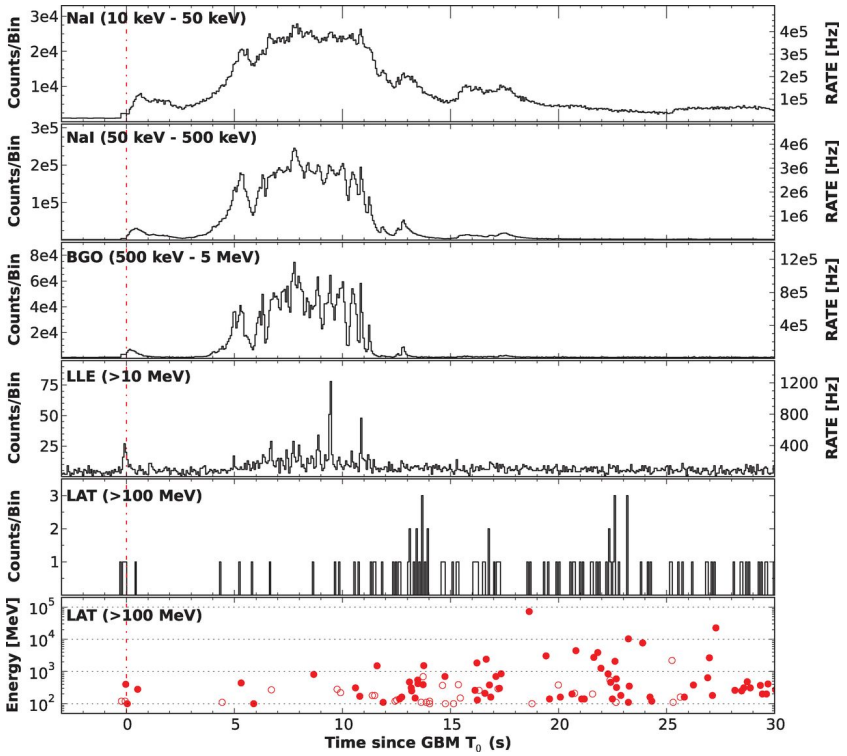

Figure 3.12: Light curve of the brightest part of GRB 130427A which was observed by the *Fermi*-GBM and LAT[57]. Each panel except for the lowest one represents the count in a 0.064-second bin in a different energy band. The top three panels are for the GBM data. The fourth panel exhibits the LLE light curve, and the fifth panel does the standard LAT light curve. In the bottom panel, the photon energy of each event is plotted individually. The solid circles indicate photons with a probability of > 0.9 of being associated with the GRB.

afterglow emission.

The distribution of spectral indices of LAT-detected GRBs is plotted in Fig. 3.14. The photon spectral index Γ for the count spectrum $dN/dE \propto E^{\Gamma}$ after the end of the prompt radiation is typically ~ -2. During the prompt phase, some GRBs exhibit softer spectra. The power-law decaying indices α_L for the count flux $dN/dE \propto t^{-\alpha_L}$ have been decided only for well observed GRBs. The index is typically ~ 1 as visualized in Fig. 3.15. Nava *et al.* found that renormalizing the high-energy light curves of multiple GRBs by the energy of the prompt emission makes them overlap, as demonstrated in Fig. 3.16 [58]. Similar correlations have also been reported in optical and X-ray data [59, 60].

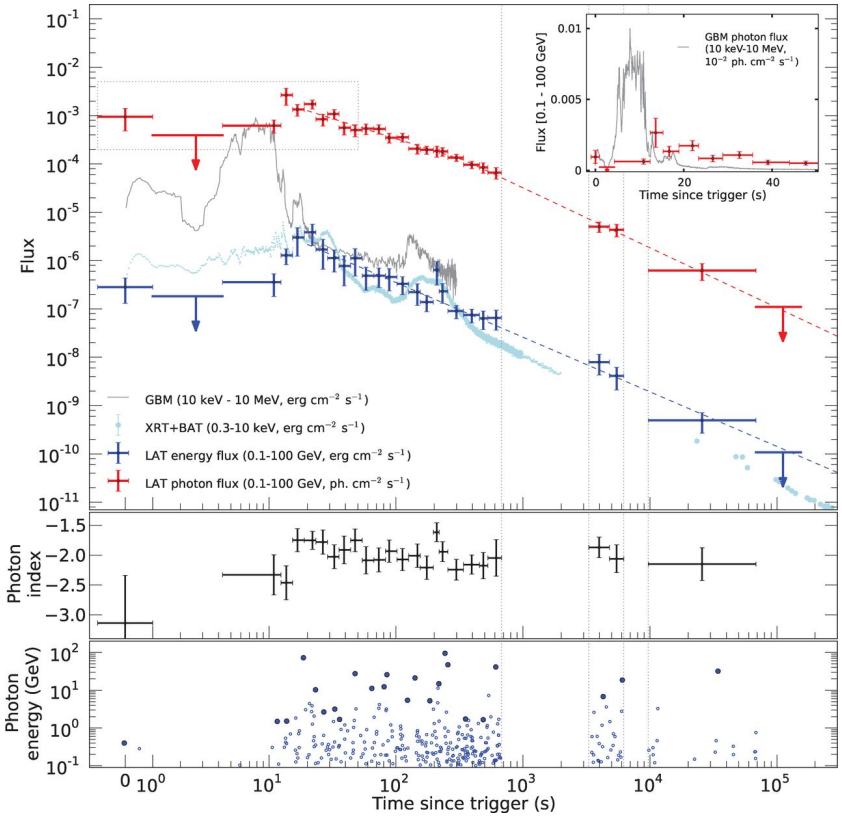

Figure 3.13: Light curves of the temporally extended emission of GRB 130427A which was observed by the *Fermi*-GBM, LAT, the *Swift*-BAT, and XRT [57]. Top: LAT photon flux (blue) and energy flux (red) light curves. The light curves in 10 keV - 10 MeV (GBM) and in 0.3 - 10 keV (BAT+XRT) are overplotted. The inset zooms the LAT and GBM photon flux light curves in the first 50 s. Middle: LAT photon index. Bottom: Energy of each LAT photon with a probability $> 90\%$ of being associated with the GRB.

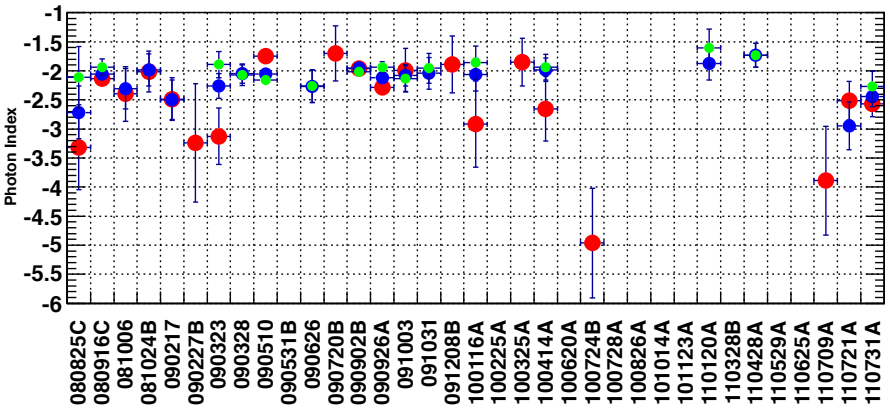

Figure 3.14: Spectral photon index of LAT-detected GRBs measured in three time windows: T_{90} of the GBM-detected emission (red), T_{90} of the LAT-detected emission (blue), and from the end of GBM T_{90} to the end of LAT T_{90} (green) [56].

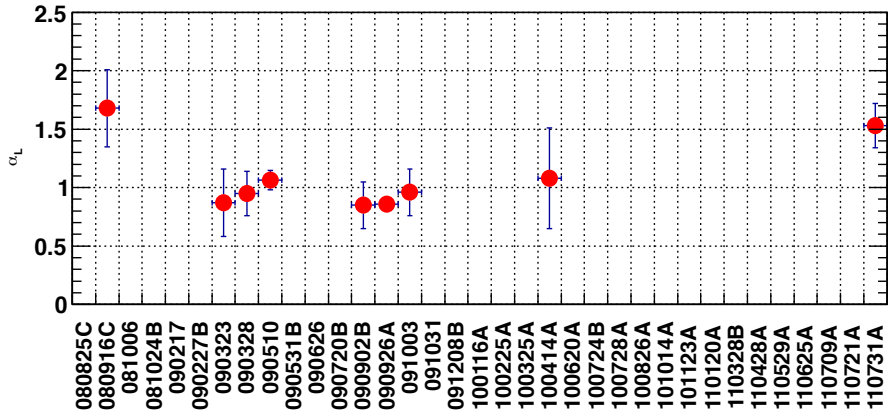

Figure 3.15: Temporal decay index of the extended high-energy emission of GRBs detected by the LAT [56].

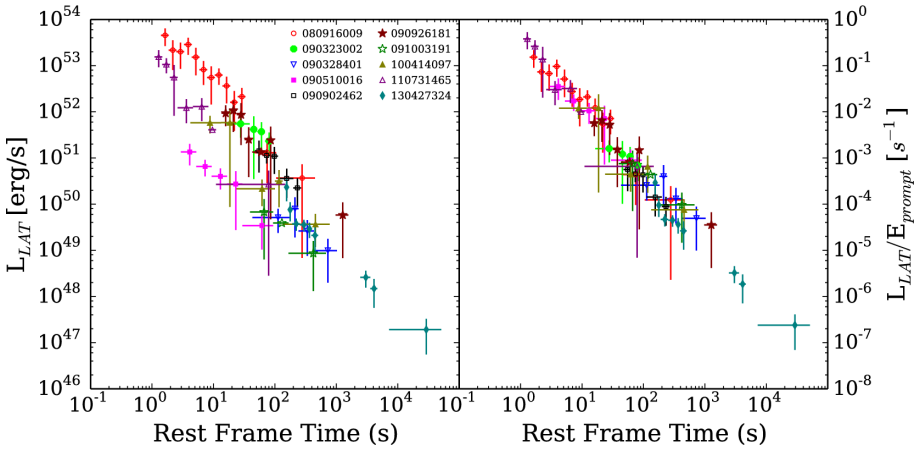

Figure 3.16: Left: the light curves of the luminosity in 0.1 - 10 GeV vs. time, which both of them are in the rest frame of the central engine, for 10 GRBs. Right: the same light curves as the left panel, but the luminosity values are renormalized by the prompt energetics in 1 keV - 10 MeV, which are estimated from the GBM data [58].

3.5.2 Emission during the prompt phase

Continuation of the Band component to the high-energy gamma ray predicts detections by the LAT in some cases. Joint GBM-LAT spectral analyses showed the Band-alone function fit spectra of a fraction of the LAT-detected GRBs better than other models [56]. The Band-alone function provides the best fit for GBM-LAT spectra of a fraction of the LAT-detected GRBs. In spectra of some GRBs, cutoffs in the LAT energy range are identified. Ackermann *et al.* examined 30 bright GBM-detected bursts and showed including the LAT upper limits drastically softens the best-fit spectral function for many of the samples, beyond the statistical errors obtained by fitting GBM data alone [61]. Vianello *et al.* reported cutoffs in the spectra of GRB 100724B and 160509A below $\sim$ 100 MeV [62].

In some cases, a harder spectral component can be identified during the prompt phase, in addition to the Band component. Figure 3.17 shows the count spectrum and spectral energy distribution (SED) of GRB 090902B during a partial interval of the prompt phase, together with the result of fitting with the Band + power-law function [63].

Fast temporal variabilities have been detected in high-energy spectra of a few GRBs. GRB 090926A [64, 65] is the most remarkable sample. The GBM and LAT light curves are displayed as Fig 3.18. There is a simultaneous sharp spike at $\sim$ 10 s. The SEDs are displayed as Fig. 3.18. At the spike time, the power-law component dominates the energy range above 1 MeV.

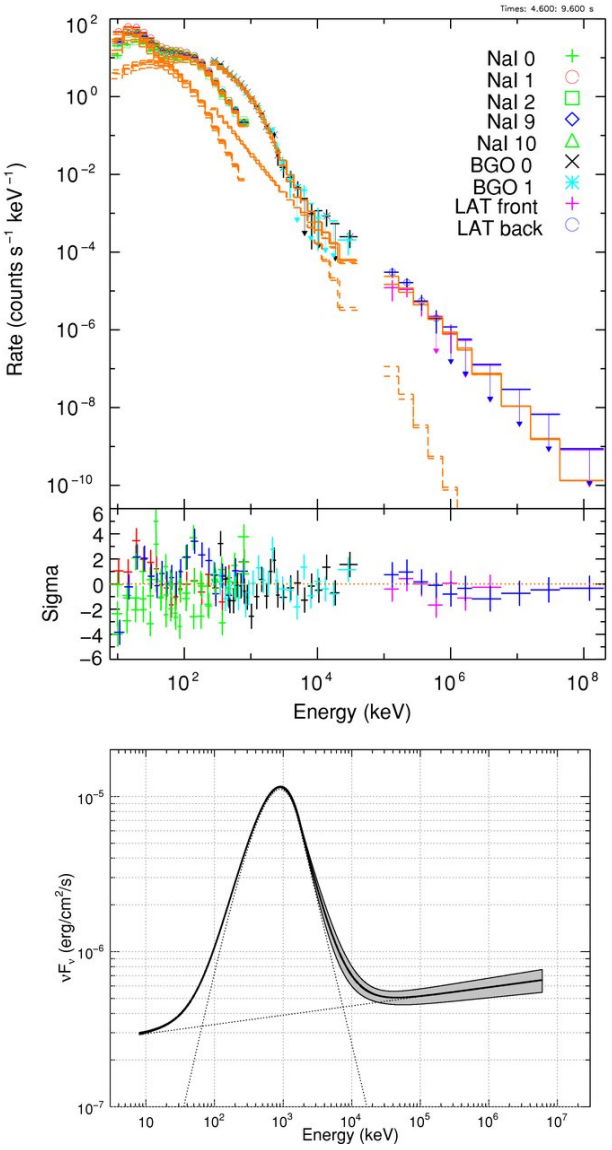

Figure 3.17: Results of a joint fit of GBM and LAT data of GRB 090902B in the interval from 4.6 s to 9.6 s with respect to the GBM trigger time, which is a part of the prompt phase. Top: Counts spectrum; separate model components are plotted, Band (dashed), power law (solid). Bottom: Unfolded SED. The extension of the > 100 MeV power-law component to the lowest energy (< 50 keV) is plotted [63].

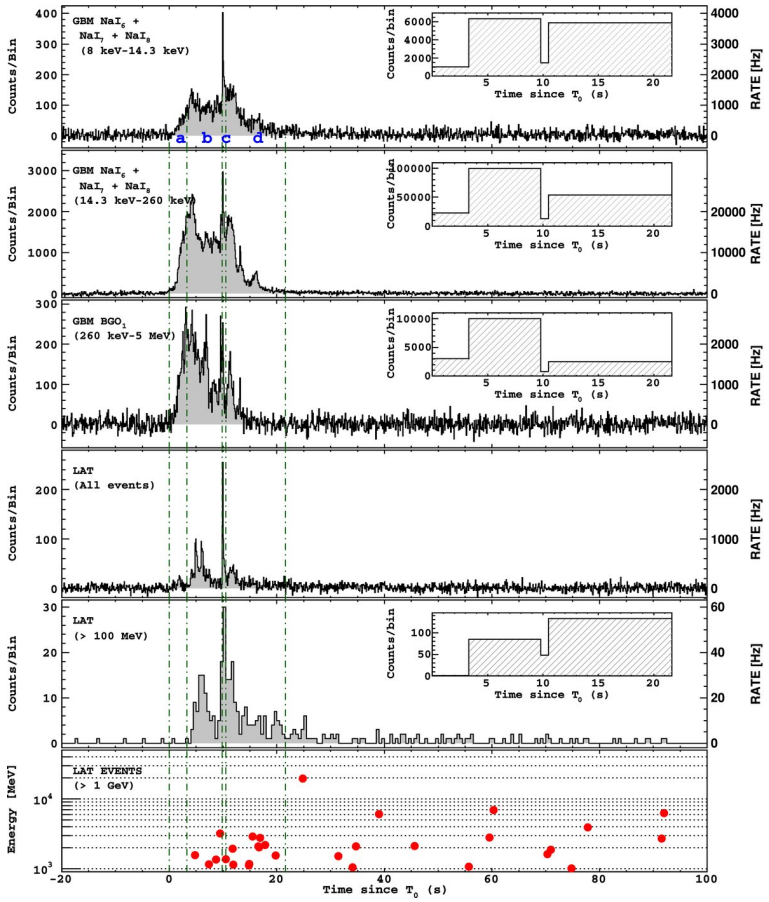

Figure 3.18: *Fermi*-GBM and LAT light curves of GRB 090926A [64]. The top three panels are for the GBM data. The fourth panel exhibits all LAT events that pass the on-board GAMMA filter (*cf.* § 5.3.2). The top four curves are for 0.1-second bins. The fifth and sixth panels show LAT data "transient" class events for energy > 100 MeV and > 1 GeV, respectively, both using 0.5-second bins. The vertical lines indicate 0, 3.3, 9.8, 10.5, 21.6 s from the GBM trigger time. The insets show the counts for each data set, binned by these boundaries.

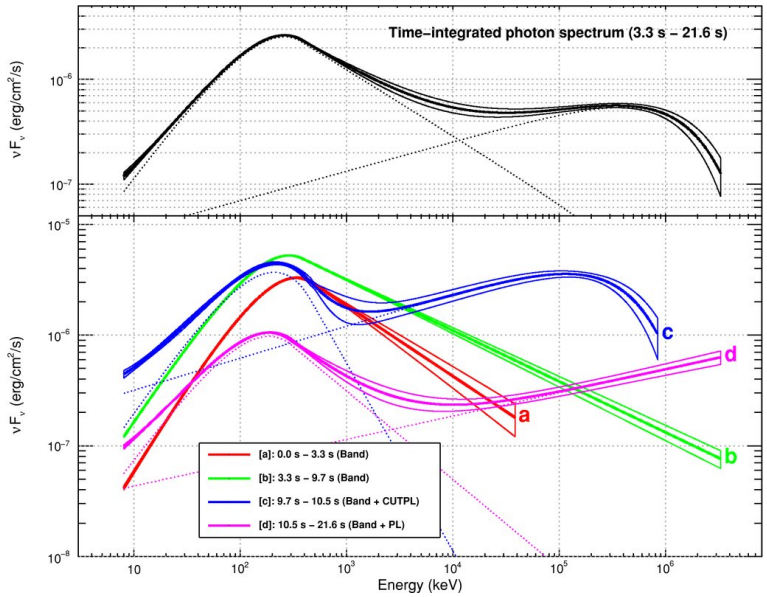

Figure 3.19: SED plots of GRB 090926A taken from [64]. Top: the best-fit (Band + power-law with a cutoff) model for the time-integrated data plotted as a SED. The $\pm 1\sigma$ error contours derived from the errors on the fit parameters are also shown. Bottom: the SED model spectra (and $\pm 1\sigma$ error contours) plotted for each of the time bins shown in Fig. 3.18.

3.5.3 Gamma-ray events ever detected above 10 GeV

The spectra of some GRBs extends beyond 10 GeV. The highest observed energy of the GRB photons ever detected is 94 GeV, of a photon from GRB 130427A [57] at 243 s after the GBM trigger. The highest redshift-corrected energy is 144 GeV of a photon from GRB 080916C, whose redshift is 4.35 [66]. This event was detected during the prompt phase which I define as the interval before the time at which 95% of the total fluence has been detected in 10 keV – 1 MeV in this thesis. Contrarily, some of such high energy photons are detected in late time. At first, the EGRET recorded a 18 GeV event from a GRB occurred on 17 February 1994 at $\sim$ 4500 s after the low energy emission ended [53]. The redshift-corrected energy of the 94-GeV event from GRB 130427A, which is mentioned at the beginning of this paragraph, is 127 GeV and highest among the GRB-photons after the end of the prompt phase. From the same burst, a 34-GeV event arrived at 34 ks after the GBM trigger. A detection of a 54-GeV photon at 17 ks after the trigger from GRB 130907A, whose redshift is 1.238, was reported in [67, 68]. From GRB 160509A, a 29-GeV photon arrived at 70 ks after the trigger [69]. The redshift is 1.17.

3.6 Attempts to detect very-high-energy photons

As mentioned in § 3.5.3, several gamma rays have been detected in the very-high-energy (VHE; above tens of GeV) range, but the numbers of the VHE photons are generally few. The sensitivity of the *Fermi*-LAT is limited by the signal statistics for this energy range. It is unrealistic to increase the effective area of an detector onboard spacecraft by more than one order of magnitude. Therefore, ground-based detectors are needed for VHE observation with little statistical uncertainty.

3.6.1 Imaging Atmospheric Cherenkov Telescopes

Two kinds of techniques for detecting gamma-rays on the ground have been developed. One is atmospheric Cherenkov telescope, which utilizes optical mirrors and photodetectors for receiving Cherenkov light produced by air showers triggered by VHE gamma-rays. When a high-energy gamma-ray enter the atmosphere, it interacts with the nuclei and produces an electromagnetic shower. The shower particles radiates Cherenkov light. The light is collected by mirror and detected by photosensors sensitive in optical band. Telescopes which are able to capture the shower profile and distinguish the gamma-ray events from hadronic showers caused by background cosmic-rays are called Imaging Atmospheric Cherenkov Telescopes (IACTs). There are three major operating IACTs in the world, Major Atmospheric Gamma Imaging Cherenkov (MAGIC), VERITAS, and the High Energy Stereoscopic System (H.E.S.S.). They are very successful in detecting VHE gamma-ray sources such as active galactic nuclei, supernova remnants, pulsar wind nebulas, and compact-object binaries. More than 200 sources are known now [70].

Detection with the IACTs has been attempted for many GRBs, but no significant detection has been reported yet ([71, 72, 73, 74]). Observing GRBs by IACTs has some difficulties. First, their FoVs are $\lesssim 5^\circ$. Hence, they need to point to the sky position reported by other instruments such as the *Fermi*-GBM and the *Swift*-BAT, whose localization accuracies are the same order of the FoV of the IACTs. Because the flux of the temporally extended high-energy component decays as $\propto t^{-1}$ or steeper, the IACTs are required to catch the GRB before the flux becomes lower than the sensitivity. Next, the duty cycles of the IACTs are not high, $\sim 10\%$. Observation with Cherenkov telescopes are not performed during daytime and interrupted by clouds and the moon light. Last, photons above ~ 100 GeV are strongly absorbed by the extragalactic background light (EBL). The EBL is a summation of light emitted by stars and dusts in the universe. Its spectrum is redshifted and has two peaks in infrared [75]. Because of the pair creation process of very high energy photons and EBL photons, the flux of cosmologically distant sources is strongly suppressed above a certain energy. In order to avoid this absorption, the threshold of the energy of the primary gamma-ray is required to be lower than ~ 100 GeV. It is challenging because the amount of Cherenkov light is roughly proportional to the energy of the primary gamma-ray. The MAGIC telescopes have realized

the energy threshold of $\sim$ 50 GeV but it increases if the zenith angle is large or the effects of the moonlight on the sky darkness are significant.

A next-generation IACT array, the Cherenkov Telescope Array (CTA) [76] is being constructed now. It has three kinds of telescopes, Large-, Medium- and Small-sized telescope, and they cover the lowest, middle and highest energy ranges respectively. The Large-sized Telescopes (LSTs) are designed so that the energy threshold is lower than $\sim$ 20 GeV. Each LST has a 23 m diameter, $400\,\mathrm{m}^2$ collecting surface, and it will be able to point to any direction within 20 s. Hence, they are promising to detect GRBs.

3.6.2 Air shower array

Another technique is air shower array. This kind of instrument detects the secondary particles produced by air showers. Plastic scintillators or water Cherenkov tanks which are arranged on the ground are used for detecting the particles. The FoV of an air shower array is large, > 1.5 sr. With air shower array, one can observe gamma ray regardless of the daylight, moonlight and weather. On the other hand, narrow effective area in low gamma-ray energy ($\lesssim 1$ TeV) used to be a disadvantage of air shower experiments.

Atkins *et al.* searched for counterparts of 54 BATSE-detected GRBs in the data of a air shower array with water-Cherenkov detectors, Milagrito [77]. They found an evidence of $\sim$TeV emission from GRB 970417 [78]. An excess of events was observed at the direction of the GRB during the prompt phase. The probability of being a background fluctuation is 1.5×10^{-3} (post-trial). The excess is likely caused by photons above 650 GeV [79]. Milagrito was a prototype of Milagro, but Milagro did not detect any GRB.

Based on the experience of the Milagro experiment, the High-Altitude Water Cherenkov (HAWC) observatory was designed. The HAWC observatory began operations in 2013, and the full array was inaugurated in 2015. It has achieved the effective area $\sim 100\,\mathrm{m}^2$ at 100 GeV. It also has promising prospects of detecting GRBs, but no detections have been reported yet [80].

Chapter 4

Theories and interpretations

4.1 Relativistic motion

Relativistic motion of the gamma-ray source is required in order to avoid the "compactness" problem [81]. This problem was pointed out by [82] and [83]. The GRB emission with high luminosity and fast variability, which is mentioned in § 3.2.1, requires a small volume of the emission region. This condition bring about electron-positron pair creation and keeps gamma rays from escaping. The optical depth $\tau_{\gamma\gamma}$ is denoted by

$$\tau_{\gamma\gamma} = \frac{f_p \sigma_T F d_L^2}{R^2 m_e c^2} \tag{4.1}$$

where F is the observed energy fluence of the burst, d_L is the luminosity distance from the earth, R is the size of the emission region and f_p is a fraction of photon pairs with energy sufficient for creating electron pairs. Using typical values, the optical depth can written as

$$\tau_{\gamma\gamma} \sim 10^{12} f_p \left(\frac{F}{10^{-7}\mathrm{erg \cdot cm^{-2}}} \right) \left(\frac{d_L}{3 \times 10^{19}\mathrm{cm}} \right)^2 \left(\frac{\delta t}{0.1\,\mathrm{s}} \right)^{-2} \tag{4.2}$$

f_p is not very small according to Fig. 3.5. Therefore, the optical thickness should be quite large. However, we observe non-thermal spectra and these are contradicting each other.

The solution of the compactness problem under the standard model of particle physics is introducing a relativistic motion of the gamma-ray source. It relaxes the problem by two relativistic effects. Set the Lorentz factor of the source Γ. First, the photon energy in the source rest frame is smaller than the observed one by a factor of Γ. This reduces f_p by $\Gamma^{-2(\beta+1)}$ where β is the high energy spectral index of the Band function, ~ -2. Next, the size of the source R is allowed to be

bigger by a factor of Γ^2. Now the optical depth is

$$\tau_{\gamma\gamma} \sim \frac{10^{12}}{\Gamma^{2-2\beta}} f_p \left(\frac{F}{10^{-7}\mathrm{erg/cm^2}}\right) \left(\frac{d_L}{3\times 10^{19}\mathrm{cm}}\right)^2 \left(\frac{\delta t}{0.1\mathrm{s}}\right)^{-2} \tag{4.3}$$

$\tau_{\gamma\gamma} < 1$ requires $\Gamma \gtrsim 100$. Consequently, the GRBs are emission originating from objects moving with relativistic speed. The detailed calculations [84] and [85] give similar constraints.

4.2 Jet collimation and true energy

The rapid drops of the phase IV suggest the GRB outflows are collimated [86]. This point is discussed in § 4.6.1. If the outflow is collimated within the angle θ_j, the required total energy amount of gamma-ray emission is reduced by a factor of $\sim \theta_j^2$. Fig. 4.1 exhibits the distribution of the isotropic-equivalent gamma-ray energy $E_{\gamma,iso}$ of long-GRBs. It ranges up to $\sim 10^{54}$ erg but the numbers are reduced by a factor of 100 if $\theta_j \sim 0.1$ radians.

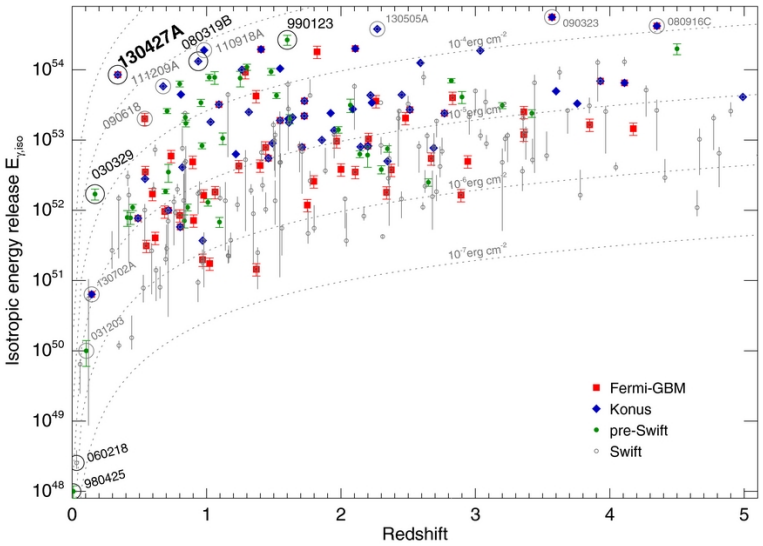

Figure 4.1: Total isotropic-equivalent gamma-ray energy release of pre-*Swift*, *Swift*, and *Fermi*-GBM long-duration GRBs vs. redshift [87]. The dotted curves are lines of constant fluence.

4.3 Launch of relativistic jets

Next I discuss how a central engine launches a jet, in other words, how to provide kinetic energy.

4.3.1 Fireball

Temperature The most broadly discussed hypothesis is the "fireball" model. Fireball means an optically thick plasma whose temperature is significantly higher than the rest mass energy. Consider a huge amount of energy concentrated within a small volume, whose scale is $\sim 10^7$ cm. Assume the radiation with the luminosity L is emitted at the initial radius R_0. From Stefan-Boltzmann law, the temperature is

$$k_B T \sim 1\,\mathrm{MeV} \left(\frac{L}{10^{52}\mathrm{erg}}\right)^{1/4} \left(\frac{R_0}{10^7\mathrm{cm}}\right)^{-1/2} \tag{4.4}$$

Thus, it is sufficiently high for electron pair creation.

Bulk Lorentz factor This model does not require any details of the progenitor. Once a fireball is created, it starts to expand the radius R adiabatically. The photons and particles are bound by Thomson scattering. In the beginning, the expansion accelerates as $\Gamma \propto R$. The radiation energy of the fireball is transformed into the kinetic energy of mainly baryons with mass M during it. The acceleration terminates when the total energy becomes equivalent with the kinetic energy ΓMc^2, or when the optical thickness becomes smaller than ~ 1, whichever first occurs.

In the former case, the fireball is accelerated up to $\Gamma_s \sim E/Mc^2 \equiv \eta$. $\eta \equiv L/\dot{M}c^2$ implies how much baryons associate with the fireball because the outflow mass M is dominated by baryons. Provided a small amount of baryons, they are accelerated to relativistic speed. The corresponding radius, which is called the "saturation radius", is $R_s = \eta R_0$.

If the amount of baryons is less than a certain value, the outflow becomes optically thin before the saturation, and the particles cannot be accelerated by adiabatic expansion any more. There is an upper limit of the Lorentz factor in context of the fireball model [88],

$$\Gamma \lesssim \left(\frac{L_{iso}\sigma_T Y \Gamma_{pre}}{4\pi m_p c^3 R_0}\right)^{1/4} \sim 1.4 \times 10^3 \left(\frac{L_{iso}}{10^{52}\mathrm{erg}\cdot\mathrm{s}^{-1}}\right)^{1/4} \left(\frac{M_{BH}}{10\mathrm{M}_\odot}\right)^{-1/4} Y^{1/4}\Gamma_{pre}^{1/4} \tag{4.5}$$

where L_{iso} is the isotropic-equivalent-luminosity of the outflow, σ_T is the cross section of Thomson scattering, Y is the ratio of the numbers of electrons per baryons in the fireball, Γ_{pre} is the Lorentz factor at the beginning of the fireball. Therefore, $\Gamma \gtrsim 10^3$ is challenging for fireball models although GRBs with very high luminosity may increase the Lorentz factor a few times higher. After the acceleration phase, the jets keep the Lorentz factors until they drop the energy through interaction with ambient matter (the coasting phase).

4.3.2 Poynting-flux-dominated outflow

Alternatives for the fireball model are Poynting-flux-dominated outflows models. Such outflows can be possibly launched from black holes with the Blandford-Znajek mechanism [89] or from spinning down millisecond magnetars [90, 91]. The jets are accelerated through magnetic field dissipation or adiabatic expansion. Generally, these magnetic mechanisms are difficult to calculate the processes and to predict the observations. Hence, I focus on the jet acceleration by the adiabatic expansion of the fireballs in the following sections.

4.4 Mechanism of the prompt emission

What mechanism and particles produce gamma-rays still remains unclear even once a relativistic jet is created.

4.4.1 Internal shock

First, I describe the most widely accepted model which is dubbed the "internal shock" model [92]. It explains the prompt emission as non-thermal emission from particles accelerated by shocks within the jets. These shocks are caused by a relativistic flow with time-dependent speed. When a slower part of the flow is caught up by a faster part, the collision produces a pair of shocks propagating into the faster shell and slower shell. The shock-heated particles radiate non-thermal gamma-rays.

A leading candidate of the gamma-ray emission process is the synchrotron radiation from electrons accelerated by the Fermi process. The main advantage of this model is that it can simply explain the fast variabilities of the prompt emission [93, 94]. On the other hand, its weakness is the difficulty to reproduce the spectra below the Band break energy. Fast-cooling of electrons inevitably leads to the photon spectral index $\sim -3/2$, but it is too soft with respect to the typical observed index ~ -1. This problem was pointed out by Ghisellini *et al.* [95], and it is being debated.

4.4.2 Photospheric radiation

The prompt emission may also be emitted as thermal radiation from the fireball. It is called the photospheric radiation. In this model, the Band spectrum is produced by up-scattering nearly thermal photons by hot electrons. Interpreting the GRB prompt emission as the photospheric radiation is supported by the fact that the observed peak energy clusters around sub-MeV. However, the observed flat spectra below the peak energy appear to be contradicting a spectrum derived from accumulation of multiple-scattering and a peak at the final frequency corresponding to the electron temperature in the photosphere [96].

4.5 The central engines and progenitors

4.5.1 Long-GRBs

Follow-up observations of afterglows by *BeppoSAX*, *HETE-II* and *Swift* have discovered some supernovae as counterparts of long-GRB such as GRB 980425/SN 1998bw [37] at $z = 0.0085$, GRB 030329/SN 2003dh [38, 39] at $z = 0.168$ and so on. They are spectroscopically categorized in Type Ic supernovae, which are produced by core collapse of massive stars whose hydrogen and helium envelopes have been blown. The GRBs associated with supernovae are typically near to the earth and classified as low-luminosity GRBs apart from some exceptions such as 030329 [38, 97] and 130427A [98]. Most of long-GRBs are harbored in irregular, star-forming galaxies and a few are in spiral star-forming galaxies [40]. The long-GRBs concentrate on the brightest regions of the host galaxies compared with core-collapse supernovae. It implies a very high star forming rate at the burst site. In addition, the long-GRBs appear to be restricted to galaxies with limited chemical evolution [40].

The follow-up observations firmly established a connection between at least some of the long-GRBs and Type Ic supernovae. A majority of the associated GRBs is faint and nearby, but this seems to be a selection bias [99]. It is because a counterpart supernova cannot be detected if it is far away, or if the GRB afterglow is much brighter than it. GRB 030329/SN 2003dh [38, 97] and GRB 130427A/SN 2013cq [98] suggested that the high-luminosity GRBs are also associated with the Ic supernovae.

Because of the reasons mentioned above, the progenitors of the long-GRBs are considered as massive stars stripped of their hydrogen and helium envelopes. However, what kind of object such stars collapse to, namely the central engines of the bursts, is still unclear. A promising candidate is a massive star directly collapsing to a black hole [100]. Collapsing to a magnetar is also viable although the extracted energy would not be enough for the most energetic GRBs [101].

The size of the emission region R is estimated from the minimum time-scale of the variability. It should be $R \lesssim c\delta t = 3 \times 10^8 (\delta t / 10\,\mathrm{ms})\,\mathrm{cm}$. *cf.* The Schwarzschild radius of a black hole with mass of $\sim 10\mathrm{M}_\odot$ is $\sim 3 \times 10^6$ cm.

4.5.2 Short-GRBs

Paczynski [102] and Eichler *et al.* [103] proposed collisions of neutron-star binaries, which occur inevitably because of gravitational radiation, as sources of GRBs with an energy scale of $\gtrsim 10^{50}$ erg. Narayan *et al.* discussed this hypothesis in more details [104]. Electromagnetic radiation can be generated via two possible processes, neutrino annihilation to electron pairs [103, 104] or an instable increase in magnetic field strength [104]. As mentioned in § 3.4.2, short-GRBs are associated to either

early-type and late-type galaxies. Comparison between short-GRBs and supernovae is visualized in Fig 4.2. The difference suggests that the short-GRB progenitors might be longer-lived than those of supernnovae Ia. This is interpreted to be because of a wide distribution of the delay time of neutron

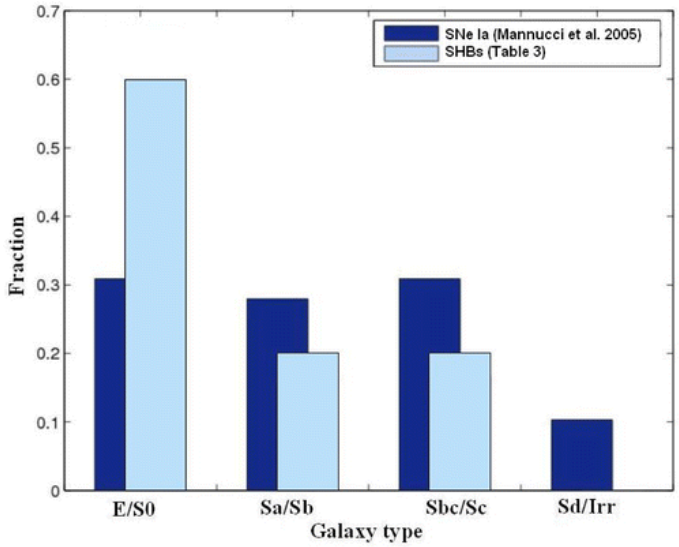

Figure 4.2: Comparison between the host galaxy types of short-GRBs (from Table 3 in [105]) and supernovae of Type Ia (from [106]). The fraction of short-GRBs in early-type galaxies is larger than the fraction of supernovae Ia observed in such galaxies in the nearby universe. The plot was taken from [105].

binary mergers, which is a summation of the time required for the initial progenitor binary to form a binary with two compact objects and the merger time of the binary [107, 108].

Lattimer *et al.* [109] and Eichler *et al.* [103] also proposed these mergers as potential sites for r-process nucleosynthesis. Ejection of neutron-rich matter causes formation of heavy radioactive elements via the r-process. The radioactive decay of these heavy elements provide a long-term source of heating [110] and drives a faint transient in near-infrared. This phenomenon is called "kilonova" or "macronova". The near-infrared excess which was found after GRB 130613B (§ 3.4.2) can be considered a kilonova associated with the GRB. It indicated that the short-GRB was caused by a NS binary merger.

GW 170817 and GRB 170817A were first jointly detected gravitational and electromagnetic radiation. The multi-messenger observations demonstrated that the progenitor of at least some short-GRBs is a binary of neutron stars [48].

4.6 Mechanism of the afterglow

Revealing the mechanism of the afterglow has been relatively progressed compared with the prompt emission.

4.6.1 External shock

Basically the afterglow is considered to be from "external shocks". They are created by collisions between the GRB jet and the surrounding medium while the internal shock is caused within the jets themselves [111, 112]. Such collisions are expected regardless of any kinds of explosion. The surrounding medium, hereafter circumburst medium (CBM), is interstellar matter or wind ejected from the progenitor such as a Wolf-Rayet star. Generally, the spatial number density distribution is formulated as $n_1(r) = (A/m_p)r^{-k}$ where r is the distance from the progenitor. The index k is considered to be zero for the uniform interstellar matter (ISM) and two for the stellar wind matter. The electrons accelerated in these shocks are considered to be responsible for the broadband afterglow emission.

Forward shock

Once the relativistic jet with the Lorentz factor Γ collides with the ambient matter, a shock front is formed. From the viewpoint of the jet co-moving frame, charged particles in the upstream enter in the shocked downstream with Γ. Here we consider protons because they dominate the kinetic energy. Then the magnetic field in the jet randomizes the direction of the velocity and the kinetic energy is transformed to thermal energy $\Gamma m_p c^2$. In the lab frame, the averaged energy of each proton in the downstream is $\Gamma^2 m_p c^2$ because the direction is randomized. At the radius R, the total energy in the shocked matter is

$$E \sim \frac{4\pi c^2 A R^{3-k} \Gamma^2}{3-k} \tag{4.6}$$

when the radiation energy losses are negligible. $4\pi A R^{3-k}\Gamma^2/(3-k)$ is the total mass of the shocked matter.

This equation determines the basic dynamics of the jet. If the circumburst medium is uniform and $k = 0$, the Lorentz factor of the jet develops as

$$\Gamma \propto R^{-3/2} \tag{4.7}$$

because the energy is conserved. In this case, setting the deceleration radius R_d as the radius at which the Lorentz factor decreases by a factor of two because of the collisions,

$$R_d \sim (1.2 \times 10^{17}) \left(\frac{E}{10^{53}\mathrm{erg}}\right)^{1/3} \left(\frac{n_1}{\mathrm{cm}^3}\right)^{-1/3} \left(\frac{\Gamma_0}{100}\right)^{-2/3} \mathrm{cm} \tag{4.8}$$

The time duration at the observer has shorten because of the Doppler effect. Using $t_{obs} \sim R/(2c\Gamma^2)$ and Eq. 4.7, we obtain

$$t_{obs} \sim \frac{R}{2\Gamma^2 c} \propto R^4 \propto \Gamma^{-8/3}. \tag{4.9}$$

Inversely,

$$\Gamma \propto t_{obs}^{-3/8} \tag{4.10}$$

and

$$R \propto t_{obs}^{1/4}. \tag{4.11}$$

The Lorentz factor starts to decay roughly from R_d. The corresponding deceleration time is

$$t_d \sim R_d/2\Gamma^2 c \sim 200 \left(\frac{E}{10^{53}\mathrm{erg}}\right)^{1/3} \left(\frac{n_1}{\mathrm{cm}^3}\right)^{-1/3} \left(\frac{\Gamma_0}{100}\right)^{-8/3} \mathrm{s}. \tag{4.12}$$

Substituting this to Eq. 4.10, the Lorentz factor at t_{obs} is

$$\Gamma(t_{obs}) \sim \Gamma_0 \left(\frac{t_{obs}}{t_d}\right)^{-3/8} \sim 55 \left(\frac{E}{10^{53}\mathrm{erg}}\right)^{1/8} \left(\frac{n_1}{\mathrm{cm}^3}\right)^{-1/8} \left(\frac{t_{obs}}{1000\,\mathrm{s}}\right)^{-3/8}. \tag{4.13}$$

Therefore, Γ is independent of the initial value Γ_0 and only very weakly depends on E and n_1 at $t_{obs} \gg t_d$.

The case in which the radiative energy losses dominate the system is discussed in detail by Ghisellini *et al.* [113]. The Lorentz factor is proportional to $t_{obs}^{-3/7}$ instead of $t_{obs}^{-3/8}$. Even if the fireball is initially radiative, it should become adiabatic after some time.

Physical conditions behind the shock

Consider a relativistic shock with the Lorentz factor Γ propagating through a uniform cold medium with particle density n_1. The physical condition of the shocked plasma is determined by the conservation of baryon number, energy, and momentum fluxes across the shock front. Blandford and McKee [114] found the following formulas,

$$\frac{e_2'}{n_2'} = \gamma_2 m_p c^2 \tag{4.14}$$

$$\frac{n_2'}{n_1'} = \frac{\hat{\gamma}_2\gamma_2 + 1}{\hat{\gamma}_2 - 1} \tag{4.15}$$

$$\Gamma^2 = \frac{(\gamma_2+1)[\hat{\gamma}_2(\gamma_2-1)+1]^2}{\hat{\gamma}_2(2-\hat{\gamma}_2)(\gamma_2-1)+2} \tag{4.16}$$

where e' and n' represent the energy density and particle number density with the subscriptions "1": the unshocked upstream medium and "2": the shocked downstream fluid in the local comoving frame, respectively; γ_2 is the Lorentz factor of the shocked fluid with respect to the unshocked matter; $\hat{\gamma_2}$ is the ratio of the adiabatic index. In the ultra-relativistic limit, $\hat{\gamma_2}$ equals the ratio of specific heats, 4/3. Then, Eq. 4.15 and Eq. 4.16 result in two simple formulas describing the physical conditions behind the shock,

$$n'_2 = 4\gamma_2 n_1 \tag{4.17}$$

and

$$\gamma_2 = \frac{\Gamma}{\sqrt{2}}, \tag{4.18}$$

respectively. In the rest frame of the shock front, the shocked fluid moves toward the burst center being accelerated by the pressure gradient [114].

I assume that the ratio of the magnetic energy density behind the shock to the total shock energy density is constant and denote it by ϵ_B. Using Eq. 4.17, we can obtain the magnetic field strength behind the shock,

$$B = \sqrt{32\pi m_p \epsilon_B n_1}\gamma_2 c. \tag{4.19}$$

Substituting Eq. 4.19 to Eq. 2.19, the cooling Lorentz factor becomes

$$\gamma_c = \frac{3m_e}{16\epsilon_B \sigma_T m_p c \gamma_2^3 n_1 t_{obs}}. \tag{4.20}$$

Concerning the minimum injection Lorentz factor, I assume a constant fraction ϵ_e of the shock energy is provided for the electrons. When the electron energy distribution is described by $dN_e/d\gamma_e \propto \gamma_e^{-p}$ with the constant power-law index $p(> 2)$,

$$\int_{\gamma_m}^{+\infty} \gamma_e m_e c^2 \gamma_e^{-p} d\gamma_e = \epsilon_e \int_{\gamma_m}^{+\infty} \gamma_2 m_p c^2 \gamma_e^{-p} d\gamma_e. \tag{4.21}$$

Solving this equation yields

$$\gamma_m = \epsilon_e \frac{p-2}{p-1}\frac{m_p}{m_e}\gamma_2 \equiv \bar{\epsilon_e}\frac{m_p}{m_e}\gamma_2. \tag{4.22}$$

Hereafter I denote $\epsilon_e(p-2)/(p-1)$ by $\bar{\epsilon_e}$.

Adiabatic evolution

If the hydrodynamic evolution is fully adiabatic, the total energy of the system is conserved. Sari *et al.* [8] used $E = 16\pi\gamma_2^2 R^3 n_1 m_p c^2/17$ instead of Eq. 4.6, $E = 8\pi n_1 m_p c^2 R^3 \gamma_2^2/3$. The difference emerges from the details of the radial energy distribution behind the shock. Using $t_{obs} \sim R/(2\Gamma^2 c) =$

$R/(4\gamma_2^2 c)$, we obtain

$$R(t_{obs}) = \left(\frac{17Ect_{obs}}{4\pi n_1 m_p}\right)^{1/4} \tag{4.23}$$

and

$$\gamma_2(t_{obs}) = \left(\frac{17E}{1024\pi n_1 m_p c^5 t_{obs}^3}\right)^{1/8}. \tag{4.24}$$

Synchrotron radiation As described in § 2.2, the synchrotron spectrum emitted by electrons with a power-law energy distribution is expressed by a broken power-law function Eq. 2.25 or 2.26. The spectral breaks and the peak flux are predictable when the conditions of hydrodynamic evolution are provided. The radiation power Eq. 2.6 and the characteristic frequency Eq. 2.7 of the synchrotron emission from the radiation region with γ_2 are boosted as

$$P(\gamma_e) = \frac{4}{3}\sigma_T c \frac{B^2}{8\pi}\gamma_2^2\gamma_e^2 \tag{4.25}$$

and

$$\nu(\gamma_e) = \gamma_2\gamma_e^2 \frac{eB}{2\pi m_e c}. \tag{4.26}$$

Using these formulas and $N_e = 4\pi n_1 R^3/3$, the peak flux equals

$$F_{\nu,max} = \frac{N_e P_{\nu,max}}{4\pi d_L^2} = \frac{N_e P(\gamma_e)}{4\pi d_L^2 \nu(\gamma_e)} = \frac{m_e c^2 \sigma_T n_1 R^3 B \gamma_2}{9e d_L^2} \tag{4.27}$$

at the luminosity distance d_L from the source. Hence, these synchrotron characteristics depend on the evolution of γ_2. Substituting R and γ_2 to Eq. 4.20 and Eq. 4.22 yields

$$\begin{aligned}\nu_c &= \frac{9}{2\sqrt{34}}\frac{m_e c^{1/2} e}{m_p \sigma_T^2}(1+z)^{-1/2}\epsilon_B^{-3/2}\left(\frac{E}{\rm erg}\right)^{-1/2}\left(\frac{n_1}{\rm cm^3}\right)^{-1}\left(\frac{t_{obs}}{\rm s}\right)^{-1/2}{\rm Hz} \\ &= 5.9\times10^{19}\left(\frac{1+z}{3}\right)^{-1/2}\left(\frac{\epsilon_B}{10^{-4}}\right)^{-3/2}\left(\frac{E}{10^{52}{\rm erg}}\right)^{-1/2}\left(\frac{n_1}{\rm cm^3}\right)^{-1}\left(\frac{t_{obs}}{\rm min}\right)^{-1/2}{\rm Hz},\end{aligned} \tag{4.28}$$

$$\begin{aligned}\nu_m &= \sqrt{\frac{17}{128}}\frac{m_p^2 e}{\pi m_e^3 c^{5/2}}(1+z)^{1/2}\bar{\epsilon_e}^2\epsilon_B^{1/2}\left(\frac{E}{\rm erg}\right)^{1/2} \\ &= 5.5\times10^{15}\left(\frac{1+z}{3}\right)^{1/2}\left(\frac{\epsilon_B}{10^{-4}}\right)^{1/2}\left(\frac{\bar{\epsilon_e}}{1/30}\right)^2\left(\frac{E}{10^{52}{\rm erg}}\right)^{1/2}\left(\frac{t_{obs}}{\rm min}\right)^{-3/2}{\rm Hz}\end{aligned} \tag{4.29}$$

and

$$\begin{aligned}F_{\nu,max} &= \frac{17}{18}\frac{m_e c\sigma_T}{e\sqrt{2\pi m_p}}(1+z)\epsilon_B^{1/2}\left(\frac{E}{\rm erg}\right)\left(\frac{n_1}{\rm cm^3}\right)^{1/2}\left(\frac{d_L}{\rm cm}\right)^{-2}\mu{\rm Jy} \\ &= 1.3\times10^2\left(\frac{1+z}{3}\right)\left(\frac{\epsilon_B}{10^{-4}}\right)^{1/2}\left(\frac{E}{10^{52}{\rm erg}}\right)\left(\frac{n_1}{\rm cm^3}\right)^{1/2}\left(\frac{d_L}{5\times10^{28}\,{\rm cm}}\right)^{-2}\mu{\rm Jy}.\end{aligned} \tag{4.30}$$

The value of F_{max} is independent of t in the case of adiabatic evolution. In other words, the peak height of the spectrum does not decrease, but slides to lower frequencies. The specific flux spectrum peaks at the smaller one of two characteristic frequencies, $\nu_c \propto t_{obs}^{-1/2}$ and $\nu_m \propto t_{obs}^{-3/2}$. Therefore, at sufficiently early times, $\nu_c < \nu_m$, *i.e.*, fast-cooling, while at later times, $\nu_m < \nu_c$, i.e., slow-cooling. The transition time t_0 is determined by $\nu_c = \nu_m$,

$$t_0 = 5.7 \times 10^{-3} \left(\frac{1+z}{3}\right) \left(\frac{\epsilon_B}{10^{-4}}\right)^2 \left(\frac{\bar{\epsilon_e}}{1/30}\right)^2 \left(\frac{E}{10^{52}\mathrm{erg}}\right) \left(\frac{n_1}{\mathrm{cm}^3}\right) \mathrm{s}. \tag{4.31}$$

The specific flux can be derived by substituting ν_c, ν_m, and $F_{\nu,max}$ to Eq. 2.25 and 2.26. I describe the dependence on the parameters here. In the fast-cooling regime,

$$F_\nu \propto \begin{cases} (1+z)^{7/6} \epsilon_B E^{7/6} n_1^{5/6} d_L^{-2} \nu^{1/3} t_{obs}^{1/6} & \nu < \nu_c \\ (1+z)^{3/4} \epsilon_B^{-1/4} E^{3/4} d_L^{-2} \nu^{-1/2} t_{obs}^{-1/4} & \nu_c < \nu < \nu_m \\ (1+z)^{(p+2)/4} \epsilon_B^{(p-2)/4} \bar{\epsilon_e}^{p-1} E^{(p+2)/4} d_L^{-2} \nu^{-p/2} t_{obs}^{-(3p-2)/4} & \nu_m < \nu. \end{cases} \tag{4.32}$$

In the slow-cooling frame,

$$F_\nu \propto \begin{cases} (1+z)^{5/6} \epsilon_B^{1/3} \bar{\epsilon_e}^{-2/3} E^{5/6} n_1^{1/2} d_L^{-2} \nu^{1/3} t_{obs}^{1/2} & \nu < \nu_m \\ (1+z)^{(p+3)/4} \epsilon_B^{(p+1)/2} \bar{\epsilon_e}^{p-1} E^{(p+3)/4} n_1^{1/2} d_L^{-2} \nu^{-(p-1)/2} t_{obs}^{-3(p-1)/4} & \nu_m < \nu < \nu_c \\ (1+z)^{(p+2)/4} \epsilon_B^{(p-2)/4} \bar{\epsilon_e}^{p-1} E^{(p+2)/4} d_L^{-2} \nu^{-p/2} t_{obs}^{-(3p-2)/4} & \nu_c < \nu. \end{cases} \tag{4.33}$$

Synchrotron self-Compton radiation The flux of the synchrotron and inverse-Compton are calculated through the ratio between the radiation power of the inverse-Compton P_{IC} and synchrotron radiation P_{sync}, which is called the Compton parameter Y. It affects the break frequencies and the development of the jet. If $Y \gg 1$, the IC component dominates the cooling losses. If $Y \ll 1$, it is negligible [13]. If the IC component is considerable, the cooling status evolves from fast-cooling to slow-cooling dominated by IC, and finally slow-cooling dominated by synchrotron. As mentioned in § 2.3.2, the spectral indices of the SSC component reproduce those of the synchrotron component under a first-order approximation. On the other hand, the break frequencies of the SSC component become

$$\nu_c^{IC} = 2\gamma_c^2 \nu_c \propto t_{obs}^{-1/4} \tag{4.34}$$

and

$$\nu_m^{IC} = 2\gamma_m^2 \nu_m \propto t_{obs}^{-9/4}. \tag{4.35}$$

The peak flux of the SSC component is proportional to the optical thickness of the shocked fluid. When only the single scattering is taken into account, the optical thickness is $\tau_e \approx (4\pi/3)\sigma_T n_1 R^3/(4\pi R^2) =$

$\sigma_T nR$. Then, the SSC peak flux is

$$F^{IC}_{\nu,max} \propto \tau_e F_{\nu,max} \propto E^{5/4} n_1^{5/4} \epsilon_B^{1/2} t^{1/4} \tag{4.36}$$

In the fast-cooling regime, the specific flux is calculated via substituting Eq. 4.34, 4.35, and 4.36 to Eq. 2.35.

$$F^{IC}_{\nu} \propto \begin{cases} \nu^{1/3} t_{obs}^{1/3} & \nu < \nu_c^{IC} \\ \nu^{-1/2} t_{obs}^{1/8} & \nu_c^{IC} < \nu < \nu_m^{IC} \\ \nu^{-p/2} t_{obs}^{-(9p-10)/8} & \nu_m^{IC} < \nu. \end{cases} \tag{4.37}$$

The slow-cooling regime is divided into the regime dominated by the IC cooling and the one dominated by the synchrotron cooling. The flux in the synchrotron-dominated slow-cooling regime is derived by substituting Eq. 4.34, 4.35, and 4.36 to Eq. 2.36.

$$F^{IC}_{\nu} \propto \begin{cases} \nu^{1/3} t_{obs}^{1} & \nu < \nu_m^{IC} \\ \nu^{-(p-1)/2} t_{obs}^{-(9p-11)/8} & \nu_m^{IC} < \nu < \nu_c^{IC} \\ \nu^{-p/2} t_{obs}^{-(9p-10)/8} & \nu_c^{IC} < \nu. \end{cases} \tag{4.38}$$

In the IC-dominated slow-cooling regime, the energy available for synchrotron radiation is reduced by a factor $(1+y)$ where y is the luminosity ratio of the SSC to the synchrotron (*cf.* § 2.3.2), and therefore γ_c is also reduced by $(1+y)$. Then, the cooling frequency ν_c is reduced by $(1+y)^2$ because of Eq. 4.26. Using the slow-cooling case of Eq. 2.33 and 2.34,

$$(1+y) \approx y \approx \sqrt{\eta \epsilon_e / \epsilon_B} = (\gamma_c/\gamma_m)^{-p/2+1} \epsilon_e^{1/2} \epsilon_B^{-1/2}, \tag{4.39}$$

Using Eq. 4.26 again, it can be written as

$$y^2 = \frac{\eta \epsilon_e}{\epsilon_B} = \left(\frac{\nu_c}{\nu_m} \right)^{-(p-2)/2} \frac{\epsilon_e}{\epsilon_B}. \tag{4.40}$$

Without IC cooling, $\nu_c \propto t_{obs}^{-1/2}$ (Eq. 4.28) and $\nu_m \propto t_{obs}^{-3/2}$ (Eq. 4.29), and thus the ratio is $\nu_c/\nu_m \propto t_{obs}$. Because this is reduced by y^2, we get

$$y^2 \propto \left(\frac{t_{obs}}{y^2} \right)^{-(p-2)/2} \tag{4.41}$$

and

$$y \propto t_{obs}^{-(p-2)/[2(4-p)]}. \tag{4.42}$$

Using Eq. 4.19, 4.20, 4.24, 4.26, 4.34, and 4.42, the time-evolution of the IC cooling frequency is

$$\nu_c^{IC} \propto \gamma_c^2 \nu_c \propto y^{-4} \gamma_2^{-10} t_{obs}^{-4} \propto t_{obs}^{2(p-2)/(4-p)-1/4} \tag{4.43}$$

Consequently, the flux formula for ν above ν_c^{IC} becomes

$$F_\nu^{IC} \propto \begin{cases} \nu^{1/3} t_{obs}^{1} & \nu < \nu_m^{IC} \\ \nu^{-(p-1)/2} t_{obs}^{-(9p-11)/8} & \nu_m^{IC} < \nu < \nu_c^{IC} \\ \nu^{-p/2} t_{obs}^{-(9p-10)/8+(p-2)/(4-p)} & \nu_c^{IC} < \nu. \end{cases} \tag{4.44}$$

The formulas for $\nu < \nu_m^{IC}$ and $\nu_m^{IC} < \nu < \nu_c^{IC}$ are the same as Eq. 4.38. More exact formulas including the logarithmic terms are documented in [14].

Synchrotron radiation under inverse-Compton-dominated cooling When the cooling is dominated by IC, the synchrotron light curve above ν_c is also affected. Using Eq. 4.19, 4.20, 4.24, 4.26, and 4.42, the time-evolution of the cooling frequency is

$$\nu_c \propto y^{-2} \gamma_2^{-4} t^{-2} \propto t^{(3p-8)/[2(4-p)]} \tag{4.45}$$

Hence, the flux above ν_c is

$$F_\nu \propto \nu^{-p/2} t^{-3p/4+1/(4-p)} \tag{4.46}$$

instead of the third formula of Eq. 4.33.

Radiative evolution

The radiative case was discussed by Katz and Piran [115]. Conservation of the energy and momentum yields

$$\gamma_2 \approx \left(\frac{R}{L}\right)^{-3}. \tag{4.47}$$

where $L = [17M/(16\pi n_1 m_p)]^{1/3}$ is the radius at which the mass swept up from the external medium of the initial ejecta mass $M = E/(\Gamma_0 c^2)$ where Γ_0 is the initial Lorentz factor of the ejecta [8]. In this case, we can get

$$R(t_{obs}) = L\left(\frac{4ct_{obs}}{L}\right)^{1/7} \tag{4.48}$$

and

$$\gamma_2 = \left(\frac{L}{4ct_{obs}}\right)^{3/7}. \tag{4.49}$$

The radiation characteristics are

$$\begin{aligned}\nu_c = 1.5 \times \left(\frac{1+z}{3}\right)^{-5/7} 10^{17} \left(\frac{\epsilon_B}{10^{-2}}\right)^{-3/2} \left(\frac{E}{10^{52}\mathrm{erg}}\right)^{-4/7} \left(\frac{\Gamma_0}{100}\right)^{4/7} \\ \times \left(\frac{n_1}{\mathrm{cm}^3}\right)^{-13/14} \left(\frac{t_{obs}}{\mathrm{s}}\right)^{-2/7} \mathrm{Hz},\end{aligned} \tag{4.50}$$

$$\begin{aligned}\nu_m = 7.7 \times 10^{21} \left(\frac{1+z}{3}\right)^{5/7} \left(\frac{\epsilon_B}{10^{-2}}\right)^{1/2} \left(\frac{\bar{\epsilon_e}}{1/3}\right)^{2} \left(\frac{E}{10^{52}\mathrm{erg}}\right)^{4/7} \left(\frac{\Gamma_0}{100}\right)^{-4/7} \\ \times \left(\frac{n_1}{\mathrm{cm}^3}\right)^{-1/14} \left(\frac{t_{obs}}{\mathrm{s}}\right)^{-12/7} \mathrm{Hz},\end{aligned} \tag{4.51}$$

and

$$\begin{aligned}F_{\nu,max} = 1.1 \times 10^4 \left(\frac{1+z}{3}\right)^{10/7} \left(\frac{\epsilon_B}{10^{-2}}\right)^{1/2} \left(\frac{E}{10^{52}\mathrm{erg}}\right)^{8/7} \left(\frac{\Gamma_0}{100}\right)^{-8/7} \\ \times \left(\frac{n_1}{\mathrm{cm}^3}\right)^{5/14} \left(\frac{d_L}{10^{28}\,\mathrm{cm}}\right)^{-2} \left(\frac{t_{obs}}{\mathrm{s}}\right)^{-3/7} \mu\mathrm{Jy}.\end{aligned} \tag{4.52}$$

The transition time from the radiative evolution to the adiabatic evolution t_a is

$$t_a = 30 \left(\frac{1+z}{3}\right) \left(\frac{\epsilon_B}{10^{-2}}\right)^{7/5} \left(\frac{\bar{\epsilon_e}}{1/3}\right)^{7/5} \left(\frac{E}{10^{52}\mathrm{erg}}\right)^{4/5} \left(\frac{\Gamma_0}{100}\right)^{-4/5} \left(\frac{n_1}{\mathrm{cm}^3}\right)^{3/5} \mathrm{min}. \tag{4.53}$$

At $t_{obs} = t_a$, the hydrodynamic evolution changes from radiative to adiabatic. Because the formulae for the fast-cooling regime are usable, the specific flux is

$$F_\nu \propto \begin{cases} (1+z)^{5/3} \epsilon_B E^{4/3} \Gamma_0^{-4/3} n_1^{1/21} d_L^{-2} \nu^{1/3} t_{obs}^{-1/3} & \nu < \nu_c \\ (1+z)^{15/14} \epsilon_B^{-1/4} E^{6/7} \Gamma_0^{-6/7} n_1^{-3/28} d_L^{-2} \nu^{-1/2} t_{obs}^{-4/7} & \nu_c < \nu < \nu_m \\ (1+z)^{5(p+2)/14} \epsilon_B^{(p-2)/4} \bar{\epsilon_e}^{p-1} E^{2(p+2)/7} \Gamma_0^{-2(p+2)/7} n_1^{-(p+2)/28} d_L^{-2} \nu^{-p/2} t_{obs}^{-2(3p-1)/7} & \nu_m < \nu. \end{cases} \tag{4.54}$$

I summarize the dependence of the synchrotron and SSC flux on the frequency and time in Table 4.1 and 4.2, respectively. Thus far, I assumed the CBM density is uniform, namely $k = 0$ for $n_1(r) \propto r^{-k}$. The case of the wind-like ambient medium $k = 2$ is discussed in [13, 116]. I refer to the dependence in this case, too.

Reverse shock

A collision with the external medium creates another shock front between the compressed region and the un-shocked region of the jet. It is dubbed the reverse shock. The forward and reverse shock fronts are depicted as Fig. 4.3. This also accelerates particles and possibly radiates afterglow emission. The

Table 4.1: Dependence of the specific flux F_ν of the synchrotron emission from the external forward shocks on the frequency ν and observation time t. These are based on [13, 116]. The "S1", "S2" and "S3" indicate the first, second and third highest frequency segment of the broken power-law spectrum respectively. The lowest frequency segment is omitted because it is not relevant to this thesis. The "S1*" means the highest frequency segment in the case when the energy loss is dominated by IC scattering.

CBM	Cooling	S3	S2	S1	S1*
ISM-like	Fast	$\nu^{1/3}t^{1/6}$	$\nu^{-1/2}t^{-1/4}$	$\nu^{-p/2}t^{-(3p-2)/4}$	$\nu^{-p/2}t^{-(3p-2)/4}$
	Slow	$\nu^{1/3}t^{1/2}$	$\nu^{-(p-1)/2}t^{-3(p-1)/4}$	$\nu^{-p/2}t^{-(3p-2)/4}$	$\nu^{-p/2}t^{-3p/4+1/(4-p)}$
	Radiative	$\nu^{1/3}t^{-1/3}$	$\nu^{-1/2}t^{-4/7}$	$\nu^{-p/2}t^{-2(3p-1)/7}$	$\nu^{-p/2}t^{-2(3p-1)/7}$
Wind-like	Fast	$\nu^{1/3}t^{-2/3}$	$\nu^{-1/2}t^{-1/4}$	$\nu^{-p/2}t^{-(3p-2)/4}$	$\nu^{-p/2}t^{-(3p-2)/4}$
	Slow	$\nu^{1/3}t^{0}$	$\nu^{-(p-1)/2}t^{-(3p-1)/4}$	$\nu^{-p/2}t^{-(3p-2)/4}$	$\nu^{-p/2}t^{-3p/4+p/(2(4-p))}$
	Radiative	$\nu^{1/3}t^{-7/9}$	$\nu^{-1/2}t^{-1/2}$	$\nu^{-p/2}t^{-(5p-2)/6}$	$\nu^{-p/2}t^{-(5p-2)/6}$

Table 4.2: Dependence of the specific flux F_ν of the synchrotron self-Compton (SSC) emission from the external forward shocks on the frequency ν and observation time t. These are based on [13, 14, 116]. The "C1", "C2" and "C3" indicate the first, second, and third highest frequency segment of the broken power-law spectrum respectively. The "C1*" means the highest frequency segment in the case when the energy loss is dominated by IC scattering. The logarithmic terms are not taken into account, and these relations are just an approximation.

CBM	Cooling	C3	C2	C1	C1*
ISM-like	Fast	$\nu^{1/3}t^{1/3}$	$\nu^{-1/2}t^{1/8}$	$\nu^{-p/2}t^{-(9p-10)/8}$	$\nu^{-p/2}t^{-(9p-10)/8}$
	Slow	$\nu^{1/3}t^{1}$	$\nu^{-(p-1)/2}t^{-(9p-11)/8}$	$\nu^{-p/2}t^{-(9p-10)/8}$	$\nu^{-p/2}t^{-(9p-10)/8+(p-2)/(4-p)}$
Wind-like	Fast	$\nu^{1/3}t^{-5/3}$	$\nu^{-1/2}t^{0}$	$\nu^{-p/2}t^{-(p-1)}$	$\nu^{-p/2}t^{-(p-1)}$
	Slow	$\nu^{1/3}t^{-1/3}$	$\nu^{-(p-1)/2}t^{-p}$	$\nu^{-p/2}t^{-(p-1)}$	$\nu^{-p/2}t^{-p(3-p)/(4-p)}$

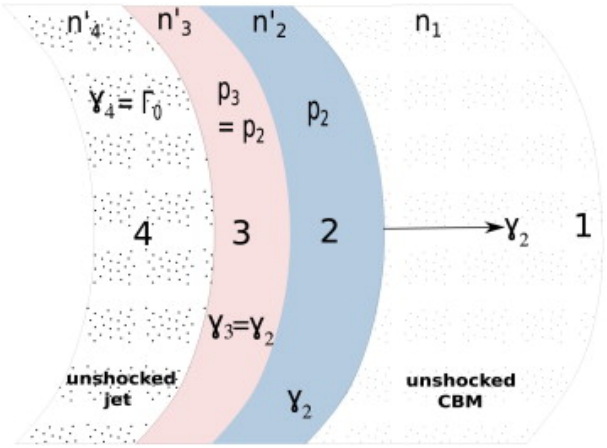

Figure 4.3: Schematic picture of a pair shock fronts produced by collision of the jet and external matter, from a viewpoint of the rest frame of the unshocked CBM in region 1 [99]. Region 2 and 3 represent the shocked CBM and GRB jet respectively. Region 4 is the unshocked jet.

reverse shock shell is expected to carry a comparable amount of energy with the forward shock shell. However, the Lorentz factors of the heated electrons are typically smaller because the mass density of the shell in the local comoving frame n'_3 is higher than the one of the forward shock n'_2. Hence, the typical frequency of the emission from the reverse shock is lower than the forward shock [117].

Jet break

The steep decay in phase IV in Fig. 3.7 is interpreted as a phenomenon dubbed the "jet break" in context of the external shock picture. It is a combination of two effects triggered by the deceleration of the jet. The description of the effects is below.

Edge effect The first one is called the edge effect [86]. The emission from a relativistic jet strongly concentrate within an angle $\sim 1/\Gamma$. Initially Γ is large and $1/\Gamma$ is smaller than the jet opening angle θ_j. In this phase, the emission from the collimated jet looks like isotropic for an obsever. The value of $1/\Gamma$ increases as the jet decelerates. After it exceeds θ_j, the edge of the jet becomes visible. The observable flux declines because the entire emission from around the edge do not reach us.

Sideways expansion The second effect is sideways expansion of the jet [118]. It is caused by sound waves across the jet in the transverse direction. The jet opening angle θ_j expands, and it leads to a slowdown of the jet due to the energy conservation $E \propto R^3\Gamma^2\theta_j^2$ which is derived from Eq. 4.6.

The breaks correspond to the phase Ⅳ in Fig. 3.7. For some of GRBs, fitting their late-time X-ray light curves with a numerical model enables us to estimate the angle between the jet axis and the line of sight. For example, see [119].

4.6.2 Refreshed shock

The plateau phase Ⅱ in Fig. 3.7 does not match the temporal development discussed above. A plausible interpretation is a continuous energy injection into the decelerating external shocks. In this case, the forward shocks keep being "refreshed", and the decaying becomes shallower. Further origins of additional energy are possible, such as long-lasting activities of the central engines or a spread of the ejecta Lorentz factor at the end of the prompt emission [49, 120, 116].

4.6.3 Late-time flares

Late-time X-ray flares, the component V in Fig. 3.7, cannot be attributed to the external shock because of the short duration relative to the happening time. Their origins are considered to be restarts of the central engines. For example of possible intermittent activities, many fragments are produced by the collapsing star [121] or outer part of the accretion disk [122] and they fall onto the central engines at different times. Another idea is that the accumulating magnetic flux around the black hole creates a temporary "magnetic barrier", and it takes time to be broken by accumulating a sufficient amount of materials [123]. For short GRBs, late-time activities of the black hole with fallback of ejected matter and magnetic reconnection is proposed [124]. It may also work for long-GRBs. For continuous activities, a magnetar without collapsing into a black hole [125] or a hyper-accreting black hole [126] may be a source of the energy injection.

4.7 Mechanism of the temporally extended high-energy emission

As mentioned in §3.5, the light curves above 100 MeV are typically described by a single power-law with an offset of the starting time. The prompt and afterglow emission are usually not clearly differentiated.

4.7.1 Synchrotron radiation

The temporal and spectral features in this energy range are basically well explained by the synchrotron radiation from the external forward shocks. In both the synchrotron flux formulae in the fast-cooling regime (Eq. 4.32) and in the slow-cooling regime (Eq. 4.33), the flux in the highest-frequency segment is $F_\nu \propto E^{(p+2)/4}\epsilon_B^{(p-2)/4}\epsilon_e^{p-1}d_L^{-2}\nu^{-p/2}t_{obs}^{-(3p-2)/4}$. It is independent of n_1 and

only weakly depends on ϵ_B although these two parameters are highly uncertain. Therefore, one can predict the specific flux with a few parameters E and ϵ_e. The dependence can be written as $f_\nu \propto E^{1.05}\epsilon_e^{1.2}\epsilon_B^{0.05}t^{-1.15}\nu^{-1.1}$ provided $p = 2.2$. This is consistent with the spectra and light curves observed by the LAT as displayed in Fig. 3.14 and 3.15. On top of that, the correlation between the high-energy luminosity and prompt energetics mentioned in § 3.5 supports this interpretation. As explained, $F_\nu(t,\nu)$ is determined by only two parameters E and ϵ_e mainly. If ϵ_e and $\xi = E_{prompt}/(E_{prompt} - E)$ are common, $F_\nu(t,\nu)$ is proportional to E_{prompt}. This explains Fig. 3.16 well. In the external shock picture, the onset of the high energy emission observed by the LAT can be interpreted as the deceleration time scale of the shocks.

4.7.2 Inverse-Compton scattering

The photon energy above tens of GeV may be too high for this model because the maximum synchrotron energy is $\sim 50\Gamma/(1+z)$ MeV. A natural solution is introducing a component of inverse-Copmpton scattering. The inverse-Compton process adds another bump in the afterglow spectrum and decreases the energy consumed by the synchrotron emission on the other hand. Beniamini *et al.* showed that for three GRBs, namely, 090926A, 090902B, and 090510, the emission at $\sim$ GeV is dominated by SSC radiation while the X-ray flux is dominated by synchrotron [127]. The authors tested whether the models of synchrotron + SSC are consistent with the LAT, X-ray and optical flux values at 100 MeV, 1 keV, $\sim$ eV respectively, at some observation times scanning the parameter space of n_1 vs. ϵ_B vs p.

4.7.3 Contribution of the prompt component

The observed starts of the high energy emission of some GRBs may be too early for the afterglow [128]. It is plausible that the prompt component contributes to the high energy emission in the early phase. This is supported by some observations, for example, coincident peaks in the LAT and GBM band [64]. If the data around the peak time is dominated by the prompt components, the onsets of the high-energy light curves can be explained by a spectral cutoff which is increasing. The cutoff may be because of $\gamma - \gamma$ absorption or Klein-Nishina cutoff of the SSC component.

4.8 The jet characteristics and emission mechanisms based on the external forward shock models

4.8.1 Closure relations

As discussed above, the spectra and light curves of the synchrotron and SSC components are roughly described by broken power-laws with the derived indices. Hence, one can derive a relation between

the temporal index α and spectral index β for each combination of the CBM profile, cooling regime, emission component and spectral segment. Such relations are called "closure relations". Comparing the data and these formulae, we can judge whether each segment is consistent. The relations of the synchrotron components in the segments for the fast-/slow-cooling regimes and the ISM-/wind-like CBM density profile are documented in Table 4.3. The relations of the SSC components are in Table 4.4.

4.8.2 Jet parameters

If the external forward shock model is correct, the afterglow emission are decided by the characteristic parameters of the jets. I overview the jet parameters in the following.

Jet kinetic energy

This quantity is the amount of the jet kinetic energy after internal dissipation and fed into the external shocked plasma. It is denoted by E in the present thesis. This value can be indirectly derived by afterglow observations if the observation band lies above the highest break energy of the synchrotron component, usually ν_c, and the inverse-Compton cooling is negligible. It is possible because the flux in this energy region, which expressed as Eq. 4.33, does not depend on n_1 and only weakly depends on ϵ_B with n_1 and ϵ_B being highly uncertain.

Isotropic-equivalent-energy of the prompt gamma-ray emission

This is the amount of energy released during the prompt phase and denoted by E_{prompt}. It depends on the angular distribution of the radiation, which is generally unknown. Therefore E_{prompt} is calculated as if the radiation is isotropic.

$$E_{prompt} = \frac{fluence \times 4\pi d_L^2}{1+z} \tag{4.55}$$

where d_L is the luminosity distance and z is the redshift of the GRB.

Prompt emission efficiency

The ratio of the above two amounts is denoted by $\xi = E_{prompt}/(E_{prompt} + E)$. It indicates the efficiency of the prompt radiation.

In some previous studies, E has been derived under the assumption that X-ray observations satisfy the conditions mentioned in the paragraph of jet kinetic energy above. For some of the bursts, relatively low values of E, and consequently, large values of ξ, which are larger than 50% have been suggested [129, 130]. Zhang *et al.* [130] analyzed X-ray data of 31 GRBs and derived the

Table 4.3: Closure relations of the synchrotron components. α and β are defined as $f_\nu \propto \nu^{-\beta} t^{-\alpha}$.

CBM	Cooling	S3	S2	S1	S1*
ISM-like	Fast	$\alpha = -1/6,\ \beta = -1/3$	$\alpha = 1/4,\ \beta = 1/2$	$\alpha = (3\beta - 1)/2$	$\alpha = (3\beta - 1)/2$
	Slow	$\alpha = -1/2,\ \beta = -1/3$	$\alpha = 3\beta/2$	$\alpha = (3\beta - 1)/2$	$\alpha = 3\beta/2 - 1/(4 - 2\beta)$
	Radiative	$\alpha = 1/3,\ \beta = -1/3$	$\alpha = 4/7,\ \beta = 1/2$	$\alpha = 2(6\beta - 1)/7$	$\alpha = 2(6\beta - 1)/7$
Wind-like	Fast	$\alpha = 2/3, \beta = -1/3$	$\alpha = 1/4, \beta = 1/2$	$\alpha = (3\beta - 1)/2$	$\alpha = (3\beta - 1)/2$
	Slow	$\alpha = 0, \beta = -1/3$	$\alpha = (3\beta + 1)/2$	$\alpha = (3\beta - 1)/2$	$\alpha = 3\beta/2 - \beta/[2(2 - \beta)]$
	Radiative	$\alpha = 7/9,\ \beta = -1/3$	$\alpha = 1/2,\ \beta = 1/2$	$\alpha = (5\beta - 1)/3$	$\alpha = (5\beta - 1)/3$

Table 4.4: Closure relations of the SSC components. α and β are defined as $f_\nu \propto \nu^{-\beta} t^{-\alpha}$

CBM	Cooling	C3	C2	C1	C1*
ISM-like	Fast	$\alpha = -1/3, \beta = -1/3$	$\alpha = -1/8, \beta = 1/2$	$\alpha = (9\beta - 5)/4$	$\alpha = (9\beta - 5)/4$
	Slow	$\alpha = -1, \beta = -1/3$	$\alpha = (9\beta - 1)/4$	$\alpha = (9\beta - 5)/4$	$\alpha = (9\beta - 5)/4 - (\beta - 1)/(2 - \beta)$
Wind-like	Fast	$\alpha = 5/3, \beta = -1/3$	$\alpha = 0, \beta = 1/2$	$\alpha = 2\beta - 1$	$\alpha = 2\beta - 1$
	Slow	$\alpha = 1/3, \beta = -1/3$	$\alpha = 2\beta + 1$	$\alpha = 2\beta - 1$	$\alpha = \beta(3 - 2\beta)/(2 - \beta)$

efficiency from a few percents to $> 90\%$. However, the efficiency is expected to be lower than such a value if the energy is dissipated through the internal shock processes [93, 94, 131]. The efficiency calculated by Kobayashi *et al.* [93] with various choices of the parameters distributes between 1% and 40%. This discrepancy posed a severe problem for the internal shock model of the prompt radiation.

Later, a doubt about the location of ν_c was pointed out. Beniamini *et al.* have proven that there is a discrepancy between E derived from the X-ray data and one from the LAT data [127]. This implies the ν_c values were located between the X-ray band and the LAT band, or the X-ray emission were strongly affected by inverse-Compton cooling. Then the LAT data are considered as a better proxy of E.

Injected-electron spectral index

The energy distribution of electrons which radiate is assumed to be $dn/d\gamma = \kappa\gamma^{-p}$. The value of p can be determined readily from X-ray observation if the segment at which the observation band is located is known. If electrons are accelerated by diffusive shock mechanism, p cannot be harder than two because of the limit of the downstream/upstream density ratio. This limit is also confirmed by Monte Carlo simulations [132].

Electron energy fraction

The parameter ϵ_e is a fraction of the energy density in electrons in shocked fluid. It is tied to the minimum Lorentz factor of the electrons by Eq. 4.56.

$$\gamma_m = g(p)\epsilon_e(\Gamma - 1)\frac{m_p n_p}{m_e n_e} \tag{4.56}$$

where $g(p)$ is a dimensionless factor for normalization. Compared with this formula, Eq. 4.22, which was used for calculating the afterglow flux, is simplified by assuming $n_p = n_e$ and $g(p) = (p-2)/(p-1)$ for $p > 2$. Santana *et al.* [133] have summarized estimated values of ϵ_e in the literature. The values of ϵ_e has a relatively narrow distribution compared with the other parameters. It typically ranges from 0.1 to 0.3. Such values of ϵ_e is supported by particle-in-cell simulations [134].

Magnetic energy fraction

The parameter ϵ_e is a fraction of the energy density in magnetic fields in shocked fluid. It is explicitly expressed as

$$\epsilon_B = \frac{B^2}{32\pi n_1 m_p c^2 \gamma_2^2} \tag{4.57}$$

where B is the co-moving magnetic field downstream of the shock front, n_1 is the density of the CBM, and γ_2 is the Lorentz factor of the shocked fluid. The magnetic field in the downstream is amplified by some mechanisms. At least, highly relativistic shocks compress the seed magnetic field in the CBM, B_0 to $B = 4\Gamma B_0$. This yields

$$\epsilon_B^{SC} = \frac{B_0^2}{2\pi n_1 m_p c^2} \tag{4.58}$$

Substituting the magnetic field of our Galaxy $\sim$ a few μG and $n_1 = 1\,\mathrm{cm}^{-3}$ to B_0, the minimal possible value is $\epsilon_B^{SC} \sim 10^{-9}\mu$G.

Santana *et al.* [133] have summarized estimated values of ϵ_B in many literatures. The values range from $\sim 10^{-5}$ to $\sim 10^{-1}$. The authors also derived the values and upper limits of ϵ_B from the optical data and X-ray data respectively, for many GRBs with a common method. Here, I refer to the values they derived from the optical data in Fig. 4.4. The distributions are very wide and have the peaks at higher than 10^{-9}. Hence, another amplification source is suggested. Some mechanisms have been proposed such as the Weibel instability [135] and density inhomogeneity of the ISM generating turbulence downstream [136, 137].

Circumburst medium density

The number density of the circumburst medium (CBM) is denoted by n_1. The density profile is described by

$$n_1(r) = (A/m_p)r^{-k}. \tag{4.59}$$

where A is a normalization constant and k is the power-law index. In this thesis I will discuss two cases with physical backgrounds.

k=0 This represents the distribution with a constant density profile. This corresponds to the case when the jet collides with the ambient interstellar matter.

k=2 This is expected if the progenitor star has ejected a free stellar wind. It is natural if the progenitor was a massive star such as Wolf-Rayet stars.

Previous studies have found the majority of afterglow observations are better described by the CBM with a uniform density [138]. If their progenitors were massive stars, this result suggests they had relatively small radii of the wind termination shocks [138]. If $k = 0$, the number density is simply denoted by a constant n_1. The value of n_1 is highly uncertain. It ranges from $\sim 10^{-3}$ to $\sim 10^2$ according to [139], as plotted in Fig. 4.5.

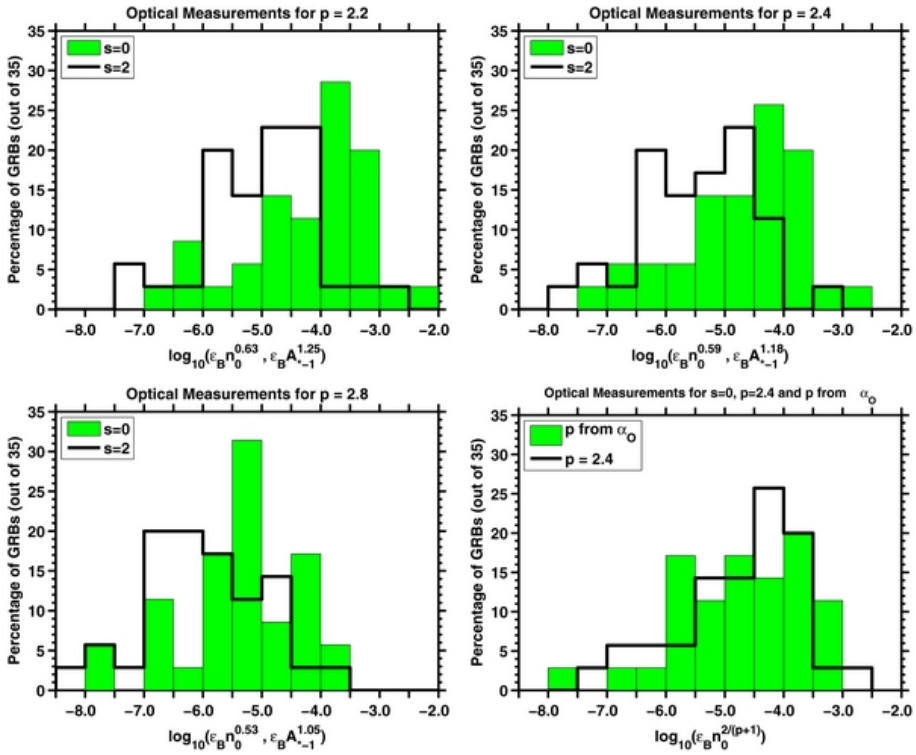

Figure 4.4: Histograms of the quantity $\epsilon_B n_0^{2/(p+1)}$ (a constant density; filled) and $\epsilon_B A_{*-1}^{4/(p+1)}$ (wind-like; unfilled) where $n_0 = n_1/10^0\,\mathrm{cm}^3$ and $A_{*-1} = A_*/(10^{-1}\times 5\times 10^{11}\,\mathrm{g\cdot cm}^{-1})$ derived by [133] with optical data. Top left, top right, and bottom left panels display the histograms of measurements, assuming $p = 2.2$, $p = 2.4$, and $p = 2.8$, respectively. The filled-in (unfilled) histograms display measurements of the quantity $\epsilon_B n_0^{2/(p+1)}$ ($\epsilon_B A_{*-1}^{4/(p+1)}$) assuming that all the GRBs in the optical sample are described by a constant density (wind) medium. Bottom right panel: the filled-in histogram displays the measurements on the quantity $\epsilon_B n_0^{2/(p+1)}$ with p determined from the optical decaying index. The unfilled histogram displays measurements on the quantity $\epsilon_B n_0^{2/(p+1)}$, assuming $p = 2.4$ for all.

In the case of wind-like, n_1 is expressed as

$$n_1(r) = 3 \times 10^{35} A_* r^{-2} \mathrm{cm}^{-3} \tag{4.60}$$

$A_* = 1$ corresponds to mass loss rate in the wind of GRB progenitor star of $1 \times 10^{-5} \mathrm{M}_\odot/\mathrm{yr}$ at wind speed of $1 \times 10^8 \mathrm{cm} \cdot \mathrm{s}^{-1}$ [99].

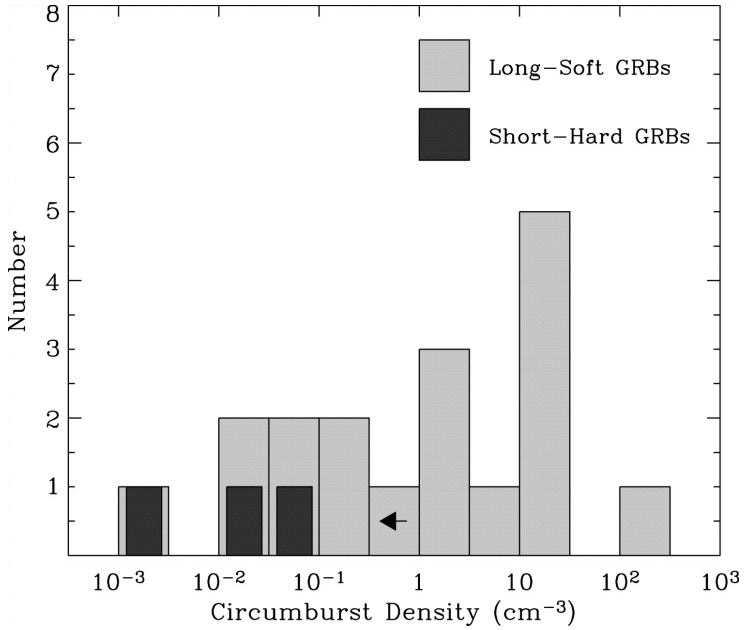

Figure 4.5: Distributions of circumburst density values for long and short GRBs which are taken from [139].

Chapter 5

Fermi Large Area Telescope

5.1 Overview

The Large Area Telescope of the *Fermi* Gamma-ray Space Telescope (*Fermi*-LAT) is an instrument for observing high-energy cosmic gamma rays with imaging, a wide FoV and unprecedented sensitivity for a space telescope. It is one of two major instruments of the *Fermi* satellite, which was launched on 11 June 2008 [140] and normal science observation started on 4 August 2008 [141]. When a high-energy gamma ray enters the LAT, it interacts with the materials and converts to an electron pair, and it produces an electromagnetic shower. The LAT measures the deposited energy and the tracks of the charged particles. The particle energy and incoming direction are reconstructed from this information. The LAT covers an energy range from 20 MeV to higher than 300 GeV.

5.2 Instruments

The *Fermi*-LAT consists of three detectors, namely, the tracker (TKR), the calorimeter (CAL), and the anti-coincidence detector (ACD).

5.2.1 Tracker

The TKR mainly provides information on the precise trajectories of the charged particles which are produced by gamma rays or parent charged particles. It consists of 18 layers of basically paired silicon strip detector (SSD) planes and tungsten foils [140]. The latter act as converters of gamma rays. The track information is used for reconstructing the event arrival direction and shower profile. The TKR consists of 12 layers of 0.03 radiation length tungsten converters (the front section), followed by four layers of 0.18 radiation length tungsten converters (the back section). In total, the thickness of the converters is 1.08 radiation lengths. A thicker converter causes large deflection of

Table 5.1: Characteristics of the Fermi-LAT [142]

Energy range	$\sim$ 20 MeV to $\geq$ 300 GeV[a]
Energy resolution	$< 15\%$ for $E^b > 100$ MeV
Effective area	$> 0.8\,\mathrm{m}^2$ at maximum for normal incidence
Single Photon Angular Resolution	$< 0°.15$ for $E > 10$ GeV; $< 3°.5$ for $E = 100$ MeV
FoV	2.4 sr for $E = 1$ GeV
Source Location Determination	$< 0'.5$ for high-latitude source
Point Source Sensitivity	$< 6 \times 10^{-9}\mathrm{ph \cdot cm^{-2}s^{-1}}$ for E > 100 MeV, 5σ detection after 1 year sky survey
Time Accuracy	$< 10\,\mu$s
Background Rejection	$< 10\%$ residual contamination of a high latitude diffuse sample for 100 MeV $< E <$ 300 GeV
Dead Time	$< 100\,\mu$s per event

[a]This is the main target energy range. The instrument response functions are provided for energies from 10 MeV to 3 TeV.

[b]Energy of each gamma ray.

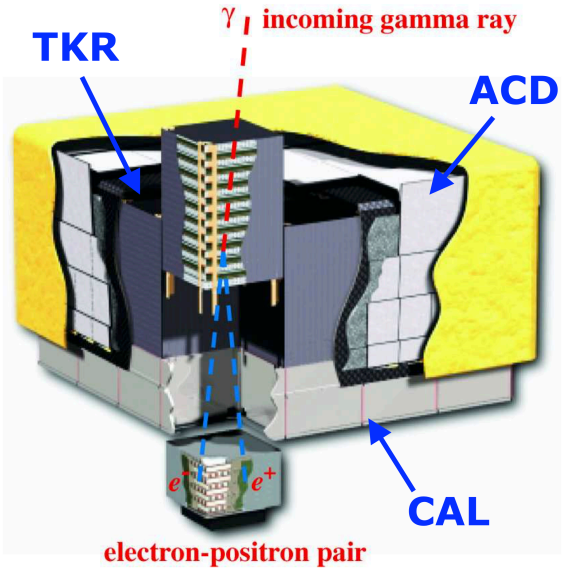

Figure 5.1: Schematic view of the *Fermi*-LAT [140]. The dimensions are $1.8 \times 1.8 \times 0.72$ m. The TKR is at the upper part and the CAL is at the bottom part. A pair of a TKR and CAL block composes a tower and 4×4 of the towers compose the internal part of the telescope. White ACD tiles and ribbons surround the internal part.

electrons and positrons because of multiple scattering and results in a worse point spread function (PSF). The arrival directions of events which convert into an electron pair in the front section are expected to be well reconstructed. The back section captures the rest of events, which pass through the front section without interactions, although the PSF is worse. This structure enables us to select events in a suitable way depending on what quality of PSF and how much statistics are desired.

5.2.2 Calorimeter

The CAL measures the amount and spatial distribution of the energy deposited by the shower. It is constructed of eight layers of twelve CsI crystal scintillator logs as visualized in Fig. 5.2. These layers are aligned alternately, and the logs have two photodiodes at each of the two edges. Each log is optically isolated. The position along each log where the scintillation light is emitted can be localized by evaluating the asymmetry of the signals at both ends. These two features enable us to reconstruct the 3D profiles of the showers. This is crucial for developing the Calorimeter-only analysis discussed in §6. The size of each log is $2.7 \times 2.0 \times 32.6$ cm. The thickness is roughly one radiation length and the total thickness of the CAL is 8.6 radiation lengths. The size of each log is also comparable to the Molière radius of electromagnetic showers, 3.8 cm [140]. These dimensions are suitable for capturing the shower position and morphology.

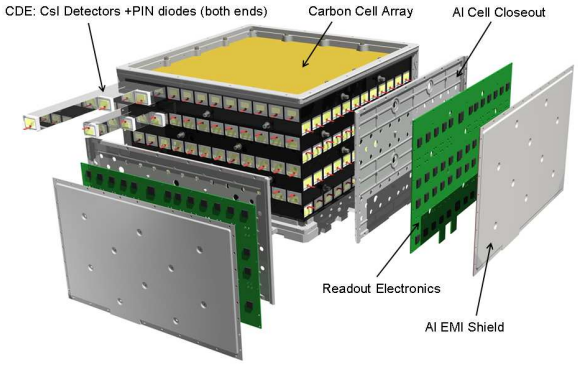

Figure 5.2: Structure of the LAT calorimeter [140]. The twelve CsI crystal logs compose one layer and eight layers are arranged alternately.

5.2.3 Anti-coincidence detector

The ACD is essential for rejecting charged background particles such as protons, other nuclei and electrons. It is a set of segmented plastic scintillators covering the upper and side surfaces of the LAT. Segmenting the ACD helps us to distinguish "backsplash" events against incident background particles. Backsplash is backscattered secondary particles. Some primary gamma rays and cosmic

rays also produce it and fire the ACD. The consistency between the position of the fired ACD segments and the backwardly extrapolated shower axis is evaluated in order to differentiate such gamma rays with backsplash from charged particles. This phenomenon is especially frequent in the high energy region above 10 GeV [140], which the present thesis focuses on.

5.3 Data processing

Next, I summarize how the LAT data are processed from the row detector signals to the photon data usable for scientific analyses.

5.3.1 Triggering

At first, the LAT hardware triggers the event readout when certain conditions are fulfilled [141]. One of them, which is important for this thesis, is dubbed `CAL_HI`. It is issued when the electric signal from any CAL photodetector exceeds a certain threshold corresponding to 1 GeV.

5.3.2 On-board filter

Not all of the read data are sent to the ground because the available telemetry bandwidth is limited. The LAT data are thus filtered on-board [141]. Three kinds of filters are implemented for different purposes, and the one for accepting gamma rays is called the GAMMA filter. It consists of a hierarchical sequence of tests which each event is required to pass. However, it accepts any event depositing more than 20 GeV in the CAL.

5.3.3 Reconstructing events

At this step, the raw data are processed to middle-level information characterizing each event [141].

Calorimeter reconstruction

The process starts from reconstructing the shower axis in the CAL. The clusters of the energy deposition and their centroids are captured, and the principal axes of the showers are estimated by analyzing the moments of the shower profiles.

Tracker reconstruction

Next, the reconstruction of the tracks in the TKR is performed. Two kinds of pattern recognition approaches are available. One is based on seeds from the CAL, and the other one is a blind search.

ACD reconstruction

In this phase, the energy deposited in each of the ACD tiles and ribbons is evaluated. In the next step, these hits are associated with the tracks which were found in the previous steps. Some quantities are calculated such as the distance of the projected trajectory to the fired ACD segments and the significance of their correlation.

5.3.4 Event analysis

In the event-level analysis step, the reconstructed information is summarized into a few hundred characteristic quantities which make physical senses. Here I document a few examples.

- Consistency between the ACD signals and the projected tracks
- Number of the tracks found
- RMS of the transverse/longitudinal shower profile
- Gamma-ray probabilities evaluated by several approaches
- Event energy
- Event arrival direction in all necessary coordinates
- Indicators of reconstruction quality of the energy and direction

5.3.5 Event classification

Background event rejection

Rejecting cosmic-ray backgrounds, which occupy most triggered events, is essential for the LAT data processing. This is performed by two kinds of the event information, the shower profile and the anti-coincidence signal [141]. As mentioned before, the raw information is converted to a number of quantities which describe characteristics of each event. Some of them have different distributions for gamma ray and cosmic-ray background. For example, the energy deposited in the ACD is large for charged particles and small for gamma rays, and the lateral distribution of hits in the TKR and CAL is broad for hadronic showers and narrow for electromagnetic ones.

For higher efficiency of discrimination, a multivariate analysis (MVA) with such characteristic parameters is performed. MVA provides a highly optimized and complicated cut through machine learning. First, multiple parameters which are promising for differentiating gamma rays and cosmic-ray backgrounds are chosen. They are called “separators”. Second, a “training” of the separation algorithm is performed by Monte Carlo (MC) simulated data. Training means letting the algorithm

determine how to separate the signals and backgrounds based on the characteristics of the dedicated MC data set. In the "testing", which is the next step, another MC data set is classified by the trained algorithm. MC data are used, because we know the true nature of the event and what it has been classified into. Then, the performance of this algorithm is evaluated, for example, the acceptance, which indicates the fraction of events that survive, and the residual background rate.

Decision Tree There are various MVA methods. The *Fermi*-LAT collaboration uses the boosted decision trees (BDT), which is one of several broadly used methods. The BDT is developed based on the "decision tree" method [143]. A decision tree (a.k.a. classification tree) is a set of successive choices between two alternatives. It looks like a tree as illustrated in Fig. 5.3. Each node is corresponding to each separator. Each choice is configured as a simple question, whether the parameter satisfies a certain threshold. It is trained by the following procedure. The training events flow the tree and are classified by the repeated choices until a certain condition is satisfied. The separator used and the cutting value at each node are optimized so that the classification power is maximized. The number of the nodes an event has passed is dubbed "depth". Each of the terminal pockets is judged whether it is signal-like or background-like, based on the majority of classified training events. After the training, one can judge whether an unknown event is signal-like or background-like by the tree.

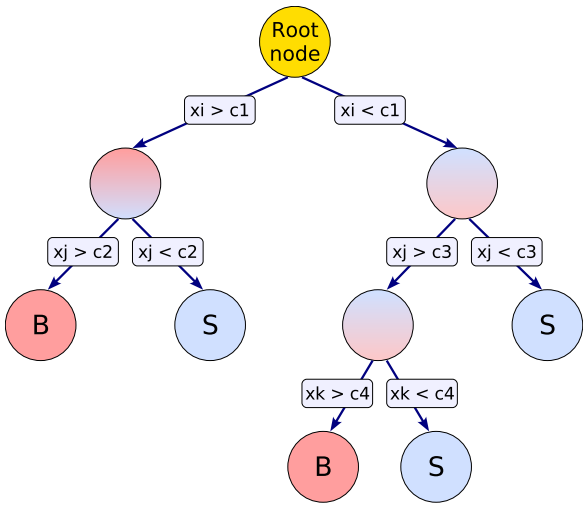

Figure 5.3: Schematic picture of a decision tree [143].

Boosted Decision Trees For BDT, a "forest" which consists of many decision trees is formed [143]. For training a forest, the same MC data set is used, but the MC events are weighted differently

for each tree. Forming a forest stabilizes the output of the classifier. The BDT determines the signal-likeness of each event as the weighted average of the result of each tree. The result of each tree is binary, *i.e.* signal-like or background-like, thus this procedure looks like a vote by many trees. If an event is misclassified by a tree, it gets higher weight in the following trees. This technique is called "boosting", and it allows us to train the trees more efficiently with limited samples and time.

Event classes

The analyzed events are classified by the photon probability and reconstruction quality. Principally, the events are categorized into the following "event classes" [i] [144].

- P8R2_TRANSIENT020
- P8R2_TRANSIENT010
- P8R2_SOURCE
- P8R2_CLEAN
- P8R2_ULTRACLEANVETO

All the event classes are hierarchical, that is, each class of this list is a subclass of the upper classes. An upper class has more statistics but the residual background rate is higher. A lower class is purer in compensation for a less number of events. The TRANSIENT classes are used for analyzing transient phenomena as named or timing studies such as pulsation. The temporal information suppresses the background contamination. P8R2_TRANSIENT020 and P8R2_TRANSIENT010 have residual backgrounds whose rate equal to two and one times the extragalactic diffuse gamma-ray background (EGB), respectively. The EGB is a gamma-ray background component which is extragalactic, unresolved, and isotropic. It is an irreducible background for gamma-ray sources, and it is therefore a good guide for the required residual background level. The SOURCE class is broadly used for analyzing point-like or moderately extended sources. The CLEAN and ULTRACLEAN classes are used for extended or diffuse sources. Accessing such sources requires small background contamination because the spatial information does not suppress the backgrounds.

Event type

In addition to the photon classes, the LAT data have three ways of organizing event partition for two different purposes. They are called "event types". A conventional type is called the "conversion type". As explained in § 5.2.1, the PSF is better for photons which converted into a pair in the front section of the TKR than one for photons which converted in the back section. All the events are categorized into the FRONT or BACK event type [140]. If one wants a good angular resolution, one can use only the FRONT type events, although the statistics become smaller by a factor of two.

[i] Here I only document frequently used classes. More extended classes for special analyses have been defined [144].

The other two partitions have been introduced from `Pass 8`, which is explained in § 5.5. One is categorizing events by the PSF and the other one is by the energy dispersion [145]. In both of them, the events are categorized into four exclusive types. They are dubbed PSF0, PSF1, PSF2, PSF3 and EDISP0, EDISP1, EDISP2, EDISP3. Larger numbers represent better PSFs or energy dispersion. Now one can use the PSF event type for selecting good PSF events instead of the conversion type.

5.4 Performance

The main performance of the *Fermi*-LAT is described by the effective area, acceptance, PSF, energy dispersion and sensitivity.

5.4.1 Effective area

The effective area is a multiplication of the geometrical area and the detection efficiency. It is a function of the energy and the incident direction of each event with respect to the telescope coordinate. It is denoted by $A_{eff}(E, \theta)$ where E is the event energy and θ is the off-axis angle of the incident direction in this thesis. The energy dependency is plotted in Fig. 5.4. It is roughly flat from ~ 1 GeV to ~ 1 TeV, $\sim 0.9\,\mathrm{m}^2$. The off-axis dependency is plotted in Fig. 5.5. The effective area is

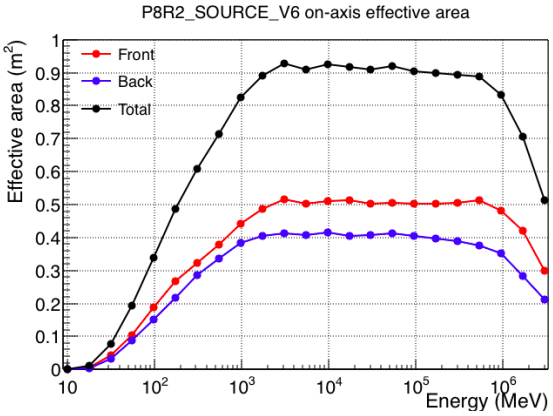

Figure 5.4: Effective area of the LAT as a function of energy for normal incidence photons ($\theta = 0$) [146].

larger for a small off-axis angle. For $\theta > 60\,°$, it is less than a half of one for a normal incident event. This angle can be considered as a rough guide of the FoV. The effective area is different depending on the event class as mentioned in § 5.3.5. It is visualized in Fig. 5.6. The statistical gain of the larger classes is relatively larger in the lowest and highest energy regions.

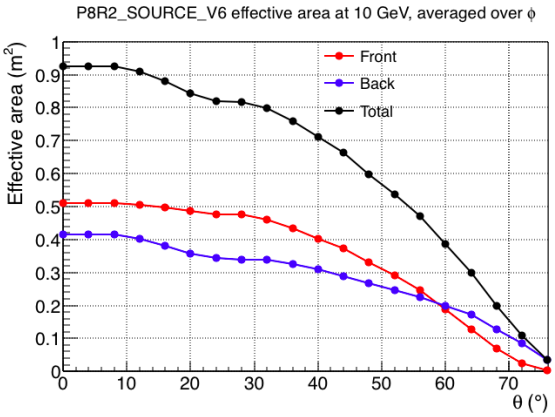

Figure 5.5: Effective area of the LAT as a function of the off-axis angle for 10 GeV photons [146].

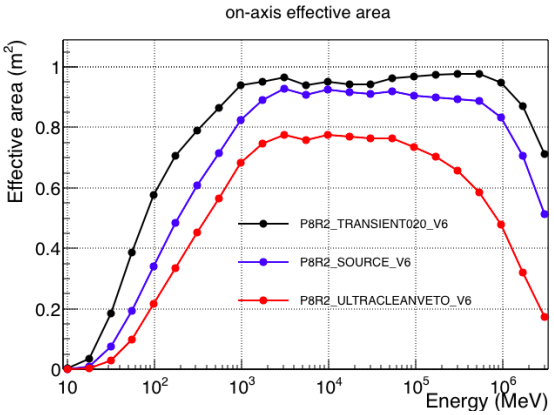

Figure 5.6: Effective area of three LAT event classes as a function of energy for normal incidence photons ($\theta = 0$) [146].

5.4.2 Acceptance

The acceptance is the effective area integrated over the entire solid angle. It represents the total signal statistics which one can obtain during a long time. The acceptance of the SOURCE and TRANSIENT class are $\sim 2.5\,\mathrm{m}^2 \cdot \mathrm{sr}$ for $1\,\mathrm{GeV} \lesssim E \lesssim 1\,\mathrm{TeV}$. Although it is hence affected by the FoV at each energy, the dependence is similar to A_{eff} as plotted in Fig. 5.7.

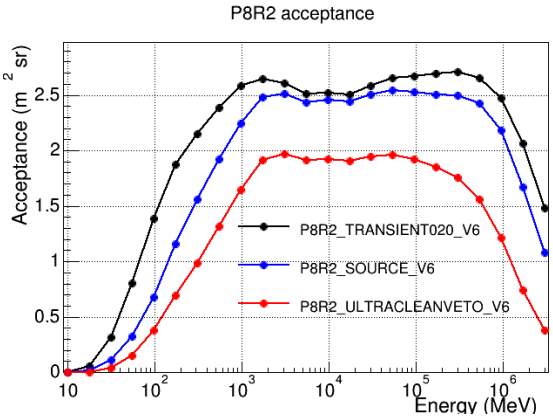

Figure 5.7: Acceptance of three LAT event classes as a function of energy for all photons [146].

5.4.3 Point spread function

The PSFs are also functions of E and θ. They are better at higher energies because deflection due to multiple scattering is smaller [141]. The 68% containment angle (PSF68%) is $\sim 5°$ at 100 MeV and $\sim 0°.8$ at 1 GeV. The PSF is determined by the geometry and spatial resolution of the SSD above a few GeV [141]. Above ~ 30 GeV, the PSF68% is roughly flat, $\sim 0°.1$. Different PSF event types provide quite different PSFs as plotted in Fig. 5.8.

5.4.4 Energy dispersion

The energy dispersion is also provided as a function of E and θ. It strongly depends on E. The 68% containment fraction (EDISP68%) is better than 10% for $1\,\mathrm{GeV} \lesssim E \lesssim 500\,\mathrm{GeV}$. The energy dispersion is typically not taken into account in the standard likelihood analysis. It is because the effect of neglecting the energy redistribution is usually small compared with a bin width in the energy range above 100 MeV [141].

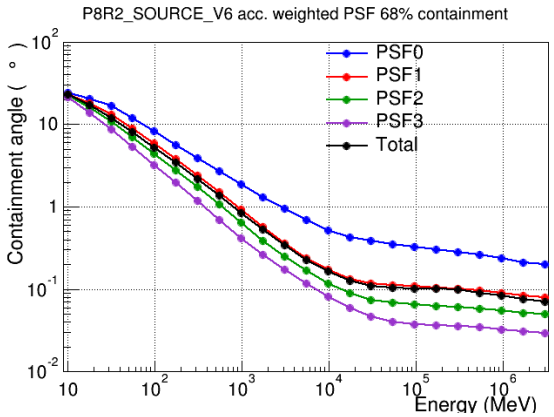

Figure 5.8: PSFs of the LAT as a function of energy for four PSF event types [146].

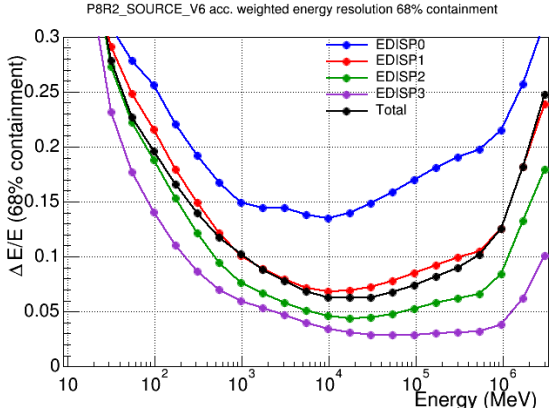

Figure 5.9: Energy dispersion of the LAT as a function of energy for the four EDISP event types [146].

5.4.5 Sensitivity

The sensitivity depends on the observational conditions and the target source. In Fig. 5.10, it is plotted as the minimum flux above 100 MeV (in photons $\cdot$ cm^{-2} $\cdot$ s^{-1}) to obtain the $5\,\sigma$ detection in 10 years of observation in survey mode, assuming a power law spectrum $\propto E^{-2}$. Here $5\,\sigma$ means the likelihood test statistics (*cf.* § A.2.2) of 25 and detection of at least 10 photons. The used event class is P8R2_SOURCE_V6. The sensitivities for a few different sky positions are drawn because they depend on the background. Above $\sim$ 10 GeV, the sensitivities are dominated by the signal statistics, not by the background under these conditions.

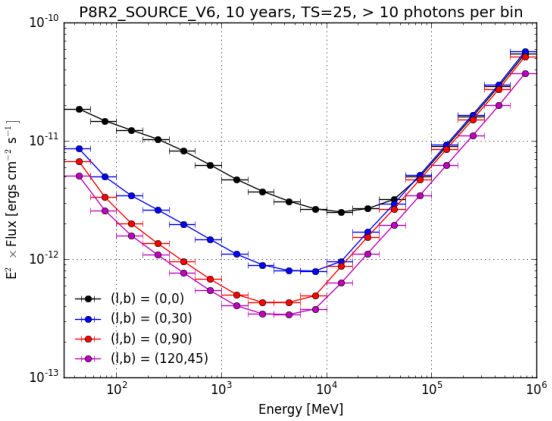

Figure 5.10: Differential sensitivities of P8R2_SOURCE_V6 for ten years in four bins per energy decade. It assumes a point source with a power-law spectrum with index -2 and uniform background around it. The curves are for four different locations in the Galactic coordinate: Galactic center, intermediate latitudes, north Galactic pole, and north Celestial pole. The effect of the point source backgrounds is ignored. A minimum of ten photons per energy bin is required [146].

5.5 Pass 8 analysis

`Pass 8` is the latest version of the LAT low-level analysis, which is periodically updated [147]. It was released on 24 June, 2015 and replaced the former version `Pass 7` for the entire mission data sets.

The experience of observations in the early phase of the LAT mission let us know some unignorable features missed by the simulations. In `Pass 8`, new event reconstruction algorithms were introduced in order to prevent this effect from reducing the acceptance. In addition, some updates in simulation, event reconstruction, and event selection realized a significant reduction in background contamination, an increase in the effective area, a better PSF, and more understood systematic uncertainties. In Fig. 5.11, the acceptance of `Pass 8` and `Pass 7` are compared. The increase in the

acceptance is relatively large in the energy ranges below 100 MeV and above 100 GeV. I focus on

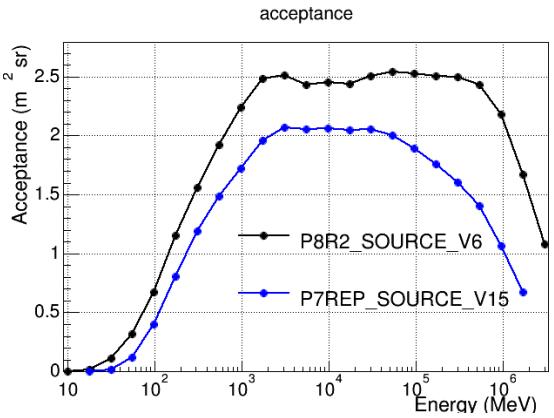

Figure 5.11: Acceptance of the SOURCE class of `Pass 8` and `Pass 7`.

some features of `Pass 8` which are relevant to this thesis in the following subsections. More details are found in [147] and a technical paper published in the future.

5.5.1 CAL clustering analysis

Clustering analysis is introduced in order to abandon the single-particle paradigm. In `Pass 6` and `Pass 7`, the shower was reconstructed under the assumption that all energy depositions were caused by a single event. However, so-called "ghost" events caused problems in reconstructing the energy and direction. The rate of cosmic rays passing through the LAT may be as high as 10 kHz. The characteristic signal shaping times of the TKR, CAL and ACD are 10, 3.5, and 4 μs, respectively. Therefore, the overlapping of the footprints of temporally proximate events happens with a non-negligible rate [148].

In `Pass 8`, multiple clusters of energy deposition are identified so that the ghost events are spatially distinguished. This is performed with the minimum spanning tree construction, which is an application of graph theory. This recovers 5 - 10% effective area above 1 GeV [147].

5.5.2 CAL direction reconstruction

Next, momentum analysis is performed on every cluster identified in the previous step. It estimates the centroid and moment direction. This information is used for connecting the cluster with tracks in the TKR and for evaluating many characteristic quantities. The cluster centroid is determined by taking an average of the displacement vectors of the hit positions weighted by the deposited energy. The principal axis of the cluster is also determined from the spatial distribution. These processes

iterate a few times so that the hits far from the shower axis are eliminated from the following cycles. This analysis reconstructs the event direction with an accuracy of a few degrees above 1 GeV.

5.5.3 Energy reconstruction

For measuring the event energy, the information from both the TKR and CAL are used. If the event energy is low, the event does not reach the CAL and the energy is reconstructed from the number of hits in the TKR. On the other hand, the amount of deposited energy in the CAL is important for higher-energy events. The amount is corrected by estimating the lost energy.

Reconstructing the energy for events above 3 GeV The main cause of the energy losses is a leakage from the CAL above 1 GeV. It happens because the thickness of the CAL is not large sufficient to stop the shower completely. An appropriate approach for the events above 3 GeV is fitting of the shower profile. The development of the shower is accurately modeled and the longitudinal profile of the deposited energy is predicted for each CAL layer. The transverse extension is also very important for events above 1 TeV because the crystals along the shower axis saturate and do not provide good information. The details will be reported in a `Pass 8` technical paper in future.

5.6 Calimeter-only event classes

5.6.1 Concept

The latest low-level analysis of the *Fermi*-LAT, `Pass 8`, recovers a significant fraction of high-energy photons which had previously not been recognized as gamma rays [147], [66]. Moreover, the clustering analysis enabled us to develop new classes of untapped events. While the conventional event classes require information from the TKR for reconstructing events, the new event classes are meant to be used when there is no usable TKR information. Typically, such events pass through the TKR without interacting because its thickness is only about one radiation length, or enter the LAT from the side plains. They are dubbed "calorimeter-only (CalOnly)" events.

5.6.2 Direction reconstruction

Reconstructing the direction of the CalOnly events is required not only for final scientific uses, but also for background rejection. The information on the direction is essential for deriving some characteristic quantities. Especially, as mentioned before, the consistency of the cluster axis and the fired ACD tiles is very important because of backsplash.

When the CAL direction is successfully reconstructed and one or more trajectories are found, the counterpart tracks are searched in the TKR. If a track is found in the TKR and the angle from the CAL direction is smaller than a certain value which depends on the reconstructed energy, the event is considered a standard event. If no tracks agree to the CAL direction, it is categorized as a CalOnly event. The CalOnly and conventional standard classes are thus completely exclusive.

5.6.3 Energy reconstruction

For the CalOnly events, the energy is reconstructed by the profile fit method described in §5.5.3. The shower axis used in the reconstruction depends on the CAL shower profile instead of the TKR.

5.6.4 Indication of the energy reconstruction quality

A parameter that indicates the quality of the energy reconstruction of each event is constructed. It is based on the BDT method in a similar way as the event classification. The classification trees were trained by a binomial MC dataset. For the event classification, the "signal" sample consists of MC gamma rays and the "background" sample consists of MC cosmic rays. For the energy quality indicator, the "signal" sample consists of gamma-ray events with small energy errors and the "background" sample consists of events with large energy errors. The LAT collaboration has developed a variation of this indicator which is optimized for the CalOnly events. The indicator is denoted by P_{BEP}, and it takes a value from 0 to 1 like a probability.

5.7 Standard high-level analysis

In this last section of this chapter, I briefly overview the LAT high-level data analysis, namely, deriving quantities such as gamma-ray fluxes and spectral indices of astronomical sources. It is performed as likelihood analysis. The fundamental ideas and formulas are reviewed in Appendix A. For the LAT data analysis, a standard analysis suit, *ScienceTools*, is released by the LAT collaboration [149].

5.7.1 Source model

For a likelihood analysis, a model of the source spectrum and spatial shape is assumed for each of the interesting sources and other nuisance sources. A variety of models are implemented in *ScienceTools*. One can also use a list of flux value at each energy and a template of spatial distribution as a model. For example, a power-law spectral model is defined as

$$\frac{dN}{dE} = N_0 \left(\frac{E}{\mathrm{E}_0} \right)^{\Gamma_\gamma}. \tag{5.1}$$

The parameters are the normalization factor N_0 and spectral index Γ_γ. The scaling energy E_0 is fixed.

5.7.2 Effective area, livetime and exposure

The predicted observational result is calculated with the chosen model and the LAT instrument response functions (IRFs) for the observation. The IRFs are factored into the effective area, PSF, and energy dispersion. These IRFs for each event class and type are implemented by the LAT collaboration. The observed gamma-ray count is predicted by integration of the flux, the effective area, and the observation time. Practical calculation is performed like the following procedure. First, a cumulative record of the telescope attitude for the analysis time period is produced. It is called the "livetime" (a.k.a. the "pointing history"). One can find how long the telescope kept each attitude during the period in it. Next, the effective area is time-integrated. Because the effective area depends on the direction with respect to the telescope coordinate, the livetime data file is utilized for the calculation. The integrated effective area is called the "exposure". It is calculated for a point-like sky position or an extended region. Finally, one can obtain the predicted count spectrum by multiplying the model flux and the exposure.

5.7.3 Point spread function

The spatial photon distributions are distorted by the PSFs [150]. The PSFs are defined in terms of an angular deviation of the reconstructed direction from the true event direction. They are provided as functions of the event energy and off-axis angle for each PSF event type (PSF0, PSF1, PSF2, and PSF3). The observable photon spatial distribution is predicted by the PSF, the model extension and the pointing history.

5.7.4 Energy dispersion

The spectrum is distorted by the dispersion of the energy reconstruction [151]. The energy dispersion is defined in terms of a fractional deviation of the reconstructed energy from the true event energy. It is provided as a function of the event energy and off-axis angle for each energy dispersion event type (EDISP0, EDISP1, EDISP2, and EDISP3) and in addition, each of PSF0/PSF1 and PSF2/PSF3.

5.7.5 Likelihood fitting

The *gtlike*[152] of *ScienceTools* combine these factors and construct the likelihood function. The observable photon spectrum is predicted with the energy dispersion, the model spectrum, and the pointing history. With the exposure $\mathcal{E}$, PSF P, and the energy dispersion D, the predicted count is

written as

$$M(E', (\boldsymbol{v}')) = \int F(E, \boldsymbol{v}) \mathcal{E}(E, \boldsymbol{v}) P(\boldsymbol{v}'; E, \boldsymbol{v}) D(E'; E, \boldsymbol{v}) d\boldsymbol{v} dE, \tag{5.2}$$

where E is the photon energy and $\boldsymbol{v}$ is the vector of the arrival direction. The primes indicate the observed quantities. Then fitting of the model is performed so that the likelihood is maximized. The input model is a combination of the spectra of gamma-ray sources and their distributions on the sky, including the intensities. The likelihood is calculated with Poisson statistics as described in § A. Both the binned and unbinned likelihood methods are available. The binned likelihood can be calculated faster, and the unbinned likelihood is used when the number of counts is small. The best estimates of the free parameters and errors are reported. The *gtlike* also calculates some secondary quantities of each source, such as photon flux, energy flux, test statistics, and predicted count.

Chapter 6

Calorimeter-only classes

In order to improve the statistics in the energy range above a few tens of GeV, I have developed the background rejection and event classification of the CalOnly events described in § 5.6, and evaluated their performance with MC data. Although the development has not yet been completed, one can apply the CalOnly classes to some scientific studies. In this chapter, I describe the development of the background rejection, configurations of the event classes, performance evaluation with MC, and validation with astronomical data. The advantages of the CalOnly classes are summarized at the end. These classes are used for the GRB studies reported in § 7.

6.1 Multivariate analysis for background rejection

As mentioned in § 5, the measured signals of each event are parametrized and they are used for the MVA of discriminating gamma-ray signals from cosmic-ray backgrounds. I had to optimize the MVA configuration for CalOnly events because the standard configuration has been constructed on the assumption that both of the TKR and CAL information are available, which does not happen for CalOnly events. I have evaluated the performance of MVAs with a variety of configurations by MC data sets for which the astronomical gamma rays and backgrounds are simulated, in order to find the best one. Evaluating the MVA performance has three steps, namely, 1) training with MC events, 2) testing MC events with the trained MVA, and 3) evaluating the acceptance of MC gamma rays at a certain residual MC background level. The MVA method is the boosted decision trees (BTD), explained in §5.3.5. All of these steps are carried out by the Toolkit for Multivariate Data Analysis with ROOT [143].

Training The classification trees are trained with MC data sets of the signal (astronomical gamma rays) and the background (cosmic rays). The background data set contains cosmic protons and other nuclei, electrons, positrons, neutrons, and secondary particles which are produced by

interaction between the primary particles and the spacecraft body. Their fluxes and interaction simulate realistic observations.

Testing MC events of the signals and backgrounds flow the trained trees. The toolkit [143] returns a gamma-likeness value for each event. The gamma-likeness of the signals and backgrounds distributes like Fig. 6.1. The BDT output takes a scaler value from 1 (signal-like) to -1 (background-like). It is usually converted to the value P_{GAM} which ranges from 0 to 1 like a probability, or its inversely-logarithmic value $-\log_{10}(1 - P_{GAM})$, which is larger for a more gamma-like event.

Evaluating Each value of the gamma-likeness corresponds to the signal and background efficiencies (survived faction) after cutting the data at this value of the gamma-likeness. The two efficiencies at each gamma-likeness are evaluated with the tested data. The correlation between two efficiencies is plotted in Fig.6.2. Once a cut value of the gamma-likeness is specified, the survived event set is determined, and the performance characteristics are evaluated with the tested data.

Through many trials, I have tested various configurations and several ideas for improvement. I explain one of the ideas which works well in § 6.1.1. Another idea is separating the classification trees into multiple categories dedicated to different types of events, for example, high-E and low-E events; large-θ and small-θ events. Developing multiple BDTs which are dedicated to different regions of the parameter space improves the performance. On the other hand, it needs to divide the samples used for training, thus may worsen the rejection of gamma-like backgrounds. I defined two categories by the off-axis angle θ, $\cos\theta \geq 0.6$ and $\cos\theta < 0.6$. This categorizing slightly improve the separation of events above ~ 350 GeV. I finally selected the best setup documented in Table 6.1 and 6.2. The separation of the MC signal (gamma rays) and background (cosmic rays) by this configuration is visualized in Fig. 6.1. The trade-off relation of the signal efficiency and the background efficiency is plotted in Fig. 6.2.

6.1.1 Newly introduced separators

For the CalOnly separation, I have defined three new separators. They are based on other event-level parameters. I would like to discuss what I intended by introducing them. I plot the distributions of these parameters for MC gamma (blue), hadrons (protons, alpha particles, heavier ions, nucleons; red), leptons (electrons and positrons; magenta) in Fig. 6.3, 6.4, and 6.5. The background datasets include secondary hadrons/leptons which are produced by primary cosmic rays via interaction with the spacecraft body. For each plot, I selected a certain energy and off-axis range where the distributions are separated well.

Table 6.1: The configurations of the MVA setup that I finally selected.

Method	Boosted Decision Trees
Precuts[a]	(E_{CAL}[b] > 20 GeV) and (Momentum analysis succeeded at least once) and (No TKR tracks consistent with CAL cluster) and ($\cos\theta_{CAL}$[c] ≥ 0.2) and (Extrapolated CAL cluster axis crosses ACD)
Number of trees	500
Number of separators	15 (*cf.* Table 6.2)
Event categories	$\cos\theta \geq 0.6$, $\cos\theta < 0.6$
Maximum depth	6
Boosting algorithm	Gradient boost [143]

[a] Criteria of the event selection applied before the MVA. They removed events which are unwanted or apparently different from the typical signals.
[b] E_{CAL}: Deposited energy in the CAL.
[c] θ_{CAL}: Off-axis angle of the incoming direction reconstructed from the CAL information.

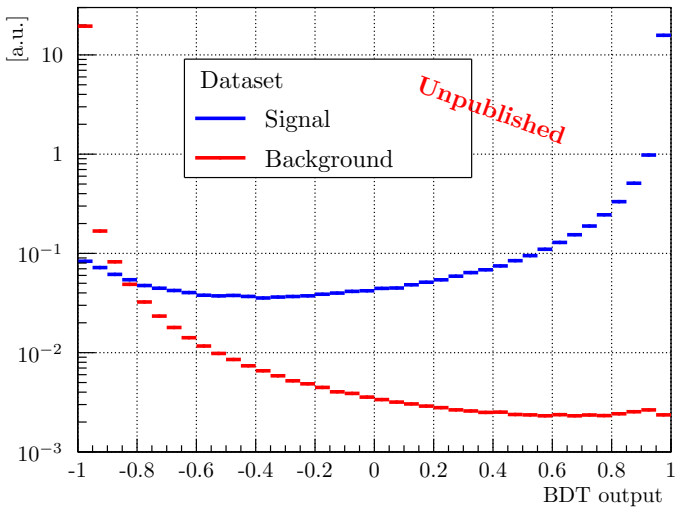

Figure 6.1: Distributions of the BDT output value for the MC signal (gamma rays) and background (cosmic rays) datasets. This plot is for the configuration that I finally selected.

Table 6.2: Parameters for the MVA configuration that I finally selected.

Parameter	Description
Fractional ACD energy	Ratio of the energy deposited in the ACD tiles to the reconstructed event energy, in log-scale
ACD energy within CAL cone	Amount of the energy deposited in the ACD within a 15°cone ahead of the reconstructed CAL cluster
ACD veto counts	Total number of vetoes fired in ACD, in log-scale
ACD energy and position deviation	Significance for which two values are combined, 1) the differential number of σ from an expected minimum ionization particle (MIP) for the observed signal and 2) the number of σ the track propagation is away from any tile or ribbon most likely to veto the first CAL cluster, in log-scale
CAL profile fit χ^2	χ^2 of the profile fit (computed over the crystals in a 100 mm radius cylinder around the trajectory), in log-scale
CAL cluster transversal RMS	CAL first cluster transversal profile RMS, in log-scale
Position of the CAL longitudinal maximum	Position of the maximum of the longitudinal profile
Fractional energy in the CAL backhalf	Ratio of total energy in back half of CAL (layers 4-7) to the raw deposited energy
CAL E_7/E_4	Ratio of E_7 to E_4 in log-scale.
CAL E_{CAL}/E_i	Ratio of E_i[a] to the corrected total energy in log-scale.
CAL $(E_{i+3}+E_{i+4})/E_i$	Ratio of E_i to $(E_{i+3}+E_{i+4})$in log-scale
CAL transverse shower size	Transverse size of shower as function of energy fraction
CAL cluster fit χ^2	χ^2 of the fit process of the first CAL cluster, in log-scale
Fraction of crystals used	Fractional Number of crystals used for determining position/centroid
Energy in CAL edges	Sum of the raw energy in each crystal for which the energy centroid is within 50 mm of the outside edge of one of the outside CAL modules, in log-scale

[a] E_i: amount of energy deposited in the i-th CAL layer ($i: 0-7$). The 0-th layer is the top and the 7-th layer is the bottom. The layer number which the particle injected is denoted by i.

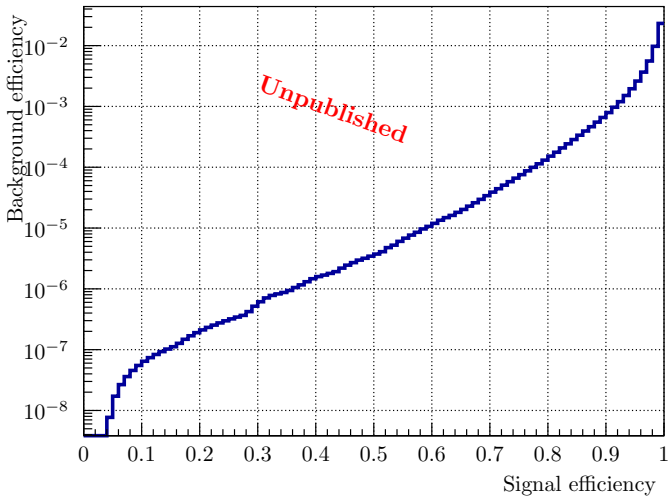

Figure 6.2: Curve of the background efficiency vs. the signal efficiency. Both of them are determined by the cut value series of the BDT output. This plot is for the configuration that I finally selected.

E_{CAL}/E_i : The ratio of the total energy deposited in the CAL to the energy deposited in the CAL layer where the particle starts depositing energy (the initial layer), in logarithmic scale. The latter is the value after correcting the effects of the leakage and the gaps of the CAL. The distributions are plotted in Fig. 6.3. This parameter represents how many orders of magnitude the shower developed. A gamma ray does not interact with the crystals until it converts to an electron pair and it typically takes about one layer ($\sim$ 1 radiation length). Gamma rays deposit only a small energy in the first layer compared with hadrons and leptons. Hence, E_{CAL}/E_i is higher for gamma rays.

$(E_{i+3} + E_{i+4})/E_i$: The ratio of the energy deposited in the $i+3$th and $i+4$th layers to the energy deposited in the initial layer. The distributions are plotted in Fig. 6.4. The idea is same as E_{CAL}/E_i.

E_7/E_4 : The ratio of the energy deposited in the layer 7 (bottom) to one in the layer 4. Although this quantity also represents the development of the shower, the information on the later half of the shower is extracted. The distributions are plotted in Fig. 6.5.

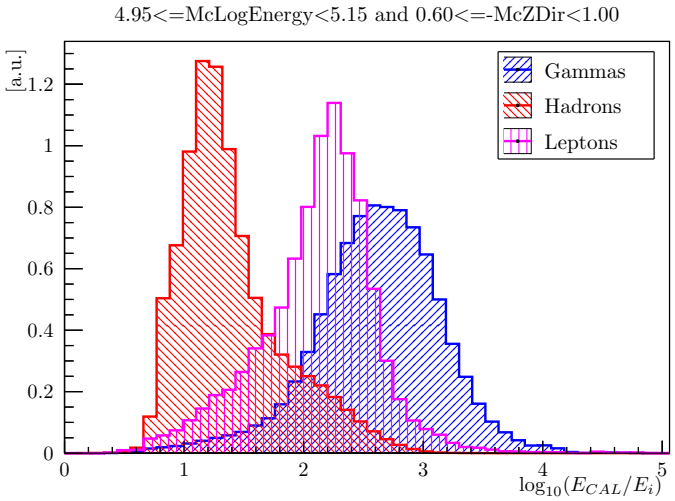

Figure 6.3: Distributions of $\log_{10}(E_{CAL}/E_i)$ of MC events with $89\,\mathrm{GeV} < E < 141\,\mathrm{GeV}$ and $0.6 < \cos\theta < 1.0$ where E is the MC event energy and θ is the event off-axis angles. The blue, red, and magenta histograms represent gamma rays, hadrons, and leptons, respectively. The distributions in these figures are normalized.

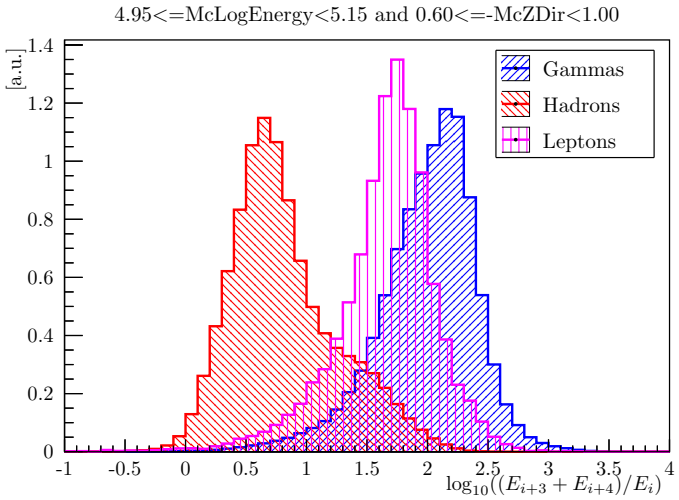

Figure 6.4: Distribution of $\log_{10}((E_{i+3} + E_{i+4})/E_i)$ of MC events with $89\,\mathrm{GeV} < E < 141\,\mathrm{GeV}$ and $0.6 < \cos\theta < 1.0$ where E is the MC event energy and θ is the event off-axis angles. The blue, red, and magenta histograms represent gamma rays, hadrons, and leptons, respectively. The distributions in these figures are normalized.

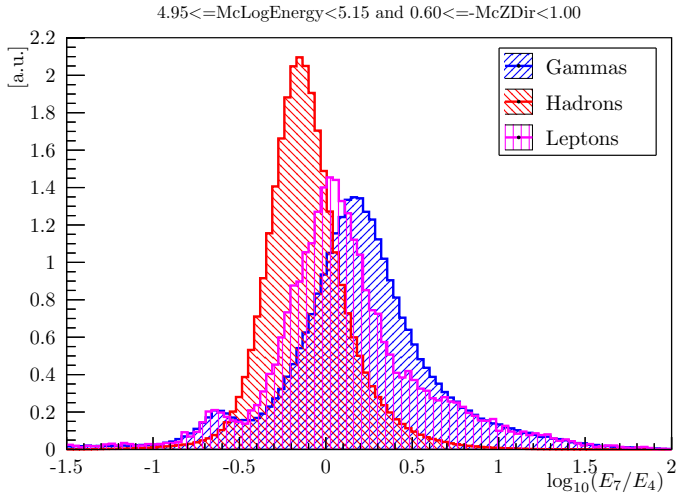

Figure 6.5: Distribution of $\log_{10}(E_7/E_4)$ of MC events with $89\,\mathrm{GeV} < E < 141\,\mathrm{GeV}$ and $0.6 < \cos\theta < 1.0$ where E is the MC event energy and θ is the event off-axis angles. The blue, red, and magenta histograms represent gamma rays, hadrons, and leptons, respectively. The distributions in these figures are normalized.

6.2 Event class definitions

The standard gamma-like events are categorized into the nested event classes for scientific analysis as described in § 5.3.5. For the CalOnly events, I have defined four nested event classes with the gamma-likeness evaluated by the MVA. The cut values of the gamma-likeness are determined based on the residual background rate relative to the level of the EGB. The criteria are listed in Table 6.3. Some of them may be eliminated when the CalOnly events are officially released to public in future. The CalOnly_R100 and CalOnly_R030 classes are the counterparts of the standard TRANSIENT classes, mainly for transients and timing studies such as GRBs and millisecond pulsars. CalOnly_R010 corresponds to the standard SOURCE class and intended for point-like sources. CalOnly_R003 is the cleanest class and may be useful for diffuse source studies.

Table 6.3: The CalOnly event classes. The lower classes are sub-classes of the upper classes.

Event class	Residual background	Uses
CalOnly_R100	$\sim 10\times$ EGB	Transients, timing studies
CalOnly_R030	$\sim 3\times$ EGB	
CalOnly_R010	$\sim 1\times$ EGB	Point sources, moderately extended sources
CalOnly_R003	$\sim 0.3\times$ EGB	Diffuse sources

6.3 Performance

In this section, I describe the performance of the CalOnly classes. It is quantified as residual background rate, acceptance, PSFs, energy dispersion, and field of view. These characteristics are evaluated by MC simulation data of the signal gamma ray and background cosmic rays.

6.3.1 Residual backgrounds

The residual background is the rate of non-gamma-ray events in a photon class after the classification. I configured the four photon classes so that they have residual backgrounds of 0.3×, 1×, 3× and 10× EGB rate as mentioned in § 6.2. The background rejection works well as demonstrated in Fig. 6.6. The residual background is suppressed just as I configured although the statistics of the residual background are not sufficient for CalOnly_R003 or in the energy range above ∼ 100 GeV.

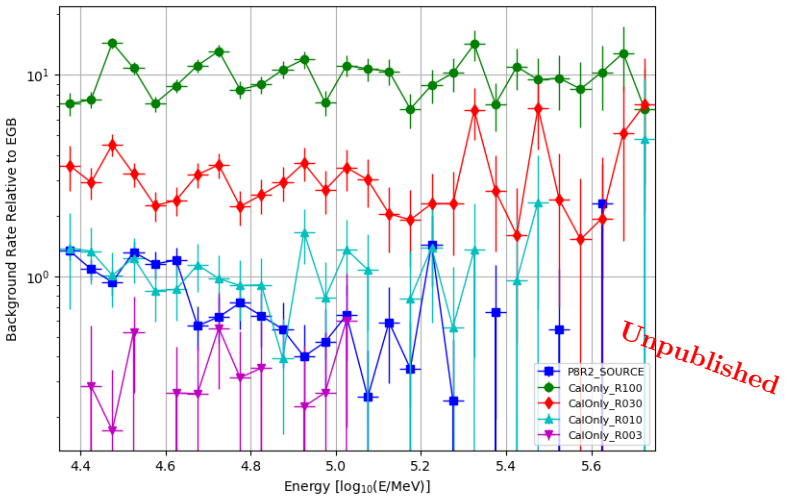

Figure 6.6: Residual background rate respect to the EGB. The abscissa is the energy in logarithmic scale, from 22.3 GeV to 562 GeV. The blue squares represent the standard P8R2_SOURCE class for comparison. The green circles, red diamonds, cyan and purple triangles represent the CalOnly_R100, R030, R010 and R003 class respectively.

6.3.2 Acceptance

The acceptance is the effective area integrated over the FoV. It yields the signal statistics we can get from a certain source during a long observation. It depends on E and θ. The dependence on only E is plotted in Fig. 6.7. The peak locates around 100 GeV. At the peak, the acceptance of

the CalOnly_R100 and R003 corresponds to $\sim$ 70% and $\sim$ 40% of the standard SOURCE class, respectively. These fractions of photons are recovered for analysis on top of the conventional data. This is a significant improvement because, at 50 - 100 GeV, the LAT sensitivity is limited by statistics for most of the sources, hence the gain in acceptance leads to a gain in sensitivity. The dependence

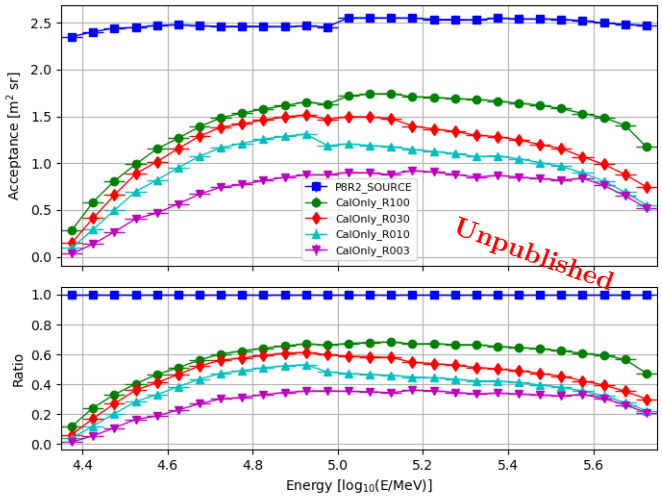

Figure 6.7: Top: Acceptance as a function of the event energy E in log-scale, from 22.3 GeV to 562 GeV. Bottom: Ratio of the CalOnly acceptance relative to the standard P8R2_SOURCE class.

on E and θ are plotted in Fig. 6.8. The acceptance is basically larger at smaller off-axis angles because most of the MVA separators work better. Exceptionally, the acceptance is suppressed for small θ in the energy range below $\sim$ 50 GeV because the thickness is small for such a direction and the deposited energy does not reach the threshold 20 GeV if a fraction of the energy leaks from the CAL. The acceptance for $\cos\theta < 0.2$ is almost zero, and hence I introduced one of the precuts, $\cos\theta \geq 0.2$ (*cf.* Table 6.1) for simplicity.

6.3.3 Point spread functions

The PSFs strongly depend on E and θ as plotted in Fig. 6.9. They are better for larger θ because the CAL is geometrically thicker, and thus the tracks become longer. The θ-integrated PSFs distribute from two to four degrees as plotted in Fig. 6.11. These are more than one order of magnitude worse than those for the standard classes. It must be mentioned that this significantly affects the background contamination in the CalOnly data analysis of point sources.

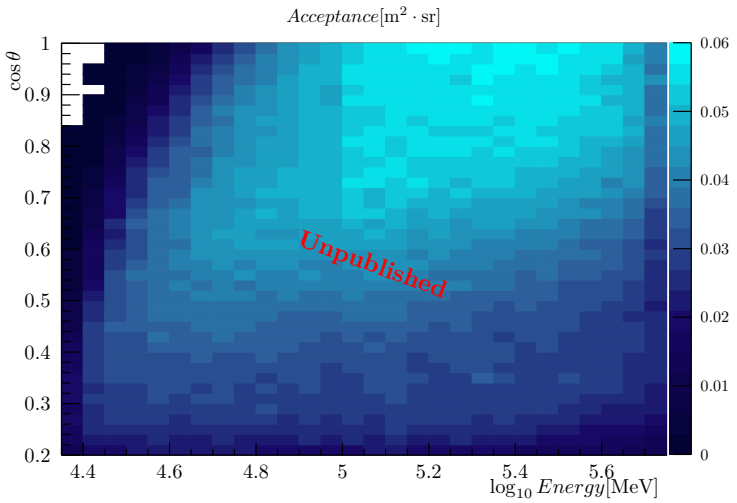

Figure 6.8: Acceptance in $\mathrm{m}^2 \cdot \mathrm{sr}$ of CalOnly_R100 as a function of $\log E$ vs. $\cos\theta$. E ranges from 22.3 GeV to 562 GeV and θ ranges from 0° to $78^\circ.5$.

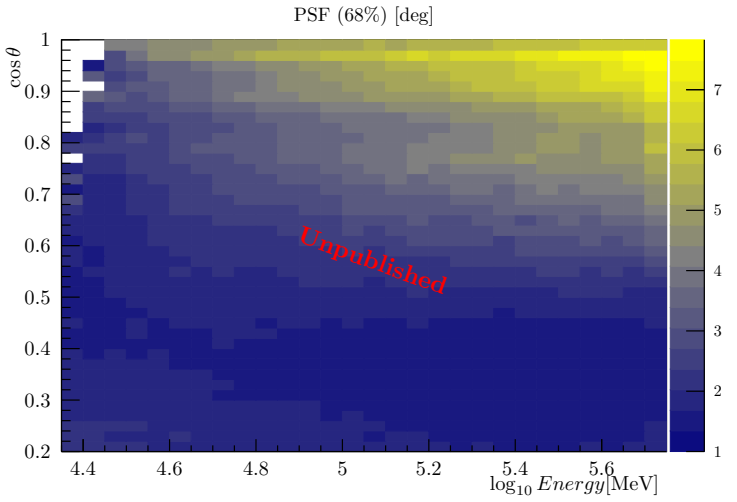

Figure 6.9: PSF (68% containment) in degrees of CalOnly_R100 as a function of $\log E$ vs. $\cos\theta$.

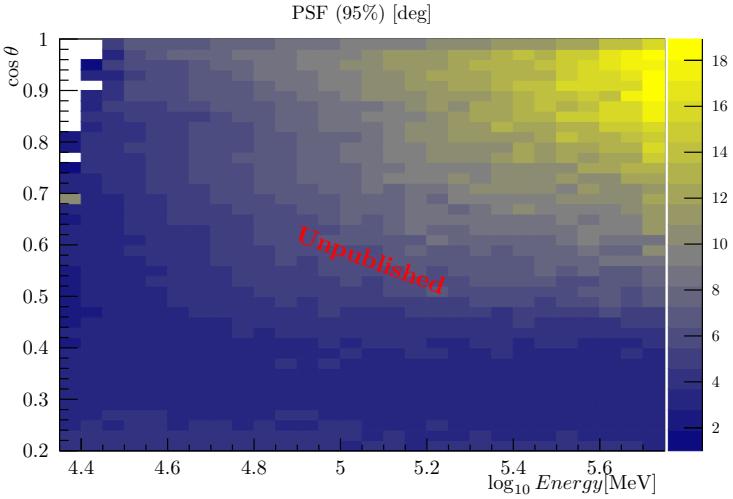

Figure 6.10: PSF (95% containment) in degrees of CalOnly_R100 as a function of $\log E$ vs. $\cos\theta$.

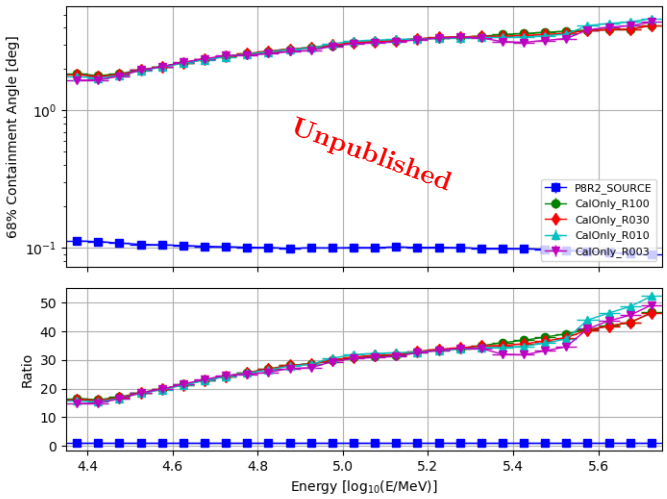

Figure 6.11: Top: PSF (68% containment) in degrees as a function of E in log-scale. Bottom: The ratio of the CalOnly PSF relative to the standard SOURCE class.

6.3.4 Energy dispersion

The energy dispersion $\Delta E/E$ also strongly depends on E and θ. It is large for high-E events and small-θ events as displayed in Fig. 6.12. Reconstructing the energy is more difficult for higher-energy events because of the energy leakage and the readout saturation. For side-entering events, the shower energy is almost entirely deposited in the CAL because of the larger size in radiation length the CAL, and therefore the energy dispersion is small. Integrated over θ, the energy dispersion of the

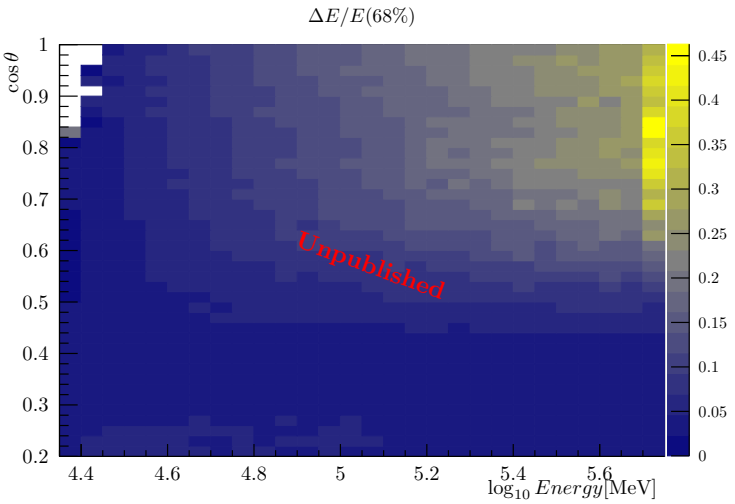

Figure 6.12: Fractional energy dispersion (68% containment) of CalOnly_R100 as a function of $\log E$ vs. $\cos\theta$.

CalOnly classes is comparable to those of the standard classes as plotted in Fig. 6.13.

6.3.5 Field of view

I plot the effective area as a function of θ in Fig.6.14. The CalOnly effective area is flatter than the standard one, although the former is smaller than the latter at most of the angles. The relative gain of the CalOnly classes is larger at large off-axis angles. The effective area at 50 GeV is small for face-on events because of the reason mentioned in § 6.3.2.

6.4 Validating with flight data

6.4.1 Sky map

The developed classes must be validated by real data, not only by MC data. In Fig. 6.15, an all sky map with the CalOnly_R010 photons is displayed. One can see the Galactic disk and some bright

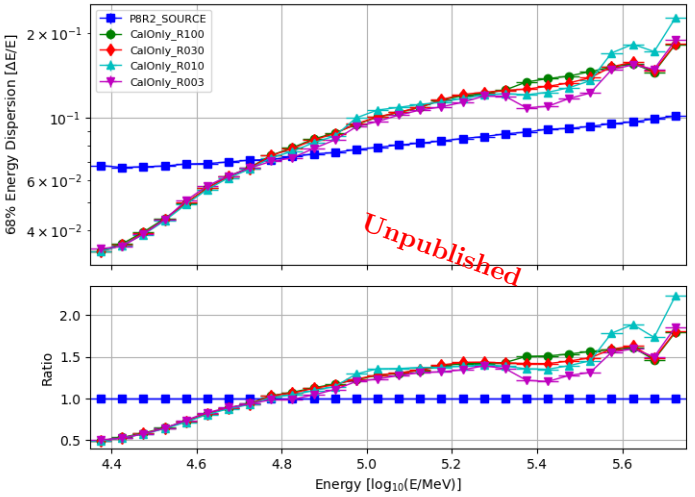

Figure 6.13: Fractional energy dispersion (68% containment) as a function of E in log-scale. Bottom: Ratio of the CalOnly energy dispersion relative to the standard P8R2_SOURCE class.

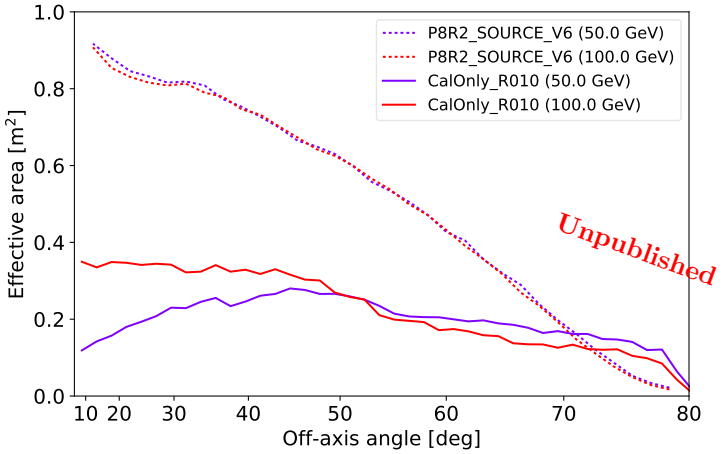

Figure 6.14: Effective area for the off-axis angle of an event. The standard P8R2_SOURCE class (dotted lines) and the CalOnly_R010 class (solid lines) are drawn for the event energy 50 GeV (purple lines) and for 100 GeV (red lines). The effective area is evaluated based on gamma-ray MC. The metric of the horizontal axis follows $\cos\theta$, which is proportional to the differential solid angle.

point sources such as Crab nebula, Mkn 421 and 3C66A. This demonstrates the event classification works.

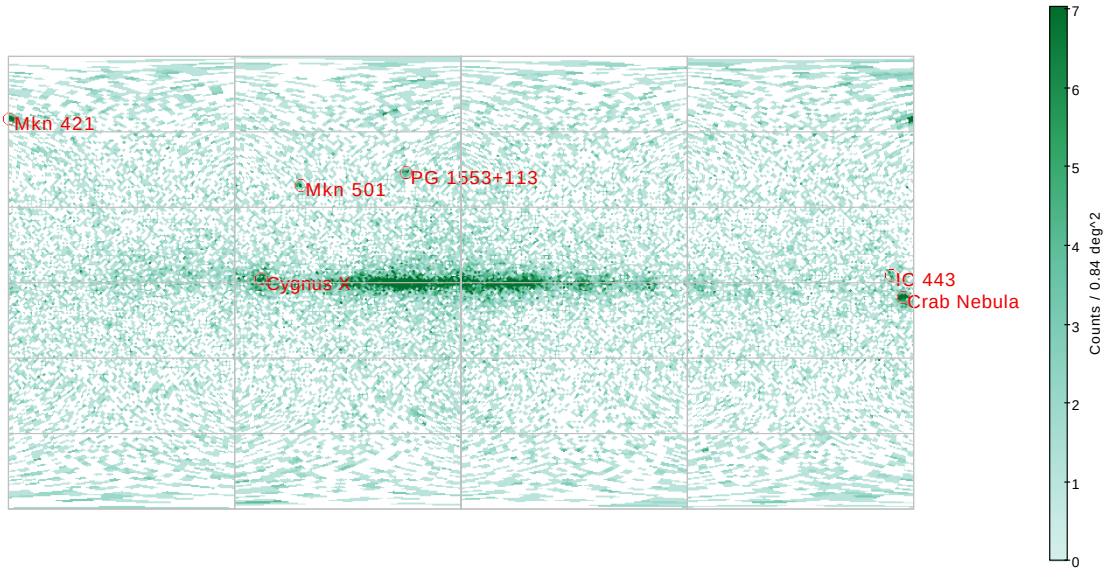

Figure 6.15: All sky map in the Galactic coordinates with the CalOnly_R010 photons for 8.3 years. Some bright gamma-ray sources are highlighted by red circles.

6.4.2 Bright point source

I evaluated the consistency between the IRFs based on MC and the observed CalOnly data, using data of a bright gamma-ray point source, Mkn 421. I analyzed standard data around Mkn 421 and constructed a spectrum model of gamma-ray sources with the result. Convolving the model and the CalOnly IRFs yields a prediction of the CalOnly data. It was compared to the observed data in a distribution of the angular separation of the CalOnly events from the sky position of Mkn 421.

Data selection

The evaluation was performed for the CalOnly_R100 data from the mission elapsed time (MET [i]) 250215883 s to 513639039 s. It equals a time range from 00:24:42 on 6 December 2008 to 21:30:34 on 11 April 2017 in Coordinated Universal Time (UTC). I excluded the earliest months just after the start of the LAT observation because the event triggering was unstable. The used RoI is within twelve degrees from Mkn 421, (RA, DEC)=(166.113808, 38.208833). The CalOnly_R100 events are filled into a histogram of the event energy vs. $1 - \cos\vartheta$ where ϑ is the angular separation from Mkn

[i]The mission elapsed time (MET) is defined as the elapsed time in the unit of second since 1 January 1994, at 00:00:00 in Coordinated Universal Time, which corresponds to 49353.0 in Modified Julian Date.

421. The energy axis has seven logarithmically equivalent bins for the range of 22.4 GeV to 562 GeV.

Modeling

I considered the observed data are composed of Mkn 421, isotropic backgrounds (the residual cosmic-rays and EGBs), and extra gamma-ray backgrounds. The isotropic backgrounds were estimated with an OFF data set, which was taken from high-galactic-latitude regions, in each of the seven energy bins. The details are described in § 7.3.2. I corrected the difference in the exposure and subtracted the expected isotropic component from the histogram of the observed CalOnly_R100 data. The exposure is calculated for six annuli centered at Mkn 421 with the internal/outer radius of 0/2, 2/4, 4/6, 6/8, 8/10, and 10/12 degrees.

In order to derive the gamma-ray flux distribution around Mkn 421, I analyzed P8R2_SOURCE_V6 data with a simple model composed of Mkn 421 as a point source and an extra background component with a spatially uniform distribution. I performed a likelihood analysis and derived their flux in each of the seven energy bins. These flux values are convolved with the CalOnly IRFs in order to predict the separation distribution of the CalOnly events. The contribution of the extra background component is divided into the six annuli, being proportional to their exposure. The flux of Mkn 421 is multiplied by the exposure at the point of the source, and the spatial dispersion is calculated with the CalOnly PSF. The PSF is a function of E and θ, and it is weighted by the exposure distribution in the parameter space of them.

Result

I plotted the result in Fig. 6.16. In the upper panel, the predicted and observed CalOnly_R100 count distributions are plotted. The abscissa is $1 - \cos\vartheta$ where ϑ is the angular separation from Mkn 421. The counts are integrated over the energy range. In the lower panel, the fractional residual of the predicted and observed counts is displayed. According to this plot, the model based on MC roughly reproduces the shape of the observed separation distribution. However, the observed counts are higher than the predicted ones in most bins. There is possibly a systematic underestimation of the CalOnly acceptance. This result is used in § 8.

6.4.3 CAL- vs. TKR-reconstructed direction

It is difficult to see the tail of the PSF of the CalOnly events because of the backgrounds. For clarifying this point, I compared the CAL-reconstructed direction to the TKR-reconstructed one of the standard events in flight data. The PSFs of the standard classes are more than one order of magnitude narrower those of the CalOnly classes. Therefore, the TKR-reconstructed direction is

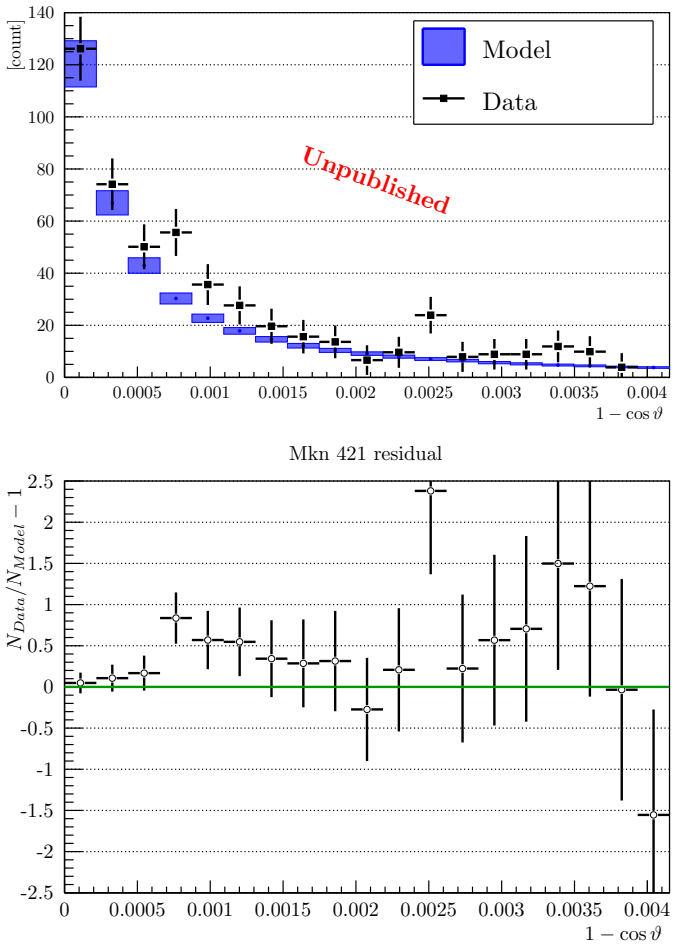

Figure 6.16: Upper: Comparison of CalOnly_R100 observational data of Mkn 421 and its model based on the standard analysis. The ordinate indicates the observable count after subtracting the isotropic backgrounds estimated by a method with high-galactic latitude OFF data, which is explained in § 7.3.2. The abscissa indicates $1-\cos\vartheta$ where ϑ is the angular separation of each event from the sky position of Mkn 421. The right edge of this plot corresponds to 5.36°. Lower: Fractional residual of the data from the model.

considered to be a guide of the true arrival direction although the profile of the standard events differs from that of the CalOnly events because the starting points of the shower are earlier.

I selected the P8R2_SOURCE_V6 class events which have only one reconstructed track in the TKR and satisfy the CalOnly_R100 criteria except for the CalOnly condition. This is for making us sure the tracks in the TKR and in the CAL are created by one gamma-ray, not by two coincidental particles. I derived the angular dispersion of the CAL-direction from the TKR direction and plotted the 68% and 95% containment angle in Fig. 6.17 and 6.18, respectively. The difference of the containment angles from those of the dispersion of the CAL-direction from the true direction of MC events is also plotted. In most of the phase space, the discrepancy between the CAL-TKR vs. CAL-MC dispersions is less than one degree. For the high energy and small off-axis events, the CAL-TKR dispersion is smaller than the CAL-MC dispersion. This difference can be interpreted to be because of the long trajectory of the early starting showers in the CAL. Consequently, these differences do not pose any crucial problems for scientific analyses in this thesis.

6.5 Advantages of the CalOnly classes

The CalOnly classes increase the instrument acceptance of gamma rays, above 20 GeV, where the performance of Fermi-LAT is limited by low photon statistics, by about 60% at the peak energy around 100 GeV. Their angular resolution is poor and it results in more background contamination in data of unextended sources compared with data with usable tracker information. However, the temporal information effectively suppresses the background contamination for transient objects and timing studies. Therefore, GRBs, AGN flares, and millisecond pulsars are good targets of the CalOnly classes. In addition, objects which do not require a good PSF could also benefit. One example is dark matter line searches at broad regions such as the Inner Galaxy.

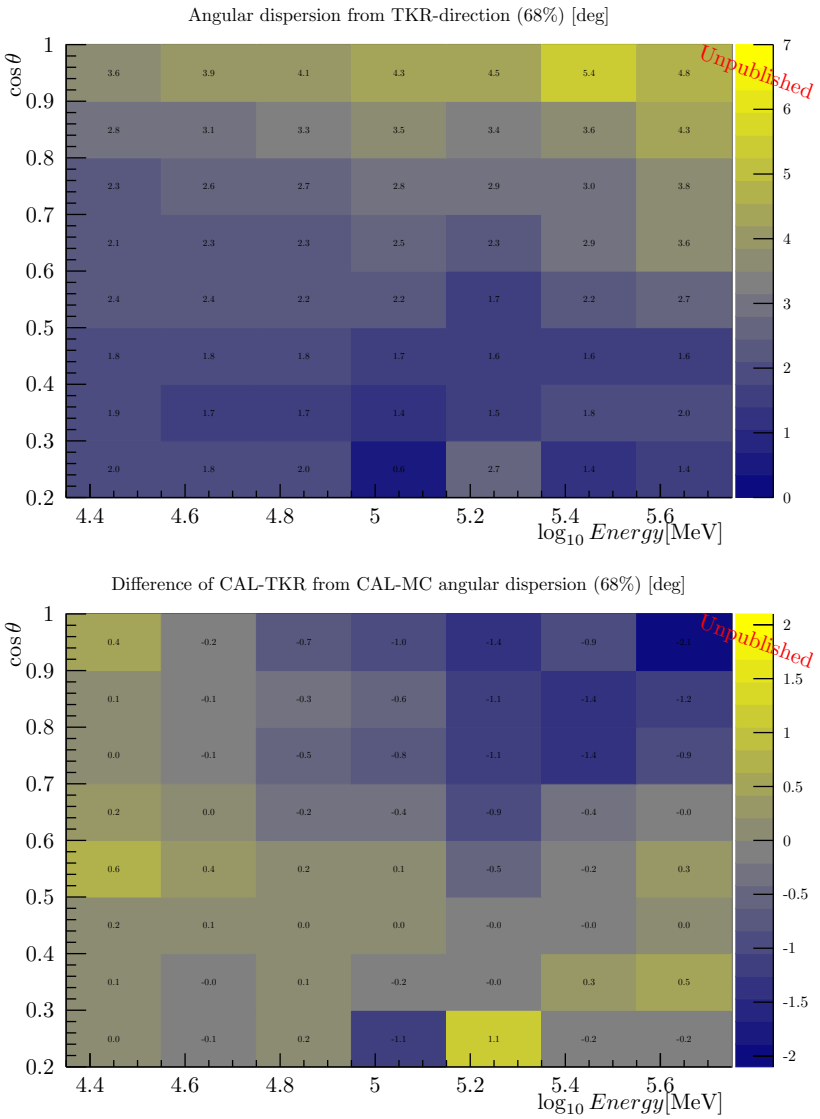

Figure 6.17: Upper: Angular deviation $\Delta\vartheta_{CAL-TKR}$ of the CAL-reconstructed direction (68% containment) from the TKR-reconstructed one of each CalOnly_R100 event of flight data. The unit is degree. Lower: Difference of $\Delta\vartheta_{CAL-TKR}$ from the PSF68% of the CalOnly_R100 events evaluated with the MC data set. Positive numbers (yellowish color) indicates the CAL-TKR dispersion is larger than the CAL-MC dispersion. Negative numbers (bluish color) indicates the CAL-TKR dispersion is smaller than the CAL-MC dispersion.The bins with $\cos\theta < 0.3$ are affected by statistical fluctuation because each bin has only a few events.

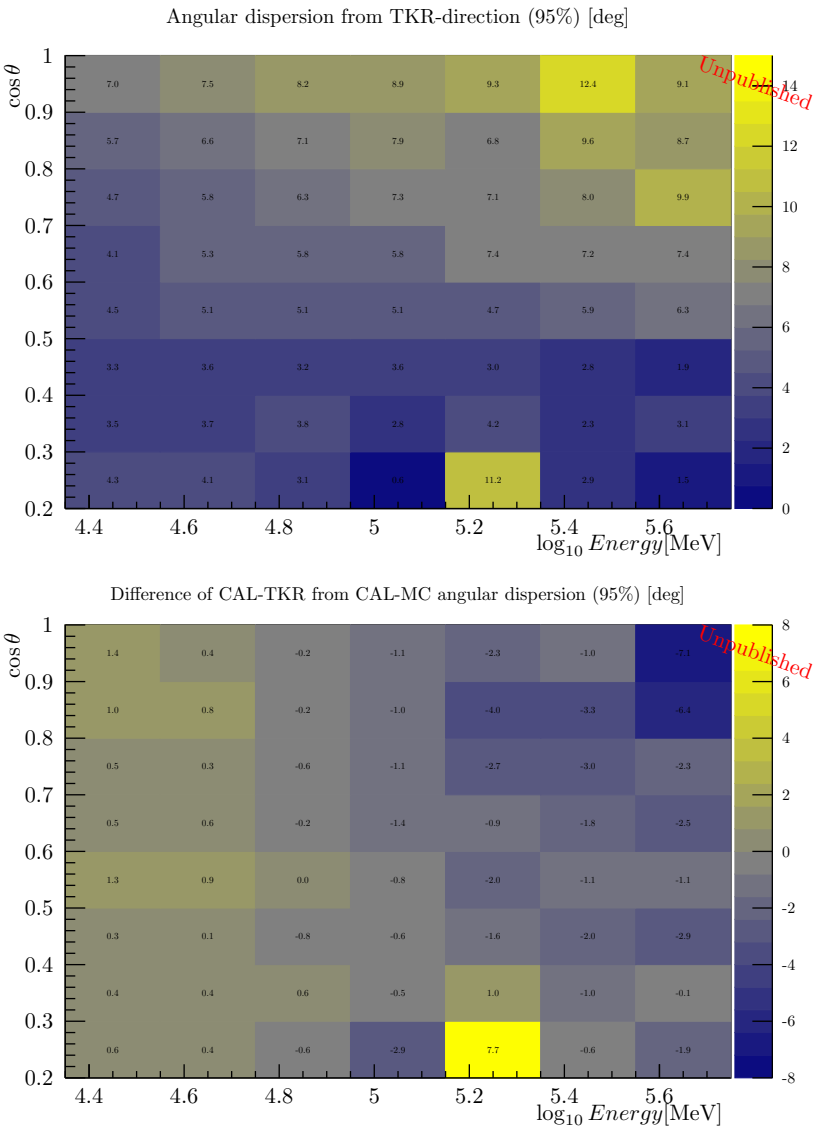

Figure 6.18: Upper: Angular deviation $\Delta\vartheta_{CAL-TKR}$ of the CAL-reconstructed direction (95% containment) from the TKR-reconstructed one of each CalOnly_R100 event of flight data. The unit is degree. Lower: Difference of $\Delta\vartheta_{CAL-TKR}$ from the PSF95% of the CalOnly_R100 events evaluated with the MC data set. Positive numbers (yellowish color) indicates the CAL-TKR dispersion is larger than the CAL-MC dispersion. Negative numbers (bluish color) indicates the CAL-TKR dispersion is smaller than the CAL-MC dispersion. The bins with $\cos\theta < 0.3$ are affected by statistical fluctuation because each bin has only a few events.

Chapter 7

Calorimeter-only photon search in the LAT data

The limit of synchrotron energy is $\sim 50\Gamma/(1+z)$ MeV where z is the redshift and Γ is the Lorentz factor of the emission region as mentioned. It equals 20 GeV for $z = 1$ and $\Gamma = 1000$ (*cf.* § 4.3.1). The CalOnly classes improve the statistics above such energy. I searched for CalOnly events spatially and temporally coincident with LAT-detected GRBs. In this chapter, I report the methods, caveats, and results of the GRB photon hunt in the CalOnly classes. After listing CalOnly gamma-like events coincident to GRBs, I elucidate the chance probabilities that they were caused by background.

7.1 Target selection

I selected the GRBs which were well localized and with spectra extending up to 10 GeV. The criteria are listed below. The localized coordinates were taken from the online LAT GRB catalogue [55]. T_0 is the trigger time of the GBM, and T_{90} is the duration of the prompt emission (90% contaminment) taken from the GBM catalogue [18, 19, 20]. If the GBM did not detect the GRB, the trigger time taken from the third *Swift* GRB catalogue [153] was used instead.

1. The burst was detected by the LAT until the end of 2016.

2. The localization error in the catalogue was smaller than $0^\circ.3$.

3. One or more P8R2_SOURCE_V6 photons above 10 GeV were detected within 1° from the catalogue position, within the time window from T_0 to $T_0 + 100$ ks.

Table 7.1: List of the LAT-detected GRBs which were localized with an error smaller than 0°.3 and accompanied by standard P8R2_SOURCE class photons above 10 GeV

GRB	#Photons	Highest energy or > 50 GeV		Red-	Duration [s]	
	> 10 GeV	$T - T_0$ [s]	E [GeV]	shift[a]	T_{90}	T_{50}
080916C	2	40.5	27	4.35	63.0 ± 0.8	32.0 ± 0.7
090510A	1	0.8	30	0.903	1.0 ± 0.1	0.3 ± 0.1
090902B	7	331.9	22	1.822	19.3 ± 0.3	9.0 ± 0.2
090926A	2	24.8	19	2.1062	13.8 ± 0.3	6.5 ± 0.1
100116A	2	379.0	33		103 ± 1	5.5 ± 0.2
100414A	2	33.4	30	1.368	26 ± 2	13.2 ± 0.3
130427A	18	18.6 243.1 256.3	77 94 57	0.3399	138 ± 3	4 ± 1
130907A [b]	1	17227.0	51	1.238	364 ± 5	59.7 ± 0.3
131018B	1	243.9	15		$(4 \pm 1) \times 10^1$	13 ± 2
131231A	2	110.3	48	0.642	31 ± 1	9.7 ± 0.4
140206B	2	75493.1	29		147 ± 4	25 ± 1
140619B	1	0.6	23		2.8 ± 0.8	1.0 ± 0.7
140810A	1	1490.2	15		81.7 ± 0.6	22.3 ± 0.4
140928A	2	2554.7	52		18 ± 7	5.4 ± 0.7
141028A	2	37826.0	11	2.33	31 ± 2	8.2 ± 0.7
141222A	2	0.7	20		2.8 ± 0.3	0.77 ± 0.09
150403A	1	25108.8	10	2.06	22.3 ± 0.8	6.4 ± 0.6
150902A	1	97.5	11		13.6 ± 0.4	4.6 ± 0.4
160310A	1	5884.5	27		18.2 ± 0.7	8.4 ± 0.2
160422A	1	769.6	12		12.3 ± 0.4	4.6 ± 0.4
160509A	3	76.5	52	1.17	370 ± 1	55 ± 1
160521B	1	422.6	13		2.8 ± 0.6	1.0 ± 0.4
160623A	1	12038.5	18	0.367	108 ± 9	51 ± 4
160625B	1	346.2	15	1.406	$(4.5 \pm 0.1) \times 10^2$	12.0 ± 0.4

[a] The redshift values were taken from [154].
[b] Not GBM-triggered. T_0, T_{90} and T_{50} were taken from the Swift-BAT catalogue [153].

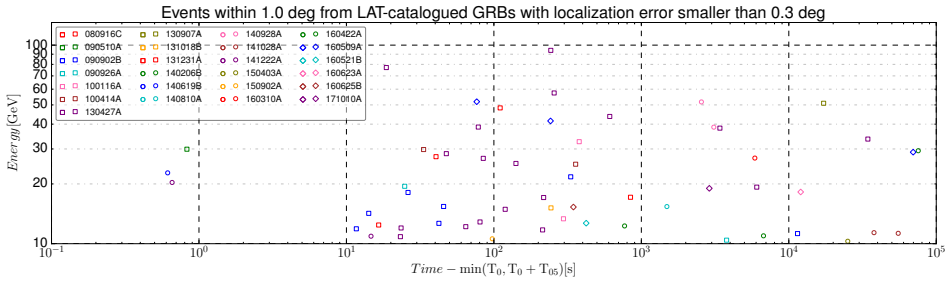

Figure 7.1: Energy vs. time of the P8R2_SOURCE_V6 events within 1°.0 from the LAT-catalogued GRBs above 10 GeV. Both the energy and arrival time are observed values and not corrected by the redshift.

I list the LAT-GRBs that meet the criteria in Table 7.1. The number of the GRBs with photons above 10 GeV is 24. The highest photon energy is 94 GeV; the photon was coincident with GRB 130427A. It was detected at T_0+243 s. The energy and arrival time of these $>$ 10 GeV events are plotted in Fig. 7.1.

7.2 Background components

The energy threshold of the CalOnly classes is 20 GeV as mentioned in §6, and it increases to about 30 GeV for face-on targets, such as GRBs being pointed at by the boresight axis of the *Fermi* telescope. The standard photon classes are almost background-free in this energy range because both the temporal and the spatial information effectively suppress the backgrounds. However, the residual backgrounds are not negligible in the CalOnly classes because of their more than one order of magnitude worse PSFs. Below I factor the background to some possible components.

Residual cosmic rays This is expected to be dominant in CalOnly_R100 and R030. The spatial distribution weakly depends on the zenith angle. The survivability in the CalOnly photon classes strongly depends on the off-axis angle of every event.

Nearby gamma-ray sources I checked whether any sources in the LAT 2FHL catalogue [155], which lists sources detected above 50 GeV, were located within ten degrees from the photon candidates. The problematic sources are discussed individually. Most of the sources are negligible compared to the GRB flux, except for few very bright ones.

Extragalactic gamma-ray background The EGBs are gamma rays, and they are therefore essentially irreducible with the gamma-likeness or spatial information. This component is important when a tight cut is applied for the cosmic-ray component.

Local diffuse gamma rays The contamination of the local Galactic gamma rays depends not only on the sky position, but also the gamma-ray acceptance of the event class, and therefore the contamination depends on the event energy and off-axis angle.

Earth-limb gamma rays The Earth-limb gamma rays are produced by interactions of cosmic-rays with the atmosphere of the Earth. Gamma rays are emitted via the decay of neutral pions and kaons, and via Bremsstrahlung of electrons and positrons [156]. The intensity of the Earth-limb gamma ray depends on the zenith angle θ_Z[i], and it peaks at about 112° [156, 141]. I rejected all events with the zenith angle $\geq 100°$, but the contamination should be taken into account because the CalOnly PSFs have not been verified with the flight data.

7.3 Methods

7.3.1 Data selection and photon search

All triggered events above 20 GeV are basically recorded as mentioned in § 5.3.2. This enables us to revisit all archival GRB data in this energy range. I selected the data by the following criteria.

Target GRBs The 24 GRBs which were accompanied by one or more standard class photons above 10 GeV, until the end of 2016. These are listed in Table 7.1.

Event class The largest class CalOnly_R100 was used, but the background probabilities were calculated for the smaller classes, CalOnly_R030, R010, and R003 if any events are included in these classes.

Time window From the GBM trigger time T_0 to $T_0 + 10$ks. If the *Fermi*-GBM was not triggered, the trigger time of the *Swift*-BAT was used instead.

Region of interest The region of interest (RoI) was configured as a circular region whose center was at the position of each GRB with the radius of (the PSF 68% containment) + (the GRB localization error). The GRB position and its error were taken from the LAT online catalogue [55]. The PSF is a function of E and θ of each event. It was determined with MC in § 6.3.3.

I consider any event which meets all of these criteria as a candidate of a GRB photon with the intention of keeping the background chance probability in each GRB data smaller than ~ 0.1. Hereafter the number of the CalOnly events found in the data of one GRB is denoted by N_{ON}.

[i] Whereas θ is the angle from the boresight of the telescope, θ_Z means the angle from the opposite direction to the Earth barycenter.

7.3.2 Background estimation

Likelihood methods which background components are taken into account were not implemented for the CalOnly classes, and the likelihood analysis was unavailable. Hence, I performed ON/OFF analyses for estimating the probability that each CalOnly detection was caused by a coincidental background. The predicted count of the coincident backgrounds N_{BKG} is calculated by Eq. 7.1.

$$N_{BKG} = N_{OFF}\mathcal{E}_{ON}/\mathcal{E}_{OFF} \tag{7.1}$$

where N_{OFF} is the observed count in the OFF data, $\mathcal{E}_{ON}$ and $\mathcal{E}_{OFF}$ are the exposure of the ON and OFF data, respectively. Then, I evaluated the probability that the detection of N_{ON} was reproduced by the background of N_{BKG}. The raw background rate and the residual rate depend on E, θ, and θ_Z besides the exposure $\mathcal{E}_{ON}$. The ON and OFF event distributions in the parameter space of θ_Z vs. θ vs. E differ, and the difference must be taken into account. To this end, I created histograms of N_{OFF}, $\mathcal{E}_{ON}$ and $\mathcal{E}_{OFF}$, and filled the OFF events and the ON/OFF telescope pointing history into the histograms, respectively. The axes of the histograms are (θ, θ_Z, E) when all of the dependence on the three quantities are taken into account and (θ_Z, E) when the dependence on θ is ignored. Calculating Eq. 7.1 gives us a histogram of the predicted background count in each bin. Derivation of N_{OFF}, $\mathcal{E}_{ON}$ and $\mathcal{E}_{OFF}$ is described below.

Exposure calculation

Generally, the exposure is calculated by integrating the effective area over the time, and the solid angle of the sky region. For calculating the solid angle easily, I utilized the HealPix (Hierarchical Equal Area isoLatitude Pixelization, [157]), which provides equal-area pixelization of a sphere, and one can choose a preferable scale of the pixels. Provided a parameter N_{side}, the HealPix divides all the sky into $12N_{side}^2$ pixels. I obtained θ and θ_Z of every HealPix pixel center in the OFF region at every 30 seconds in the OFF time window. Then, I filled the livetime duration of these short intervals into a two-dimensional (2D) histogram of θ vs. θ_Z. Multiplying this histogram by the 2D effective-area histogram of E vs. θ yields an exposure histogram. The effective-area histograms of the CalOnly classes are based on MC as explained in § 6.3. The calculation of the exposure is illustrated in Fig. 7.2.

ON exposure The region for counting events and the region for calculating exposure should be equivalent, but I used a slightly different region for calculating $\mathcal{E}_{ON}$ from the RoI for N_{ON} above in order to save the calculation resources. The region for N_{ON} is defined as a circular region within (PSF68% + localization error) from the catalogue position. The PSF is a function of the event energy and off-axis direction as explained in Fig. 6.9. In short, the ON region varies depending on E and θ. Calculating the exposure of this varying region takes a large amount of the computational

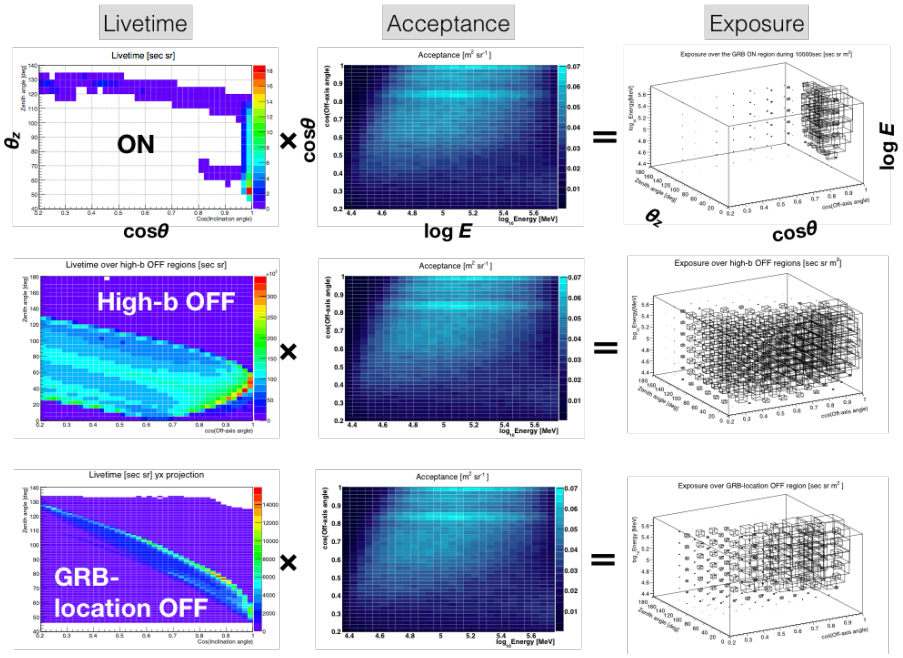

Figure 7.2: Calculation of the exposure of the ON (top), high-b OFF (middle), and GRB-location OFF (bottom). The definition of the ON/OFF data sets are described in text. In the left plots, the color indicates the livetime distribution depending on the zenith angle θ_Z and off-axis angle $\cos\theta$. In the middle plots, the color indicates the acceptance depending on the off-axis angle $\cos\theta$ and energy $\log E$. In the right plots, the size of cubes indicates the exposure distribution, where the absolute scale is arbitrary. The exposure distributions are obtained by multiplying the livetime and the acceptance distribution.

resources, so that I simplified it as below. I defined the region for $\mathcal{E}_{ON}$ as a collection of HealPix pixels with $N_{side} = 32$. The approximate resolution is 1°.83 and the maximum angular distance between any pixel center and its corners is about 1°.90. I calculated the exposure for this region as described above, and multiplied the $\mathcal{E}_{ON}$ histogram by the ratio of the solid angles of the count region to those of the exposure region so that the discrepancy in solid angle is corrected.

For the OFF sample, I tried two approaches with different OFF data sets focusing on different background components.

Approach 1: High-b OFF analysis

For the first approach, I utilized the high-galactic-latitude ("high-b") regions as the OFF data. The high-b regions were used in [141] for calibrating the LAT standard analysis. I basically followed the definition in § 3.6.4 of the paper, $|b| > 50°$, $90° < l < 270°$ where b and l is the galactic latitude and the longitude, respectively. The time window of the OFF data is the same as the ones used for the validation of the CalOnly classes with Mkn 421 in § 6.4.2, MET 250215883 s to 513639039 s. All the CalOnly events whose the reconstructed direction and arrival time meet the criteria are included in the OFF data set. The data set is statistically large, and this enables us to access the dependence on E vs. θ vs. θ_Z. The uniform background components, namely, the cosmic rays and the EGBs are correctly dealt with by this approach. Equation 7.1 was calculated as an operation of the three-dimensional (3D) histograms.

OFF event counting The OFF region is defined as a collection of HealPix pixels whose center meets the definition of the above high-b regions. The N_{side} of the pixels is 16. In this case, the number of pixels in the entire sphere is 3072, the approximate resolution is about 3°.66, the maximum angular distance between any pixel center and its corners is about 3°.78. I excluded the pixels including any 2FHL sources from this collection. I counted the CalOnly class events which were detected in the OFF region and in the OFF time window. The events with $\theta_Z > 100°$ were excluded.

OFF exposure calculation The region for $\mathcal{E}_{OFF}$ is identical to the one for N_{OFF}. I calculated the 3D exposure histogram for the pixels that were included in the region. The time window is identical to the one for N_{ON}, namely T_0 to $\mathrm{T}_0 + 10\,\mathrm{ks}$.

Local gamma-ray background estimation The local gamma-ray background components are not taken into account in the estimation with the high-b OFF. Among those local gamma-ray backgrounds, the Galactic diffuse component is important in many cases. It dominates the local background, especially when the PSF is small and the contribution of the background point-like sources are negligible. In order to estimate its contribution, I performed a likelihood analysis with

the standard photon classes. The RoI is the region within five degrees from the GRB position. The time window is from MET 239557417 to 501033396, but a period from $T_0 - 2$ days to $T_0 + 20$ days is excluded. The energy range is from 22.4 GeV to 562 GeV so that it is identical to the entire CalOnly range. I added the isotropic background and the galactic diffuse component to the model. I fixed all model parameters except for the normalization of the galactic diffuse.

Approach 2: GRB-location OFF analysis

In the second approach, I restricted the OFF region to the spatially identical one with the ON region, but shifting the time window in order to evaluate the local gamma ray backgrounds correctly. I ignored the dependence on the off-axis angle in order to have a large event statistics. This may cause misestimation of the cosmic rays, but does not affect the gamma rays. It is because the dependence on the rate of the gamma-ray survivability is already included in the exposure. Equation 7.1 is calculated as an operation of the 2D histograms of E vs. θ_Z.

OFF event counting The OFF region is similar to the ON region, but they differ in what follows. The radius of the ON region for counting depends on the energy and off-axis angle of each event. For the OFF region, the radius is fixed at a value for the off-axis angle of the detected CalOnly event while the radius varies depending on the energy. That is because I calculated the expected background for each energy bin separately, but integrated the background over the off-axis angles. The off-axis angle distributions depend on the observation period, and therefore the calculation would be unfair if the size of the regions varied depending on the off-axis angle.

OFF exposure calculation The OFF exposure was calculated the same way as the ON exposure.

I move back to the methodology common for the two approaches.

Deriving the predicted background count and the coincidence probability The resultant histogram of Eq. 7.1 was projected to the axis of the energy. Then, I determined the predicted residual background above a certain energy threshold by integrating the projected histogram. This process is illustrated in Fig. 7.3. The background probability $p_{BKG}(k)$ is calculated as a cumulative Poisson probability that k or more backgrounds contaminate in the ON dataset. It must be noted that I derived only the pre-trial probabilities but did not take the trials in the data sets of the 24 GRBs into account. It is because the potential background contamination is strongly dependent on the off-axis angle and the sky position of the GRB, and the effective observation duration in which the GRB was not hidden by the Earth.

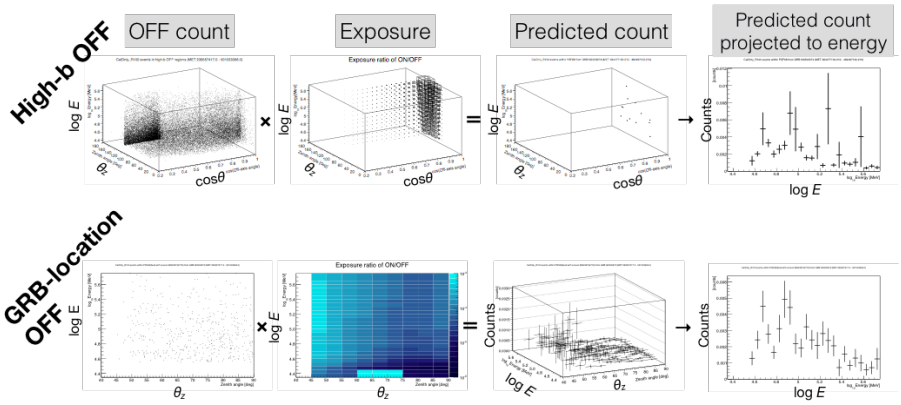

Figure 7.3: Calculation of the predicted background counts in the ON data based on the high-b OFF data (top) and the GRB-location OFF data (bottom). Multiplying the OFF count and the exposure results in the predicted count in the ON data set. Projecting the 3D (high-b OFF) or 2D (GRB-location OFF) resultant histograms to the energy axis, the predicted counts above a certain energy threshold are obtained.

Caveat: OFF data cut

The ON/OFF analysis shows arbitrarinesses when selecting the OFF data cut. The residual background rate depends on the cuts on the energy, arrival time, angular distance, gamma-likeness, and zenith angle. There is not any objective strategy for selecting these cuts. The most conservative choice is using the exactly same cut as used for selecting the ON data, but it reduces the significance of the detections. In this study, I followed this philosophy for the energy, arrival time, angular distance and zenith angle. For the gamma-likeness, I selected the purest CalOnly class that contains the GRB photon candidate under study.

7.3.3 Energy uncertainty

When one focuses on an individual event, its energy uncertainty is as important as the background probability. Most of the gamma-ray sources have soft spectra in the energy above 30 GeV, and such spectra arise contamination of lower energy events as mentioned in §5.5.3.

The raw deposited energy As mentioned in §6.3.4, the quality of the reconstructed energy strongly depends on the event characteristics. Even when the reconstructed energy has large uncertainty, the raw deposited energy in the CAL is a robust measurement of the lowest possible energy of the event, independent from the estimation described in §5.5.3.

Estimation based on MC events with similar reconstruction quality I derived the uncertainty from the distribution of the true energy of the MC gamma-ray events similar in both the

reconstructed energy and the reconstruction quality. I restricted the MC events so that they meet $|P_{BEP}/P_{BEP,target} - 1| < 0.05$ and $|\log(E_{rec}/E_{rec,target})| < 0.1$ where the subscript "target" indicates the GRB event in question, the "rec" indicates reconstructed quantities. I filled these events into a histogram of $\log(E_{true}/E_{rec})$ where E_{true} is the true MC energy. This histogram gives us the information of the IRF effects. It must be noted that the energy uncertainty depends not only on the IRF effects, but also on the true spectral distribution of the gamma-ray source, *i.e.* the GRB, or possibly the background sources. The filled events should be weighted so that they follow the true distribution, but it is unknown. To solve this, I assumed three power-law distributions with the photon index -1, -2 and -3. I calculated the 68% and 95% containment values of E_{true}/E_{rec} for each of the upper and lower side. Then, I obtained the energy uncertainty by multiplying $E_{rec,target}$ by them.

7.4 Results

7.4.1 Detected gamma-like events

Analyzing the data of the 24 GRBs recovered four gamma-like CalOnly events coincident with three GRBs: 090926A, 150902A, and 160509A. Outstandingly, the event related to GRB 090926A has a high gamma-likeness, good spatial agreement and high reconstructed energy in the GRB rest frame. The reconstructed energy is 50 GeV. As the redshift is 2.1062 [158], it is 157 GeV in the GRB-rest frame. In the data of GRB 160509A, I found two CalOnly events coincident with the GRB thousands of seconds after the burst. The reconstructed energy for these events is 116 GeV and 63 GeV. As the redshift is 1.17 [159], they are 252 GeV and 137 GeV in the GRB-rest frame. The prompt emission of these two bursts is remarkably bright in the GBM band [ii], and their afterglow was detected for long times as mentioned in § 7.4.2 and § 7.4.3. The reconstructed energy of the event related to GRB 150902A is 84 GeV, and the redshift of the GRB is unknown. The event class, arrival time, reconstructed energy, angular separation from the GRB, off-axis angle, zenith angle, and energy quality indicator are reported in Table 7.2. In what follows, I focus on the details of the three events related to GRB 090926A and 160509A. I added these photons to Fig. 7.1 and display them in Fig. 7.4.

7.4.2 CalOnly event related to GRB 090926A

Observations

***Fermi* Observatory** GRB 090926A was detected by both of the two detectors of the *Fermi* observatory, the GBM [160] and LAT [161]. The *Fermi*-GBM was triggered at 04:20:26.99 in UTC

[ii] GRB 090926A: the 19th largest fluence, and GRB 160509A: the 14th largest fluence among 2132 bursts in the GBM catalogue [18, 19, 20]

Table 7.2: Characteristics of the CalOnly events correlated with three of the 24 GRBs

Coincidental GRB	0909026A	150902A	160509A	
Event class	CalOnly_R003	CalOnly_R030	CalOnly_R100	CalOnly_R100
Arrival time	$T_0 + 424$ s	$T_0 + 2064$ s	$T_0 + 2057$ s	$T_0 + 5779$ s
Energy	50 GeV	84 GeV	116 GeV	63 GeV
Angular separation	0°.8	3°.6	4°.6	3°.7
cf. PSF68%	1°.7	5°.2	5°.6	5°.0
Off-axis angle	62°	8°.7	9°.9	9°.5
Zenith angle	97°.7	86°.0	77°.9	69°.0
Energy quality	0.824	0.0029	0.0627	0.259
Redshift	2.1062	unknown	1.17	
Energy in GRB-frame	157 GeV	$>$ 84 GeV	252 GeV	137 GeV

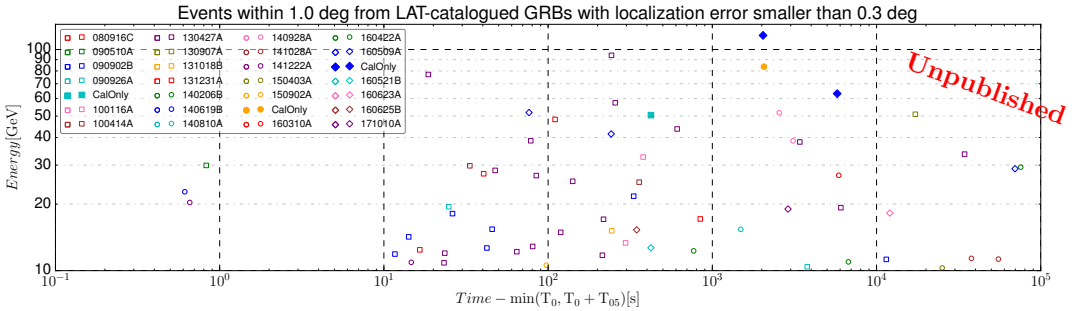

Figure 7.4: CalOnly events spatially and temporally coincident to the GRBs are added to Fig. 7.1. The CalOnly events are represented by the filled markers while the shape and color are same as the counterparts of the standard events. Both the energy and arrival time are observed values and not corrected by the redshift.

on 26 September 2009 (275631628.98 s in MET; hereafter T_0) [19, 18, 20]. The GBM localized the GRB at $(\mathrm{RA}, \mathrm{DEC}) = (354°.5, -64°.2)$ in J2000. The angle of this position with respect to the LAT boresight was 52° at the time of the trigger. An autonomous repoint request was ordered, but the *Fermi* spacecraft did not re-point at the GRB immediately because the Earth avoidance angle condition was not satisfied by the GRB direction [64]. The duration T_{90} of the prompt emission observed by the GBM is 13.760 ± 0.286 s, and its beginning is $T_0 + 2.176$ s [18, 19, 20].

***Neil Gehrels Swift* Observatory** The GRB also triggered the *Swift*-BAT, and *Swift* target-of-opportunity observations were carried out [162]. The XRT [162] and UVOT [163] detected the afterglow. In the end, the GRB position was localized at $(\mathrm{RA}, \mathrm{DEC}) = (353°.400154, -66°.324067)$ by the *Swift*-UVOT with the smallest 90% error radius $0'.11$ [163] among the reported locations, and I refer to these coordinates as the GRB position hereafter. The XRT observed the GRB in photon counting mode from $T_0 + 46.7$ ks for the following three weeks [119]. The light curve exhibited a decaying behavior with some flaring activities [164].

Very Large Telescope Very Large Telescope observations have determined the redshift as $z = 2.1062$ [158], using the X-shooter spectrograph, which covers the wavelength range from the UV to the infrared, namely from 300 to 2500 nm [165].

Characteristics of the event

The CalOnly gamma-ray candidate was detected at $T_0 + 424$ s. The reconstructed energy E is 50 GeV, and the off-axis angle θ is 62°. The effective area of the CalOnly analysis is comparable with the standard P8R2_SOURCE for these values of E and θ (*cf.* § 6.3.5). The angular separation from the catalogue position is $0°.8$, which is about a half of the PSF68% for the values of E and θ, $1°.7$. The event is classified as CalOnly_R003, which is cleanest among the four CalOnly classes. These characteristics are summarized in Table 7.2. The event profile in the LAT is visualized in Fig. 7.6. The high gamma-likeness and spatial agreement to the GRB are clearly outstanding, as visualized in Fig. 7.5. The redshift of GRB 090926A is 2.1062, and the energy in the rest frame is hence 157 GeV.

Background evaluation

I revisit the background components focusing on GRB 090926A and the event class CalOnly_R003.

Cosmic ray The CalOnly_R003 class is constructed so that the residual cosmic-ray rate is about 30% of the irreducible gamma-ray backgrounds, as mentioned in § 6.2. Hence, the cosmic-ray component does not dominate the residual background even if a considerable fraction of it remains.

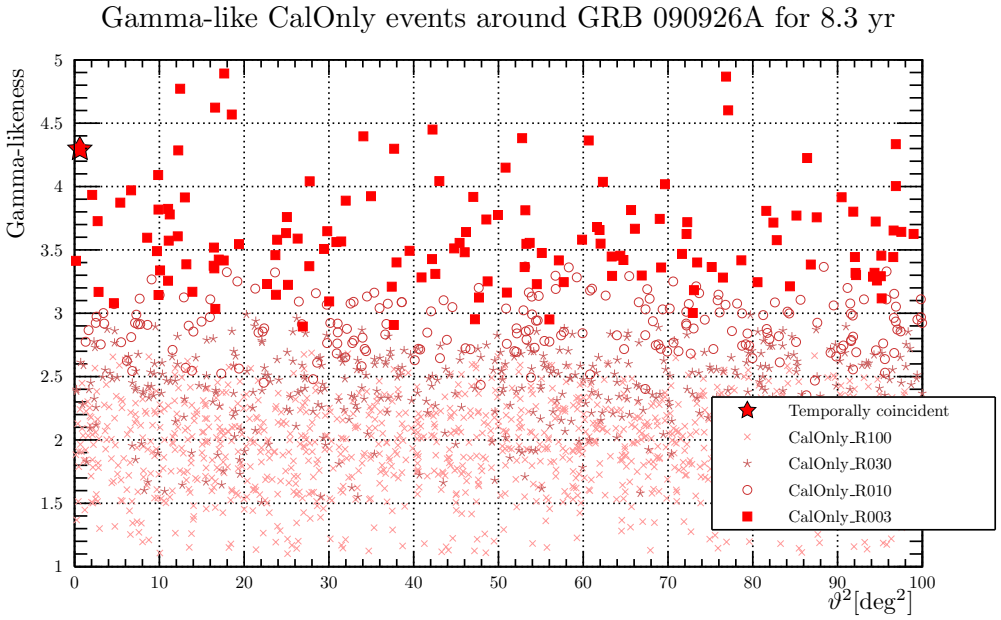

Figure 7.5: Gamma-likeness vs. ϑ^2 of the CalOnly events where ϑ is the angular separation of the event arrival direction from the catalogue position of GRB 090926A [55]. The time window is the same as the OFF data explained in the text, and for 8.3 years ($\sim 2.6 \times 10^8$ s). The event which was temporally coincident to the GRB is highlighted by a star.

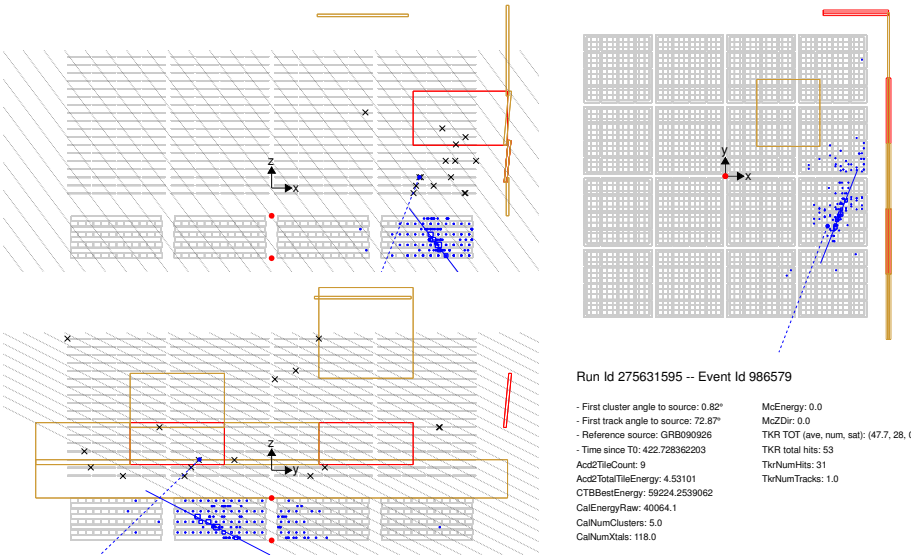

Figure 7.6: Event display of the CalOnly event related to GRB 090926A. The black crosses represent the SSD hits in the TKR. The blue squares represent the energy deposition in the CAL. The size is proportional to the square of the energy deposited.The blue solid line represents the reconstructed shower axis in the CAL. The blue dashed line represents a track candidate in the TKR. The red and orange rectangles are fired ACDs. The red ones were significantly fired whereas the signals of the yellow ones were lower than the predicted signal of the minimum ionization particle. The gray tilted lines indicate the direction of GRB 090926A taken from the online LAT-GRB catalogue.

Nearby VHE gamma-ray sources Only one 2FHL source is located within ten degrees from the CalOnly event, 1RXS J005117.7-624154. The distances from the GRB and CalOnly event are 9°.06 and 8°.44 respectively. Another 2FHL source, 2FHL J2352.0-7558 locates at 9°.75 from the GRB. They are sufficiently distant compared to the CalOnly_R003 PSF95%, 3°.13 as plotted in Fig. 7.7.

Extra-galactic gamma-ray background (EGB) This is the most important component in this case because we applied the tightest cut for the cosmic-ray component.

Local diffuse gamma ray The GRB was located at $(l, b) = (214°.926, -69°.361)$ in the Galactic coordinate. It is far away from the Galactic plane, therefore the contribution of Galactic diffuse is expected to be small.

Earth-limb gamma ray The zenith angle of the event $\theta_Z = 97°.7$ is close to the Earth-limb cut $\theta_Z = 100°$. I kept taking the Earth-limb component into account although the contamination probability is expected to be small thanks to the narrow PSF 1°.8 (68%) and 4°.0 (95%).

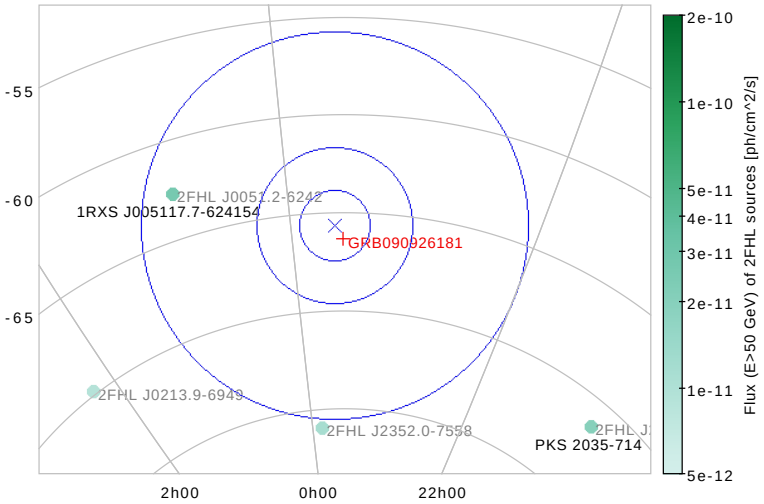

Figure 7.7: Red plus represents the sky position of GRB 090926A. The blue cross shows the reconstructed direction of the CalOnly event. The greenish points are nearby 2FHL sources and the color dense indicates the log-scaled flux values above 50 GeV, which are taken from the 2FHL catalogue [155]. The radii of the red circles are 1°.7 (PSF 68%), 4°.0 (PSF 95%), and 10°; the centers are at the GRB position.

Background coincidence probability

The predicted background count based on the high-b OFF turned out to be $(1.7 \pm 0.2) \times 10^{-4}$ where the error is only statistical. The standard analysis stated the predicted counts of the isotropic

and the galactic components above 22 GeV are 149 and 37.5 counts, respectively, for $\sim 2.6 \times 10^8$ s within five degrees from the GRB. The amount of the local diffuse is estimated as about 25% of the isotropic component. Adding this fraction, I concluded that the predicted background count is $(2.1 \pm 0.3) \times 10^{-4}$. Provided the Poisson distribution, this number means the probability that one or more background coincidences happened in the ON data equals 0.021%.

Energy uncertainty

The quality indicator $P_{BEP} = 0.824$ for the CalOnly event. The value of P_{BEP} ranges from zero to one, and thus the energy of the GRB event was relatively well reconstructed. I plot in Fig. 7.8 the distributions of $\log(E_{true}/E_{rec})$ of the MC gamma events with similar energy and P_{BEP}. The raw deposited energy is 40.0 GeV. The true energy is without doubt higher than it, regardless of the evaluation above. The 68% and 95% intervals are $50.5^{+2.7}_{-1.8}$ GeV and $50.5^{+8.5}_{-4.4}$ GeV respectively if the power-law index of the true photon spectrum is -2. The final numbers of the energy uncertainty are summarized in Table 7.3.

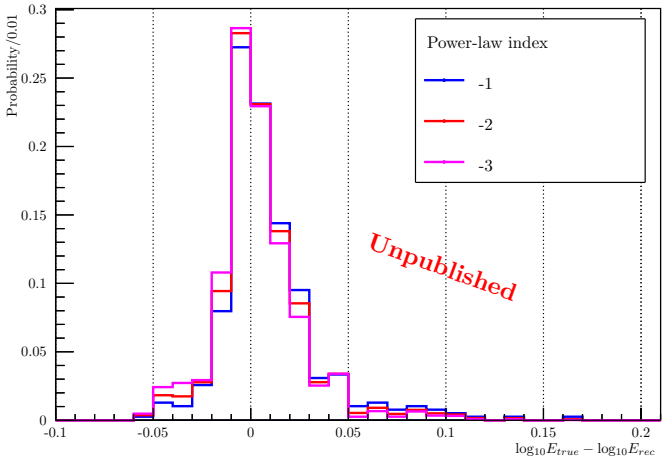

Figure 7.8: Probability density functions of the true energy of MC events with $|\log_{10}(E_{rec}/\mathrm{MeV}) - 4.70| < 0.1$ and $|P_{BEP}/0.824 - 1| < 0.05$. Three cases of the true source spectrum are assumed; $dN_\gamma/dE_{true} \propto E_{true}^{-1}$ (blue), $\propto E_{true}^{-2}$ (red), and $\propto E_{true}^{-3}$ (magenta).

7.4.3 CalOnly events related to GRB 160509A

Observations

***Fermi* Observatory** GRB 160509A was detected by both the *Fermi*-LAT [166] and GBM [167]. The GBM was triggered at 08:58:46.219 in UTC on 9 May 2016 (484477130.219 s in MET; hereafter

Table 7.3: Energy uncertainty of the CalOnly event at $T_0 + 423$ s. The lower/upper limits of the reconstructed energy 50 GeV were quantified in the unit of GeV for three cases, with different power-law indices of the assumed true spectra.

Containment	68%		95%	
Limits	Lower	Upper	Lower	Upper
$dN_\gamma/dE_{true} \propto E_{true}^{-1}$	48.7	53.2	46.4	60.8
$dN_\gamma/dE_{true} \propto E_{true}^{-2}$	48.7	52.9	46.1	59.0
$dN_\gamma/dE_{true} \propto E_{true}^{-3}$	48.6	52.8	45.7	57.8

T_0) [19, 18, 20]. The GRB position was (RA, DEC) = (311°.75371, 76°.108033) according to the LAT burst catalogue [55]. The prompt emission consisted of two episodes, from $T_0 + 0$ to 40 s and from $T_0 + 280$ to 420 s, separated by a quiescent period [69]. The duration T_{90} for the entire emission is 369.7 ± 0.8 s [18, 19, 20].

***Neil Gehrels Swift* Observatory** The *Swift* observatory started observations at T_0 + 7 ks. The XRT detected the afterglow [168]. The UVOT provided only the upper limits [169].

Gemini North Follow-up observations with the Gemini North Telescope started about 28 hours after the burst [159]. Optical spectroscopy and near-infrared imaging were carried out. The spectroscopy of a detected emission line and determined the redshift as $z = 1.17$.

I analyzed the two events related to GRB 160509A together, because the same OFF data set was usable for them.

Characteristics of the events

The first CalOnly gamma-ray candidate was detected at $T_0 + 2057$ s. The reconstructed energy E is 116 GeV, the off-axis angle θ is 9°.9. The effective area of the CalOnly class is less than one fifth of the standard P8R2_SOURCE for this angle and energy (*cf.* § 6.3.5). The angular separation from the catalogue position is 4°.6, which is smaller than the PSF68% for the values of E and θ, 5°.6. The event is classified as CalOnly_R100, the largest one among the four CalOnly classes. These are summarized in Table 7.2. The event profile is visualized in Fig. 7.10.

The second CalOnly event was detected at $T_0 + 5779$ s. The reconstructed energy is 63 GeV, and the off-axis angle of this event is 9°.5. The angular separation from the catalogue position is 3°.7, which is smaller than the PSF68% for this energy and event, 5°.0. The event is classified as CalOnly_R100. These are summarized in Table 7.2. The event profile is visualized in Fig. 7.11.

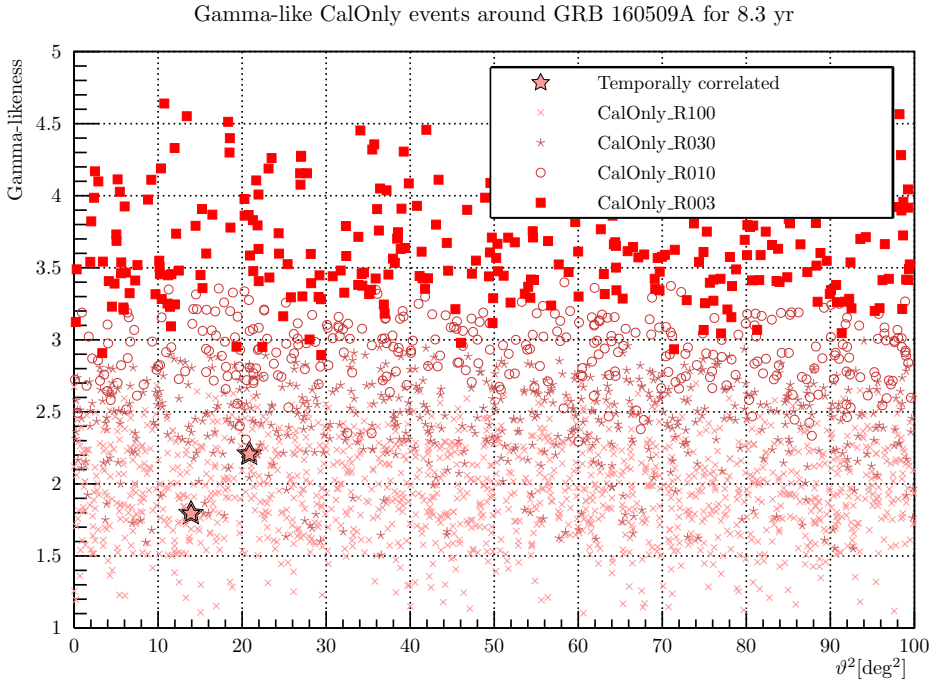

Figure 7.9: Gamma-likeness vs. ϑ^2 of the CalOnly events where ϑ is the angular separation between the events and the catalogue position of the GRB 160509A [55]. The time window is the same as the OFF data explained in the text, and it is for 8.3 years ($\sim 2.6 \times 10^8$ s). The events which are temporally coincident with the GRB are highlighted by stars.

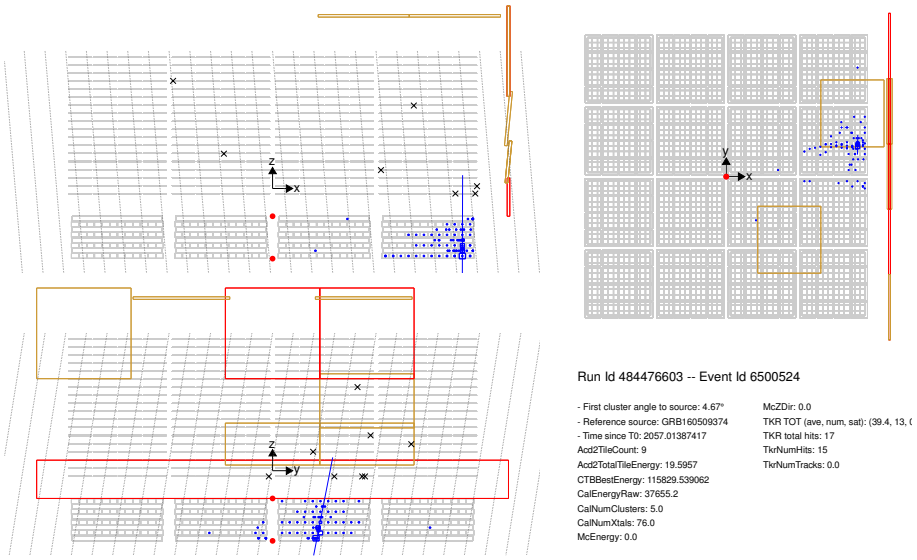

Figure 7.10: Event display of the CalOnly photon candidate detected 2056.8 sec after T_0. The symbols are the same as Fig. 7.6

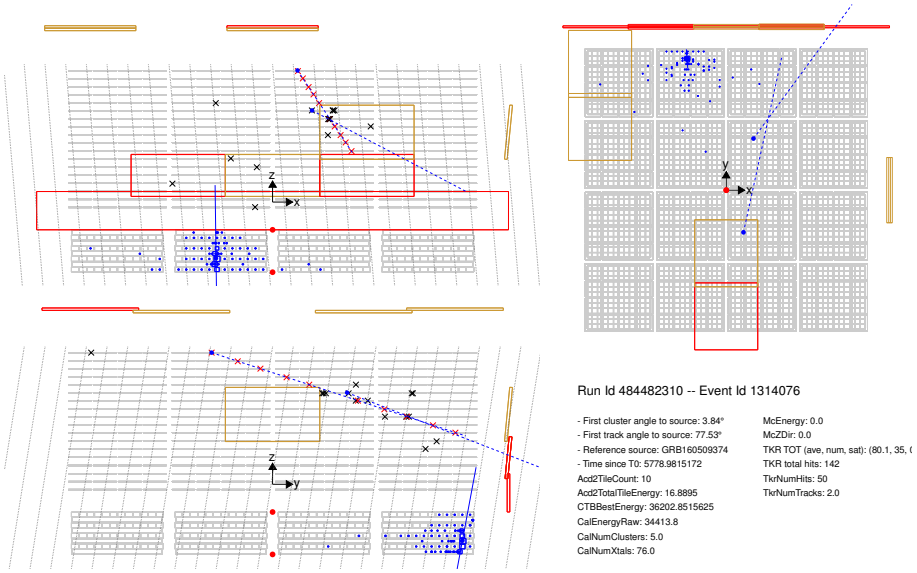

Figure 7.11: Event display of the CalOnly photon candidate detected 5778.8 sec after T_0. The symbols are the same as Fig. 7.6.

The gamma-likeness and angular separation are plotted in Fig. 7.9. Although they are not outstanding in it, but the temporal agreement to the burst suppresses the backgrounds. The characteristics of the burst are described in § 7.4.3.

Background evaluation

For the combination of GRB 160509A and the event class CalOnly_R100, the background components were evaluated like the following.

Cosmic ray CalOnly_R100 corresponds to a relatively loose cut on cosmic rays with respect to the gamma-ray backgrounds. Hence, the cosmic-ray component is anticipated to occupy the largest fraction of the residual background.

Nearby VHE gamma-ray sources There is one bright nearby VHE gamma-ray source, 1ES1959+650. The angular distance is $11^\circ.5$ from the GRB and $15^\circ.6$ from the reconstructed direction of the first event. Although 1ES1959+650 was active around that moment [170], I concluded the contribution is still negligible. The details are reported in Appendix C.

Extra-galactic gamma-ray background (EGB) The contribution of the EGB is relatively small because the rate of the residual cosmic rays is ten times higher than the EGB rate.

Local diffuse gamma ray The GRB is located at $(l, b) = (110^\circ.0, b = 19^\circ.84)$ in the Galactic coordinates, and thus the contribution of Galactic diffuse is not negligible.

Earth-limb gamma ray Although the event zenith angles $\theta_Z = 78^\circ$ and 69° are far from the Earth-limb cut $\theta_Z = 100^\circ$, the Earthlimb background is taken into account.

Background coincidence probability

The predicted background counts above 22 GeV based on the high-b OFF and on the GRB-location OFF turned out to be $(6.3 \pm 0.5) \times 10^{-2}$ and $(6.8 \pm 0.4) \times 10^{-2}$ respectively. The two numbers are consistent. These similar results suggest that the main component of the background is common, namely, the residual cosmic rays. The Poisson probability that a coincidence of one or more backgrounds happened in the whole time window up to T_0 +100 ks is 6.1% and 6.6%. These numbers are relatively conservative as mentioned in § 7.3.2. The predicted background for some different energy thresholds and time windows are elucidated in Table 7.4. If the highest energy threshold and the shortest time window which includes the first CalOnly event in the table is used, the predicted background is 0.013 ± 0.001 (high-b OFF) and 0.014 ± 0.001 (GRB-location OFF). The probability that a coincidence of two or more backgrounds happened in the whole time window up to T_0 +100 ks is 0.19% (high-b OFF) and 0.20% (GRB-location OFF).

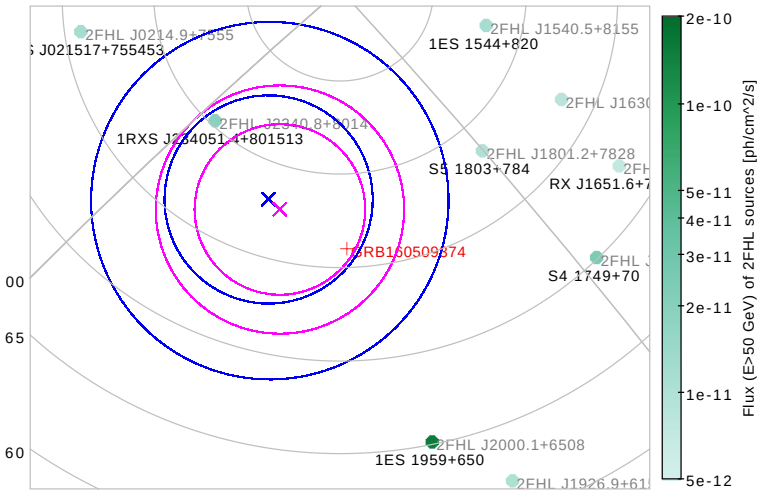

Figure 7.12: Sky positions of GRB 160509A and nearby 2FHL sources. The radii of the blue circles are PSF 68% (5°.6) and PSF 95% (9°.7) of the first CalOnly event. The radii of the magenta circles are PSF 68% (4°.6) and PSF 95% (6°.7) of the second CalOnly event. The other symbols are the same as Fig. 7.7.

Table 7.4: Dependence of the expected background count on the energy threshold. The energy threshold 22 GeV is the lower limit of the CalOnly IRFs. $T_0 + 2524$ s is the time the GRB was occulted by Earth for the first time after the burst.

Time window	from T_0 to T_0 +2524 s		from T_0 to T_0 +10000 s	
OFF data	high-b	GRB-location	high-b	GRB-location
$E > 22$GeV	0.027 ± 0.002	0.031 ± 0.002	0.063 ± 0.005	0.068 ± 0.004
$E > 50$GeV	0.023 ± 0.001	0.025 ± 0.002	0.054 ± 0.004	0.057 ± 0.004
$E > 100$GeV	0.013 ± 0.001	0.014 ± 0.001	0.032 ± 0.004	0.031 ± 0.003

Energy uncertainty

The first CalOnly event The energy quality indicator is $P_{BEP} = 0.0627$, and it is relatively bad. The raw deposited energy is 37.7 GeV. The 68% and 95% intervals are 116^{+18}_{-13} GeV and 116^{+61}_{-26} GeV, respectively if the power-law index of the true photon spectrum is -2. The numbers in the case of -1 and -3 are documented in Table 7.5. The probability distributions are plotted in Fig. 7.13.

Table 7.5: Energy uncertainty of the CalOnly event at 2057 s. The lower/upper limits of the reconstructed energy (115.8 GeV) are presented in the unit of GeV for three cases, with different power-law indices of the assumed true photon spectra.

Containment	68%		95%	
Limits	Lower	Upper	Lower	Upper
$dN_\gamma/dE_{true} \propto E_{true}^{-1}$	105	158	92.4	296
$dN_\gamma/dE_{true} \propto E_{true}^{-2}$	103	134	90.1	176
$dN_\gamma/dE_{true} \propto E_{true}^{-3}$	102	129	87.9	157

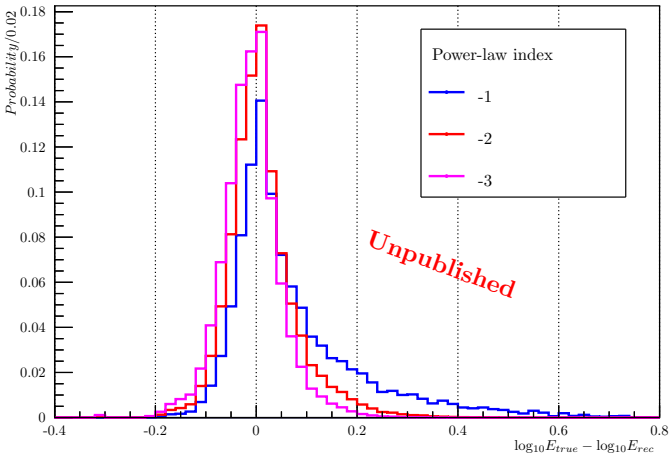

Figure 7.13: Probability density function of the true energy of events with $|\log_{10}(E_{rec}/\mathrm{MeV}) - 5.06| < 0.1$ and $|P_{BEP}/0.063 - 1| < 0.05$. Three cases of the true source spectrum are assumed; $dN_\gamma/dE_{true} \propto E_{true}^{-1}$ (blue), $\propto E_{true}^{-2}$ (red), and $\propto E_{true}^{-3}$ (magenta).

The second CalOnly event The quality indicator was $P_{BEP} = 0.259$. The raw deposited energy is 34.4 GeV. The 68% and 95% intervals are 63^{+5}_{-4} GeV and 63^{+16}_{-9} GeV, respectively if the power-law index of the true photon spectrum is -2. The numbers in the case of -1 and -3 are documented in Table 7.6.

Table 7.6: Energy uncertainty of the CalOnly event at 5759 s. The lower/upper limits of the reconstructed energy (63.2 GeV) are presented in the unit of GeV for three cases, with different power-law indices of the assumed true photon spectra.

Containment	68%		95%	
Limits	Lower	Upper	Lower	Upper
$N_\gamma \propto E_{true}^{-1}$	59.9	69.4	54.9	92.5
$N_\gamma \propto E_{true}^{-2}$	59.6	67.9	54.2	79.3
$N_\gamma \propto E_{true}^{-3}$	59.3	67.0	53.7	75.5

Chapter 8

Likelihood analyses

In the previous chapters, it has been elucidated that the spectra of some GRBs extend to the energy range above tens of GeV. In this chapter, I report a detailed likelihood study of the two GRBs with the CalOnly events, 090926A and 160509A for two purposes. One is clarifying whether their spectral and temporal features are consistent with the model of the synchrotron emission from external forward shocks. The other one is deriving the statistical significance that the afterglow spectra extend beyond the synchrotron energy limit. The study consists of two analyses. One is for time-resolved data, and I constrained the spectral indices via a spectral likelihood analysis. In the other one, I jointed the likelihood value in each time bin in order to constrain the combinations of the spectral and temporal indices.

8.1 Data selection

I skimmed the data of GRB 090926A and 160509A by the conditions below.

Time window

I used the data from T_0 to $T_0 + 100\,\mathrm{ks}$ for each GRB.

Photon class

I selected the P8R2_SOURCE_V6 class events as recommended in the case of a point-source observation for longer than 200 s.

Energy range

I defined four energy ranges and performed analyses for them independently. The energy ranges are named "entire-E", "low-E", "middle-E", and "high-E" energy range. Their definitions are

documented in Table 8.1. The upper bounds of the entire-E and the high-E, E_{ceil} was selected from logarithmic quartiles of each energy decade so that the maximum photon energy was included. It is 100 GeV for GRB 090926A and 178 GeV for 160509A. The lower bounds of the entire-E and the low-E depends on the maximum zenith angle. This is explained next.

Event zenith angle

I excluded the events with zenith angles above 90° as recommended. In spite of that, I recovered those events under three conditions in order to increase the statistics. The criteria are 1) the recovery was only for periods when the GRB was positioned in a zenith angle range from 90°to 100°, 2) the period must be considerably long compared to the elapsed time from T_0, and 3) the zenith cut at 100° and the energy threshold of 0.316 GeV were applied for each event. The higher energy threshold enables us to recover events with $90° < \theta_Z < 100°$ because the spatial spread from the Earthlimb shrinks. I decreased the radius of the RoI from twelve degrees to six degrees. The RoI-based cut was disabled so that a part of the data was kept even if the GRB was close to the Earthlimb.

GRB off-axis angle

I excluded the periods when the off-axis angle of the GRB to the boresight axis of the telescope was larger than 65° in order to avoid a big discrepancy between the nominal time window and the time range which effectively contributed to the observation. I prevented such a discrepancy in order to configure reasonable time bins. The time binning is described in § 8.2.1.

Table 8.1: Definitions of the energy ranges for the stacking analysis, the radius of the RoI, and the cut on the zenith angle for each range

Energy ranges	Entire-E		Low-E		Middle-E	High-E
Minimum E	0.1 GeV	0.316 GeV	0.1 GeV	0.316 GeV	1 GeV	10 GeV
Maximum E	E_{ceil} [a]		1 GeV		10 GeV	E_{ceil}
r_{ROI}	12°	6°	12°	6°	3°	1°
Maximum θ_Z	90°	100°	90°	100°	100°	100°

[a] 100 GeV for GRB 090926A and 178 GeV for GRB 160509A.

8.1.1 Calorimeter-only data

On top of the standard data, I utilized the CalOnly_R100 data. The RoI is the PSF68% of CalOnly_R100 at each energy value. The time window is identical to the standard one, from T_0 to T_0 +100 ks. The CalOnly data from T_0 +10 ks to T_0 +100 ks were used only for the likelihood analyses, and not for discussing individual events because the predicted background count was

anticipated to be comparable to unity.

8.2 Methods

8.2.1 Time binning

I divided the data by the following procedures for the time-resolved and time-joint analyses. Here I use notations of T_{05} and T_{75}. T_{05} and T_{75} are the time at which 5% and 75% of the total fluence has been detected in the GBM band, respectively. T_{05} is provided in the GBM online catalogue [18, 19, 20], and T_{75} is derived from the values in the catalogue.

1. I excluded time intervals when the off-axis angle and the zenith angle of the GRB was above 100°and above 65°, respectively, from the time window. After that, the data set consists of multiple periods segmented by the Earth occultation and exiting from the FoV.

2. The first bin was defined as from T_0 to T_{05}.

3. A time range from T_{05} to T_{75} was divided into multiple bins so that each bin had a certain number of events more events within 12°from the GRB. This number is twelve for GRB 090926A and eight for GRB 160509A.

4. For the remaining periods, I defined a function $f(t) = t^{-0.5 \log_{10} 2} \approx t^{-1.15}$ where t is the time from T_0, and divided the data so that the time intervals were equivalent in the space of $f(t)$. While the logarithmic binning provides a equivalent count in each bin for a light curve decaying $\propto t^{-1}$, this binning does it for $\propto t^{-0.5 \log_{10} 2 - 1}$. The absolute duration was normalized so that a time range from 10 ks to 100 ks would have been divided into two bins if they had not been interrupted by the Earth occultation or exiting from the FoV. This leads to that a time range from 100 s to 1 ks would be divided into four bins, and another one from 1 ks to 10 ks would be divided into three bins. This function was used as below. First, I calculated the normalized number of the time bins which were given by substituting the beginning and the end of each period to the above formula. Generally, the bin number is not an integer. Next, if the bin number was larger than one, I rounded off the number and divided the period into this number of bins equivalently in the space of $f(t)$. Early periods after T_{75} were included in this group. Finally, the remaining periods were combined into one. I calculated the bin number for the combined period, and rounded off it. The period was divided into this number of bins equivalently in the space of $f(t)$. Late periods were arranged like this.

8.2.2 Gamma-ray burst model

Likelihood analysis needs a certain model of the source. For the time-resolved analysis, I defined the source model as a spectral function whose independent variable is the energy. The function

has two free parameters, namely, the normalization factor and spectral index. On the other hand, for the time-joint analysis, the independent variable of the model is not only the energy, but also the time because of the following reason. The external shock models predict a temporal decay of the GRB flux as mentioned in § 4.6.1. Model spectra must be, however, functions of only the energy in each likelihood process. A usual strategy for constraining the spectral and the temporal behavior is to fit a time-evolution curve, which is produced by independent spectral analyses, of a certain representative flux quantity. This approach confuses the correlation between the spectral and temporal characteristics. For disentangling the coupling of them, I introduced a model which described not only the spectrum but also the temporal behavior. I defined a common normalization factor at a certain time and scaled the normalization factor in each time bin by the temporal model.

In addition, I introduce a model with a spectral exponential cutoff which decays by time for inspecting the existence of the synchrotron limit. The cutoff energy is fixed to a constant which is expected with Eq 2.29 and 4.13 in each time bin. This is a simple model which is expected by the synchrotron emission from the decelerated jets. I compare the likelihood the model with that of the simple power-law model only with the EBL cutoff. The latter model does not assume a specific emission mechanism, but it is consistent with the IC component which is not distorted by the Klein-Nishina effect.

Power-law model

Spectral model The source is treated as if it is constant in each time bin. Therefore, the source model is described by a function of only the energy. The functional form was assumed to be a power-law. It is natural because the emissions in the LAT band seems to be non-thermal. I used Eq. 8.1, which is an "integral" expression of the power-law with an EBL-attenuation factor.

$$\frac{dN(E)}{dE} = \mathrm{e}^{-\tau(E,z)} \frac{N(\Gamma_\gamma + 1)E^{\Gamma_\gamma}}{{\mathrm{E_{max}}}^{\Gamma_\gamma+1} - {\mathrm{E_{min}}}^{\Gamma_\gamma+1}} \tag{8.1}$$

where dN/dE: the differential photon flux at energy E, N: the normalization factor, which corresponds to the integral flux, Γ_γ: the constant power-law index, $\mathrm{E_{max}}(\mathrm{E_{min}})$: the upper (lower) limit of the energy range, respectively, and τ: the optical depth of the source as a function of E and the redshift z. I used an EBL model given by Franceschini *et al.* published in 2008 [171]. This formula is implemented in *ScienceTools* as "EblAtten::PowerLaw2". It has two free parameters N and Γ_γ if the source redshift is known.

Temporal model For the time-joint analysis, the spectral model in the i-th time bin is

$$\frac{dN_i(E)}{dE} = \mathrm{e}^{-\tau(E,z)} \frac{N_i(\Gamma_\gamma + 1)E^{\Gamma_\gamma}}{{\mathrm{E_{max}}}^{\Gamma_\gamma+1} - {\mathrm{E_{min}}}^{\Gamma_\gamma+1}} \tag{8.2}$$

where the normalization constant N_i depends on the common normalization factor N_0 and a temporal power-law index α. I defined N_0 as the integral flux at a certain time, which is $\mathrm{T}_0 + 100$ s in the present thesis. The external shock models predict a power-law temporal decay of the GRB flux as long as the cooling-regime does not change and the observation band is included in one spectral segment. Therefore, I provided N_i by a power-law function of time. For each time bin, I calculated the barycentric time by weighting with $(t - \mathrm{T}_0)^{-\alpha}$. The observational gaps were not taken into account, in other words, the barycentric time was determined only by the beginning and end time for simplicity. N_i was decided for each of the barycentric times t_i as

$$N_i = N_0 \left(\frac{t_i - T_0}{100\,\mathrm{s}} \right)^{-\alpha}. \tag{8.3}$$

Exponential cutoff model

The spectral model for the synchrotron cutoff is defined as below:

$$\frac{dN_j(E)}{dE} = \mathrm{e}^{-\tau(E,z)} N_j \times \begin{cases} \left(\frac{E}{\mathrm{E}_0}\right)^{\Gamma_\gamma} & E \leq C_j \\ \left(\frac{E}{\mathrm{E}_0}\right)^{\Gamma_\gamma} \mathrm{e}^{-(E-C_j)/C_j} & E > C_j \end{cases} \tag{8.4}$$

where E_0 is the scaling energy, which is fixed, N_j is the normalization factor, which corresponds to the differential flux at E_0 and is scaled as the same as Eq. 8.3, and C_j is the cutoff energy, which depends on the time bins. Based on Eq. 2.29 and 4.13, the C_j in each bin is determined as

$$C_j = 50\mathrm{MeV} \times 55 \left(\frac{\xi E_{prompt}}{10^{53}\mathrm{erg}} \right)^{1/8} \left(\frac{n_1}{\mathrm{cm}^3} \right)^{-1/8} \left(\frac{t_j - \mathrm{T}_0}{1000\,\mathrm{s}} \right) (1+z)^{-5/8} \tag{8.5}$$

where E_{prompt} is the isotropic-equivalent energy of the prompt emission, ξ is the efficiency of the prompt energy release, n_1 is the proton number density of the CBM, and t_j is the beginning time of each time bin. I use $E_{prompt} = 1.89 \times 10^{54}$ erg [119] for GRB 090926A and $E_{prompt} = 5.76 \times 10^{53}$ [172] for GRB 160509A. I assume $\xi = 0.01$ and $n_1 = 10^{-3}\,\mathrm{cm}^{-3}$ for a conservative limit. This limit is discussed in § 9.2.1 and § 9.2.2 again.

8.2.3 Background model

I considered isotropic background, galactic diffuse emission, and sources listed in the 3FGL catalogue [173] as background components.

Isotropic emission The isotropic background includes the EGBs and residual cosmic-rays. The spectral model is provided as a template of the differential flux at each energy point for every photon class and type [174]. The template is from a fit in a sky region with the galactic

latitude $|b| > 30^\circ$. The template is distributed at [174]. In this study, I fixed the intensity of the isotropic component.

Galactic diffuse emission The Galactic diffuse emission, which is including photons from the decay of neutral pions, the bremsstrahlung radiation of electrons and positrons, and the inverse-Compton scattering, is expressed as a spatial and spectral template for every photon class and type [174]. The model is based on a combination of maps for interstellar gas column density and for the inverse-Compton emission in the Galaxy. The details are discussed in [175]. In this study, I freed the normalization of the Galactic diffuse component and fixed the spectral shape.

3FGL sources The sources which are listed in the 3FGL catalogue are included in the model if the angular distance from the circumference of the RoI is smaller than ten degrees. The spectral and spatial shape of each source is taken from the catalogue and fixed. The normalization factors are free.

8.2.4 Likelihood scan

I scanned the likelihood values of the above model with different parameter values. I scanned the 2D parameter plane of N vs. Γ_γ for the time-resolved analyses and the 3D parameter space of N_0 vs. Γ_γ vs. α for the time-joint analyses. The 3D scan was performed for the time bins only after $\mathrm{T}_0 + \mathrm{T}_{90}$. Hereafter I call these time bins the "afterglow phase" of the GRB. Once a point in the parameter space is specified, the corresponding values of the integral photon flux, the integral energy flux, and the specific energy flux are decided. The spectral index Γ_γ was scanned only in the range of $-5 \leq \Gamma_\gamma \leq 2$.

8.2.5 Constraints on the model parameter

I constrained the model parameters with the likelihood maps above. This step was not trivial, especially in the cases when the photon statistics was rather Poissonian than Gaussian. I tried two approaches for these different statistical domains.

d-loglikelihood approach

The first approach is the standard d-loglikelihood method. I applied this method to the time-resolved analyses if the event number was ten or more. In such a case the likelihood values should be asymptotic to χ^2 distribution, and this approach provides a more or less reasonable result. This method was also used for the time-joint analyses.

I handled the standard LAT data as unbinned data. The likelihood values in each time bin were derived with a python module of *ScienceTools*. On the other hand, I implemented the likelihood calculation of the CalOnly data as a binned analysis because the unbinned likelihood calculation was not implemented. The CalOnly data were binned into spatially a single bin and into spectrally multiple bins. The spatial single-bin is identical with the ON region used in § 7. Spectrally, each energy decade was divided into four bins. I calculated the predicted count, which is a sum of the signals and backgrounds in each bin. The predicted signal was calculated by multiplying the model flux by the exposure and the spatial cut efficiency 0.68. The predicted background was taken from the high-b OFF analysis reported in § 7. I derived the likelihood value for the observed count in each bin. The total log-likelihood value is a sum of the logarithmic values in all the standard and CalOnly bins.

Systematic effect In § 6.4.2, I reported the possible systematic misestimation of the CalOnly IRFs based on the data of Mkn 421. Using this result, I evaluated the effect of the systematics on the parameter constraints. First, I take a possible systematic error by fitting the residual histogram, which represents the deviation of the observed CalOnly count from the model based on the standard data and the MC-based CalOnly IRFs, in Fig. 6.16 with a constant for each GRB case. The fitting range should be the radius of the RoI, but it depends on time and event energy. I fixed the fitting range for each GRB so that it is similar to the RoI, namely the PSF68% containment range, when the CalOnly events were found to be correlated with the GRBs (*cf.* the sixth row of Table 7.2). It is because the data with this RoI radius are anticipated to be most effective in the likelihood. For GRB 090926A, the fitting range is from 0°to 1°.7, and the fitted residual values turned out to be $+0.07 \pm 0.10$ where the error is 1σ. For GRB 160509A, the fitting range is from 0°to 5°.1, and the residual is $+0.21 \pm 0.08$. These positive offsets imply the possibility that the CalOnly exposure is underestimated. In order to evaluate the effect of this uncertainty, I performed the same d-loglikelihood analysis using the CalOnly exposure scaled artificially. I defined the scaling factor by adding the offset and 1σ statistical error to unity corresponding to the component expected with MC so that the effect of the systematic uncertainties was conservatively evaluated. It is 1.17 for GRB 090926A and 1.29 for 160509A. The obtained parameter constraints are compared to those with the unscaled exposure. The results are reported in § 8.3.1 and in § 8.3.2.

Likelihood-ratio-ordering approach

In the case of small statistics, assuming the χ^2 distribution is no longer justified. I used the "likelihood-ratio-ordering" approach which was proposed by Feldman and Cousins [176] if the event number of each time-resolved dataset was less than ten. The details are described in Appendix A.2.4. This method eliminates the assumption of a certain distribution such as χ^2 if the data are discrete.

I reshaped the data into a series of the observed count in each energy bin. These counts are summations of the standard events and the CalOnly events. The bin number is four per decade, and four or five in total.

8.2.6 Significance of a spectrum beyond the synchrotron cutoff

I derived the test statistics of a spectrum extending beyond the synchrotron cutoff as below:

$$TS = -2 \ln \left(\frac{L(\text{without cutoff})}{L(\text{with cutoff})} \right), \tag{8.6}$$

where L is the maximized likelihood value with each model. See § A.2.2, too. At the limit of a large number of count, $\sqrt{TS}$ approximates to the number of sigmas of the Gaussian distribution. However, TS cannot be interpreted like that because it is contributed by only few events. Hence, I derived TS as just a rough guide of the significance here.

8.3 Results

8.3.1 GRB 090926A

Highest energy photons

Before reporting the likelihood results, I summarize photons possibly beyond the synchrotron limit. Two standard photons above 10 GeV were found to be correlated to GRB 090926A, a 19 GeV event at $T_0 + 24.8$ s and a 10 GeV event at $T_0 + 3785$ s. The angular separations were $0°.08$ and $0°.04$. The CalOnly gamma-ray candidate was found at $T_0 + 424$ s, and the reconstructed energy was 50 GeV. The angular separation from the catalogue position was $0°.8$, which was about a half of the PSF68% for this energy and event, $1°.7$. The event was classified as CalOnly_R003, which is the cleanest class among the four CalOnly classes.

Light curves

The photon flux and the spectral photon index in each time bin which were determined by the time-resolved analysis are plotted in Fig. 8.1. The energy and arrival time of each event above 100 MeV are also plotted individually.

Constraints on the power-law parameters

I performed the time-joint analysis for the afterglow phase from $T_0 + 22.4$ s to $T_0 + 95.7$ ks. The resultant constraints by the 3D scanning are plotted as three contours in Fig. 8.2. Here I treated the common normalization factor as a nuisance parameter, and projected the 3D confidence region

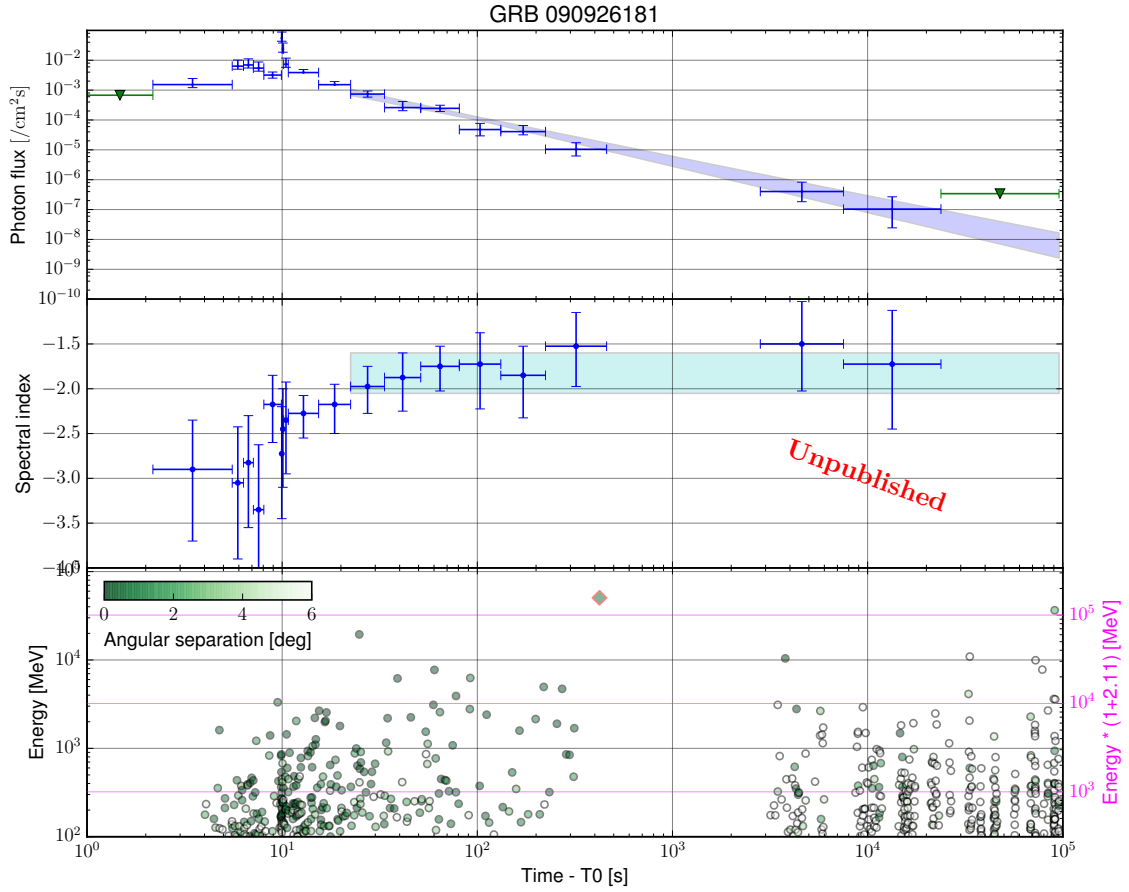

Figure 8.1: Light curves of GRB 090926A from T_0 to T_0 + 100 ks. From top to bottom, the integral photon flux, the spectral power-law index and the energy of each event are displayed. In the top panel, the vertical error bars represent 1σ range allowed by the d-loglikelihood method. The green triangles are the 2σ upper limits. The blue band represents 1σ-allowed values at each time determined by the likelihood scanning described in § 8.2. In the middle spectral index plot, the vertical error bars are 1σ. The cyan band represents 2σ-allowed range of the averaged value determined by the same analysis. The red-edge diamond in the bottom plot indicates the CalOnly event. The color of the circles in the plot represents the angular distance of each event to the GRB. Deep color indicates the reconstructed direction of the event is close to the GRB position. The vertical axis on the right side and magenta grids of the bottom plot indicate the intrinsic energy after correcting the redshift.

to the 2D plane of β vs. α. Every point in the 3D space with any scanned normalization value is included in the projected confidence regions if the joint-likelihood is over the threshold. The 1σ statistical confidence intervals are $\alpha = 1.41 \pm 0.14$ and $\beta = 0.81 \pm 0.14$.

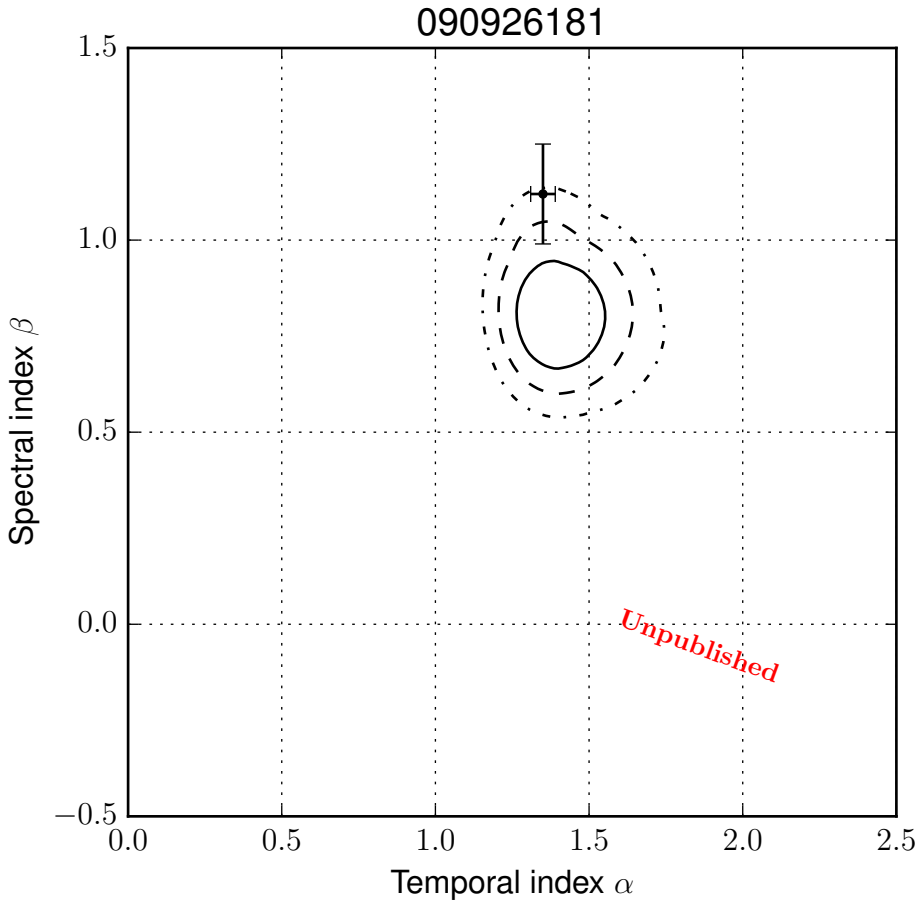

Figure 8.2: Result of the 3D parameter scan of GRB 090926A. The contours represent $1, 2, 3\sigma$ confidence region determined by the time-joint analysis of the LAT afterglow data. They contain all allowed $\beta - \alpha$ combinations with any normalization factors. The black point represents the result of fitting the *Swift*-XRT light curve of [119]. The XRT observations were not simultaneous with the LAT observation. The error bars indicate 68% confidence level uncertainty.

Systematic effect In Fig. 8.3, the results of the 3D scan with the CalOnly exposure evaluated by MC and the one scaled by 1.17 as explained in the paragraph of the systematic effect in § 8.2.5. The 1σ confidence intervals are $\alpha = 1.41 \pm 0.14$ and $\beta = 0.81 \pm 0.14$ for the scaled exposure. *cf.* $\alpha = 1.41 \pm 0.14$ and $\beta = 0.81 \pm 0.14$ for the unscaled exposure. The difference between the

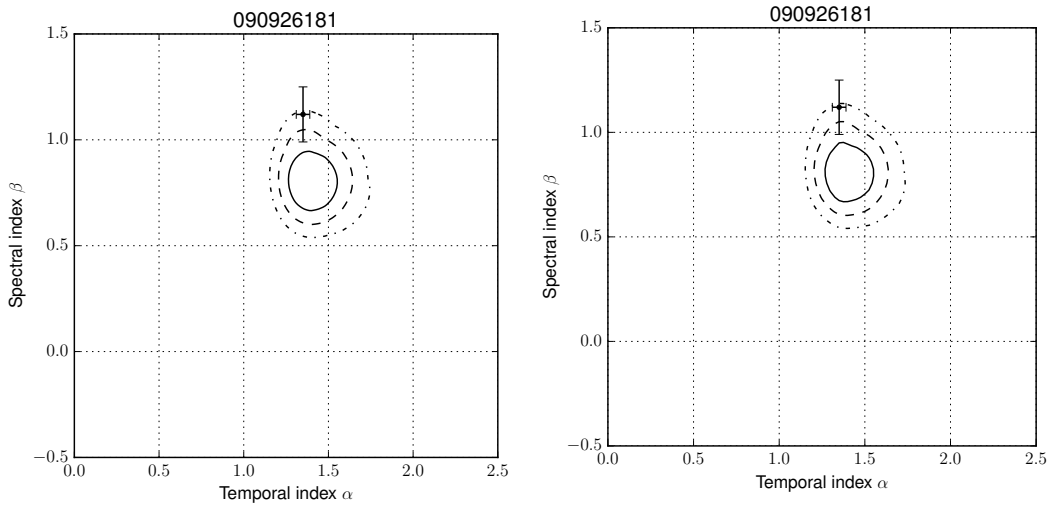

Figure 8.3: Comparison of the β vs. α constraints for evaluating the effect of the systematic uncertainty of the CalOnly effective area. Left: Result of the 3D parameter scan of GRB 090926A with the CalOnly exposure evaluated with MC. This is identical with Fig. 8.2. Right: Result of the 3D parameter scan of GRB 090926A with the CalOnly exposure scaled by 1.17 artificially.

statistical intervals is negligible compared to their widths.

Significance of a component beyond the synchrotron limit

The value of TS turned out to be 6.4. When TS was calculated without adding the CalOnly data, $TS = 1.4$. Hence, the existence of another component is preferred because of the CalOnly data.

Results of observations in X-ray band

In Fig. 8.2, I also plotted the results of the X-ray late-time afterglow observed by the *Swift*-XRT, which was derived by Cenko *et.al.* [119]. It is indicated by a black point with error bars. The authors performed fitting of the X-ray light curve by a single power-law, and obtained $\alpha_X = 1.43 \pm 0.03$ with a reasonable quality, $\chi^2/d.o.f. = 120.8/97$ where $d.o.f.$ is the degrees of freedom. They found a slightly better quality by a broken power-law, $\chi^2/d.o.f. = 111.9/95$. The break time is $t_b = 9.1^{+2.1}_{-1.4}$ days, which equals $7.9^{+1.8}_{-1.2} \times 10^5$ s. The decay indices before and after the break time are $\alpha_{X,1} = 1.35 \pm 0.04$ and $\alpha_{X,2} = 2.6^{+0.9}_{-0.5}$. They fitted the X-ray spectrum by a single power-law and, obtained the spectral index $\beta_X = 1.12 \pm 0.13$, which equals $\Gamma_X = -2.12 \pm 0.13$. I referred to the $\alpha_{X,1}$ and β_X as values for the time interval from $T_0 + 46.7$ ks to $T_0 + 786$ ks ($T_0 + 9.1$ days) in Fig. 9.2. Although fitting of the spectrum was not performed for this time range, I consider the fitting statistics are dominated by the time range up to 9.1 days because the flux rapidly drops after that. The fitting of the optical

data was also reported in [119], but I did not use it in this study because selecting the fitting time range was controversial.

8.3.2 GRB 160509A

Highest energy photons

Three standard photons above 10 GeV were found to be correlated to GRB 160509A, a 52 GeV event at $T_0 + 76.5$ s, a 42 GeV event at $T_0 + 242$ s, and a 29 GeV event at $T_0 + 70$ ks. The angular separations were $0°.34$, $0°.45$, and $0°.04$, respectively. The first CalOnly gamma-ray candidate was detected at T_0 +2057 s and the reconstructed energy was 116^{+43}_{-14} GeV. The second CalOnly event was detected at T_0 + 5779 s and the reconstructed energy was 63^{+10}_{-4} GeV.

Light curves

I performed the time-joint analysis for the afterglow phase from $T_0 + 571$ s to $T_0 + 99.3$ ks. The results of the time-resolved analysis in each time bin are plotted in Fig. 8.4.

Constraints on the power-law parameters

The resultant constraints by the 3D scanning are plotted as contours in Fig. 8.5.The 1σ statistical confidence intervals are $\alpha = 1.03 \pm 0.45$ and $\beta = 0.12 \pm 0.50$.

Systematic effect In Fig. 8.6, the results of the 3D scan with the CalOnly exposure evaluated by MC and the one scaled by 1.29 as explained in the paragraph of the systematic effect in § 8.2.5. The 1σ confidence intervals are $\alpha = 1.02 \pm 0.44$ and $\beta = 0.13 \pm 0.50$ for the scaled exposure. *cf.* $\alpha = 1.03 \pm 0.45$ and $\beta = 0.12 \pm 0.50$ for the unscaled exposure. The difference between the statistical intervals is tens of times smaller than their widths.

Significance of a component beyond the synchrotron limit

The value of TS turned out to be 31.3. When TS was calculated without adding the CalOnly data, $TS = 25.0$.

Results of observations in X-ray band

The black point in Fig. 8.5 are the results of fitting of the *Swift*-XRT data performed by Laskar *et al.* [172]. The count light curve exhibited a break at $\sim 4 \times 10^4$ s. The authors determined the photon spectral indices $\Gamma_{X,1} = 2.01 \pm 0.05$ in the time interval from 7.3×10^3 s to 3.7×10^4 and $\Gamma_{X,2} = 2.12 \pm 0.05$ from 4.3×10^4 s to 1.3×10^6 s. The difference is about 2σ, and the authors concluded that softening is only marginal.

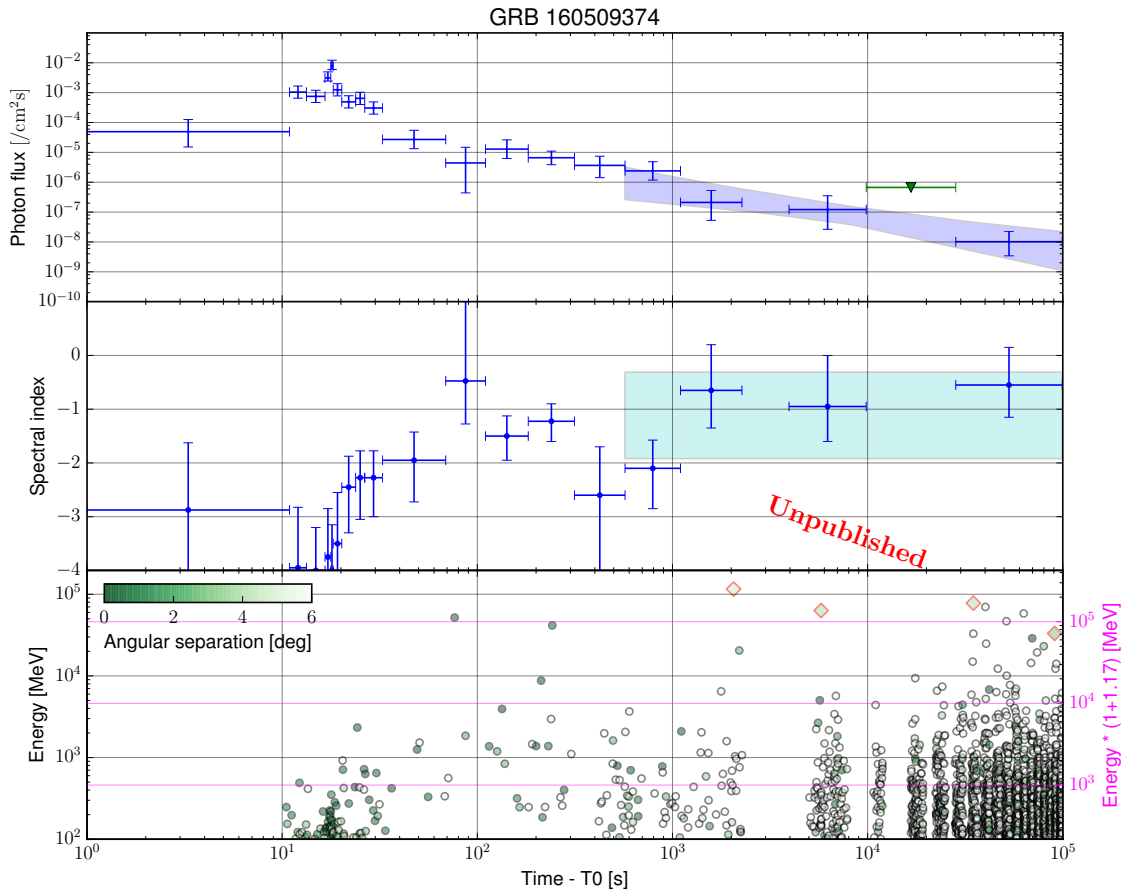

Figure 8.4: Light curves of GRB 160509A from T_0 to T_0 + 100 ks. The symbols are the same as Fig. 8.1.

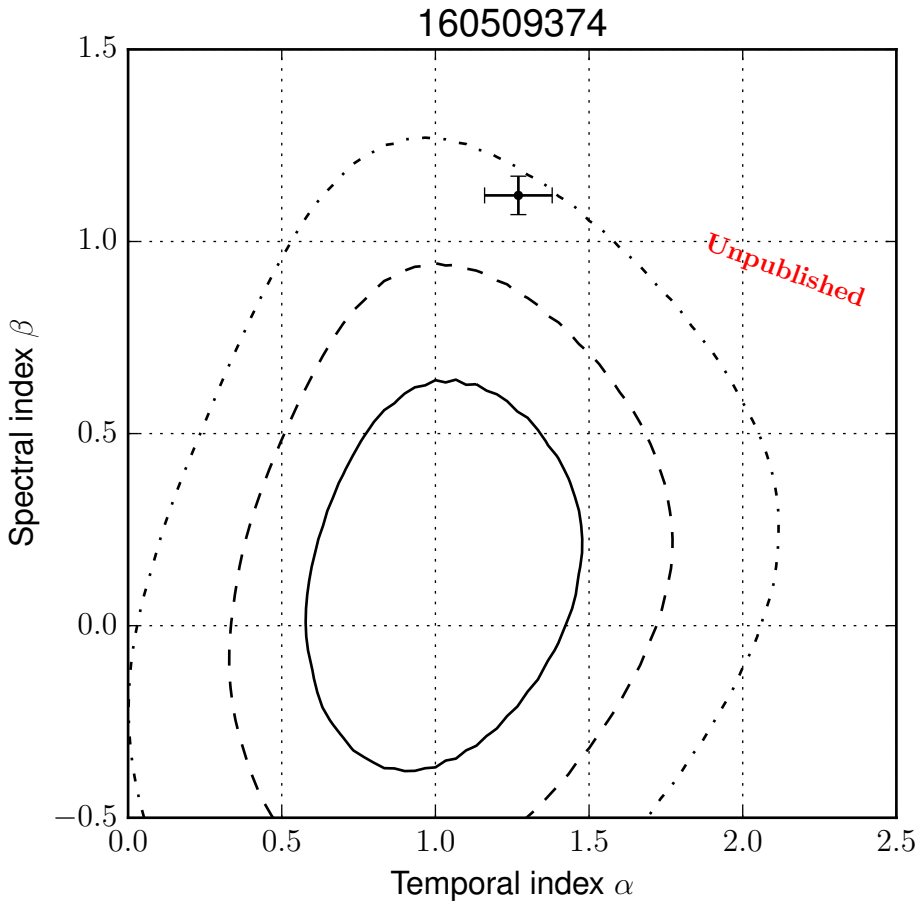

Figure 8.5: Results of the 3D parameter scan of GRB 160509A. The symbols are the same as Fig. 9.2. The contours represent $1, 2, 3\sigma$ confidence region determined by the time-joint analysis of the LAT afterglow data. The black points are from Swift-XRT light curve fitting of [172]. The error bars indicate 68% uncertainty.

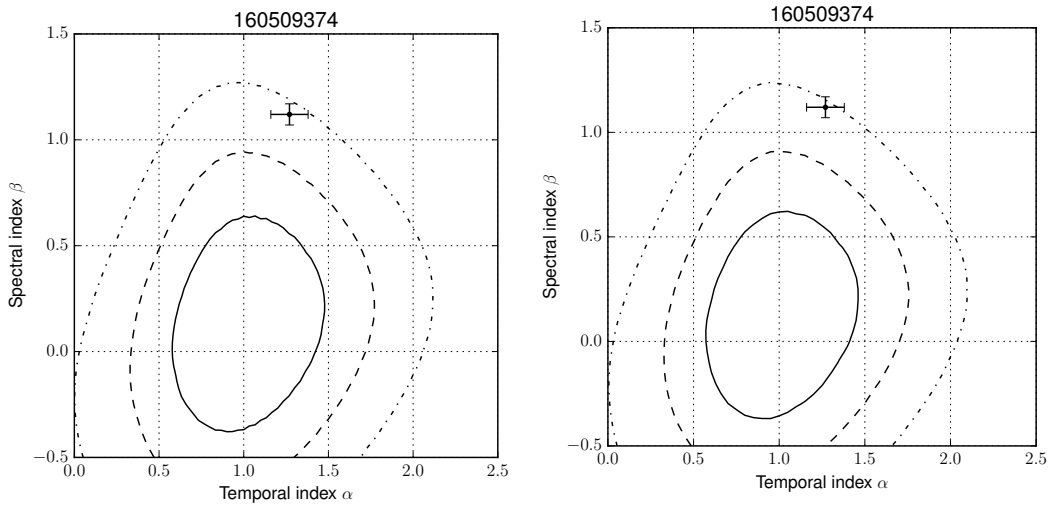

Figure 8.6: Comparison of the β vs. α constraints for evaluating the effect of the systematic uncertainty of the CalOnly effective area. Left: Result of the 3D parameter scan of GRB 160509A with the CalOnly exposure evaluated with MC. This is identical with Fig. 8.5. Right: Result of the 3D parameter scan of GRB 160509A with the CalOnly exposure scaled by 1.29 artificially.

They also performed fitting the light curve by a power-law with two temporal breaks. The first break occurred at $t_{b,1} = 0.37 \pm 0.14$ days, which was equal to $(3.2 \pm 1.2) \times 10^4$ s, and the decline rate steepened from $\alpha_{X,1} = 0.51 \pm 0.12$ to $\alpha_{X,2} = 1.27 \pm 0.11$. At $t_{b,2} = 5.4 \pm 2.3$ days, which was equal to $(4.7 \pm 2.0) \times 10^5$ s, the light curve steepened again to $\alpha_{X,3} = 2.2 \pm 0.3$. For Fig. 8.5, I refer to the combination of $\beta_{X,2} = 1.12 \pm 0.05$, which equals $\Gamma_{X,2} = -2.12 \pm 0.05$, and $\alpha_{X,2} = 1.27 \pm 0.11$.

Comparison of the constraints with/without the CalOnly data

Additionally, I compared the results of the 3D scanning with/without the CalOnly data in Fig. 8.7. Adding the CalOnly data moved the contours to the side of harder spectrum.

Detailed scrutiny of the time-resolved spectra

The photon spectral index Γ_γ turned out to be harder than -2 in three of the five time intervals in the afterglow phase. The indices are plotted in Fig. 8.4 and documented in Table 8.2. Because this is an intriguing result, I report a more careful inspection. In these time intervals, the signal of the GRB in the low energy range is almost lost among the backgrounds. Then, the likelihood analysis is dominated by less than ten high-energy photons in each bin. The statistics are Poisson-like, and the d-loglikelihood method which requires χ^2 assumption is no longer validated in such a situation. I analyzed the time-resolved data in each of the energy ranges, entire-E, low-E, middle-E, and high-E

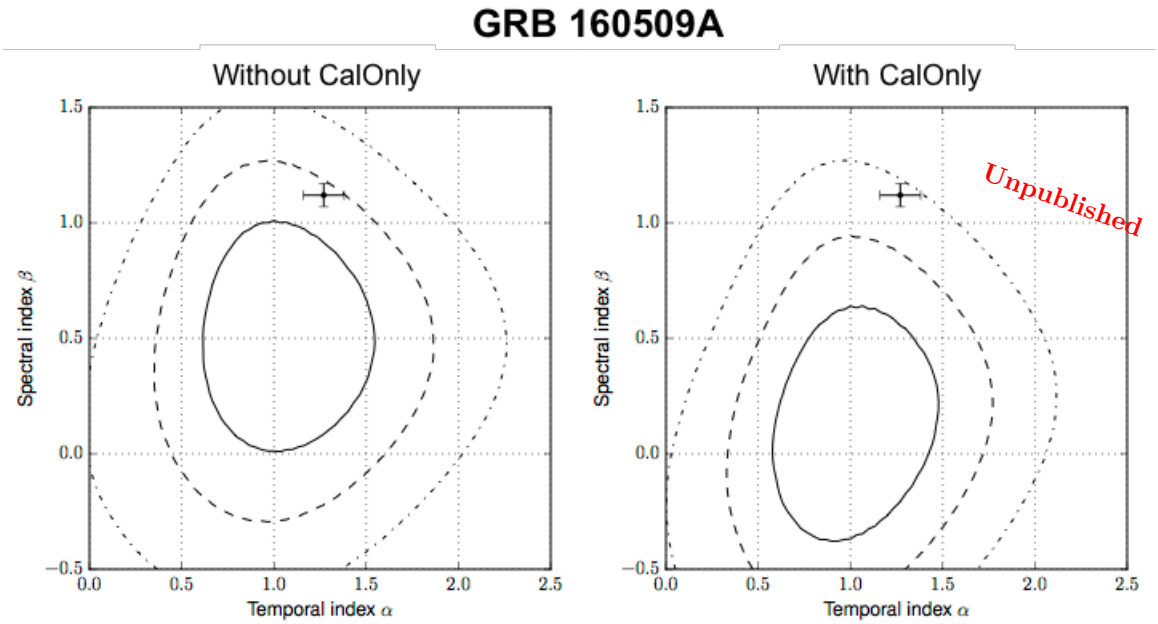

Figure 8.7: Left: the results of the 3D parameter constraining for GRB 160509A without the CalOnly data. Right: the results with the CalOnly data.

independently. I applied the likelihood-ratio ordering if the event number was less than ten. Otherwise, the d-loglikelihood method was used. Here I compare the results and demonstrate the spectral hardness in the three time intervals. The results are displayed in Fig. 8.8, 8.9, and 8.10. In these time ranges, the d-loglikelihood method was used for the entire-E and low-E, and the likelihood-ratio ordering was used for the middle-E and high-E. I constrained the (N, Γ_γ) combinations by 1σ and 2σ in the four energy ranges assuming a power-law spectrum. The differential energy flux values which are provided by these combinations at each energy are indicated in those figures.

Table 8.2: Photon spectral index and 1σ statistical error in five time bins in the afterglow phase of GRB 160509A. The energy range is from 0.1 to 178 GeV.

Bin number	15	16	17	18	19
Time range [ks]	0.57 – 1.1	1.1 – 2.3	4.0 – 9.8	9.8 – 28	28 – 99
Photon spectral index	$-2.1^{+0.5}_{-0.8}$	$-0.7^{+0.9}_{-0.7}$	$-1.0^{+1.0}_{-0.6}$	...[a]	$-0.6^{+0.8}_{-0.6}$

[a]The index in the 18th time bin is omitted because the significance of the GRB is less than 2σ in the bin.

The 16th interval: T_0 +1.0 to 2.3 ks In this time range, the d-loglikelihood analysis yields $\Gamma_\gamma = -0.7^{+0.9}_{-0.7}$ for the entire-E range, and it is plotted as the dense green area in Fig. 8.8. The

thin green area, which represents the 2σ results, does not exclude $\Gamma_\gamma < -2$ by 2σ. However, the 2σ lower limit in the high-E range exceeds the 2σ upper limit in the low-E range. Therefore, any single component softer than $\Gamma_\gamma = -2$ over the energy range from 0.1 GeV to 178 GeV is rejected at 2σ level.

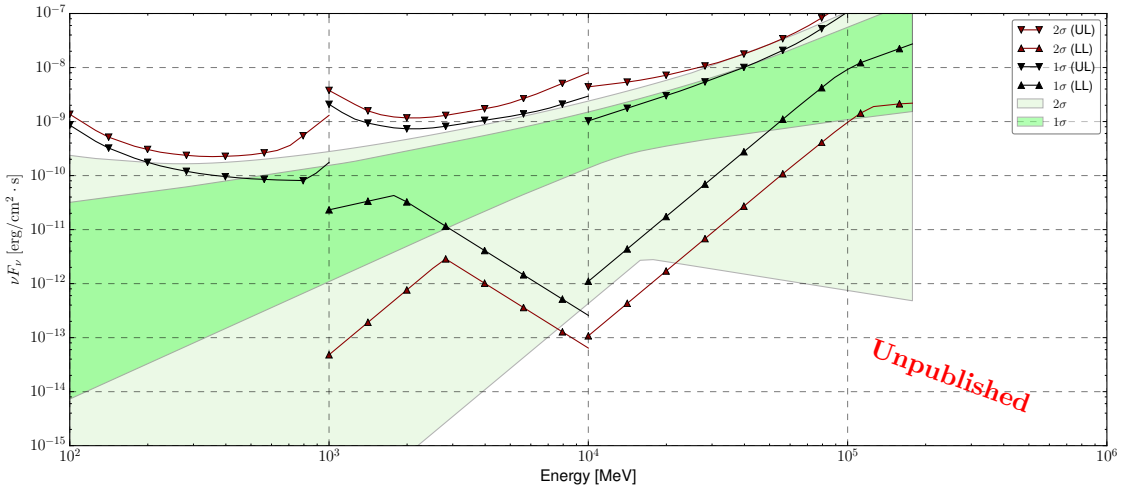

Figure 8.8: SED plot of GRB 160509A for the time range from T_0 +1.0 ks to +2.3 ks (the 16th time bin). The ordinate is νF_ν in the unit of erg $\cdot$ cm^{-2} $\cdot$ s^{-1} and the abscissa is the energy. The greenish bow ties represent the d-loglikelihood result in the entire-E energy range. The black (1σ) and darkred (2σ) curves with triangles represent the upper limits (UL) and lower limits (LL) in the low-E, middle-E, and high-E energy range. The analysis method is d-loglikelihood for low-E and likelihood-ratio ordering for middle-E and high-E. The spectral parameter Γ_γ was scanned only in $-5 \leq \Gamma_\gamma \leq 2$, and some of the lower limit curves touch $\Gamma_\gamma = -5$ or $\Gamma_\gamma = 2$. Hence, the spectrum is possible to be partially harder or softer than plotted here.

The 17th interval: T_0 +4.0 to 9.8 ks For the entire-E range, $\Gamma_\gamma = -1.0^{+1.0}_{-0.6}$. The comparison of the low-E and high-E analyses rejects any single component softer than $\Gamma_\gamma = -2$ over the energy range from 0.1 GeV to 178 GeV at 2σ level.

The 19th interval: T_0 +28 to 99 ks For the entire-E range, $\Gamma_\gamma = -0.6^{+0.8}_{-0.6}$. In this time period, the entire-E analysis and the comparison of the low-E/high-E analyses exhibited the spectral index is harder than -2 by 2σ.

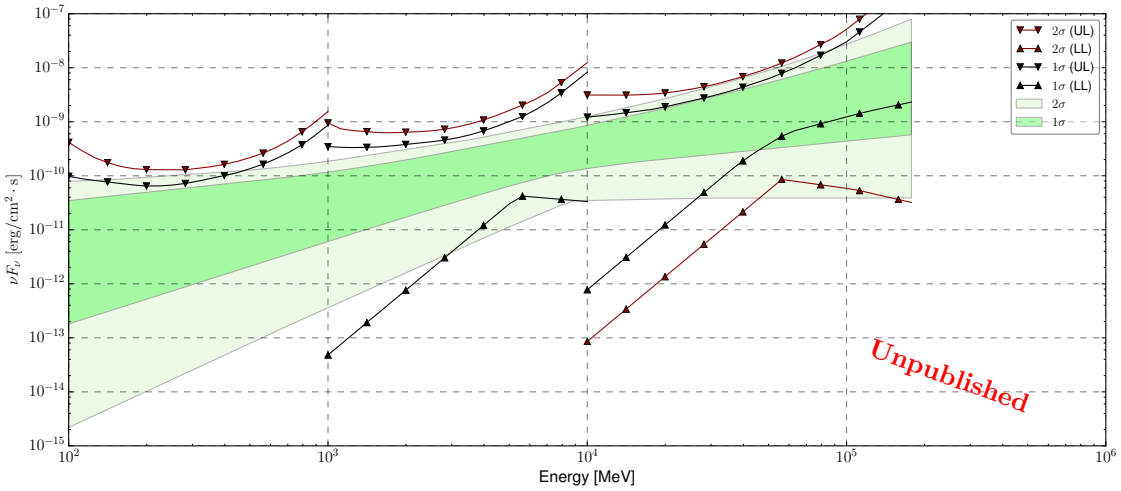

Figure 8.9: SED plot of GRB 160509A from T_0 +4.0 to +9.8 ks (the 17th time bin). The symbols and caveats are the same as Fig. 8.8.

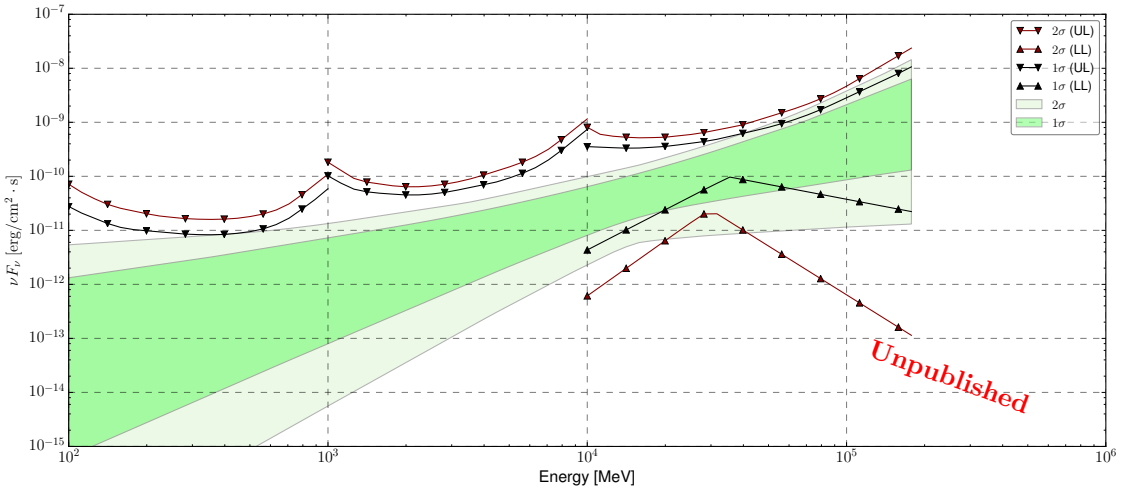

Figure 8.10: SED plot of GRB 160509A from T_0 +28 to +99 ks (the 19th time bin). The symbols and caveats are the same as Fig. 8.8.

Chapter 9

Discussions

9.1 Benefits of the Calorimeter-only classes

I found four CalOnly gamma-ray candidates with energy above 50 GeV from the data sets of the 24 GRBs. Compared to six gamma-rays in the standard classes, this is a significant increase of the signals. This number of > 50 GeV events is consistent with the effective area of CalOnly classes, in comparison to that of the standard P8_SOURCE class. Especially, the CalOnly event associated with GRB 090926A has proven the ability of recovering the data with high off-axis angles.

9.2 Emission mechanisms and scenarios

In this section, I discuss GRB 090926A and GRB 160509A, asking the question whether these results can be explained by synchrotron emission from external shocks, which is described in § 4.6.1. Otherwise, another emission component or particle acceleration mechanism is required. To this end, I discuss two topics. First, I evaluate the maximum synchrotron photon energy at the moment the highest energy events were detected. Next, I compare the constraints on the parameter plane of the spectral index β vs. the temporal index α with the closure relations predicted for each spectral segment, which is described in § 4.6.1, by the synchrotron and SSC models in order to clarify which component is dominant in the LAT energy band.

9.2.1 GRB 090926A

Synchrotron energy limit

As reported in § 7.4, the gamma-like CalOnly event was detected at T_0 +423 s, and the probability of background coincidence is about 0.021%. The reconstructed energy is 50^{+9}_{-5} GeV where the errors

indicate 95% confidence level uncertainty, and the raw deposited energy in the CAL 40 GeV is a quite robust lower limit. The photon energy at the location of the GRB is 155^{+26}_{-14} GeV.

The maximum energy of the synchrotron emission depends on the Lorentz factor Γ. Before the maximum Γ at the detection time, I estimate its maximum possible value before deceleration with Eq. 4.5.

$$L \sim \frac{L_{prompt}}{\xi} = \frac{E_{prompt}}{\xi \mathrm{T}_{50}/(1+z)} = 9.0 \times 10^{55} \mathrm{erg/s} \tag{9.1}$$

where L is the isotropic-equivalent-luminosity of the fireball, E_{prompt} and L_{prompt} is the isotropic-equivalent-energy and the isotropic-equivalent-luminosity of the prompt emission observed in gamma ray, respectively, and $\mathrm{T}_{50} = 6.5$ s is a time duration which contained 50% of the total fluence taken from the GBM catalogue. Dividing T_{50} by $1 + z$ is a correction of the redshift. I use $E_{prompt} = 1.89 \times 10^{54}$erg which is taken from [119] and $z = 2.1062$. I assume the small prompt efficiency $\xi \sim 0.01$ for a conservative limit. The internal shock models predict the efficiency above 1%, which is consistent with observational research, as mentioned in § 4.8.2. The dependence of ξ on Eq. 4.5 is weak. Substituting Eq. 9.1 to Eq. 4.5, the initial Lorentz factor becomes

$$\Gamma_0 \lesssim 1.4 \times 10^4 \left(\frac{M_{BH}}{10\,\mathrm{M}_\odot} \right)^{-1/4}. \tag{9.2}$$

I presumed $Y = 1$ and $\Gamma_{pre} = 1$.

This upper limit is much larger than a typical value $\sim 1.4 \times 10^3$, and it yields the synchrotron limit $\sim 6.8 \times 10^2/(1+z)$ GeV. However, the Lorentz factor decreases when the observation time t_{obs} is much later than the deceleration time t_d. If $\Gamma_0 < 800$, the synchrotron limit is $E \lesssim 13$ GeV, and thus it is much lower than the observed energy 50 GeV. On the other hand, the observable deceleration time $(1+z)t_d$ is much earlier than the arrival time 424 s for $\Gamma_0 > 800$ according to Eq. 4.12. In this case, we can utilize Eq. 4.13. I assume $\xi = 0.01$ and the CBM density $n_1 = 1 \times 10^{-3}\,\mathrm{cm}^{-3}$ for a conservative limit. The former is the same as mentioned above. The latter is taken from the lower bound of the distribution referred in § 4.8.2. At $t_{obs} = 424$ s, $\Gamma \lesssim 7.1 \times 10^2$ and the synchrotron limit in the observer frame is ~ 11 GeV. The CalOnly event energy 50 GeV is more than four times higher than it.

The significance of exceeding the synchrotron limit is quantified in § 8.3.1 as the entire afterglow emission. The likelihood of the power-law spectrum model without the cutoff is larger than that of the model with the cutoff. The test statistics turned out to be $TS = 6.4$ with the CalOnly data, and $TS = 1.4$ without the CalOnly data. A component extending beyond the synchrotron limit is preferred although this quantity is not easily converted to a probability.

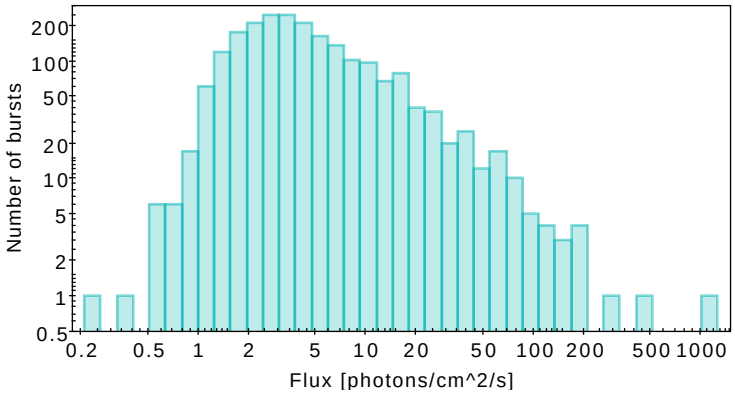

Figure 9.1: Histogram of the peak flux (in 1024 ms) values of the GBM-GRBs [18, 19, 20].

The conclusion changes if the energy injection from the central engine to the external shocks lasted until a time comparable to t_{obs} in spite of non-detection of the GBM signal. I estimated the upper limit on Γ_0 just before 424 s by the following steps. L_{prompt} should have decreased at that time because the GBM signal was not observed. As exhibited in Fig. 9.1, the flux of the GBM-detected bursts peaks at $\sim 3\,\mathrm{photons \cdot cm^{-2} \cdot s^{-1}}$. It equals about 3.7% of the prompt emission of GRB 090926A. Scaling Eq. 9.1 by 0.037 gives

$$L' \lesssim 0.037L = 3.3 \times 10^{53}\mathrm{erg/s}. \tag{9.3}$$

The upper limit on Γ'_0 becomes

$$\Gamma'_0 \lesssim 6.0 \times 10^3 \left(\frac{M_{BH}}{10\,\mathrm{M}_\odot}\right)^{-1/4}. \tag{9.4}$$

The synchrotron limit is $50\Gamma'_0/(1+z)\,\mathrm{MeV} \lesssim 96$ GeV. Therefore, the event energy 50 GeV is too high as synchrotron emission from external shocks of jets accelerated by a fireball except for a case when the energy injection was continued up to > 100 s, and the electron acceleration is very fast. Consequently, the standard combination of the fireball acceleration and external shock afterglow need another emission process or energy injection up to > 100 s after the burst.

The highest synchrotron break energy

Identifying the emission component only based on the spectral index is difficult because the shapes of the synchrotron and SSC spectral bumps are hard to be distinguished. The "S2" component produces a hard emission as the "C2" does it. Before comparing the data with the closure relations, I calculate the highest break frequency of the synchrotron and confirm whether the "S2" segment

extends to the LAT energy band. In this chapter, I use the formulae which were discussed in § 4.6.1.

Fast-cooling regime The highest break frequency is ν_m in this regime. The "S2" scenarios require the synchrotron critical frequency ν_m to be higher than the LAT band. Substituting $z = 2.1062$ to Eq. 4.29, the highest break energy is

$$h\nu_m = 2.5 \left(\frac{E}{1.89\times10^{54}\mathrm{erg}}\right)^{1/2} \left(\frac{\bar{\epsilon_e}}{0.25}\right)^{2} \left(\frac{\epsilon_B}{0.1}\right)^{1/2} \left(\frac{t_{obs}}{22.4\,\mathrm{s}}\right)^{-3/2} \mathrm{MeV}. \tag{9.5}$$

The value of $h\nu_m$ may exceed 100 MeV only if $E \gtrsim 1000 E_{prompt} \sim 2\times10^{57}$erg.

Slow-cooling regime The highest break frequency is ν_c in this regime. The "S2" scenarios require the synchrotron critical frequency ν_c to be higher than the LAT band. Substituting $z = 2.1062$ to Eq. 4.28, the highest break energy is

$$h\nu_c = 29 \left(\frac{E}{1.89\times10^{54}\mathrm{erg}}\right)^{-1/2} \left(\frac{\epsilon_B}{1\times10^{-6}}\right)^{-3/2} \left(\frac{n_1}{\mathrm{cm}^3}\right)^{-1} \left(\frac{t_{obs}}{22.4\,\mathrm{s}}\right)^{-1/2} \mathrm{MeV}. \tag{9.6}$$

Provided $E \sim E_{prompt}$ and $n_1 \sim 1\,\mathrm{cm}^3$, $\epsilon_B \lesssim 1\times10^{-6}$ is required by $h\nu_c \gtrsim 100$MeV. This constraint is relaxed as $\epsilon_B \lesssim 1\times10^{-4}$ for smaller $n_1 \sim 1\times10^{-3}\mathrm{cm}^3$.

Comparison with the closure relations and interpretations

For comparing the observed data with the closure relations, I use Fig. 8.2. I display the allowed combinations of the spectral β and the temporal index α in Fig. 9.2 together with their closure relations predicted by the synchrotron and SSC models. Although the figure has four plots which are dedicated to different CBM density profiles (ISM- or wind-like) and cooling regimes (fast- or slow-cooling), the identical results are plotted in them. Each of the rainbow lines and gray dots represents the closure relation in each spectral segment of the synchrotron and SSC emission components. Each observational result is anticipated to be associated with one of these lines and dots, or a mixture of two of them. Because the observations of the LAT and the XRT were not simultaneous, the two results are not required to be associated with an identical segment. The color of the lines indicates the value of the power-law index p of the spectrum of electrons which were injected into the radiation region, $dN_e/d\gamma_e \propto \gamma_e^{-p}$. The gray dots mean α and β do not depend on p for the scenario. If a single radiation region is responsible for both the LAT and the XRT data, p is common, and then, an identical color coincides with both of the contours and points in the plots. Here I consider combinations of spectral segments which meet the following criteria as plausible scenarios.

- The closure relation of one segment coincides with the LAT constraint with a certain value of $p \geq 2$.

- The closure relation of the same or another spectral segment coincides with the XRT constraint with the same value of p as the LAT constraint is done.
- If the segment of the XRT corresponds to higher frequency than the segment of the LAT, the break frequency between the segments should move from the LAT band down to the XRT band within the their observations.

I consider the scenarios as follows.

1. If the relation do not coincide with the LAT constraint by 2σ, the scenario is unlikely.
2. If the relations coincide with both the LAT and XRT constraints by 1σ with an identical p, the scenario is plausible.
3. If the relation coincides with the LAT constraint by 2σ, the scenario is possible.

When a scenario which the LAT result is explained by a component which fulfills the second or third case, I inspect what parameters can reproduce the observed LAT and XRT light curves.

It should be noted that the constraints on the LAT data are possibly biased. The data which I used in § 8 included the time periods starting from $T_0 + 22$ s. It was later than the end of the prompt emission observed by the GBM, and the flux light curves (Fig. 8.1) looks consistent with the afterglow. In spite of the consistency, the data are possibly contaminated by the prompt emission because the considerable statistical uncertainty might hide the features of internal radiation. Hereafter I assume the data are dominated by the afterglow component with a power-law spectrum and power-law temporal decay. In some previous GRB studies, the LAT data from the beginning of the burst or from the peak in the LAT light curve are used for the analysis of an external shock component; for example, [113] for the former and [177] for the latter. Compared to them, data in a restricted time range are used in this study. The reason is that the LAT light curves of these two GRBs have a spiky pulse which correlates to their prompt component observed by the GBM [64, 65, 62]. These pulses cannot be explained by the external shock models because of the short time scale. Under this afterglow assumption, only "S2" in the slow-cooling regime and "S1R" are consistent with the LAT result by 2σ among the synchrotron-alone scenarios. The segment "C2" with ISM-like medium in the slow-cooling regime is consistent by 1σ. These are illustrated in Fig. 9.3.

Synchrotron emission in the fast-cooling regime No single spectral segment of the adiabatic fast-cooling regime explains the LAT constraints by 3σ. One may think the break frequency ν_m is possibly located in the LAT band and an intermediate case of "S1" and "S2" reproduce the LAT result. This is indicated in Fig. 9.3a. However, in this case, $\beta < 1$ requires $h\nu_m > 100\,\mathrm{MeV}$ and needs very large E, ϵ_e and ϵ_B as demonstrated in § 9.2.1. Such values inevitably yield too high

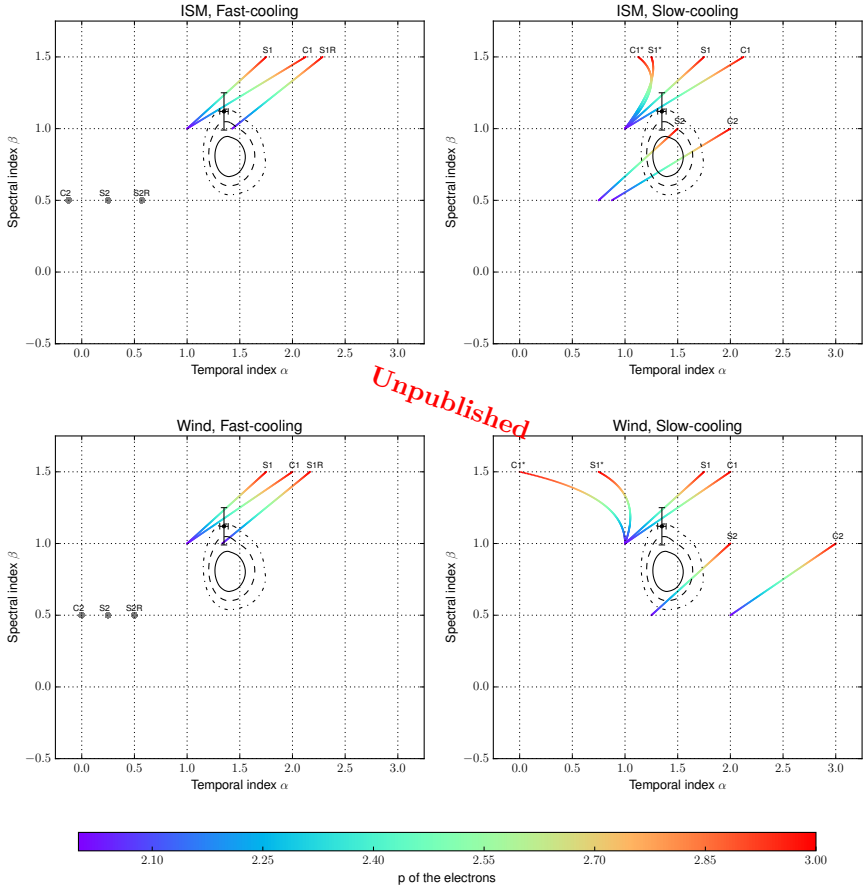

Figure 9.2: Comparison of the the result of the 3D parameter scan of GRB 090926A (Fig. 8.2) and the closure relations. The contours and the points with error bars are identical although they are plotted in four plots dedicated to the ISM-/wind-like CBM density profile and the fast-/slow-cooling regimes. The black contours represent $1, 2, 3\sigma$ confidence regions determined by the time-joint analysis of the LAT afterglow data. The black points represent the result of fitting the *Swift*-XRT light curve of [119]. The rainbow lines and gray dots exhibit the closure relations described in § 4.6.1. The color indicates the spectral index p of the injected electron spectrum. The text labels indicate the emission mechanisms ("S": synchrotron, "C": SSC) and broken power-law segments ("1": the highest-energy segment, "2": the second-highest-energy segment). The "R" and "*" after these labels indicate the cases of radiative evolution and the cases in which the energy losses are dominated by IC radiation, respectively.

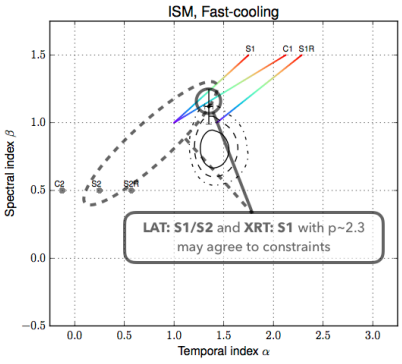

(a) LAT:S1/S2 and XRT: S1 in fast cooling and ISM-like CBM

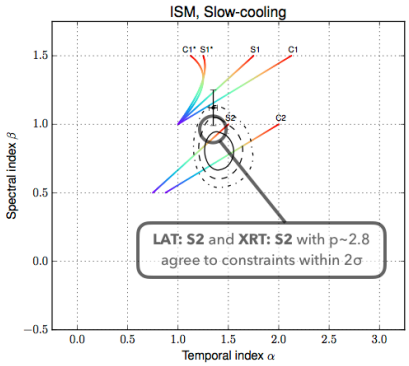

(b) LAT:S2 and XRT: S2 in slow cooling and ISM-like CBM

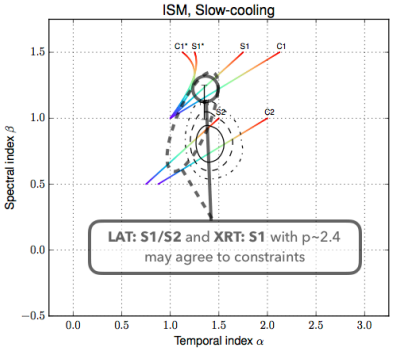

(c) LAT:S1/S2 and XRT: S1 in slow cooling and ISM-like CBM

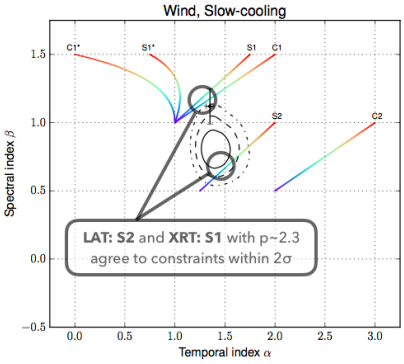

(d) LAT:S2 and XRT: S1 in slow cooling and wind-like CBM

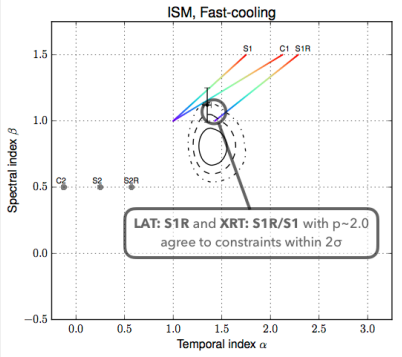

(e) LAT:S1R and XRT: S1R/S1 in slow cooling and ISM-like CBM

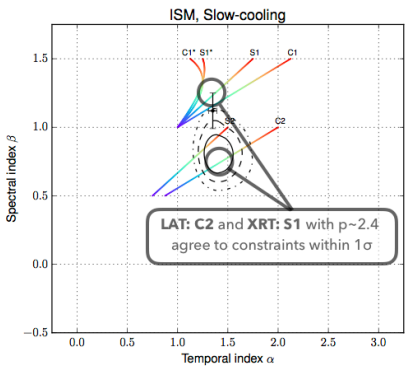

(f) LAT:C2 and XRT: S1 in slow cooling and ISM-like CBM

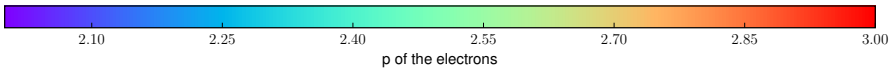

(g) Color bar indicating the spectral index of the electron p.

Figure 9.3: Combination of closure relations which coincides with the LAT and XRT constraints is roughly indicated at the consistent value of p in one of plots in Fig. 9.2. (a) and (c) show the possibility that a mixture of "S1" and "S2" produces the signal observed by the LAT by the dashed ovals.

flux as described below. I calculate the integral energy flux and the spectral index in each time bin which is used in § 8 with Eq. 4.28, 4.29, and 4.30. These are converted into the integral flux for comparison with the observed flux. I set the model parameters as $p = 2.8$, $E = 1.89 \times 10^{57}$ erg, $\epsilon_e = 0.5$, and $\epsilon_B = 0.1$. The calculation starts at 22.4 s after T_0, which is the beginning of the first time bin after the end of T_{90} of the GBM and the beginning of the time interval used for the time-joint analysis. The result is displayed in Fig. 9.4. The predictions exceed the measured flux by more than two orders of magnitude. Lower values of E, ϵ_e, and ϵ_B do not make the cooling regime fast. Consequently, the adiabatic fast-cooling regime is not responsible for the emission in the afterglow phase by 3σ.

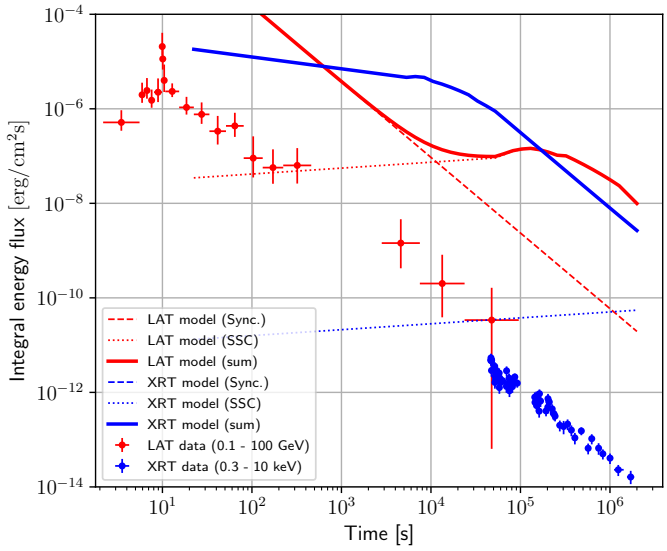

Figure 9.4: Comparison of the observed energy flux light curve of GRB 090926A and the predicted one with $p = 2.8$, $E = 1.89 \times 10^{57}$ erg, $\epsilon_e = 0.5$, $\epsilon_B = 0.1$, and $n_1 = 1\,\mathrm{cm}^{-3}$. These parameter values are required by the adiabatic evolution and fast cooling. The predicted flux is obviously too high.

Synchrotron interpretation in the slow-cooling regime with ISM-like CBM In this case, both the LAT and XRT observation bands are located in "S2". This case is indicated in Fig. 9.3b. A value of ϵ_B smaller than $\sim 10^{-6}$ is required by ν_c higher than the 100 MeV as discussed in § 9.2.1. The comparable flux in the LAT and XRT band requires even higher ν_c. This is possible with smaller E or ϵ_B according to Eq. 9.6, but such values result in too small flux as $F_\nu \propto \epsilon_B^{1.9} E^{1.45}$ (*cf.* Eq. 4.33). Only one solution is a combination of small ϵ_B and large E. Consequently, $\epsilon_B \lesssim 1 \times 10^{-8}$ is required. The suggested range of ϵ_B, or indeed, a combination of ϵ_B and n_1, is almost the lowest value ever

suggested for any bursts (*cf.* § 4.8.2). $\epsilon_B = B^2/(32\pi n_1 m_p c^2 \Gamma)$, and B is given by $B = 4B_1\Gamma$ if the magnetic field is amplified only by shock compression. B_1 is the strength of the magnetic field in CBM and ranges from a few μG to 20 μG [178]. Then, assuming $B_1 \sim 10\mu$G and $n_1 \sim 1\,\mathrm{cm}^{-3}$ gives us $\epsilon_B \sim 10^{-8}$. For such parameters, however, the IC scattering must be suppressed by a certain mechanism and negligible in spite of the natural expectation of its existence. Otherwise, the IC component is anticipated to overcome the synchrotron. Then ν_c is reduced, and the emission in the LAT energy band is dominated by the IC component. The case when $\epsilon_B = 1\times10^{-8}$, $E = 3\times10^{55}$ erg, $\epsilon_e = 0.5$, $p = 2.8$, and $n_1 = 1\,\mathrm{cm}^{-3}$ are visualized as Fig. 9.5. The light curves are not reproduced if the IC is effective. Consequently, this synchrotron-alone interpretation appears to be unlikely by 3σ statistical uncertainty.

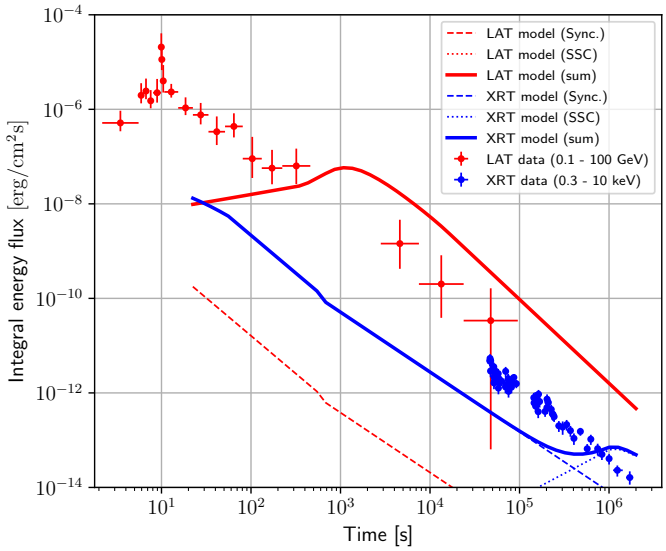

Figure 9.5: Comparison of the observed energy flux light curve of GRB090926A and the predicted one with $p = 2.8$, $E = 3 \times 10^{55}$ erg, $\epsilon_e = 0.5$, $\epsilon_B = 1 \times 10^{-8}$, and $n_1 = 1\,\mathrm{cm}^{-3}$. These parameters are required for explaining the LAT data with the "S2" segment. The observed light curves are not reproduced because of the IC component and reduction of ν_c by the IC cooling.

In the upper right plot of Fig. 9.2, the possibility that the LAT result is reproduced by an intermediate case of "S1" and "S2" looks open. This is indicated in Fig. 9.3c. However, this interpretation is essentially included in the discussion above, and the extreme parameter $\epsilon_B \lesssim 1 \times 10^{-8}$ and avoiding the reduction of ν_c by SSC cooling via a certain suppression mechanism are required for $\nu_m > 100$ MeV.

Synchrotron interpretation in the slow-cooling regime with wind-like CBM According to the left lower plot in Fig. 9.2, the LAT result looks possible to be attributed to "S2" with the wind-like CBM. This case is indicated in Fig. 9.3d. In this case, however, the XRT data must be interpreted as "S1" because "S2" is too distant from it. The break energy $h\nu_c$ should had traveled from the LAT range (0.1 - 100 GeV) to the XRT range (0.3 - 10 keV) because the energy of "S1" is always higher than "S2". The beginning of the analyzed LAT data is 22 s while the XRT data are contributed mainly by the period until ~ 100 ks. It is impossible for the break frequency to go down by five orders of magnitude within time of four orders of magnitude because $\nu_c \propto t_{obs}^{1/2}$ [13].

Radiative evolution interpretation Another possibility to explain the result with the synchrotron model is that the dominant energy loss is radiative. In this case, the LAT and XRT data are described by "S1R" and the intermediate stage of "S1R" and "S1", respectively, with ~ 2.0 by 2σ as indicated in Fig. 9.3e. The radiative phase of the predicted light curves with $p = 2.2$, $\epsilon_B = 0.1$, $\epsilon_e = 0.5$, $E = 3 \times 10^{54}$ erg, $\Gamma_0 = 1000$ are drawn in Fig. 9.6. If the transition from the radiative to the adiabatic evolution occurs before $t_{obs} \sim 10^4$ s, the observed light curves cannot be reproduced because the model light curves shallow. This shallowing is seen at $\sim \mathrm{T}_0 + 30$ ks in Fig. 9.6. After the transition time, ν_c exceeds ν_m, and the system becomes adiabatic. If the IC cooling is effective, the transition becomes later. Keeping the radiative evolution for a long time and avoiding the IC flux higher than the synchrotron require $\epsilon_B \gtrsim 0.1$; otherwise, the SSC becomes a dominant component in the LAT energy range. Figure 9.6 visualize a marginal case when the two component is comparable. The value of ϵ_B which is required by reproducing the LAT curve is large compared to the values obtained for other bursts (*cf.* § 4.8.2).

The radiative cooling for several GRBs including GRB 090926A is discussed by Ghisellini *et al.* [113]. They applied a variation of the radiative external shock model (§ 4.6.1) with "pair-enriched" ISM. This scenario may be possible when the prompt emission spectrum extends above $m_e c^2$. A fraction of the prompt photons are scattered along non-radial directions. The scattered photons interact with the incoming high-energy prompt photons, and they produce electron pairs. This process creates pair-enriched CBM in advance of the arrival of the forward shocks, and the electrons and positrons are accelerated by the shocks. In this scenario, the closure relation for "S1R": $\alpha = 2(6\beta - 1)/7$ is modified as $\alpha = 2(4\beta + 1)/7$ [113]. They are however difficult to be distinguished in our data because both of them provide $\alpha \sim 10/7$ for our $\beta \sim 1$. The authors successfully reproduced the LAT light curve of the GRB as plotted in Fig. 9.7, but the value of $p = 2.5$ which they used does not agree to the spectrum in the LAT band which I derived. Thus, at least the model parameters should be modified so that $\lesssim 2.1$ although this pair-enriched scenario is not rejected in this thesis.

Inverse-Compton interpretation The "C2" with $p \sim 2.4$ is consistent with 1σ with the LAT contours in the slow-cooling regime with ISM-like CBM as indicated in Fig. 9.3f. The X-ray emission

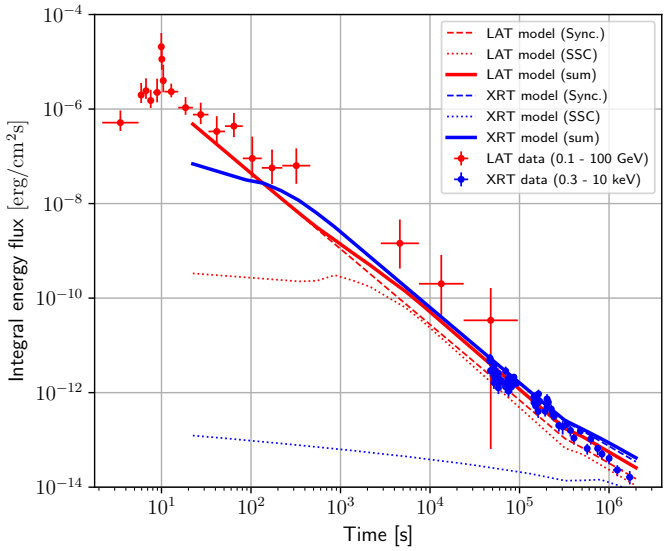

Figure 9.6: Comparison of the observed energy flux light curve of GRB 090926A and the predicted one with $p = 2.2$, $E = 3 \times 10^{54}$ erg, $\epsilon_e = 0.5$, $\epsilon_B = 0.1$, $\Gamma_0 = 10^3$, $n_1 = 1\,\mathrm{cm}^{-3}$. The evolution phase transits from radiative to adiabatic at $t_{obs} \sim 4 \times 10^5$ s. The observed XRT light curve negatively deviates from the model, but this might be because of the jet break.

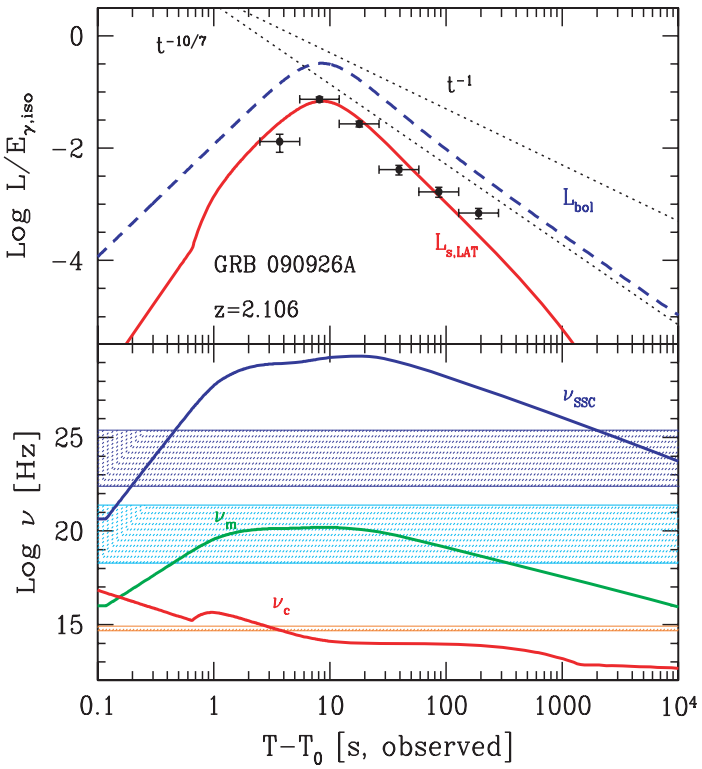

Figure 9.7: Light curves of the radiative fireball scenario with pair-enriched ISM taken from [113]. Top: Luminosity integrated in the energy range of 0.1 – 100 GeV (solid line) and the bolometric flux (dashed thick line); both of them are normalized to the prompt emission energy. Bottom: Time profiles of the characteristic frequencies ν_m, ν_c, and $\nu_{SSC} \equiv \gamma_m^2 \nu_m$. The hatched areas represent the energy ranges of the LAT (0.1 – 100 GeV), the GBM (8 – 1000 keV) and the optical range (corresponding to the U and R filters). These are modeled by radiative external shocks with pair-enriched ISM. The parameters are $\epsilon_e = 0.9$, $\epsilon_B = 0.1$, $\Gamma_0 = 670$, $E_{prompt} = 2 \times 10^{54}$, $\xi = 0.14$, $n_1 = 3$ cm^{-3}, and $p = 2.5$.

is considered as the "S1" component with the similar p. This coincidence is depicted in Fig. 9.3f. In Fig. 9.8, the observed light curves are roughly reproduced with $p = 2.5$, $E = 1 \times 10^{55}$ erg, $\epsilon_e = 0.03$, $\epsilon_B = 3 \times 10^{-5}$, and $n_1 = 1\,\mathrm{cm}^{-3}$.

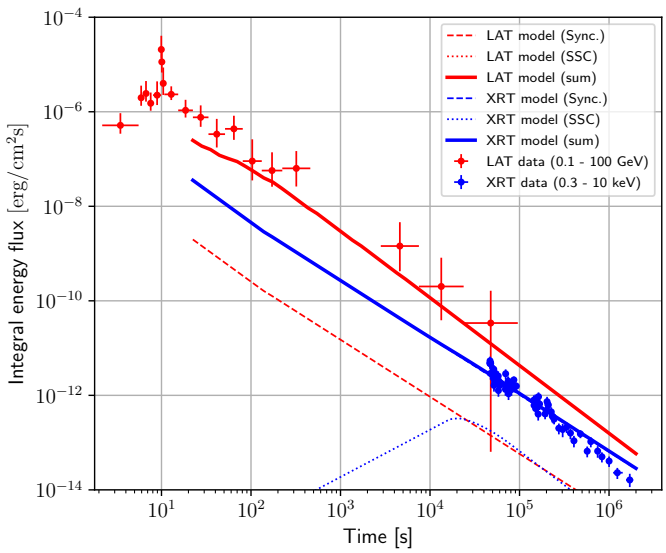

Figure 9.8: Comparison of the observed energy flux light curve of GRB 090926A and the predicted one with $p = 2.5$, $E = 1 \times 10^{55}$ erg, $\epsilon_e = 0.03$, $\epsilon_B = 3 \times 10^{-5}$, and $n_1 = 1\,\mathrm{cm}^{-3}$. This is just a possible example of the parameters. The observed light curves are roughly reproduced.

As mentioned in § 4.7.2, Beniamini *et al.* [127] showed that the LAT data was dominated by the SSC emission through a different method. In this thesis, I have proven the inconsistency of the synchrotron-alone model more intuitively, by the existence of the photon energy beyond the synchrotron limit and the relation of the spectral and temporal indices. Wang *et al.* [11] also succeeded reproducing the light curves of GRB 090926A by a model of synchrotron + SSC. These previous studies support the SSC interpretation.

The break of the XRT light curve from $\alpha_{X1} = 1.35 \pm 0.04$ to $\alpha_{X2} = 2.6^{+0.9}_{-0.5}$ at $7.9^{+1.8}_{-1.2} \times 10^5$ s as mentioned in § 8.3.1. I used α_{X1} for the comparison with the closure relations. Because the X-ray data are explained by "S1", a jet break is only one plausible interpretation.

Systematic effect In § 8.3.1, I derived the LAT constraints with the CalOnly exposure scaled by 1.17. In Fig. 9.9, the LAT constraints of Fig. 9.2 are replaced by them in order to confirm the

systematic uncertainty of the CalOnly IRFs does not affect the discussion in this subsection. The same conclusions are derived from Fig. 9.9 as from Fig. 9.2.

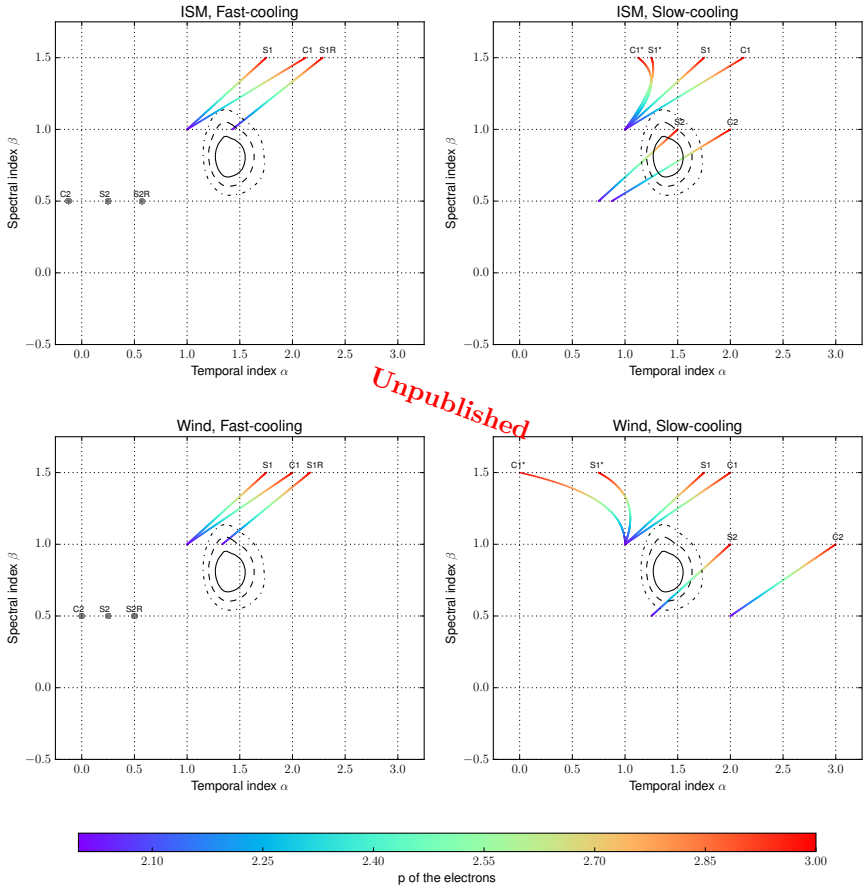

Figure 9.9: Same plot as Fig. 9.2 but the LAT contours were derived with the CalOnly exposure scaled by 1.17 (Fig. 8.3) for clarifying the effect of the systematic uncertainty in the CalOnly IRFs.

Summary of GRB 090926A

The discovered CalOnly event is highly likely to be associated with the GRB. The intrinsic energy 155 GeV exceeded the synchrotron limit if the jet was accelerated by the fireball mechanism, and no additional energy was injected into jets in late time. Assuming the LAT data after $T_0 + 22$ s were dominated by the external shock emission and the adiabatic energy losses predominated the radiative ones, the comparison with the closure relations demonstrated that the LAT band should have been located in the second highest spectral segment of synchrotron or inverse-Compton. The other scenarios were rejected by the statistical uncertainty of 3σ. The synchrotron second highest

segment is implausible for the LAT range because ν_c above 100 MeV is difficult. The simplest interpretation is that the LAT and the XRT data were dominated by the second highest energy segment of the SSC and the synchrotron respectively, in the slow-cooling regime and uniform CBM. This is consistent with the data by 1σ. The closure relations can be still explained by the synchrotron alone by $\sim 2\sigma$ when the energy losses were dominated by radiation. In this case, $\epsilon_B \gtrsim 0.1$ is preferred.

In addition, no adiabatic scenarios with the wind-like CBM is consistent with the observations by 3σ. This result is supported by the result on GRB 090926A included in a statistical survey by Schulze *et al.* [138], which was based on the late-time optical and X-ray data. The wind-like CBM remains possible if the evolution is radiative.

9.2.2 GRB 160509A

Synchrotron energy limit

As reported in § 7.4, two gamma-like CalOnly events correlated to GRB 160509A were detected. The values of the reconstructed energy are 116^{+61}_{-26} GeV and 63^{+16}_{-9} GeV where the errors are 95% uncertainty. The energy corrected the redshift of the GRB is 252^{+132}_{-56} GeV and 134^{+35}_{-20} GeV.

The prompt gamma-ray luminosity is $L_{prompt} \sim 2.5 \times 10^{53} \mathrm{erg \cdot s^{-1}}$ [62]. I assume $\xi = 0.01$ and $n_1 = 1 \times 10^{-3}\,\mathrm{cm^{-3}}$ again. Then, the isotropic-equivalent-luminosity of the outflow is $L \sim 2.5 \times 10^{55} \mathrm{erg \cdot s^{-1}}$. The maximal initial Lorentz factor is

$$\Gamma_0 \lesssim 9.9 \times 10^3 \left(\frac{M_{BH}}{10\,\mathrm{M_\odot}} \right)^{-1/4}. \tag{9.7}$$

After deceleration, the possible Lorentz factors are $\Gamma \lesssim 2.9 \times 10^2$ at $t_{obs} = 2.1$ ks and $\Gamma \lesssim 2.0 \times 10^2$ at $t_{obs} = 5.8$ ks. The synchrotron limits of the observed energy are 7 GeV and 5 GeV, respectively. The significance of exceeding the synchrotron limit is quantified in § 8.3.2 as the entire afterglow emission. The likelihood of the power-law spectrum model without the cutoff is larger than that of the model with the cutoff, and TS turned out to be 31.3. Another component besides the synchrotron emission from the decelerated jets is preferred.

For possible central engine activities at $t_{obs} > 400$ s, the upper limit on the GBM flux is estimated to be 4.1% of the prompt peak flux. The Lorentz factor before deceleration $\Gamma'_0 \lesssim 4.5 \times 10^3$, and the synchrotron limit is $\sim 1.0 \times 10^2$ GeV. The energy of 116 GeV and 63 GeV appears to be challenging for the synchrotron emission at the time stage of thousands of seconds from $\mathrm{T_0}$ although it is not conclusive.

In addition, one standard-class event was detected at 70 ks. The reconstructed energy is 29 GeV, and the deposited energy is 19 GeV. The synchrotron limit at this time is 1.8 GeV. Hence, this event, which arrived in late time compared with the typical plateau phase (*cf.* § 3.4.3) also requires another component besides the synchrotron.

Comparison with the closure relations

The constraint by the LAT is weaker than the case of 090926A because of the later beginning of the afterglow phase. All single spectral domains with β softer than 1.0 are inconsistent with the LAT constraints by 2σ, and only the "S2" and "C2" survived. This is illustrated in Fig. 9.11.

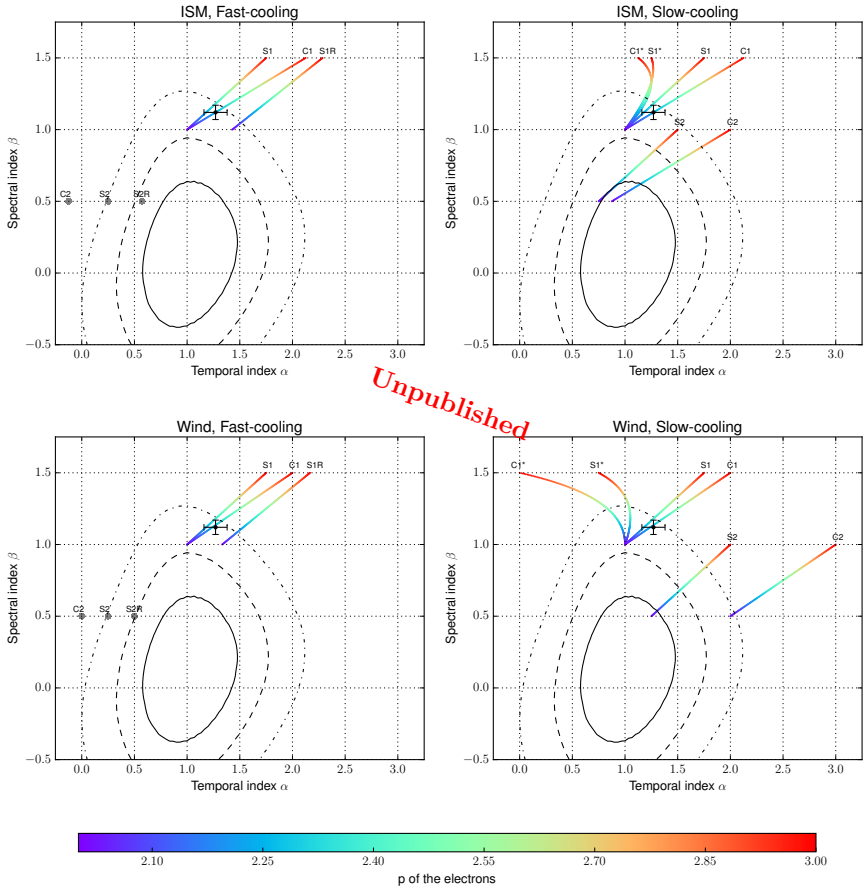

Figure 9.10: Comparison of the results of the 3D parameter scan of GRB 160509A (Fig. 8.5) and the closure relations. The contours and crosses are identical although they are plotted in four plots dedicated for the ISM-/wind-like CBM density profile and fast/slow-cooling regimes. The symbols are the same as Fig. 9.2. The black points are from *Swift*-XRT light curve fitting of [172].

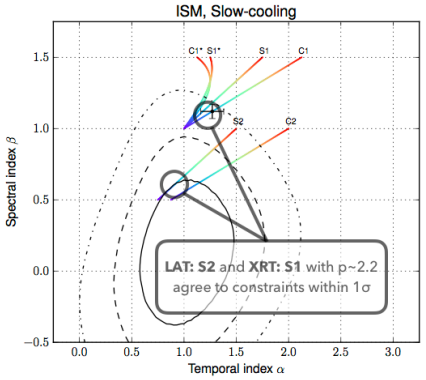

(a) LAT:S2 and XRT: S1 in slow cooling and ISM-like CBM

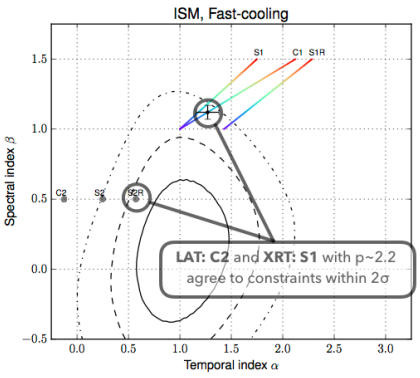

(b) LAT:S2R and XRT: S1 in fast cooling and ISM-like CBM

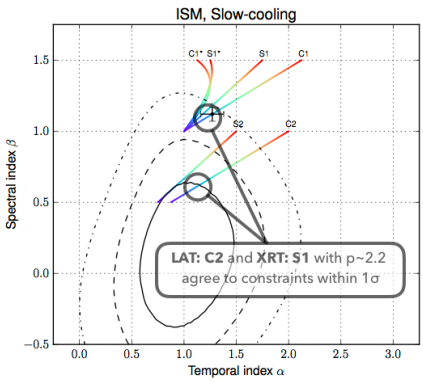

(c) LAT:C2 and XRT: S1 in slow cooling and ISM-like CBM

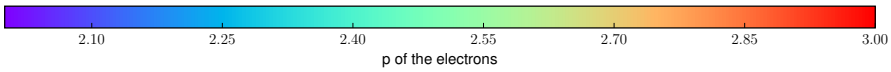

(d) Color bar indicating the spectral index of the electron p.

Figure 9.11: Combination of closure relations which coincides with the LAT and XRT constraints for GRB 160509A is roughly indicated at the consistent value of p in one of plots in Fig. 9.10.

Synchrotron interpretation If the LAT data correspond to "S2", the XRT band must have been in "S2" or "S1". The former case is also very difficult because there are no values of p which are consistent with both the LAT and XRT results by 2σ. In the latter case, which is indicated in Fig. 9.11a, ν_c should have quickly moved from the LAT band (0.1 - 178 GeV) to the XRT (0.3 - 10 keV) band within the time of one or two orders of magnitude. This is impossible because $\nu_c \propto t_{obs}^{-1/2}$. A case when the LAT data are contributed by "S1" and "S2" comparably is difficult by 2σ because of the same reason. If the statistical uncertainty up to 3σ is allowed, both the LAT and XRT data are consistent with "S1" with $p \sim 2.1$.

Radiative evolution interpretation If the radiative evolution phase is responsible for the emission observed by the LAT, the XRT data are interpreted as the emission after the transition to the adiabatic evolution. This case is indicated in Fig. 9.11b and consistent by 2σ. In the radiative evolution, the second highest break energy ν_m is given by Eq. 4.51. Substituting $z = 1.17$, $p = 2.3$, $\epsilon_B = 0.1$, $\epsilon_e = 0.5$, $E = 5.8 \times 10^{54}$ erg, $\Gamma_0 = 100$, $n_1 = 1\,\mathrm{cm}^{-3}$ to Eq. 4.51 yeilds $h\nu_m \sim 8.5$ keV at $t_{obs} = 500$ s. It is much lower than the LAT energy band. Therefore, the LAT energy band should correspond to "S1R" for the radiative evolution interpretation. However, the "S1R" segment is rejected by the 2σ LAT constraint. Hence, the radiative evolution interpretation cannot explain the LAT data by 2σ level.

Inverse-Compton interpretation The "C2" in the slow-cooling with ISM-like medium is indicated in Fig. 9.11c and consistent with the LAT contours by 1σ. In this scenario, the X-ray point agrees to the "S1" relation provided $p \sim 2.2$. The modeled light curves with a possible set of parameters are visualized in Fig. 9.12. As mentioned in § 8.3.2, the light curve of the XRT has two breaks possibly, and the fit value of α_X steepens from 0.51 ± 0.12 to 1.27 ± 0.11 at $(3.2 \pm 1.2) \times 10^4$ s, and to 2.2 ± 0.3 at $(4.7 \pm 2.0) \times 10^5$ s. I referred the value of α between the breaks. Because the change in the spectral index β_X is only ~ 0.1, the first temporal break is interpreted as the end of the shallow decay phase rather than the transition from "S2" to "S1", which predicts spectral softening of 0.5. The second temporal break appears to be consistent with a jet break.

Systematic effect In § 8.3.2, I derived the LAT constraints with the CalOnly exposure scaled by 1.29. In Fig. 9.13, the LAT constraints of Fig. 9.10 are replaced by them in order to confirm the systematic uncertainty of the CalOnly IRFs does not affect the discussion in this subsection. The same conclusions are derived from Fig. 9.13 as from Fig. 9.10.

Summary of GRB 160509A

The afterglow phase had multiple accompanying photon candidates with energy beyond the synchrotron limit for the decelerated jets, including three events above 20 GeV. This result is an evidence ($TS = 31.3$) of another emission component; otherwise, the jet energy was injected into the

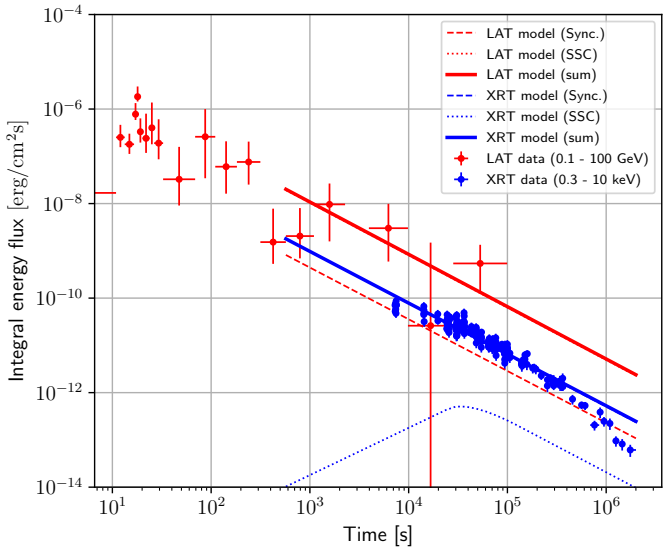

Figure 9.12: Comparison of the observed energy flux light curve of GRB 160509A and the predicted one with $p = 2.2$, $E = 5 \times 10^{54}$ erg, $\epsilon_e = 0.1$, $\epsilon_B = 3 \times 10^{-5}$, and $n_1 = 1\,\mathrm{cm}^{-3}$. This is just a possible example of the parameters. The observed light curves are roughly reproduced. The LAT band and XRT band are dominated by the SSC and the synchrotron, respectively.

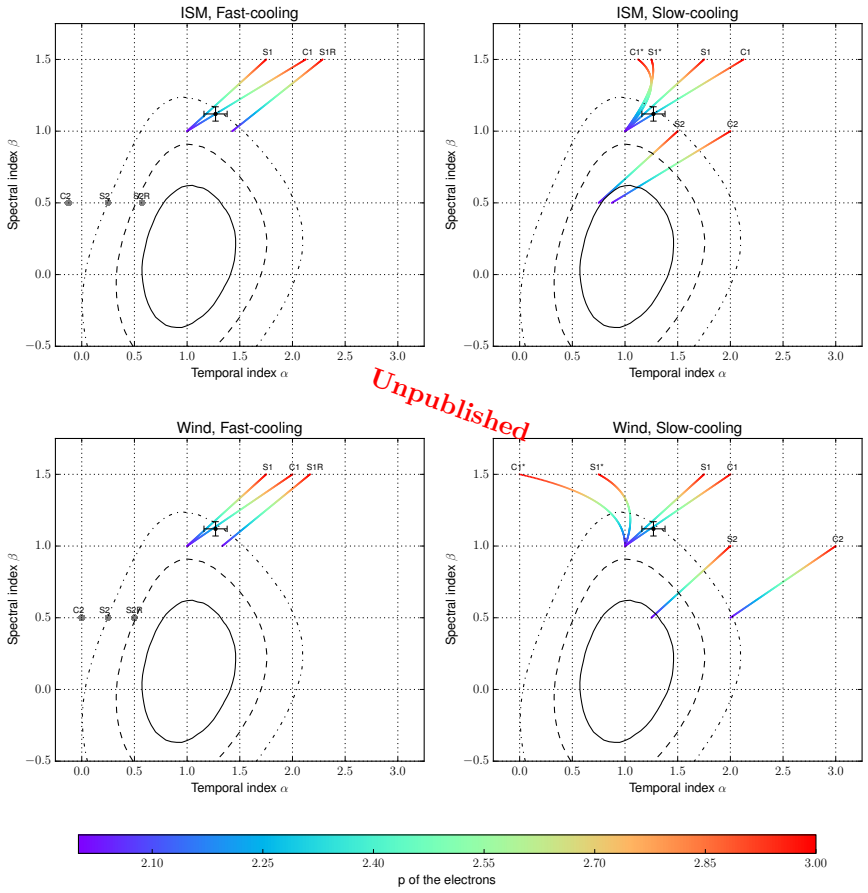

Figure 9.13: Same plot as Fig. 9.10 but the LAT contours were derived with the CalOnly exposure scaled by 1.29 (Fig. 8.6) for clarifying the effect of the systematic uncertainty in the CalOnly IRFs.

external medium even at 10^3 - 10^5 s after the burst, or the assumption of the fireball jet acceleration and the external shock afterglow is not valid. The spectral index β, which is harder than one in the afterglow phase, also demonstrated the inconsistency with the synchrotron models. Although the significance is about 2σ and not very high, the LAT result turned out to be difficult for the synchrotron component with any p. On the other hand, the SSC hypothesis is well consistent with both the LAT and XRT results in the slow-cooling regime and in the uniform CBM. This is only one plausible scenario within 1σ.

9.2.3 Effects on the jet parameter estimation

As mentioned in § 4.8.2, light curves in the LAT band were considered as a good proxy of the jet kinetic energy instead of X-ray data. It was because the LAT band was expected to locate above $h\nu_c$, and the responsible electrons had high energy so that their IC scattering was suppressed by the Klein-Nishina effect. However, the results we discussed in this chapter require us to reconsider this expectation. If the evolution is dominated by the radiation, the flux is considerably affected by the initial Lorentz factor Γ_0. If the evolution is adiabatic and the emission process is synchrotron alone, both the LAT and XRT bands locate in the second highest segment. If the LAT band is dominated by SSC, it cannot be used as the proxy, at least, directly. The XRT band is in the synchrotron highest energy segment in this case, but the IC energy losses are not expected to be negligible. If the prompt or late flare components are considerable in the LAT data, the afterglow flux is overestimated.

9.2.4 The highest photon energy and EBL absorption

A very high energy photon which came from a distant source can be a probe into the EBL density, which is difficult to measure directly. I calculated the optical depth of the highest energy events of GRB 090926A and 160509A for some EBL models and checked if they are consistent. The results are summarized in Table 9.1 and visualized in Fig. 9.14. The models evaluated here are consistent with the detections.

Table 9.1: Optical depth of the CalOnly events correlated to GRB 090926A and 160509A.

GRB	Redshift	Energy	F08[a]	D11[b]	G12[c]	F17[d]
090926A	2.1062	50 GeV	0.72	-	1.8	0.73
160509A	1.17	116 GeV	1.3	1.3	2.2	1.2
		63 GeV	0.38	0.37	0.79	0.37

[a] Franceschini *et al.* 2008 [171].
[b] Domínguez *et al.* 2011 [75]. Provided only for $z \leq 2$.
[c] Gilmore *et al.* 2012 [179].
[d] Franceschini *et al.* 2017 [180].

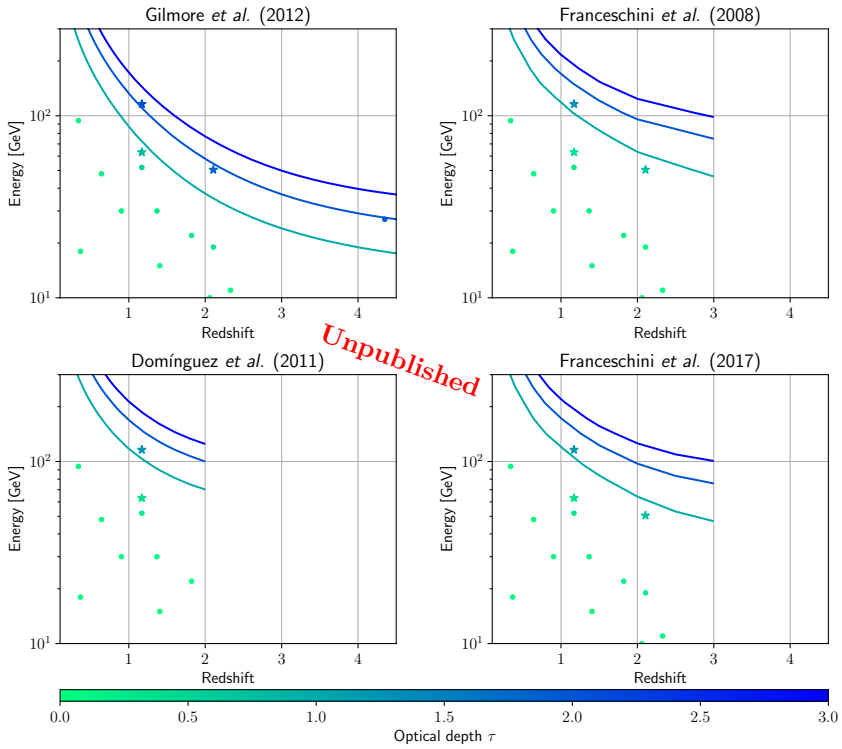

Figure 9.14: Optical depth τ of the LAT-detected events correlated to GRBs. The values are calculated for four EBL models, namely, Gilmore *et al.* 2011[179], Domínguez *et al.* 2011[75], Franceschini *et al.* 2008 [171], and Franceschini *et al.* 2017 [180]. The stars and circles represent the CalOnly- and standard-class photons respectively. The three curves in each panel indicate the optical depth of 1, 2 and 3. Domínguez *et al.* (2011) [75] provided the depth only for $z \leq 2$.

These values of the optical depth around or beyond unity imply GRBs are a great potential for measuring the EBL density if we have an instrument with better sensitivity for detecting gamma-rays with the energy from tens of GeV to hundreds of GeV.

9.3 Toward observations by IACTs

As depicted in Table 7.1 and § 7, a number of GRB photons with energy higher than 10 GeV have been detected by the *Fermi*-LAT. However, the results in the previous sections are not very conclusive. There are some reasons for that:

- The numbers of the detected events above GeV are small, namely 22 and 15 events for the afterglow phase of GRB 090926A and 160509A, respectively, and thus the statistical uncertainties of the likelihood analysis are large.
- The effects of unobserved prompt components and late-time flares cannot be excluded.
- Some different mechanisms of jet acceleration are possible.

The first and second reasons originate from the limited photon statistics in the LAT data, and will be solved by the CTA. The collection area of an array of four LSTs is $\sim 10^5\,\mathrm{m}^2$ at 100 GeV [181]. It is more than four orders of magnitude larger than that of the LAT. It will provide us the data with little statistical uncertainty.

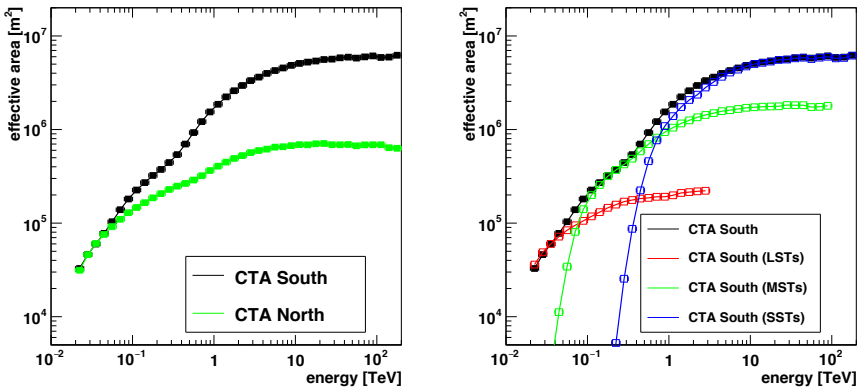

Figure 9.15: Effective collection area values of arrays of the CTA each as a function of the true gamma-ray energy passing the background separation [181].

In Fig. 9.16 and 9.17, I compared the CTA sensitivity curves based on MC with the flux of GRB 090926A and 160509A extrapolated from the LAT band. The CTA sensitivity curves were taken from [181]. The sensitivities were determined by the following criteria in five energy bins per decade.

- The significance of the detection is 5σ.
- At least ten gamma rays are detected.
- The signal/background ratio is at least 1/20.

The zenith angles are 20° for all of them. The GRB flux curves in some of the LAT analysis time bins were extrapolated by a power-law from the values at 1 GeV, which were determined by the time-resolved analysis of the LAT data. The power-law indices for extrapolating were decided by the second highest energy segment of the SSC component (*cf.* Table 4.2) with the most plausible electron index p, namely, $p = 2.4$ for GRB 090926A and $p = 2.2$ for 160509A. Here, I neglected all uncertainties of the measurement. The curves with the same colors are comparable only roughly because the LAT analysis periods do not coincide with the duration assumed for the MC.

According to these comparisons, the detection of the late-time afterglow is promising until ~ 10 ks after the burst if the GRB is as bright as these two GRBs and the SSC highest energy break $h\nu_c^{IC}$ is higher than tens of GeV. It must be noted that these sensitivity curves are for nice observational conditions, namely, a small zenith angle and a dark sky without the moon. Keeping the energy threshold $\lesssim 100$ GeV even in bad conditions is thus important for detecting the afterglows by the CTA. If the conditions are good, the detection is possible even after one day.

Detailed light curves enable us to differentiate the prompt and late-time flare emission with fast variabilities from the afterglow emission with power-law decaying. On the other hand, the signals are limited in less than one decade of the energy range, and they suffer from a strong cutoff because of the EBL absorption. Determining the spectral index needs the LAT data in a case when the detection by CTA is restricted in a narrow energy range because of the EBL effect.

If a light curve with energy above tens of GeV exhibits fast variabilities, the origins of the variabilities are attributed to the intermittent activities of the central engine. Correlations with X-ray and optical flares could be seen if a simultaneous observation is performed in these bands. The broadband spectra of these flares may enable us to derive the magnetic field strength and photon density in the emission region.

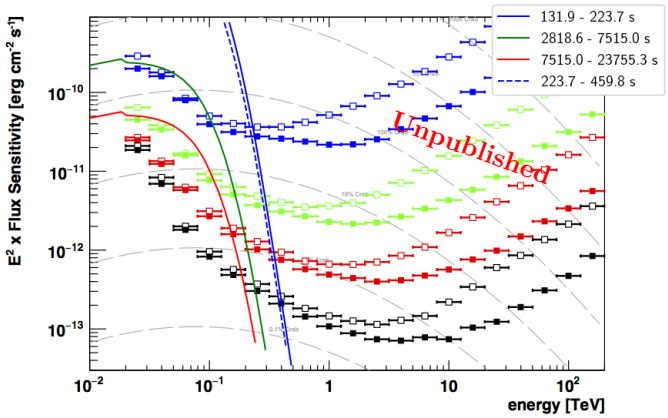

Figure 9.16: Comparison of the CTA differential sensitivity curves [181] and the extrapolation of the energy flux of GRB090926A observed by the LAT. The abscissa is the gamma-ray energy E over the CTA range. The ordinate is the differential count flux multiplied by E^2. The binned curves represent the sensitivity curves of the CTA. The color indicates the observation time (blue: 100 s, green: 1,800 s, red: 18,000 s, and black: 180,000 s). The open and filled squares represent the CTA's northern array in La Palma and southern array in Chile, respectively. The four smoothed solid or dashed curves are the prediction based on the results in § 8. I took the νF_ν at 1 GeV with the best-likelihood value and extrapolated it with the assumed photon spectral index $\Gamma_\gamma = -1.7$. The EBL model is Franceschini *et al.* 2008 [171].

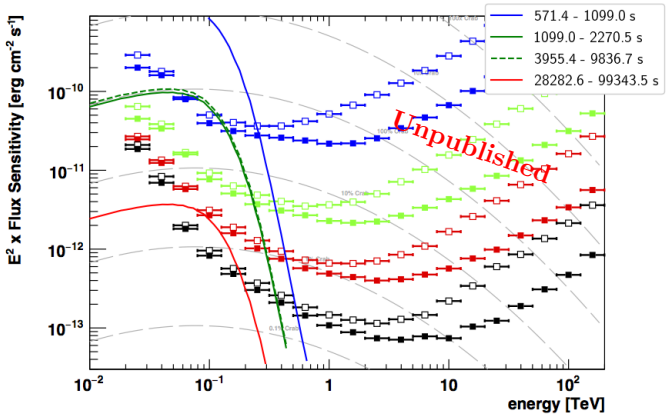

Figure 9.17: Comparison of the CTA differential sensitivity curves [181] and the extrapolation of the energy flux of GRB160509A observed by the LAT. The symbols are the same as Fig. 9.16. The photon spectral index $\Gamma_\gamma = -1.6$ is assumed for extrapolating the flux in the LAT band. The EBL model is Franceschini *et al.* 2008 [171].

Chapter 10

Summary and conclusions

The *Fermi*-LAT has detected more than 20 GRBs accompanied by photons with energy above 10 GeV. Such values of energy may be too high for the standard model of the GRB afterglows, namely, the synchrotron radiation originated from external forward shocks. I performed a detailed study whether the afterglows of the two long-GRBs 090926A and 160509A are consistent with the synchrotron models. In this study I used the novel photon classes of the *Fermi*-LAT which I have developed.

In § 6, I reported the development and performance of the CalOnly classes of the LAT, which can be used to recover tens of percents of untapped events with energy above 20 GeV. I optimized the multivariate analysis for rejecting background events and achieved an increase of about 70% in the acceptance around the peak energy, 100 GeV, according to the MC evaluation.

I found four new photon candidates in the CalOnly classes which correlated to GRBs spatially and temporally. Their observed energy is above 50 GeV. The number of the GRB photon candidates in this energy range increased from six to ten. This is a considerable increase and consistent with the evaluation mentioned in the previous paragraph. Remarkably, GRB 090926A and 160509A were highly likely accompanied by the CalOnly photons with energy above 50 GeV, because of a very good agreement of the arrival direction and of a coincidence of two CalOnly events, respectively. I calculated the probability that each of the detections is produced by a coincidence of residual background events. The ON/OFF analyses show that the background probabilities of the CalOnly events related to GRB 090926A and 160509A are about 0.02% and 0.2%, respectively.

The redshift-corrected energy of the event that correlates to GRB 090926A is 157 GeV. That of the two photons that correlate to GRB 160509A is 257 GeV and 137 GeV. All the redshift-corrected energy is higher than that of events ever correlated to GRBs after the end of the prompt phase

(*cf.* § 3.5.3), which is defined as the time at which 95% of the total fluence was detected in 10 keV – 1 MeV in this thesis. The CalOnly events arrived at 4.2×10^2 s (GRB 090926A), 2.1 ks and 5.8 ks (GRB 160509A) after the triggers. Their arrival time is much later than the durations of the prompt emission which were captured by the GBM. Consequently, the values of the energy are more than four times higher than the synchrotron limit at each arrival time with the decelerated jet. This result requires another gamma-ray emission mechanism such as the inverse-Compton scattering. Otherwise those photons had to be created by long-lasting or intermittent activities of the central engines with unidentified jet-internal processes.

Even if the highest energy photons are created by the IC scattering, it is unclear which component is dominant in the LAT energy range. I performed the detailed inspections on the spectra and light curves of these GRBs in the afterglow phases. In order to constrain combinations of the spectral index β and temporal indices α, I resolved the data into multiple time intervals and defined the source model as a function of energy and time. This enabled us to constrain the $\beta - \alpha$ plane although the possibility that the prompt and late-time flare components contaminate the afterglow data remained. I compared the resulting constraints and the referred results of the observations by the *Swift*-XRT with the closure relations expected by the external forward shock models.

The constraints on the afterglow emission of GRB 090926A in the LAT band turned out to be inconsistent with the highest energy spectral segment of the synchrotron radiation by a statistical uncertainty of 3σ if the hydrodynamic evolution of the shocked fluid is adiabatic. The highest segment was usually considered to be responsible for the emissions in the LAT and XRT band. On the other hand, the scenario of the SSC second-highest segment for the LAT data and the synchrotron highest segment for the XRT data is consistent with $p \sim 2.4$ by 1σ. Alternatively, contamination of internal components and significant radiative energy losses of the external shocked fluid are possible. Both of them made the flux decay more rapid and likely reproduced the relatively steep light curve of GRB 090926A. The latter scenario appears to require a considerable fraction ($\gtrsim 10\%$) of the jet energy to go to the magnetic field in the shocked fluid.

The spectrum of GRB 160509A after $\sim$ $T_0 + 1$ ks is harder than $\beta = 1$ and inconsistent with the synchrotron interpretation with a statistical uncertainty of 2σ. Although the standard d-loglikelihood method is no longer justified because of the small photon statistics, I confirmed the the spectral hardness by the likelihood-ratio-ordering approach, which eliminates the χ^2 assumption of the test statistics. The scenario of the SSC second-highest segment for the LAT data and the synchrotron highest segment for the XRT data is consistent with $p \sim 2.2$ by $\sim 1\sigma$.

Considering the breaks of the synchrotron limits and the consistencies with the closure relations, the simplest explanation of these afterglows is that they are dominated by the SSC emissions of the

external shocks. This conclusion is not decisive, because each discussion needs the aforementioned assumptions or has a considerable statistical uncertainty, namely, $\alpha = 1.0 \pm 0.4$ and $\beta = 0.1 \pm 0.5$ of the afterglow phase of GRB 160509A where the errors are 1σ confidence level. These interpretations demand revisiting the previous jet energy estimations. The estimations are based on the assumptions that the afterglow phase is dominated by radiations from external shocks, the synchrotron highest energy segment is responsible for the emissions in the LAT and XRT bands, and the inverse-Compton energy losses are negligible. Which component and spectral segment are responsible for an observation band is important for determining the total release energy and the prompt radiation efficiency. These are keys for revealing the GRB progenitors and the dissipation mechanism responsible for the prompt emissions. Another conclusion is that both GRBs prefer the uniform profile of the CBM to the wind-like profile, except for GRB 090926A in the case of the radiative cooling.

This study demonstrates the usability of the CalOnly classes for transient observations. For GRB 090926A, the good response function of the CalOnly classes for $\theta \sim 60^\circ$ resulted in the detection. Namely, the effective area is comparable to that of the standard classes, and the PSF is a few times narrower than that for $\theta \sim 10^\circ$. For the spectrum of GRB 160509A extending beyond tens of GeV, the CalOnly effective area peaking around 100 GeV worked well. I intend to integrated these classes into the standard LAT data analysis, and eventually publish it. In this thesis, I improved the statistics of the very-high-energy gamma-ray data with a currently operating instrument. In the next twenty years, the CTA will provide data with much less statistical uncertainties. The time-evolution of the afterglow flux is clearly captured for more than 10 ks if a bright GRB is detected with good conditions. The detailed light curves will enable us to differentiate effects of the long-term activities of the central engines from the external shock afterglows. The fact that the GRB spectra extend beyond 100 GeV encourages people to pursue a detection with ground-based gamma-ray detectors. If a spectrum is measured in both the LAT and CTA, the energy range over six decades is covered, and detailed modeling should be possible.

Appendices

Appendix A

Statistics in gamma-ray astronomy

A small number of detectable high-energy photons often makes the analyses challenging. It requires to introduce Poisson statistics instead of the Gaussian.

A.1 Poisson distribution

The number of high energy photons from a constant source detected by an instrument is considered to follow the Poisson distribution. If the photon number is countable, the Poisson distribution is expressed by the following probability mass function,

$$P(X = k) = \frac{\lambda^k e^{-\lambda}}{k!} \tag{A.1}$$

where k is the photon count; the parameter λ equals the mean and the variance.

A.2 Likelihood analyses

"Likelihood" means the quantity how likely a hypothesis produces a result of experiments. If you have a hypothesis H and an observed data $\boldsymbol{x}$, the probability with which H produces $\boldsymbol{x}$ is considered as a probability density function of H, $P(\boldsymbol{x}|H)$. It can be defined as the likelihood function $L(H) = P(\boldsymbol{x}|H)$. If H is described by parameters $\boldsymbol{\theta}$, the likelihood can be written as $L(\boldsymbol{\theta}) = P(\boldsymbol{x}|\boldsymbol{\theta})$. The function L is used for several purposes, described in the following subsections.

A.2.1 The likelihood formula for the Poisson data

Single likelihood for the Poisson distribution

First, we consider the simplest case in which the datum $\boldsymbol{x}$ consists of only a single count number n and it follows the Poisson distribution with the parameter λ. When the hypothesis H provides the mean of the count m, the likelihood $L(H|\boldsymbol{x})$ equals

$$P(n|m) = \frac{m^n e^{-m}}{n!} \tag{A.2}$$

Binned likelihood for the Poission distribution

Sometimes a data set is considered as a series of single independent counts in multiple bins. Naturally, the likelihood is a multiplication of the probability for each bin.

$$L = \prod_i P_i(n_i|m_i) = \prod_i \frac{m_i^{n_i} e^{-m_i}}{n_i!} = e^{-M} \prod_i \frac{m_i^{n_i}}{n_i!} \tag{A.3}$$

where $M = \sum_i m_i$ is the total count predicted by the model.

Unbinned likelihood for the Poission distribution

Because binning coarsens the data, the sensitivity of the likelihood is better for finer binning. If one bins the data infinitely finer, the n_i falls into zero or unity. Then, Eq. A.3 becomes

$$L = e^{-M} \prod_i m_i \tag{A.4}$$

where i now runs over each count instead of each bin. If the total count is large, the calculating the unbinned likelihood is generally time-consuming. That is why the binned likelihood analysis is used instead of the unbinned one.

A.2.2 Test statistics

Test statistics (TS) is a statistical quantity evaluating how much a null hypothesis H_0 disagrees with the observed data, compared with an alternative hypothesis H_1. The test statistics is a function of the observed data. One of its major uses is to quantify the significance of the detection of a source. I introduce a definition of TS which is typically used for LAT analyses [182], although other definitions are also possible. It is defined as

$$TS = -2 \ln \lambda(\boldsymbol{x}) \tag{A.5}$$

by a ratio of the likelihood values,

$$\lambda(\boldsymbol{x}) = \frac{L(\boldsymbol{x}|H_1)}{L(\boldsymbol{x}|H_0)}, \tag{A.6}$$

In the limit of a large number of counts, TS follows the χ^2 distribution asymptotically.

If the data and the model have N bins and M free parameters, TS asymptotically follows the χ^2 distribution. The degree of freedom equals the number of additional parameters in H_1. Under the assumption that TS follows a χ^2 distribution, it is transferred to p-value as

$$p = \int_{\chi^2}^{\infty} f(z; n_d) dz \tag{A.7}$$

where $f(z; n_d)$ is the probability density function of the χ^2 distribution with n_d degrees of freedom. I do not report the p-value every time in this thesis because it is not appropriate when the count number is small.

A.2.3 Parameter estimation

Another use of the likelihood function is determining an estimator $\hat{\boldsymbol{\theta}}$ of a model parameter $\boldsymbol{\theta}$ based on the observed data. The estimated parameters are functions of the data.

Maximum likelihood method

Maximizing the likelihood function with free parameters provides an unbiased and efficient estimator of them although it is not a unique way to construct the estimators. For the data $\boldsymbol{x}$ and the likelihood $L(\boldsymbol{\theta}) = P(\boldsymbol{x}|\boldsymbol{\theta})$, the maximum likelihood estimator is defined by the $\boldsymbol{\theta}$ values which maximize L. Using $\ln L$ is often easier than L.

$$\frac{\partial \ln L}{\partial \theta_i} = 0, i = 1, ..., N \tag{A.8}$$

Solving this equation yields the best estimated values. For the studies reported in § 8, I simply calculated L for many combinations of $\boldsymbol{\theta}$ which covered the relevant parameter space, and found the minimum value of L and θ which provided it.

A.2.4 Parameter constraining

Frequentist confidence interval

One may want to know the statistical precision of the parameter estimation. Here, I review the construction of the parameter interval by the "frequentist" inference, which was established by Neyman [183]. The likelihood function provides an interval of the parameter which is consistent

with the observed data with a certain probability level, and it is called the "confidence interval". This probability is called the "coverage probability". The observational data would fluctuate if one repeated the experiment many times. The coverage probability means that the fraction of intervals in such a set of the results contain the true value in them.

Neyman construction

Assume the observable $\boldsymbol{x}$ and parameter $\boldsymbol{\theta}$ are single scalars (x and θ respectively) for simplicity. Neyman's construction needs the probability density function of the observable x, $f(x;\theta)$. For a probability $1-\alpha$, which is called the "confidence level", one can find a set of two values of x, x_1 and x_2 which satisfy

$$P(x_1 < x < x_2;\theta) = \int_{x_1}^{x_2} f(x;\theta)dx \geq 1-\alpha. \tag{A.9}$$

This is illustrated in Fig. A.2. For a certain value of the parameter $\theta = \theta_0$, $x_1(\theta_0)$ and $x_2(\theta_0)$ are found so that they meet Eq. A.9. The aggregation of $x_1 < x < x_2$, for all of the θ values, $D(\alpha)$ is known as the "confidence belt". One result of the measurement x_0 is one vertical line in

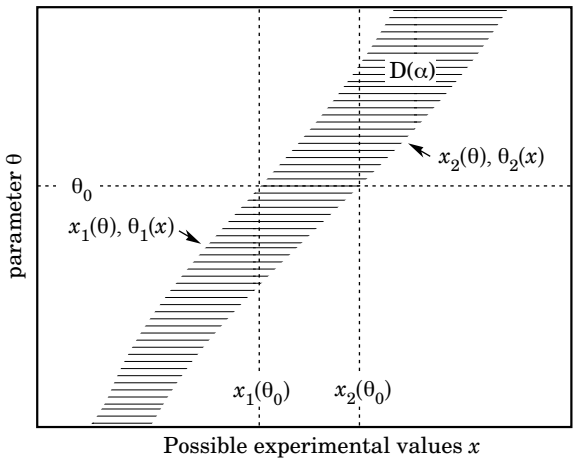

Figure A.1: Construction of a confidence belt [184].

Fig. A.2. The confidence interval of θ is the set of all values which meet $x_1(\theta) \leq x_0 \leq x_2(\theta)$. Set the corresponding end points of θ to θ_1 and θ_2. They are functions of the observational outcome $x = x_0$. Iterating the measurement would vary $[\theta_1, \theta_2]$[i]. For the true value of θ_{true}, $x(\theta_{ture})$ results in $x_1 \leq x \leq x_2$ in a fraction of $(1-\alpha)$ of these trials. In the cases of $x_1 \leq x \leq x_2$, θ_{true} is included in $[\theta_1(x), \theta_2(x)]$ and otherwise not included. Consequently, the interval of $[\theta_1(x), \theta_2(x)]$ covers θ_{true}

[i]Such iteration is unrealistic for astronomical observations.

by the probability of $(1-\alpha)$. Now, I drop the subscript 0 and "true", and then

$$1-\alpha = P(x_1(\theta) \leq x \leq x_2(\theta)) = P(\theta_2(x) \leq \theta \leq \theta_1(x)). \tag{A.10}$$

Choice of intervals

I discussed the condition which a confidence interval must meet in the previous paragraph, but the choice of x_1 and x_2 still remains ununique. One possibility is to choose the "central interval" such that $P(x \leq x_1) = P(x \geq x_2) = \alpha/2$. Another option is to set one of $P(x \leq x_1)$ or $P(x \leq x_2)$ to α and the other one to zero in order to derive an upper or lower limit. The central interval seems to be reasonable if the x distribution is symmetric like the Gaussian distribution.

Generalizing the central interval, one can construct an interval which consists of x values which are most plausible. In other words, each of x values is picked up in the order of the likeliness and gets tagged as an included value until the sum of $P(x;\theta)$ reaches $1-\alpha$. Only if x is discrete or $f(x;\theta)$ is known and integrable, this procedure is uniquely performable apart from an arbitrariness of defining the likeliness.

Case of large statistics

Gaussian distributed measurements If the data set is composed of a single or multiple random variables $\boldsymbol{x}$, the Gaussian distribution or multivariate-Gaussian distribution is usable for constructing a confidence interval, respectively. Even if the data are not Gaussian, the approximation is valid in the large-sample limit because of the central limit theorem. I refer to the errors of estimated values with this method as the "d-loglikelihood" results in § 8.

Single-variate measurements The probability that the observed value x falls in $\pm\delta$ from its true value μ is

$$1-\alpha = \frac{1}{\sqrt{2\pi}\sigma}\int_{\mu-\delta}^{\mu+\delta} \exp\left[-\frac{(x-\mu)^2}{2\sigma^2}\right] dx = \mathrm{erf}\left(\frac{\delta}{\sqrt{2}\sigma}\right) = 2\Phi\left(\frac{\delta}{\sigma}\right) - 1 \tag{A.11}$$

where erf is the Gaussian error function, and Φ is the Gaussian cumulative distribution. This choice of the interval is illustrated in Fig. A.2. If you take $\delta = 1\,\sigma$, Eq. A.11 gives the standard error whose $1-\alpha = 68.27\%$. Here, I refer to a part of a table of α for several δ values in [184] as Table A.1.

Multivariate measurements Just as in the case of a single variate, the estimators of $\boldsymbol{\theta}$ follow a multivariate Gaussian distribution which centered at the true values. One can find a contour which indicates the confidence region for the distribution.

$$\ln L(\boldsymbol{\theta}) \geq \ln L_{max} - \Delta \ln L \tag{A.12}$$

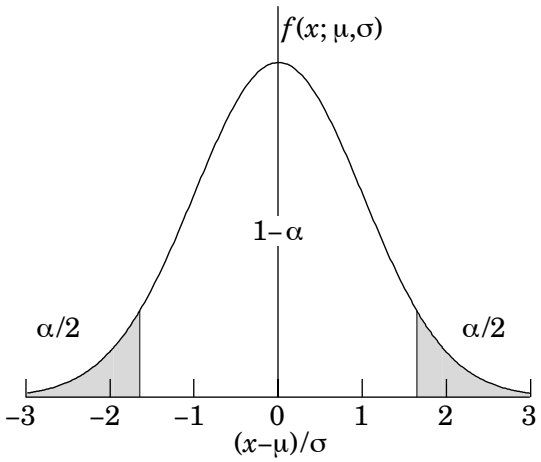

Figure A.2: Gaussian symmetric confidence interval with $\alpha = 0.1$ [184].

Table A.1: Integral of the α intervals outside $\pm\delta$ from the mean of the Gaussian distribution [184].

α	δ
0.3173	1σ
4.55×10^{-2}	2σ
2.7×10^{-3}	3σ
6.3×10^{-5}	4σ
5.7×10^{-7}	5σ

I refer to the table A.2 which elucidates $2\Delta \ln L$ for several combinations of α and the number of the parameters in [184] again.

Table A.2: Values of $2\Delta \ln L$ corresponding to a probability α in the large sample limit and for the number of estimated parameters m.

α	$m = 1$	$m = 2$	$m = 3$
0.3173	1.00	2.30	3.53
4.55×10^{-2}	4.00	6.18	8.03
2.7×10^{-3}	9.00	11.83	14.16

Case of small statistics

In the limit of small statistics, the central limit theorem and the Gaussian approximation are not longer valid. In this thesis, I utilized a more generalized method, the "likelihood ratio ordering".

Idea of likelihood ordering Before the likelihood-ratio-ordering method, I explain the idea of "likelihood ordering". In advance of the observation, one can calculate the probability of any possible count series for a certain source model. This probability is the multiplication of the Poisson probability in each bin. The sum of the probabilities of all the cases is 100%. Then all the cases are ordered by their probabilities. If the observed case is ranked at a position higher than where the cumulative probability of the more probable cases is 68% (95%), the source model is considered consistent with the observed result by 1σ (2σ). In other words, if the sum of the probabilities of more probable cases is less than 68% (95%), the source model is accepted by 1σ (2σ). One can iterate this procedure for various models with different N and Γ_γ and constrain the parameter plane.

Idea of likelihood-ratio ordering However, Feldman and Cousins pointed out a problem of this method [176]. Even if a possible case yields a small value of the likelihood for a certain model, it does not mean this possibility is negligible when the observed result is a rare case. They proposed to order the cases by the ratio of the likelihood value and the possible maximal value instead of the likelihood value itself. This method is called "likelihood ratio ordering". The possible maximal probability is given by the model which is exactly identical with the observed count series.

Appendix B

Event display plots of CalOnly photon candidates

In this chapter, I exhibit several event display examples of LAT CalOnly events for comparison with the events related to GRB 160509A. Gamma-ray event samples are displayed in Fig. B.1, B.2 and B.3. They are taken from the MC data set. Cosmic-ray event samples are displayed in Fig. B.4,

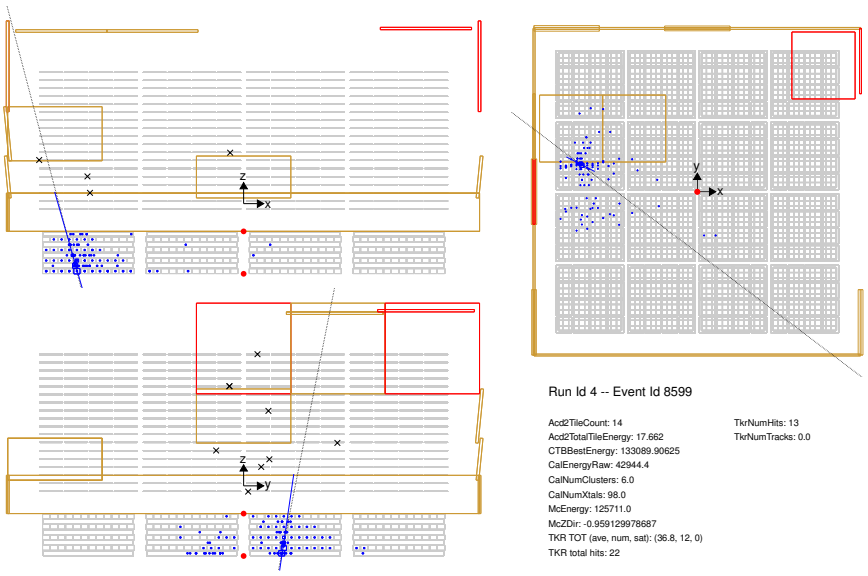

Figure B.1: MC gamma-ray event 1 with similar energy, off-axis angle and deviation of the CAL cluster position from the LAT axis to the first CalOnly event related to GRB 160509A (*cf.* Fig. 7.10).

B.5 and B.6. They are taken from the high-b OFF region (§ 7.3.2) of the flight data set.

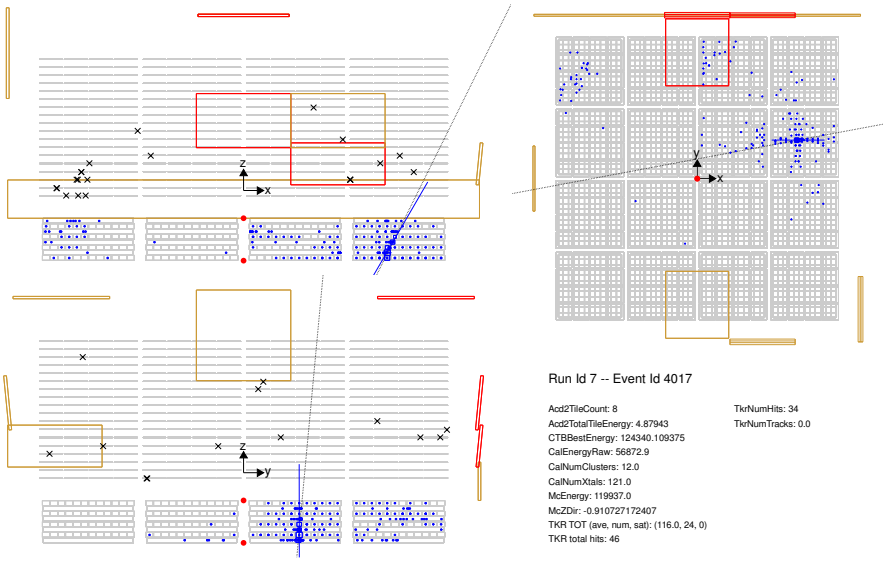

Figure B.2: MC gamma-ray event 2 with similar energy, off-axis angle and deviation of the CAL cluster position from the LAT axis to the first CalOnly event related to GRB 160509A (*cf.* Fig. 7.10).

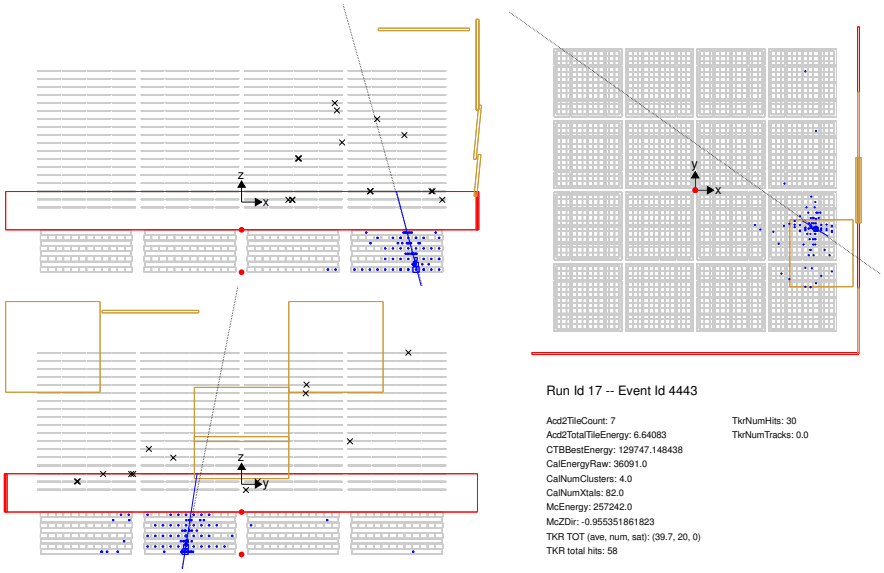

Figure B.3: MC gamma-ray event 3 with similar energy, off-axis angle and deviation of the CAL cluster position from the LAT axis to the first CalOnly event related to GRB 160509A (*cf.* Fig. 7.10).

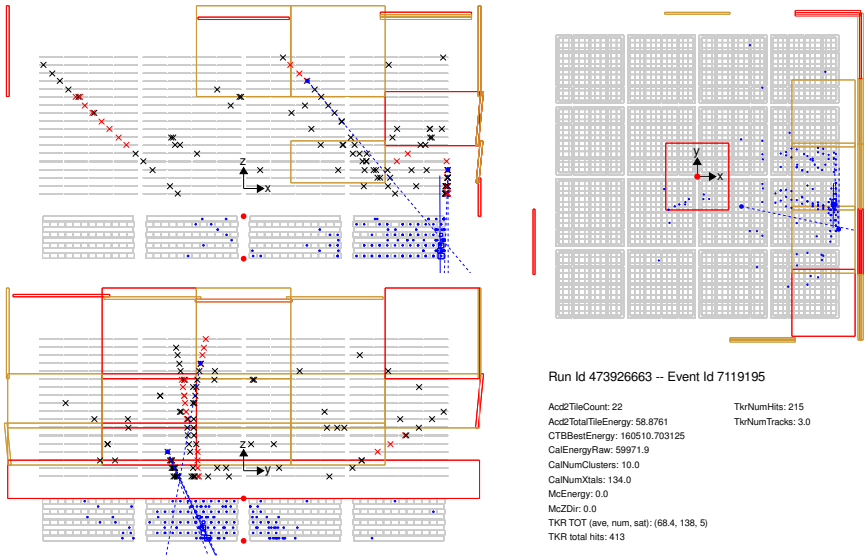

Figure B.4: "High-b" sky region event 1 with similar energy, off-axis angle and deviation of the CAL cluster position from the LAT axis to the first CalOnly event related to GRB 160509A (Fig. 7.10).

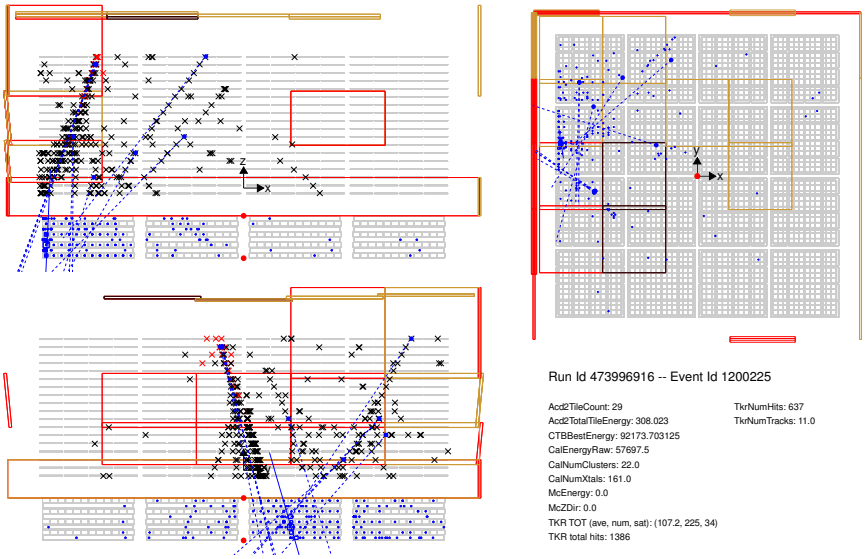

Figure B.5: "High-b" sky region event 2 with similar energy, off-axis angle and deviation of the CAL cluster position from the LAT axis to the first CalOnly event related to GRB 160509A (Fig. 7.10).

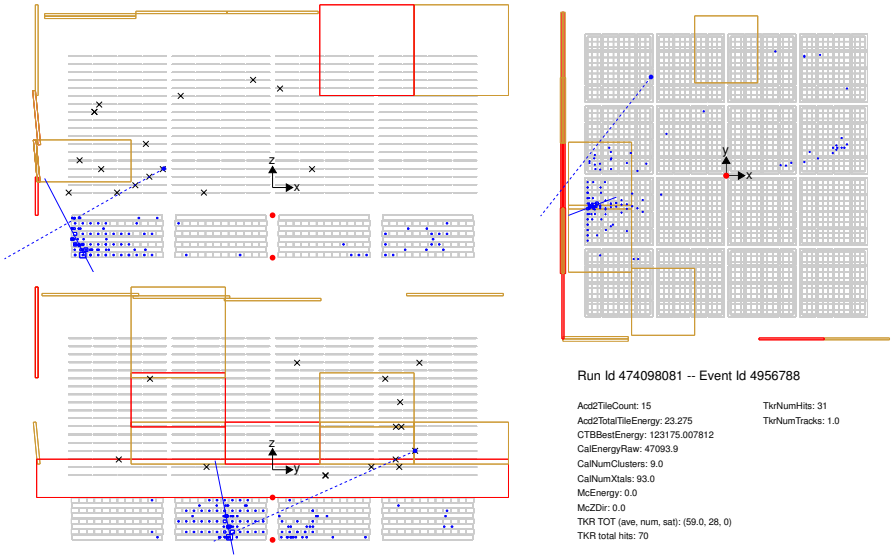

Figure B.6: "High-b" sky region event 3 with similar energy, off-axis angle and deviation of the CAL cluster position from the LAT axis to the first CalOnly event related to GRB 160509A (Fig. 7.10).

The high-b events in Fig. B.4 and B.5 exhibited many hits in the TKR and the shower energy depositions more spread in the CAL. The energy deposition of the event in Fig. B.6 is relatively clean, but the extrapolated shower axis was close to the significantly fired (red) ACD tiles. It therefore looks like an electron or positron.

Appendix C

Contribution of 1ES1959+650

I derived the light curves of 1ES1959+650 from the LAT data as plotted in Fig. C.1. The flux values were determined by aperture photometry analysis [185]. In this analysis, the flux within a RoI is calculated as it is, without background subtractions. This method thus provides a conservative estimation of the contamination of the source.

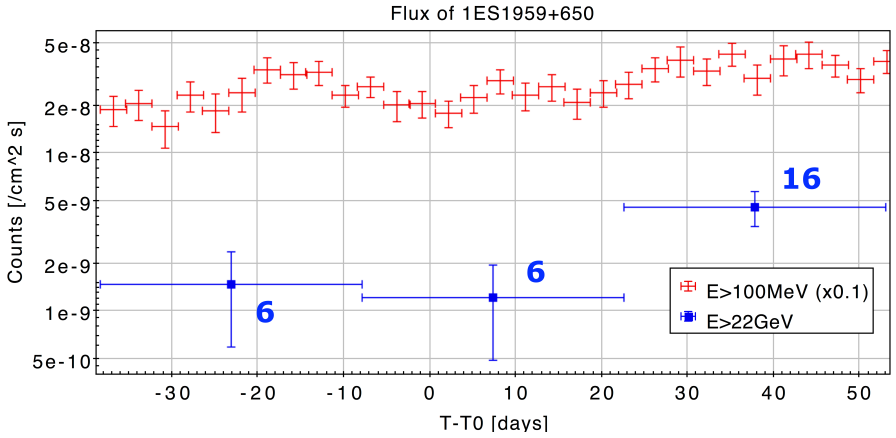

Figure C.1: Light curves of 1ES1959+650 for the time periods around GRB 160509A for two energy thresholds, 100 MeV (red) and 22 GeV (blue). The photon flux values were derived with aperture photometry analysis. The origin corresponds to the GBM trigger time of GRB 160509A. Each of the three numbers represents the detected P8R2_SOURCE_V6 count above 22 GeV in each time bin, whose duration is about one month.

In the time periods around GRB 160509A, the photon flux above the CalOnly energy threshold 22 GeV is $\lesssim 2 \times 10^{-9}\mathrm{cm}^{-2} \cdot \mathrm{s}^{-1}$. The effective area of the CalOnly_R100 for the GRB is $0.43\,\mathrm{m}^2$. Consequently, the predicted count for 10 ks is roughly expected to be 0.086 events. The PSF95% for

an event with $E = 116\,\mathrm{GeV}$ and $\theta = 9°.9$ is $9°.65$. The PSF95% for an event with $E = 63\,\mathrm{GeV}$ and $\theta = 9°.5$ is $6°.72$. The angular distance values of the reconstructed event direction and the GRB position from 1ES1959+650 are $15°.6$ and $11°.5$ respectively. Because both of them are further than the PSF95%, the contamination is much smaller than 4.3×10^{-3} events. This is much lower than the uniform backgrounds reported in § 7.4.3.

Bibliography

[1] Katharine C. Walker, Bradley E. Schaefer, and E. E. Fenimore. Gamma-Ray Bursts Have Millisecond Variability. *The Astrophysical Journal*, 537(1):264, 2000. URL http://stacks.iop.org/0004-637X/537/i=1/a=264.

[2] G. J. Fishman, C. A. Meegan, R. B. Wilson, et al. The first BATSE gamma-ray burst catalog. *ApJS*, 92:229–283, May 1994. doi: 10.1086/191968.

[3] D. Band, J. Matteson, L. Ford, et al. BATSE observations of gamma-ray burst spectra. I - Spectral diversity. *Astrophysical Journal*, Part 1 (ISSN 0004-637X), vol. 413(1):281–292, 8 1993. URL http://adsbit.harvard.edu//full/1993ApJ...413..281B/0000281.000.html.

[4] M. Ackermann, M. Ajello, K. Asano, et al. Multiwavelength Observations of GRB 110731A: GeV Emission from Onset to Afterglow. *The Astrophysical Journal*, 763(2):71, 2013. URL http://stacks.iop.org/0004-637X/763/i=2/a=71.

[5] S. B. Cenko, D. A. Frail, F. A. Harrison, et al. The Collimation and Energetics of the Brightest Swift Gamma-ray Bursts. *The Astrophysical Journal*, 711(2):641, 2010. URL http://stacks.iop.org/0004-637X/711/i=2/a=641.

[6] Alan P. Lightman George B. Rybicki. *RADIATIVE PROCESSES IN ASTROPHYSICS*. John Wiley & Sons, 1985.

[7] M. Longair. *High Energy Astrophysics*. CAMBRIDGE UNIVERSITY PRESS, third edition edition, 2011.

[8] Re'em Sari, Tsvi Piran, and Ramesh Narayan. Spectra and Light Curves of Gamma-Ray Burst Afterglows. *The Astrophysical Journal Letters*, 497(1):L17, 1998. URL http://stacks.iop.org/1538-4357/497/i=1/a=L17.

[9] O. C. de Jager, A. K. Harding, P. F. Michelson, et al. Gamma-Ray Observations of the Crab Nebula: A Study of the Synchro-Compton Spectrum. *ApJ*, 457:253, January 1996. doi: 10.1086/176726.

[10] P. Kumar, R. A. Hernández, Ž. Bošnjak, and R. Barniol Duran. Maximum synchrotron frequency for shock-accelerated particles. *Monthly Notices of the Royal Astronomical Society: Letters*, 427(1):L40–L44, 2012. doi: 10.1111/j.1745-3933.2012.01341.x. URL + http://dx.doi.org/10.1111/j.1745-3933.2012.01341.x.

[11] Xiang-Yu Wang, Ruo-Yu Liu, and Martin Lemoine. On the Origin of > 10 GeV Photons in Gamma-Ray Burst Afterglows. *The Astrophysical Journal Letters*, 771(2):L33, 2013. URL http://stacks.iop.org/2041-8205/771/i=2/a=L33.

[12] F. A. Aharonian. *Very High Energy Cosmic Gamma Radiation: A Crucial Window On The Extreme Universe*. World Scientific Publishing Co. Pte. Ltd., 2004.

[13] A. Panaitescu and P. Kumar. Analytic Light Curves of Gamma-Ray Burst Afterglows: Homogeneous versus Wind External Media. *The Astrophysical Journal*, 543(1):66, 2000. URL http://stacks.iop.org/0004-637X/543/i=1/a=66.

[14] Re'em Sari and Ann A. Esin. On the Synchrotron Self-Compton Emission from Relativistic Shocks and Its Implications for Gamma-Ray Burst Afterglows. *The Astrophysical Journal*, 548(2):787, 2001. URL http://stacks.iop.org/0004-637X/548/i=2/a=787.

[15] Re'em Sari, Ramesh Narayan, and Tsvi Piran. Cooling Timescales and Temporal Structure of Gamma-Ray Bursts. *The Astrophysical Journal*, 473(1):204, 1996. URL http://stacks.iop.org/0004-637X/473/i=1/a=204.

[16] R. W. Klebesadel, I. B. Strong, and R. A. Olson. Observations of Gamma-Ray Bursts of Cosmic Origin. *ApJL*, 182:L85, June 1973. doi: 10.1086/181225.

[17] Gerald J. Fishman and Charles A. Meegan. Gamma-Ray Bursts. *Annual Review of Astronomy and Astrophysics*, 33(1):415–458, 1995. doi: 10.1146/annurev.aa.33.090195.002215. URL https://doi.org/10.1146/annurev.aa.33.090195.002215.

[18] D. Gruber, A. Goldstein, V. Weller von Ahlefeld, et al. The Fermi GBM Gamma-Ray Burst Spectral Catalog: Four Years of Data. *ApJS*, 211:12, March 2014. doi: 10.1088/0067-0049/211/1/12.

[19] A. von Kienlin, C. A. Meegan, W. S. Paciesas, et al. The Second Fermi GBM Gamma-Ray Burst Catalog: The First Four Years. *ApJS*, 211:13, March 2014. doi: 10.1088/0067-0049/211/1/13.

[20] P. Narayana Bhat, C. A. Meegan, A. von Kienlin, et al. The Third Fermi GBM Gamma-Ray Burst Catalog: The First Six Years. *ApJS*, 223:28, April 2016. doi: 10.3847/0067-0049/223/2/28.

[21] J. P. Lestrade G. J. Fishman C. A. Meegan R. B. Wilson T. A. Parnell R. W. Austin F. A. Berry J. M. Horack S. D. Storey W. S. Paciesas, G. N. Pendleton. Performance Of The Large-Area Detectors For The Burst And Transient Source Experiment (BATSE) On The Gamma Ray Observatory, 1989. URL https://doi.org/10.1117/12.962574.

[22] P. N. Bhat, G. J. Fishman, C. A. Meegan, et al. Evidence for sub-millisecond structure in a γ-ray burst. *Nature*, 359:217 EP –, 09 1992. URL http://dx.doi.org/10.1038/359217a0.

[23] E. P. Mazets, S. V. Golenetskii, V. N. Il'Inskii, et al. Catalog of cosmic gamma-ray bursts from the KONUS experiment data. *Astrophysics and Space Science*, 80(1):3–83, Nov 1981. ISSN 1572-946X. doi: 10.1007/BF00649140. URL https://doi.org/10.1007/BF00649140.

[24] C. Kouveliotou, C. A. Meegan, G. J. Fishman, et al. Identification of two classes of gamma-ray bursts. *ApJL*, 413:L101–L104, August 1993. doi: 10.1086/186969.

[25] T. L. Cline, U. D. Desai, R. W. Klebesadel, and I. B. Strong. Energy Spectra of Cosmic Gamma-Ray Bursts. *ApJL*, 185:L1, October 1973. doi: 10.1086/181309.

[26] T. L. Cline and U. D. Desai. Observations of cosmic gamma-ray bursts with IMP-7 - Evidence for a single spectrum. *ApJL*, 196:L43–L46, February 1975. doi: 10.1086/181740.

[27] E. P. Mazets, S. V. Golenetskii, V. N. Ilinskii, et al. Venera 11 and 12 observations of gamma-ray bursts - The Cone experiment. *Soviet Astronomy Letters*, 5:163–167, January 1979.

[28] E. P. Mazets and S. V. Golenetskii. Recent Results from the Gamma-Ray Burst Studies in the KONUS Experiment. *Ap&SS*, 75:47–81, March 1981. doi: 10.1007/BF00651384.

[29] E. P. Mazets, S. V. Golenetskii, V. N. Ilyinskii, et al. Cosmic gamma-ray burst spectroscopy. *Astrophysics and Space Science*, 82(2):261–282, Mar 1982. ISSN 1572-946X. doi: 10.1007/BF00651438. URL https://doi.org/10.1007/BF00651438.

[30] S. M. Matz, D. J. Forrest, W. T. Vestrand, et al. High-energy emission in gamma-ray bursts. *ApJL*, 288:L37–L40, January 1985. doi: 10.1086/184417.

[31] C. Winkler, K. Bennett, H. Bloemen, et al. The gamma-ray burst of 3 May 1991 observed by COMPTEL on board GRO. *A&A*, 255:L9–L12, February 1992.

[32] E. J. Schneid, D. L. Bertsch, C. E. Fichtel, et al. EGRET detection of high energy gamma rays from the gamma-ray burst of 3 May 1991. *A&A*, 255:L13–L16, February 1992.

[33] Michael S. Briggs, William S. Paciesas, Geoffrey N. Pendelton, et al. The isotropy of gamma - ray bursts: Dipole and quadrupole tests. *AIP Conference Proceedings*, 307(1):44–48, 1994. doi: 10.1063/1.45847. URL https://aip.scitation.org/doi/abs/10.1063/1.45847.

[34] Adam Goldstein, J. Michael Burgess, Robert D. Preece, et al. The Fermi GBM Gamma-Ray Burst Spectral Catalog: The First Two Years. *The Astrophysical Journal Supplement Series*, 199(1):19, 2012. URL http://stacks.iop.org/0067-0049/199/i=1/a=19.

[35] E. Costa, F. Frontera, J. Heise, et al. Discovery of an X-ray afterglow associated with the γ-ray burst of 28 February 1997. *Nature*, 387:783 EP –, 06 1997. URL http://dx.doi.org/10.1038/42885.

[36] J. van Paradijs, P. J. Groot, T. Galama, et al. Transient optical emission from the error box of the γ-ray burst of 28 February 1997. *Nature*, 386:686 EP –, 04 1997. URL http://dx.doi.org/10.1038/386686a0.

[37] T. J. Galama, P. M. Vreeswijk, J. van Paradijs, et al. An unusual supernova in the error box of the γ-ray burst of 25 April 1998. *Nature*, 395:670 EP –, 10 1998. URL http://dx.doi.org/10.1038/27150.

[38] Jens Hjorth, Jesper Sollerman, Palle Møller, et al. A very energetic supernova associated with the γ-ray burst of 29 March 2003. *Nature*, 423:847 EP –, 06 2003. URL http://dx.doi.org/10.1038/nature01750.

[39] K. Z. Stanek, T. Matheson, P. M. Garnavich, et al. Spectroscopic Discovery of the Supernova 2003dh Associated with GRB 030329. *The Astrophysical Journal Letters*, 591(1):L17, 2003. URL http://stacks.iop.org/1538-4357/591/i=1/a=L17.

[40] A. S. Fruchter, A. J. Levan, L. Strolger, et al. Long γ-ray bursts and core-collapse supernovae have different environments. *Nature*, 441:463 EP –, 05 2006. URL http://dx.doi.org/10.1038/nature04787.

[41] N. Gehrels, G. Chincarini, P. Giommi, et al. The Swift Gamma-Ray Burst Mission. *The Astrophysical Journal*, 611(2):1005, 2004. URL http://stacks.iop.org/0004-637X/611/i=2/a=1005.

[42] N. Gehrels, C. L. Sarazin, P. T. O'Brien, et al. A short γ-ray burst apparently associated with an elliptical galaxy at redshift z = 0.225. *Nature*, 437:851 EP –, 10 2005. URL http://dx.doi.org/10.1038/nature04142.

[43] Ehud Nakar. Short-hard gamma-ray bursts. *Physics Reports*, 442(1):166 – 236, 2007. ISSN 0370-1573. doi: https://doi.org/10.1016/j.physrep.2007.02.005. URL http://www.sciencedirect.com/science/article/pii/S0370157307000476. The Hans Bethe Centennial Volume 1906-2006.

[44] N. R. Tanvir, A. J. Levan, A. S. Fruchter, et al. A 'kilonova'associated with the short-duration γ-ray burst GRB 130603B. *Nature*, 500:547 EP –, 08 2013. URL http://dx.doi.org/10.1038/nature12505.

[45] E. Berger, W. Fong, and R. Chornock. An r-process Kilonova Associated with the Short-hard GRB 130603B. *The Astrophysical Journal Letters*, 774(2):L23, 2013. URL http://stacks.iop.org/2041-8205/774/i=2/a=L23.

[46] V. Connaughton, M. S. Briggs, A. Goldstein, et al. Localization of Gamma-Ray Bursts Using the Fermi Gamma-Ray Burst Monitor. *The Astrophysical Journal Supplement Series*, 216(2): 32, 2015. URL http://stacks.iop.org/0067-0049/216/i=2/a=32.

[47] B. P. Abbott, R. Abbott, T. D. Abbott, et al. GW170817: Observation of Gravitational Waves from a Binary Neutron Star Inspiral. *Phys. Rev. Lett.*, 119:161101, Oct 2017. doi: 10.1103/PhysRevLett.119.161101. URL https://link.aps.org/doi/10.1103/PhysRevLett.119.161101.

[48] B. P. Abbott, R. Abbott, T. D. Abbott, et al. Multi-messenger Observations of a Binary Neutron Star Merger. *The Astrophysical Journal Letters*, 848(2):L12, 2017. URL http://stacks.iop.org/2041-8205/848/i=2/a=L12.

[49] Bing Zhang, Y. Z. Fan, Jaroslaw Dyks, et al. Physical Processes Shaping Gamma-Ray Burst X-Ray Afterglow Light Curves: Theoretical Implications from the Swift X-Ray Telescope Observations. *The Astrophysical Journal*, 642(1):354, 2006. URL http://stacks.iop.org/0004-637X/642/i=1/a=354.

[50] S. Vaughan, M. R. Goad, A. P. Beardmore, et al. Swift Observations of the X-Ray-Bright GRB 050315. *The Astrophysical Journal*, 638(2):920, 2006. URL http://stacks.iop.org/0004-637X/638/i=2/a=920.

[51] Giancarlo Cusumano, Vanessa Mangano, Lorella Angelini, et al. Swift XRT Observations of the Afterglow of GRB 050319. *The Astrophysical Journal*, 639(1):316, 2006. URL http://stacks.iop.org/0004-637X/639/i=1/a=316.

[52] D. N. Burrows, P. Romano, A. Falcone, et al. Bright X-ray Flares in Gamma-Ray Burst Afterglows. *Science*, 309(5742):1833–1835, 2005. ISSN 0036-8075. doi: 10.1126/science.1116168. URL http://science.sciencemag.org/content/309/5742/1833.

[53] K. Hurley, B. L. Dingus, R. Mukherjee, et al. Detection of a [gamma]-ray burst of very long duration and very high energy. *Nature*, 372(6507):652–654, 12 1994. URL http://dx.doi.org/10.1038/372652a0.

[54] V. Pelassa, R. Preece, F. Piron, et al. The LAT Low-Energy technique for Fermi Gamma-Ray Bursts spectral analysis. *ArXiv e-prints*, February 2010.

[55] Daniel Kocevski, J.D. Myers, Nicola Omodei, et al. Fermi LAT GRBs, 2017. URL https://fermi.gsfc.nasa.gov/ssc/observations/types/grbs/lat_grbs.

[56] M. Ackermann, M. Ajello, K. Asano, et al. The First Fermi-LAT Gamma-Ray Burst Catalog. *The Astrophysical Journal Supplement Series*, 209(1):11, 2013. URL http://stacks.iop.org/0067-0049/209/i=1/a=11.

[57] M. Ackermann, M. Ajello, K. Asano, et al. Fermi-LAT Observations of the Gamma-Ray Burst GRB 130427A. *Science*, 343(6166):42–47, 2014. ISSN 0036-8075. doi: 10.1126/science.1242353. URL http://science.sciencemag.org/content/343/6166/42.

[58] L. Nava, G. Vianello, N. Omodei, et al. Clustering of LAT light curves: a clue to the origin of high-energy emission in gamma-ray bursts. *Monthly Notices of the Royal Astronomical Society*, 443(4):3578–3585, 2014. doi: 10.1093/mnras/stu1451. URL + http://dx.doi.org/10.1093/mnras/stu1451.

[59] Yuki Kaneko, Enrico Ramirez-Ruiz, Jonathan Granot, et al. Prompt and Afterglow Emission Properties of Gamma-Ray Bursts with Spectroscopically Identified Supernovae. *The Astrophysical Journal*, 654(1):385, 2007. URL http://stacks.iop.org/0004-637X/654/i=1/a=385.

[60] Edo Berger. Short-Duration Gamma-Ray Bursts. *Annual Review of Astronomy and Astrophysics*, 52(1):43–105, 2014. doi: 10.1146/annurev-astro-081913-035926. URL https://doi.org/10.1146/annurev-astro-081913-035926.

[61] The Fermi Large Area Telescope Team, M. Ackermann, M. Ajello, et al. Constraining the High-energy Emission from Gamma-Ray Bursts with Fermi. *The Astrophysical Journal*, 754 (2):121, 2012. URL http://stacks.iop.org/0004-637X/754/i=2/a=121.

[62] G. Vianello, R. Gill, J. Granot, et al. The Bright and the Slow – GRBs 100724B & 160509A with high-energy cutoffs at $\lesssim 100$ MeV. 2017.

[63] A. A. Abdo, M. Ackermann, M. Ajello, et al. Fermi Observations of GRB 090902B: A Distinct Spectral Component in the Prompt and Delayed Emission. *The Astrophysical Journal Letters*, 706(1):L138, 2009. URL http://stacks.iop.org/1538-4357/706/i=1/a=L138.

[64] M. Ackermann, M. Ajello, K. Asano, et al. Detection of a Spectral Break in the Extra Hard Component of GRB 090926A. *The Astrophysical Journal*, 729(2):114, 2011. URL http://stacks.iop.org/0004-637X/729/i=2/a=114.

[65] Yassine, M., Piron, F., Mochkovitch, R., and Daigne, F. Time evolution of the spectral break in the high-energy extra component of GRB 090926A. *A&A*, 606:A93, 2017. doi: 10.1051/0004-6361/201630353. URL https://doi.org/10.1051/0004-6361/201630353.

[66] W. B. Atwood, L. Baldini, J. Bregeon, et al. New Fermi-LAT Event Reconstruction Reveals More High-energy Gamma Rays from Gamma-Ray Bursts. *The Astrophysical Journal*, 774(1): 76, 2013. URL http://stacks.iop.org/0004-637X/774/i=1/a=76.

[67] G. Vianello, D. Kocevski, J. Racusin, and V. Connaughton. GRB 120916A: Fermi-LAT detection of a burst., 2013. URL http://adsabs.harvard.edu/abs/2013GCN.15196....1V.

[68] Qing-Wen Tang, Pak-Hin Thomas Tam, and Xiang-Yu Wang. An Inverse Compton Origin for the 55 GeV Photon in the Late Afterglow of GRB 130907A. *The Astrophysical Journal*, 788 (2):156, 2014. URL http://stacks.iop.org/0004-637X/788/i=2/a=156.

[69] Pak-Hin Thomas Tam, Xin-Bo He, Qing-Wen Tang, and Xiang-Yu Wang. An Evolving GeV Spectrum from Prompt to Afterglow: The Case of GRB 160509A. *The Astrophysical Journal Letters*, 844(1):L7, 2017. URL http://stacks.iop.org/2041-8205/844/i=1/a=L7.

[70] Scott Wakely and Deirdre Horan. TeVCat, 4 2018. URL http://tevcat.uchicago.edu.

[71] Aharonian, F., Akhperjanian, A. G., Barres de Almeida, U., et al. HESS observations of bursts in 2003-2007. *A&A*, 495(2):505–512, 2009. doi: 10.1051/0004-6361:200811072. URL https://doi.org/10.1051/0004-6361:200811072.

[72] C. Hoischen, A. Blazer, E. Bissaldi, et al. GRB Observations with H.E.S.S. II. *ArXiv e-prints*, August 2017.

[73] Alessandro Carosi, Michele Peresano, Markus Gaug, et al. Recent follow-up observations of GRBs in the very high energy band with the MAGIC telescopes. *PoS*, page 809, 2015.

[74] A. U. Abeysekara, A. Archer, W. Benbow, et al. A Strong Limit on the Very-high-energy Emission from GRB 150323A. *The Astrophysical Journal*, 857(1):33, 2018. URL http://stacks.iop.org/0004-637X/857/i=1/a=33.

[75] A. Domínguez, J. R. Primack, D. J. Rosario, et al. Extragalactic background light inferred from AEGIS galaxy-SED-type fractions. *Monthly Notices of the Royal Astronomical Society*, 410(4):2556–2578, 2011. doi: 10.1111/j.1365-2966.2010.17631.x. URL + http://dx.doi.org/10.1111/j.1365-2966.2010.17631.x.

[76] Rene A. Ong. Cherenkov Telescope Array: The Next Generation Gamma-ray Observatory. In *Proceedings, 35th International Cosmic Ray Conference (ICRC 2017): Bexco, Busan, Korea, July 12-20, 2017*, 2017. URL https://inspirehep.net/record/1624131/files/arXiv:1709.05434.pdf.

[77] R. Atkins, W. Benbow, D. Berley, et al. Milagrito, a TeV air-shower array. *Nuclear Instruments and Methods in Physics Research Section A: Accelerators, Spectrometers, Detectors and Associated Equipment*, 449(3):478 – 499, 2000. ISSN 0168-9002. doi: https://doi.org/10.1016/S0168-9002(00)00146-7. URL http://www.sciencedirect.com/science/article/pii/S0168900200001467.

[78] R. Atkins, W. Benbow, D. Berley, et al. Evidence for TeV Emission from GRB 970417a. *The Astrophysical Journal Letters*, 533(2):L119, 2000. URL http://stacks.iop.org/1538-4357/533/i=2/a=L119.

[79] R. Atkins, W. Benbow, D. Berley, et al. The High-Energy Gamma-Ray Fluence and Energy Spectrum of GRB 970417a from Observations with Milagrito. *The Astrophysical Journal*, 583 (2):824, 2003. URL http://stacks.iop.org/0004-637X/583/i=2/a=824.

[80] R. Alfaro, C. Alvarez, J. D. Álvarez, et al. Search for Very-high-energy Emission from Gamma-Ray Bursts Using the First 18 Months of Data from the HAWC Gamma-Ray Observatory. *The Astrophysical Journal*, 843(2):88, 2017. URL http://stacks.iop.org/0004-637X/843/i=2/a=88.

[81] Tsvi Piran. Gamma-ray bursts and the fireball model. *Physics Reports*, 314(6):575 – 667, 1999. ISSN 0370-1573. doi: https://doi.org/10.1016/S0370-1573(98)00127-6. URL http://www.sciencedirect.com/science/article/pii/S0370157398001276.

[82] M. Ruderman. THEORIES OF γ-RAY BURSTS. *Annals of the New York Academy of Sciences*, 262(1):164–180, 1975. ISSN 1749-6632. doi: 10.1111/j.1749-6632.1975.tb31430.x. URL http://dx.doi.org/10.1111/j.1749-6632.1975.tb31430.x.

[83] WOLFGANG K. H. SCHMIDT. Distance limit for a class of model γ-ray burst sources. *Nature*, 271:525 EP –, 02 1978. URL http://dx.doi.org/10.1038/271525a0.

[84] E. E. Fenimore, R. I. Epstein, and C. Ho. The escape of 100 MeV photons from cosmological gamma-ray bursts. *A&AS*, 97:59–62, January 1993.

[85] E. Woods and A. Loeb. Empirical Constraints on Source Properties and Host Galaxies of Cosmological Gamma-Ray Bursts. *ApJ*, 453:583, November 1995. doi: 10.1086/176421.

[86] James E. Rhoads. How to Tell a Jet from a Balloon: A Proposed Test for Beaming in Gamma-Ray Bursts. *The Astrophysical Journal Letters*, 487(1):L1, 1997. URL http://stacks.iop.org/1538-4357/487/i=1/a=L1.

[87] D. A. Perley, S. B. Cenko, A. Corsi, et al. The Afterglow of GRB 130427A from 1 to 10^{16} GHz. *The Astrophysical Journal*, 781(1):37, 2014. URL http://stacks.iop.org/0004-637X/781/i=1/a=37.

[88] P. Mészáros and M. J. Rees. Steep Slopes and Preferred Breaks in Gamma-Ray Burst Spectra: The Role of Photospheres and Comptonization. *The Astrophysical Journal*, 530(1):292, 2000. URL http://stacks.iop.org/0004-637X/530/i=1/a=292.

[89] P. Mészáros and M. J. Rees. Poynting Jets from Black Holes and Cosmological Gamma-Ray Bursts. *The Astrophysical Journal Letters*, 482(1):L29, 1997. URL http://stacks.iop.org/1538-4357/482/i=1/a=L29.

[90] V. V. Usov. On the nature of non-thermal radiation from cosmological γ-ray bursters. *Monthly Notices of the Royal Astronomical Society*, 267(4):1035–1038, 1994. doi: 10.1093/mnras/267.4.1035. URL http://dx.doi.org/10.1093/mnras/267.4.1035.

[91] J. I. Katz. Yet Another Model of Gamma-Ray Bursts. *The Astrophysical Journal*, 490(2):633, 1997. URL http://stacks.iop.org/0004-637X/490/i=2/a=633.

[92] M. J. Rees and P. Meszaros. Unsteady outflow models for cosmological gamma-ray bursts. *ApJL*, 430:L93–L96, August 1994. doi: 10.1086/187446.

[93] Shiho Kobayashi, Tsvi Piran, and Re'em Sari. Can Internal Shocks Produce the Variability in Gamma-Ray Bursts? *The Astrophysical Journal*, 490(1):92, 1997. URL http://stacks.iop.org/0004-637X/490/i=1/a=92.

[94] F. Daigne and R. Mochkovitch. Gamma-ray bursts from internal shocks in a relativistic wind: temporal and spectral properties. *Monthly Notices of the Royal Astronomical Society*, 296(2):275–286, 1998. doi: 10.1046/j.1365-8711.1998.01305.x. URL http://dx.doi.org/10.1046/j.1365-8711.1998.01305.x.

[95] Gabriele Ghisellini, Annalisa Celotti, and Davide Lazzati. Constraints on the emission mechanisms of gamma-ray bursts. *Monthly Notices of the Royal Astronomical Society*, 313(1):L1–L5, 2000. doi: 10.1046/j.1365-8711.2000.03354.x. URL + http://dx.doi.org/10.1046/j.1365-8711.2000.03354.x.

[96] G. Ghisellini, editor. *Radiative Processes in High Energy Astrophysics*, volume 873 of *Lecture Notes in Physics, Berlin Springer Verlag*, 2013. doi: 10.1007/978-3-319-00612-3.

[97] Paolo A. Mazzali, Jinsong Deng, Nozomu Tominaga, et al. The Type Ic Hypernova SN 2003dh/GRB 030329. *The Astrophysical Journal Letters*, 599(2):L95, 2003. URL http://stacks.iop.org/1538-4357/599/i=2/a=L95.

[98] D. Xu, A. de Ugarte Postigo, G. Leloudas, et al. Discovery of the Broad-lined Type Ic SN 2013cq Associated with the Very Energetic GRB 130427A. *The Astrophysical Journal*, 776(2): 98, 2013. URL http://stacks.iop.org/0004-637X/776/i=2/a=98.

[99] Pawan Kumar and Bing Zhang. The physics of gamma-ray bursts and relativistic jets. *Physics Reports*, 561(Supplement C):1 – 109, 2015. ISSN 0370-1573. doi: https://doi.org/10.1016/j.physrep.2014.09.008. URL

http://www.sciencedirect.com/science/article/pii/S0370157314003846. The physics of gamma-ray bursts and relativistic jets.

[100] S. E. Woosley. Gamma-ray bursts from stellar mass accretion disks around black holes. *ApJ*, 405:273–277, March 1993. doi: 10.1086/172359.

[101] Hou-Jun Lü and Bing Zhang. A Test of the Millisecond Magnetar Central Engine Model of Gamma-Ray Bursts with Swift Data. *The Astrophysical Journal*, 785(1):74, 2014. URL http://stacks.iop.org/0004-637X/785/i=1/a=74.

[102] B. Paczynski. Gamma-ray bursters at cosmological distances. *ApJL*, 308:L43–L46, September 1986. doi: 10.1086/184740.

[103] David Eichler, Mario Livio, Tsvi Piran, and David N. Schramm. Nucleosynthesis, neutrino bursts and γ-rays from coalescing neutron stars. *Nature*, 340:126 EP –, 07 1989. URL http://dx.doi.org/10.1038/340126a0.

[104] R. Narayan, B. Paczynski, and T. Piran. Gamma-ray bursts as the death throes of massive binary stars. *ApJL*, 395:L83–L86, August 1992. doi: 10.1086/186493.

[105] Avishay Gal-Yam, Ehud Nakar, Eran O. Ofek, et al. New Imaging and Spectroscopy of the Locations of Several Short-Hard Gamma-Ray Bursts. *The Astrophysical Journal*, 686(1):408, 2008. URL http://stacks.iop.org/0004-637X/686/i=1/a=408.

[106] Mannucci, F., Della Valle, M., Panagia, N., et al. The supernova rate per unit mass. *A&A*, 433(3):807–814, 2005. doi: 10.1051/0004-6361:20041411. URL https://doi.org/10.1051/0004-6361:20041411.

[107] Krzysztof Belczynski, Rosalba Perna, Tomasz Bulik, et al. A Study of Compact Object Mergers as Short Gamma-Ray Burst Progenitors. *The Astrophysical Journal*, 648(2):1110, 2006. URL http://stacks.iop.org/0004-637X/648/i=2/a=1110.

[108] Zheng Zheng and Enrico Ramirez-Ruiz. Deducing the Lifetime of Short Gamma-Ray Burst Progenitors from Host Galaxy Demography. *The Astrophysical Journal*, 665(2):1220, 2007. URL http://stacks.iop.org/0004-637X/665/i=2/a=1220.

[109] J. M. Lattimer, F. Mackie, D. G. Ravenhall, and D. N. Schramm. The decompression of cold neutron star matter. *ApJ*, 213:225–233, April 1977. doi: 10.1086/155148.

[110] Li-Xin Li and Bohdan Paczyński. Transient Events from Neutron Star Mergers. *The Astrophysical Journal Letters*, 507(1):L59, 1998. URL http://stacks.iop.org/1538-4357/507/i=1/a=L59.

[111] B. Paczynski and J. E. Rhoads. Radio Transients from Gamma-Ray Bursters. *ApJL*, 418:L5, November 1993. doi: 10.1086/187102.

[112] P. Mészáros and M. J. Rees. Optical and Long-Wavelength Afterglow from Gamma-Ray Bursts. *The Astrophysical Journal*, 476(1):232, 1997. URL http://stacks.iop.org/0004-637X/476/i=1/a=232.

[113] G. Ghisellini, G. Ghirlanda, L. Nava, and A. Celotti. GeV emission from gamma-ray bursts: a radiative fireball? *Monthly Notices of the Royal Astronomical Society*, 403(2):926–937, 2010. doi: 10.1111/j.1365-2966.2009.16171.x. URL http://dx.doi.org/10.1111/j.1365-2966.2009.16171.x.

[114] R. D. Blandford and C. F. McKee. Fluid dynamics of relativistic blast waves. *The Physics of Fluids*, 19(8):1130–1138, 1976. doi: 10.1063/1.861619. URL https://aip.scitation.org/doi/abs/10.1063/1.861619.

[115] J. I. Katz and T. Piran. Persistent Counterparts to Gamma-Ray Bursts. *The Astrophysical Journal*, 490(2):772, 1997. URL http://stacks.iop.org/0004-637X/490/i=2/a=772.

[116] A. Panaitescu, P. Mészáros, N. Gehrels, D. Burrows, and J. Nousek. Analysis of the X-ray emission of nine Swift afterglows. *Monthly Notices of the Royal Astronomical Society*, 366(4):1357–1366, 2006. doi: 10.1111/j.1365-2966.2005.09900.x. URL http://dx.doi.org/10.1111/j.1365-2966.2005.09900.x.

[117] Shiho Kobayashi. Light Curves of Gamma-Ray Burst Optical Flashes. *The Astrophysical Journal*, 545(2):807, 2000. URL http://stacks.iop.org/0004-637X/545/i=2/a=807.

[118] Re'em Sari, Tsvi Piran, and J. P. Halpern. Jets in Gamma-Ray Bursts. *The Astrophysical Journal Letters*, 519(1):L17, 1999. URL http://stacks.iop.org/1538-4357/519/i=1/a=L17.

[119] S. B. Cenko, D. A. Frail, F. A. Harrison, et al. Afterglow Observations of Fermi Large Area Telescope Gamma-ray Bursts and the Emerging Class of Hyper-energetic Events. *The Astrophysical Journal*, 732(1):29, 2011. URL http://stacks.iop.org/0004-637X/732/i=1/a=29.

[120] J. A. Nousek, C. Kouveliotou, D. Grupe, et al. Evidence for a Canonical Gamma-Ray Burst Afterglow Light Curve in the Swift XRT Data. *The Astrophysical Journal*, 642(1):389, 2006. URL http://stacks.iop.org/0004-637X/642/i=1/a=389.

[121] Andrew King, Paul T. O'Brien, Michael R. Goad, et al. Gamma-Ray Bursts: Restarting the Engine. *The Astrophysical Journal Letters*, 630(2):L113, 2005. URL http://stacks.iop.org/1538-4357/630/i=2/a=L113.

[122] Rosalba Perna, Philip J. Armitage, and Bing Zhang. Flares in Long and Short Gamma-Ray Bursts: A Common Origin in a Hyperaccreting Accretion Disk. *The Astrophysical Journal Letters*, 636(1):L29, 2006. URL http://stacks.iop.org/1538-4357/636/i=1/a=L29.

[123] Daniel Proga and Bing Zhang. The late time evolution of gamma-ray bursts: ending hyperaccretion and producing flares. *Monthly Notices of the Royal Astronomical Society: Letters*, 370(1):L61–L65, 2006. doi: 10.1111/j.1745-3933.2006.00189.x. URL + http://dx.doi.org/10.1111/j.1745-3933.2006.00189.x.

[124] Shota Kisaka and Kunihito Ioka. Long-lasting Black Hole Jets in Short Gamma-Ray Bursts. *The Astrophysical Journal Letters*, 804(1):L16, 2015. URL http://stacks.iop.org/2041-8205/804/i=1/a=L16.

[125] Yun-Wei Yu, K. S. Cheng, and Xiao-Feng Cao. The Role of Newly Born Magnetars in Gamma-ray Burst X-ray Afterglow Emission: Energy Injection and Internal Emission. *The Astrophysical Journal*, 715(1):477, 2010. URL http://stacks.iop.org/0004-637X/715/i=1/a=477.

[126] Pawan Kumar, Ramesh Narayan, and Jarrett L. Johnson. Mass fall-back and accretion in the central engine of gamma-ray bursts. *Monthly Notices of the Royal Astronomical Society*, 388(4):1729–1742, 2008. doi: 10.1111/j.1365-2966.2008.13493.x. URL + http://dx.doi.org/10.1111/j.1365-2966.2008.13493.x.

[127] Paz Beniamini, Lara Nava, Rodolfo Barniol Duran, and Tsvi Piran. Energies of GRB blast waves and prompt efficiencies as implied by modelling of X-ray and GeV afterglows. *Monthly Notices of the Royal Astronomical Society*, 454(1):1073–1085, 2015. doi: 10.1093/mnras/stv2033. URL http://dx.doi.org/10.1093/mnras/stv2033.

[128] Amanda Maxham, Bin-Bin Zhang, and Bing Zhang. Is GeV emission from Gamma-Ray Bursts of external shock origin? *Monthly Notices of the Royal Astronomical Society*, 415(1):77–82, 2011. doi: 10.1111/j.1365-2966.2011.18648.x. URL + http://dx.doi.org/10.1111/j.1365-2966.2011.18648.x.

[129] Nicole M. Lloyd-Ronning and Bing Zhang. On the Kinetic Energy and Radiative Efficiency of Gamma-Ray Bursts. *The Astrophysical Journal*, 613(1):477, 2004. URL http://stacks.iop.org/0004-637X/613/i=1/a=477.

[130] Bing Zhang, Enwei Liang, Kim L. Page, et al. GRB Radiative Efficiencies Derived from the Swift Data: GRBs versus XRFs, Long versus Short. *The Astrophysical Journal*, 655(2):989, 2007. URL http://stacks.iop.org/0004-637X/655/i=2/a=989.

[131] D. Guetta, M. Spada, and E. Waxman. Efficiency and Spectrum of Internal Gamma-Ray Burst Shocks. *The Astrophysical Journal*, 557(1):399, 2001. URL http://stacks.iop.org/0004-637X/557/i=1/a=399.

[132] Donald C. Ellison, Donald C. Warren, and Andrei M. Bykov. Monte Carlo Simulations of Nonlinear Particle Acceleration in Parallel Trans-relativistic Shocks. *The Astrophysical Journal*, 776(1):46, 2013. URL http://stacks.iop.org/0004-637X/776/i=1/a=46.

[133] Rodolfo Santana, Rodolfo Barniol Duran, and Pawan Kumar. Magnetic Fields in Relativistic Collisionless Shocks. *The Astrophysical Journal*, 785(1):29, 2014. URL http://stacks.iop.org/0004-637X/785/i=1/a=29.

[134] Lorenzo Sironi and Anatoly Spitkovsky. Particle Acceleration in Relativistic Magnetized Collisionless Electron-Ion Shocks. *The Astrophysical Journal*, 726(2):75, 2011. URL http://stacks.iop.org/0004-637X/726/i=2/a=75.

[135] Mikhail V. Medvedev and Abraham Loeb. Generation of Magnetic Fields in the Relativistic Shock of Gamma-Ray Burst Sources. *The Astrophysical Journal*, 526(2):697, 1999. URL http://stacks.iop.org/0004-637X/526/i=2/a=697.

[136] Lorenzo Sironi and Jeremy Goodman. Production of Magnetic Energy by Macroscopic Turbulence in GRB Afterglows. *The Astrophysical Journal*, 671(2):1858, 2007. URL http://stacks.iop.org/0004-637X/671/i=2/a=1858.

[137] Tsuyoshi Inoue, Katsuaki Asano, and Kunihito Ioka. Three-dimensional Simulations of Magnetohydrodynamic Turbulence Behind Relativistic Shock Waves and Their Implications for Gamma-Ray Bursts. *The Astrophysical Journal*, 734(2):77, 2011. URL http://stacks.iop.org/0004-637X/734/i=2/a=77.

[138] Schulze, S., Klose, S., Björnsson, G., et al. The circumburst density profile around GRB progenitors: a statistical study. *A&A*, 526:A23, 2011. doi: 10.1051/0004-6361/201015581. URL https://doi.org/10.1051/0004-6361/201015581.

[139] A. M. Soderberg, E. Berger, M. Kasliwal, et al. The Afterglow, Energetics, and Host Galaxy of the Short-Hard Gamma-Ray Burst 051221a. *The Astrophysical Journal*, 650(1):261, 2006. URL http://stacks.iop.org/0004-637X/650/i=1/a=261.

[140] W. B. Atwood, A. A. Abdo, M. Ackermann, et al. The Large Area Telescope on the Fermi Gamma-Ray Space Telescope Mission. *The Astrophysical Journal*, 697(2):1071, 2009. URL http://stacks.iop.org/0004-637X/697/i=2/a=1071.

[141] M. Ackermann, M. Ajello, A. Albert, et al. The Fermi Large Area Telescope on Orbit: Event Classification, Instrument Response Functions, and Calibration. *The Astrophysical Journal Supplement Series*, 203(1):4, 2012. URL http://stacks.iop.org/0067-0049/203/i=1/a=4.

[142] The Fermi Science Support Center. Overview of the LAT, September 2015. URL https://fermi.gsfc.nasa.gov/ssc/data/analysis/documentation/Cicerone/Cicerone_Introduction/LAT_overview.html.

[143] A. Hoecker, P. Speckmayer, J. Stelzer, et al. TMVA - Toolkit for Multivariate Data Analysis. *ArXiv Physics e-prints*, March 2007.

[144] The Fermi Science Support Center. FSSC_ Fermi Data >> Data Analysis >> Online Documentation >> Cicerone - Data, July 2016. URL https://fermi.gsfc.nasa.gov/ssc/data/analysis/documentation/Cicerone/Cicerone_Data/LAT_DP.html.

[145] The Fermi Science Support Center. FSSC_ Fermi Data >> Data Analysis >> Online Documentation >> Science Tools_ Cicerone - Data, 7 2018. URL https://fermi.gsfc.nasa.gov/ssc/data/analysis/documentation/Cicerone/Cicerone_Data/LAT_DP.html.

[146] Matthew Wood, Regina Caputo, Riccardo Rando, et al. Fermi LAT Performance, June 2016. URL http://www.slac.stanford.edu/exp/glast/groups/canda/lat_Performance.htm.

[147] *Pass 8: Toward the Full Realization of the Fermi-LAT Scientific Potential*, number C121028, 2012. eConf. URL http://lanl.arxiv.org/abs/1303.3514v1.

[148] Philippe Bruel and on behalf of the Fermi-LAT collaboration). Gamma rays, electrons and positrons up to 3 TeV with the Fermi Gamma-ray Space Telescope. *Journal of Physics: Conference Series*, 404(1):012033, 2012. URL http://stacks.iop.org/1742-6596/404/i=1/a=012033.

[149] The Fermi Science Support Center. FSSC_ Fermi Data >> Data Analysis >> Online Documentation >> Fermi Science Tools: Instllation, 2 2018. URL https://fermi.gsfc.nasa.gov/ssc/data/analysis/software.

[150] The Fermi Science Support Center. FSSC_ Fermi Data >> Data Analysis >> Online Documentation >> Cicerone - LAT IRFs The Point Spread Function (PSF), 4 2016. URL https://fermi.gsfc.nasa.gov/ssc/data/analysis/documentation/Cicerone/Cicerone_LAT_IRFs/IRF_PSF.html.

[151] The Fermi Science Support Center. FSSC_ Fermi Data >> Data Analysis >> Online Documentation >> Cicerone - LAT IRFs Energy Dispersion, 6 2016. URL https://fermi.gsfc.nasa.gov/ssc/data/analysis/documentation/Cicerone/Cicerone_LAT_IRFs/IRF_E_dispersion.html.

[152] The Fermi Science Support Center. gtlike, 7 2015. URL https://fermi.gsfc.nasa.gov/ssc/data/analysis/scitools/help/gtlike.txt.

[153] Amy Lien, Takanori Sakamoto, Scott D. Barthelmy, et al. The Third Swift Burst Alert Telescope Gamma-Ray Burst Catalog. *The Astrophysical Journal*, 829(1):7, 2016. URL http://stacks.iop.org/0004-637X/829/i=1/a=7.

[154] Jochen Greiner. GRBs localized with BSAX or BATSE/RXTE or ASM/RXTE or IPN or HETE or INTEGRAL or Swift or AGILE or Fermi or MAXI, 2017. URL http://www.mpe.mpg.de/ jcg/grbgen.html.

[155] M. Ackermann, M. Ajello, W. B. Atwood, et al. 2FHL: The Second Catalog of Hard Fermi-LAT Sources. *The Astrophysical Journal Supplement Series*, 222(1):5, 2016. URL http://stacks.iop.org/0067-0049/222/i=1/a=5.

[156] A. A. Abdo, M. Ackermann, M. Ajello, et al. Fermi large area telescope observations of the cosmic-ray induced γ-ray emission of the Earth's atmosphere. *Phys. Rev. D*, 80:122004, Dec 2009. doi: 10.1103/PhysRevD.80.122004. URL https://link.aps.org/doi/10.1103/PhysRevD.80.122004.

[157] K. M. Górski, E. Hivon, A. J. Banday, et al. HEALPix: A Framework for High-Resolution Discretization and Fast Analysis of Data Distributed on the Sphere. *The Astrophysical Journal*, 622(2):759, 2005. URL http://stacks.iop.org/0004-637X/622/i=2/a=759.

[158] D. Malesani, P. Goldoni, J. P. U. Fynbo, et al. GRB 090926A: VLTX-shooter redshift, 2009.

[159] N. R. Tanvir, A. J. Levan, S. B. Cenko, et al. GRB 160509A Gemini North redshift, 5 2016.

[160] Elisabetta Bissaldi and reports on behalf of the Fermi GBM Team. GRB 090926: Fermi GBM detection, 2009.

[161] Takeshi Uehara, Hiromitsu Takahashi, Julie McEnery, and report on behalf of the Fermi LAT team. GRB 090926: Fermi LAT detection, 2009.

[162] D. Grupe, S. D. Barthelmy, J. R. Cummings, et al. GRB 090926B: Swift detection of a burst, 9 2009. URL https://gcn.gsfc.nasa.gov/gcn3/9935.gcn3.

[163] C. Gronwall and L. Vetere report on behalf of the Swift/UVOT team. GRB 090926A: Swift/UVOT detection of an optical afterglow, 2009.

[164] L. Vetere and reports on behalf of the Swift-XRT team. GRB090926A: Swift-XRT refined analysis, 2009.

[165] Vernet, J., Dekker, H., D'Odorico, S., et al. X-shooter, the new wide band intermediate resolution spectrograph at the ESO Very Large Telescope. *A&A*, 536:A105, 2011. doi: 10.1051/0004-6361/201117752. URL https://doi.org/10.1051/0004-6361/201117752.

[166] F.Longo, E.Bissaldi, J. Bregeon, et al. GRB 160509A: Fermi-LAT prompt detection of a very bright burst, 2016.

[167] O.J. Roberts, G. Fitzpatrick, P. Veres, and report on behalf of the Fermi GBM Team. GRB 160509A: Fermi GBM Detection, 5 2016.

[168] J. A. Kennea, T.G.R. Roegiers, J.P. Osborne, et al. GRB 160509A: Swift-XRT afterglow detection, 2016.

[169] F. E. Marshall and T.G.R. Roegiers report on behalf of the Swift/UVOT team. GRB 160509A: Further Swift/UVOT Observations. Technical report, 2016.

[170] Navpreet Kaur, S. Chandra, Kiran S Baliyan, Sameer, and S. Ganesh. Multi-wavelength study of flaring activity in HBL 1ES 1959+650 during 2015-16, Jun 2017. URL arXiv:1706.04411v1.

[171] Franceschini, A., Rodighiero, G., and Vaccari, M. Extragalactic optical-infrared background radiation, its time evolution and the cosmic photon-photon opacity. *A&A*, 487(3):837–852, 2008. doi: 10.1051/0004-6361:200809691. URL https://doi.org/10.1051/0004-6361:200809691.

[172] Tanmoy Laskar, Kate D. Alexander, Edo Berger, et al. A Reverse Shock in GRB 160509A. *The Astrophysical Journal*, 833(1):88, 2016. URL http://stacks.iop.org/0004-637X/833/i=1/a=88.

[173] F. Acero, M. Ackermann, M. Ajello, et al. Fermi Large Area Telescope Third Source Catalog. *ApJS*, 218:23, June 2015. doi: 10.1088/0067-0049/218/2/23.

[174] FSSC. FSSC_ Fermi Data >> Data Access >> LAT Background Models, 9 2016. URL https://fermi.gsfc.nasa.gov/ssc/data/access/lat/BackgroundModels.html.

[175] F. Acero, M. Ackermann, M. Ajello, et al. Development of the Model of Galactic Interstellar Emission for Standard Point-source Analysis of Fermi Large Area Telescope Data. *The Astrophysical Journal Supplement Series*, 223(2):26, 2016. URL http://stacks.iop.org/0067-0049/223/i=2/a=26.

[176] Gary J. Feldman and Robert D. Cousins. Unified approach to the classical statistical analysis of small signals. *Phys. Rev. D*, 57:3873–3889, Apr 1998. doi: 10.1103/PhysRevD.57.3873. URL https://link.aps.org/doi/10.1103/PhysRevD.57.3873.

[177] A. Panaitescu. Seven-year Collection of Well-monitored Fermi-LAT Gamma-Ray Burst Afterglows. *The Astrophysical Journal*, 837(1):13, 2017. URL http://stacks.iop.org/0004-637X/837/i=1/a=13.

[178] J.L. Han. Observing Interstellar and Intergalactic Magnetic Fields. *Annual Review of Astronomy and Astrophysics*, 55(1):111–157, 2017. doi: 10.1146/annurev-astro-091916-055221. URL https://doi.org/10.1146/annurev-astro-091916-055221.

[179] Rudy C. Gilmore, Rachel S. Somerville, Joel R. Primack, and Alberto Domínguez. Semi-analytic modelling of the extragalactic background light and consequences for

extragalactic gamma-ray spectra. *Monthly Notices of the Royal Astronomical Society*, 422(4):3189–3207, 2012. doi: 10.1111/j.1365-2966.2012.20841.x. URL + http://dx.doi.org/10.1111/j.1365-2966.2012.20841.x.

[180] Franceschini, Alberto and Rodighiero, Giulia. The extragalactic background light revisited and the cosmic photon-photon opacity. *A&A*, 603:A34, 2017. doi: 10.1051/0004-6361/201629684. URL https://doi.org/10.1051/0004-6361/201629684.

[181] G. Maier, L. Arrabito, K. Bernlöhr, et al. Performance of the Cherenkov Telescope Array. *ArXiv e-prints*, September 2017.

[182] The Fermi Science Support Center. FSSC_ Fermi Data >> Data Analysis >> Online Documentation >> Science Tools_ Cicerone - Likelihood, 2 2012. URL https://fermi.gsfc.nasa.gov/ssc/data/analysis/documentation/Cicerone/Cicerone_Likelihood/Likelihood_overview.html.

[183] J. Neyman. X—Outline of a Theory of Statistical Estimation Based on the Classical Theory of Probability. *Philosophical Transactions of the Royal Society of London A: Mathematical, Physical and Engineering Sciences*, 236 (767):333–380, 1937. ISSN 0080-4614. doi: 10.1098/rsta.1937.0005. URL http://rsta.royalsocietypublishing.org/content/236/767/333.

[184] C. Patrignani and Particle Data Group. Review of Particle Physics. *Chinese Phys. C*, 40(10), 2016.

[185] The Fermi Science Support Center. FSSC_ Fermi Data >> Data Analysis >> Analysis Threads >> Fermi-LAT Aperture Photometry, 2 2018. URL https://fermi.gsfc.nasa.gov/ssc/data/analysis/scitools/aperture_photometry.html.